Catalysts for Improved Selectivity and Performance in Ethanol Electrolysis Cells

By

©Diala Akram Alqdeimat

A thesis submitted to the School of Graduate Studies in partial fulfillment of
the requirements for the degree of Doctor of Philosophy

Department of Chemistry
Memorial University of Newfoundland

September 2022

St. John's Newfoundland and Labrador

Abstract

The importance of direct ethanol fuel cell (DEFC) technology for a sustainable energy future has resulted in comprehensive studies of the electrochemical oxidation of ethanol. Ethanol is oxidized completely to produce CO_2 during the ethanol oxidation reaction (EOR). However, many studies found that ethanol is oxidized to produce acetic acid, acetaldehyde, and CO_2. As a result, the efficiency of the DEFC is decreased. Furthermore, many issues have hampered DEFC adoption, including low current densities, low faradic efficiencies. To overcome these problems, anode catalysts (binary and ternary) have been developed to increase the efficiency of DEFCs.

Our research focused on the development of catalysts that have high activity for the EOR and selectivity for breaking the C-C bond to form CO_2. Moreover, a secondary objective is the evaluation of catalysts to investigate the performance and selectivity of an electrolysis cell. To avoid any chemical reaction between ethanol and oxygen, an electrolysis cell was employed instead of a fuel cell (an ethanol electrolysis cell is similar to an ethanol fuel cell, but oxygen gas is replaced by nitrogen gas at the cathode and the cell reaction is driven by an applied potential). As a result, accurate results are possible.

$PtNi_x/C$ catalysts (x is the Ni:Pt atomic ratio) were synthesized in various solvents (propylene glycol (PG) and ethylene glycol (EG)) by using a polyol method. Then, they were treated with acetic acid to increase the coverage of Pt at the surface. Electrochemical analysis was carried out by cyclic voltammetry in 0.100 M ethanol and 1 M H_2SO_4 (aq) (at ambient temperature) to study the activity of these catalysts toward the oxidation of ethanol. A catalyst prepared in propylene glycol was more active toward the oxidation of ethanol than a catalyst prepared in the same way in ethylene glycol, exhibiting less poisoning at the PtNi/C(PG) catalyst by adsorbed CO. Treatment

of the PtNi/C(PG) catalyst with acetic acid to remove surface Ni further enhanced the activity toward ethanol oxidation, while it did not affect the activity of PtNi/C(EG).

The performance and selectivity toward the EOR were investigated for $PtNi_x/C$ catalysts in a nine-anode PEM electrolysis cell. It was found that acid treatment of PtNi/C(PG) and PtNi/C(EG) increased the production of CO_2. However, it did not enhance the performance of catalyst. Also, there was no improvement in the performance for $PtNi_x/C$ catalysts relative to Pt, indicating that the incorporation of Ni with Pt does not improve the slow kinetics at low potentials.

Furthermore, the nine-anode PEM electrolysis cell was used to evaluate the performance and selectivity of commercial catalysts (PtNi/C, PtCu/C, and PtFe/C) for the EOR. The goal of this research was to figure out how each metal (Ni, Cu, and Fe) impacts the activity of Pt on the EOR. Results showed that Cu as a secondary metal has more ability to produce CO_2 than Fe and Ni. However, none of these metals increase the performance at low potentials relative to Pt.

Finally, PtRu/C and PtRuCu/C catalysts were synthesized. The effect of Cu with Pt and Ru on the EOR and CO_2 yield was explored. It was found that Cu with Pt and Ru increases the production of CO_2 relative to PtRu. Also, the performance at low potentials was higher for PtRuCu/C and PtRu/C relative to Pt. Based on our results, preparing catalyst with Cu would increase the faradaic efficiency of a DEFC and decrease the production of acetic acid.

Acknowledgements

I'd like to use this opportunity to express my gratitude to everyone who has helped and supported me along this trip. First, Prof. Peter Pickup, my supervisor, has taught and mentored me to be a good researcher and scientist. Your thoughtful and constructive remarks encouraged me to improve my thinking and elevate my work to new heights. Throughout my studies, I am appreciative for your unwavering support, encouragement, and excellent counsel.

Also, I would like to thank the members of my supervisory committee: Prof. Mike Katz and Prof. Yuming Zhao, for their comments and ideas of my research path. Also, I would like to acknowledge my thesis examiners: Prof. Elena Baranova, Prof. Francesca M. Kerton, and AP. Lindsay S. Cahill, who gave me useful suggestion and comments to establish the final version of this thesis.

To all of our group at Prof. Pickup lab, I am thankful for the insightful discussions and beautiful memories we had. Special mention to Hui (PhD, 2022) and Jasmine (PhD candidate). Also, I would like to thank Dr. Jane Stockmann and her group for all the best time that we had together.

Dearest husband, I am ecstatic to have you here. Thank you for your unwavering love and support. I am grateful for all your efforts in helping me achieve my objective. Thank you very much for your unwavering support for me.

My mother, father, sisters, brother, and friends, thank you very much for your unwavering support. I adore each of you for everything that you have provided to me.

I am grateful for the School of Graduate Studies of Memorial University, the Natural Sciences and Engineering Research Council of Canada for funding, and Dr. Liqin Chen scholarships in Chemistry. Finally, I want to express my gratitude to all of lab instructors, technicians, my colleagues, staff, and academics in the Chemistry Department.

Contents

List of Tables

List of Figures

List of Abbreviation and Symbols

A	Ampere
AA	Acetic acid
AAL	Acetaldehyde
AFC	Alkaline fuel cell
℃	Celsius degree
ca.	Approximately
CO	Carbon monoxide
CO_2	Carbon dioxide
CV	Cyclic voltammetry
D_e	Energy density
D_p	Power density
DAFC	Direct alcohol fuel cell
DEFC	Direct ethanol fuel cell
DFT	Density functional theory
DHE	Dynamic hydrogen electrode
D_2O	Deuterium oxide
e^-	Electron
E	Potential
E^o	Standard potential
E_{rev}	Reversible cell potential
EEC	Ethanol electrolysis cell
EG	Ethylene glycol

ε_F	Faradaic efficiency
EOR	Ethanol oxidation reaction
eV	Electron Volt
F	Faraday constant
fcc	Face centered cubic
FTIR	Fourier transform infrared spectroscopy
H	Hour
HFC	Hydrogen fuel cell
I	Current
I_{lim}	Limiting current
G	Gibbs energy
MEA	Membrane electrode assembly
min	Minute
N	Moles of products
n_{av}	Average number of electrons
NDIR	Non-dispersive infrared
ORR	Oxygen reduction reaction
PAFC	Phosphoric acid fuel cell
PEM	Proton exchange membrane
PG	Propylene glycol
ppm	Parts per millions
Q	Charge
R	Gas constant

s	Second
SCE	Saturated calomel electrode
SHE	Standard hydrogen electrode
SOFC	Solid oxide fuel cell
TEM	Transmission electron microscopy
TGA	Thermogravimetric analysis
u	Flow rate
XRD	X-ray diffraction
η	Overpotential
ε	Efficiency
ε_E	Potential efficiency
ε_{rev}	Theoretical efficiency
Ω	Ohm
Θ	Diffraction angle

Chapter 1

1. Introduction

Fossil fuels (coal, oil, natural gas) are currently the world's main energy source. Fossil energy has been widely used in transportation and other applications. It is a fundamental driver of technology. In 2019, around 84% of global primary energy came from oil, gas, and coal.[1] However, fossil fuels are unrenewable energy because they require millions of years to form again. Also, fossil fuels are expensive.[2–5] Besides that, the most negative impact of fossil fuels is the production of a huge amount of greenhouse gases such as CO_2 through combustion. Greenhouse gases contribute to many environmental problems including global warming, ocean pollution, and air pollution. Based on these reasons, it is essential to improve and increase the use of renewable energy sources such as wind energy, solar energy, and biomass energy.

Nowadays, fuel cells can be represented as one of the most promising technologies for a renewable source of power.[6] A fuel cell is defined as a device (environmentally friendly) that converts the chemical energy of a fuel (through a redox reaction) into electrical energy. In 1839, Sir William Grove discovered the fuel cell principle.[7] However, it was in the second half of the 20th century, that understanding of fuel cell principles was expanded. The first application of fuel cells was developed by NASA for their space program in the early 1960s. They used alkaline fuel cells (AFCs) and polymer electrolyte membrane fuel cells (PEMFCs). The program productively used hydrogen as a fuel to provide heat, electricity, and pure water for space shuttle applications and vehicles.[7]

Fuel cells differ fundamentally from combustion engines because they convert chemical energy totally to electric energy without losing heat. Also, fuel cells provide low harmful emissions (greenhouse gases) and high theoretical efficiency. Thus, they cover a wide range of applications like electronic devices and transportation.[8] Moreover, when fuel cells are compared with batteries, the reactants are supplied continuously into the fuel cell .[9] Also, in the fuel cell, unlike the battery, electrodes are not consumed.[9] Moreover, fuel cells can use different fuels to generate power (e.g.

hydrogen, methanol, ethanol, etc.). Additionally, fuel cells have longer operating times than batteries and a wide range of temperatures (70 ℃ to 700 ℃).[7,8]

There are many different types of fuel cells, as shown in Figure 1.1.[10] They are differentiated based on the electrolyte (solid or liquid), the fuel (e.g. H_2), operating conditions (high or low temperature), and the applications.[6,8] For example, AFCs use alkaline as an electrolyte,[11] while phosphoric acid fuel cells (PAFCs) use phosphoric acid.[12] Moreover, molten carbonate fuel cells (MCFCs)[13] and solid oxide fuel cells (SOFCs)[14] are operated at high temperatures (e.g. 700 ℃ for MCFCs and 1000 ℃ for SOFCs). Furthermore, direct methanol fuel cells (DMFCs) and proton exchange membrane fuel cells (PEMFCs) are types of fuel cells.[15,16] Each of these cell types has its advantages, limitations, and applications. Even though the commercialization of fuel cells has been increased, there are still many limitations and challenges. For instance, the cost of cell materials (e.g. the cost of catalyst that is used to carry out the redox reaction on its surface) is one of the main challenges that reduce the ability to improve fuel cells.[17] Also, increasing the efficiency of the fuel cell is another challenge in developing fuel cells.[18] Loss of efficiency comes from several reasons based on the type of fuel cell. For example, in PEMFCs, the slow kinetic of the oxygen reduction reaction (ORR), and CO poisoning at the anode, decrease the efficiency. On the other hand, the production of carbonate salt in AFCs decreases the ion conductivity of the electrolyte, as a result, the efficiency will be decreased.

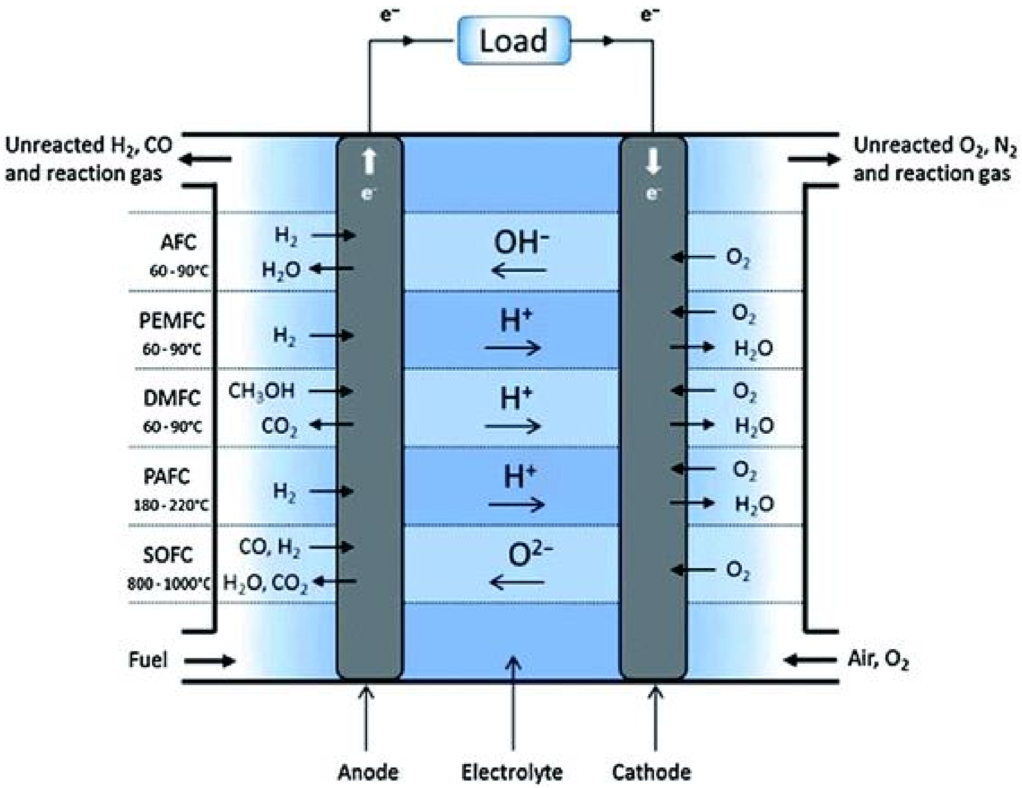

Figure 1.1: A schematic overview of different types of fuel cells. Reproduced with permission from ref.[17] Copyright 2020, ©Royal Society of Chemistry.

1.1. Proton exchange membrane fuel cells (PEMFCs)

PEMFCs have been studied widely.[10] Also, they are called polymer electrolyte membrane fuel cells because a solid polymer electrolyte membrane (e.g. Nafion) is used instead of liquid electrolyte. The operating temperature of PEMFCs is between 70 and 90 ℃ under 1–2 bar pressure.[8] There are many advantages for PEMFCs including high power density, vast power range (1 W to 500 kW), short start-up time, and low emissions (greenhouse gases).[19] These advantages allow the PEMFCs to be useful in a variety of applications such as chemical sensors and power generation.[2,20–23] Moreover, they have longer operating times; and they are smaller than batteries, thus, they are used in portable electronic devices (e.g. laptops and video recorders). Also, they do not need to be recharged from the grid.[24] Furthermore, PEMFCs have been used in the transportation field. Honda Clarity and Toyota Mirai are two examples of fuel cell vehicles (FCVs) that have been designed and exhibited.[25] In particular, Toyota commercialized its first FCV, the Mirai, in 2017.[19]

Figure 1.2 shows a schematic diagram of PEMFC. PEMFC consists mainly of a proton exchange membrane, the anode, and the cathode.[24,26,27] These components are held together to form the membrane electrode assembly (MEA), which is the heart of the fuel cell. It is clear from Figure 1.2 that the solid membrane separates electrodes from each other and the fuel (e.g. H_2) from the oxidant (e.g. O_2). When a certain fuel (e.g. H_2) is supplied into the anode, it will be oxidized electrochemically (not chemically) and protons and electrons will be produced. Through the solid membrane, protons will migrate and reach the cathode, while electrons will pass through an external electrical circuit. As a result, the electric power will be generated.

Fuels such as methanol and ethanol can be compared based on important parameters: specific energy (gravimetric; W_s), energy density (volumetric; W_e), and power density (D_p).[28] Specific energy can be defined as the energy that is stored in the fuel per unit mass (kWh kg^{-1}), while energy density is the stored energy per unit volume (kWh L^{-1}), as shown in eq. 1.1 and 1.2.[29] On the other hand, the power density is the amount of producing energy from the fuel per unit mass, volume, or area (eq. 1.3). Moreover, power is defined as the production energy per time (J/s).

$$W_s = \frac{-\Delta G^0}{M} \tag{1.1}$$

$$W_e = \frac{-\rho \Delta G^0}{M} \tag{1.2}$$

$$D_p = current\ density \times E_{cell} \tag{1.3}$$

where $\Delta G°$ is Gibbs free energy at the standard conditions, M is the molar mass of the fuel, E_{cell} is the operating potential, ρ is the density of the fuel, and current density is the current per unit area or mass.

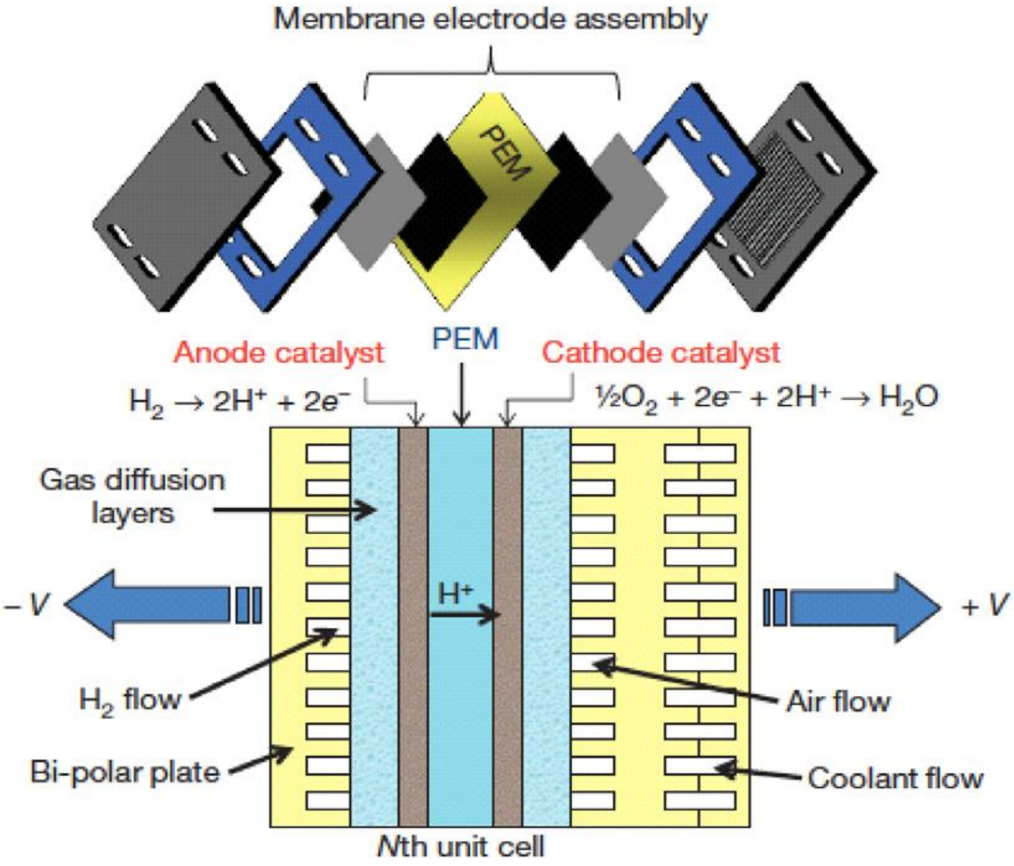

Figure 1.2: A schematic diagram of a PEMFC. Reprinted from ref,[19] Copyright (2020), with permission from Elsevier.

1.1.1. Proton exchange membrane (PEM)

The most common PEM is Dupont's Nafion® for acidic PEMFCs. It is a type of perfluorosulfonic acid membrane.[29–31] Nafion consists of polytetrafluoroethylene (PTFE, the hydrophobic backbone) and perfluorinated side-chains. Perfluorinated side-chains contain hydrophilic sulfonic acid groups (-SO_3H) at the terminals. Figure 1.3 shows the general structure of Nafion. The hydrophobic backbone provides high stability and rigidity to the membrane. Moreover, the sulfonic groups provide high conductivity of protons ($0.13\ S\ cm^{-1}$ at 75 °C)[19], and high acidity. However, the dissociation of -SO_3H occurs in the presence of water, therefore, the Nafion membrane should be hydrated.[32,33]

Additionally, Nafion membrane can be modified to prevent the crossover of the fuel (e.g. ethanol) and products of the oxidation process (e.g. acetic acid) through the membrane.[34] Gore and associates introduced a perfluorinated composite membrane reinforced with polytetrafluoroethylene, as a result, the mechanical and stability for the fuel cell with thin PEM was enhanced.[35] Moreover, Dresch et al. showed that a hybrid Nafion with 6.5 wt% SiO_2 provided better proton conductivity than unmodified Nafion.[31]

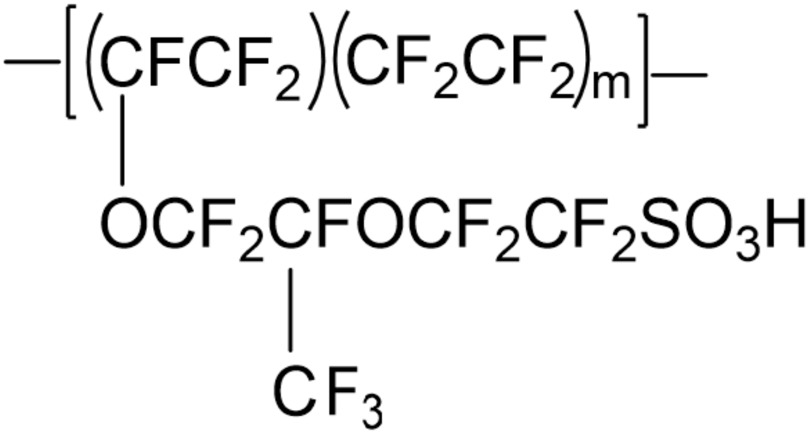

Figure 1.3: The chemical structure of Nafion.

1.1.2. Electrodes

Electrodes in PEMFCs mainly consist of a catalyst layer, a diffusion layer, and two bipolar plates. The catalyst layer is made of platinum (Pt) or platinum (Pd). The role of the catalyst layer is to carry out the electrochemical reactions on its surface. On the other hand, the diffusion layer is usually composed of a support layer (which is usually carbon cloth or carbon fiber) and a microporous layer. The microporous layer contains a mixture of carbon black and a hydrophobic polymer (polytetrafluoroethylene PTFE).[24,36] The diffusion layer is placed between the catalyst layer and the bipolar plates. Moreover, it is used to transport reactants and conduct electrons between the catalyst layers and bipolar plates.[19] Additionally, it works as mechanical support for the catalyst layers and membrane; and it protects the catalyst layers from corrosion during the reactions. On the other hand, bipolar plates are composed of carbon-based composites or metals, where the MEA and flow channels are placed.[19]

Commonly, the electrodes (anode and cathode) are made from carbon-based materials with a high surface area.[37] The carbon-based material is covered with catalyst nanoparticles as an active layer to reduce the oxidant and oxidize the fuel. Before coating the catalyst onto the diffusion layer, the catalyst should be mixed with 5% Nafion solution (in the presence of another solvent such as isopropanol and water) to increase the electronic and ionic conductivities of the catalyst.[36] The catalyst layer (ink or paste) can then be applied onto the diffusion layer surface by several methods. These methods include painting, evaporative deposition, and spraying.[36]

1.1.3. Oxygen reduction reaction (ORR)

ORR is an important reaction for many fuel cell devices. It also has a special role in the electrocatalysis field.[38] Oxygen (in the air) is used as an oxidant at the cathode in fuel cells. In the ORR, oxygen is electrochemically reduced to produce water. However, in contrast to the oxidation of hydrogen, the ORR is a complex reaction and has slow (sluggish) kinetics. Thus, the best Pt-based catalyst for the ORR requires high Pt loading (~0.4 mg cm^{-2}) to achieve a desirable fuel cell performance.[38]

In general, when oxygen is supplied at the cathode, there are two possible pathways of the ORR. In the first pathway, oxygen will be reduced to produce water with a thermodynamic standard potential of 1.229 V, as shown in eq. 1.4. However, in the second pathway, oxygen will be reduced and hydrogen peroxide will be produced, as shown in eq. 1.5,

$$O_2 + 4H^+ + 4e^- \rightarrow 2H_2O \qquad E^0 = 1.229\,V \qquad (1.4)$$

$$O_2 + 2H^+ + 2e^- \rightarrow H_2O_2 \qquad E^0 = 0.67\,V \qquad (1.5)$$

Since the standard cell potential is affected by the cathode potential ($E^0_{cell} = E^0_{cathode} - E^0_{anode}$), the first pathway (complete reduction reaction) is more efficient and favored due to its high thermodynamic standard potential. On the other hand, the second pathway (indirect two-electron pathway; partial reduction reaction) is less efficient and unfavored because of the lower thermodynamic standard potential (0.67 V) than the first pathway. Furthermore, by comparing both pathways, the first pathway produces water (environmentally friendly), while the second pathway produces hydrogen peroxide.

Usually, Pt is the most used catalyst for the ORR. However, the ORR was found to be affected by the crystalline facets and particle form of Pt.[39] The following equations show the possible mechanism of the ORR on the surface of Pt:

$$O_2 + Pt \rightarrow Pt - O_2 \qquad (1.6)$$

$$Pt - O_2 + H^+ + e^- \rightarrow Pt - HO_2 \qquad (1.7)$$

$$Pt - HO_2 + Pt \rightarrow Pt - OH + Pt - O \quad (1.8)$$

$$Pt - OH + Pt - O + 4H^+ + e^- \rightarrow 2Pt + 2H_2O \quad (1.9)$$

However, Pt-based are used more than pure Pt catalysts due to the high cost of Pt metal. Instead, many studies have been focused on developing the morphology of Pt-based catalysts to enhance the efficiency of the ORR.

1.2. Direct ethanol fuel cells (DEFCs)

Hydrogen fuel cells (HFCs) have been used as a first-generation in fuel cells. This fuel cell has a high theoretical energy density (33.3 kWh kg^{-1}), high thermodynamic standard potential (1.229 V), and zero-emission of CO_2.[40] Over the past few years, PEMs types of HFCs were used to manufacture many vehicles including motorcycles, bicycles, boats, and buses in several countries.[41,42] However, the production of pure hydrogen gas is the most challenging problem in commercializing HFCs. Pure hydrogen gas is not available in nature and is expensive to be produced. Moreover, hydrogen gas is known as a flammable gas that can react easily with oxygen, and it is difficult to transport the hydrogen gas and store it. For these reasons, scientists have been developing alcohol fuel cells to be used as a renewable power source.[43]

Direct alcohol fuel cells (DAFCs) have been utilized as an alternative renewable power source.[28,44] The use of liquid fuels like ethanol and methanol in fuel cells would eliminate the need for completely new infrastructure, which is required when using hydrogen as a fuel source. Methanol has been used as a fuel in DMFCs.[45] It has a higher volumetric density (4.82 kWh L^{-1}) than hydrogen (0.18 kWh L^{-1}). However, methanol is a harmful fuel, and inhaling too much of it can cause permanent blindness or have a bad effect on the optical nerve.[28] On the other hand, ethanol has been used largely as a fuel in the internal combustion engines for vehicles in several countries.[28] Thus, studies have started to develop direct ethanol fuel cells (DEFCs).

Ethanol is a renewable energy source because it can be produced in large quantities via fermentation process from various sources of biomass (e.g. corn, sugarcane, etc.). Also, ethanol can be handled and stored easily; and ethanol has lower toxicity than methanol. Moreover, ethanol has a higher specific energy (8.0 kWh kg^{-1}) than methanol (6.09 kWh kg^{-1}). This means that more energy may be extracted from ethanol for the same amount of methanol, consequently, fuel usage will be reduced. On the other hand, ethanol has a higher volumetric density (6.28 kWh L^{-1}) than both hydrogen and methanol.[28,46,47]

Ethanol can be oxidized in two different environments: acidic media and alkaline media. As a result, there are two types of DEFCs: proton exchange membrane direct ethanol fuel cells (PEM-DEFCs) and alkaline exchange membrane direct ethanol fuel cells (AEM-DEFCs).[2,48] Although having different types of DEFCs, the fundamental goal of the DEFC is converting ethanol to carbon dioxide through a full oxidation reaction (production of 12 electrons).

In AEM-DEFCs, the oxidation of ethanol occurs at a high pH value (> 8). In AEM-DEFCs, an anion exchange membrane (i.e. hydroxide exchange membrane) is used as a membrane that allows anions to diffuse through the membrane from the anode to the cathode.[46] At the anode, ethanol solution (ethanol with alkali (e.g. KOH)) is supplied and oxidized to produce water and carbon dioxide, as shown in eq. 1.10. Water will transport through the membrane and arrive at the cathode, while electrons will transport through the external circuit to the cathode. At the cathode, oxygen will react with water and electrons to produce hydroxide ions (OH^-), as shown in eq. 1.11. The latter will migrate through the membrane to the anode. The combination of eq. 1.10 and eq. 1.11 results in the overall reaction (1.12).

$$CH_3CH_2OH + 12OH^- \rightarrow 2CO_2 + 9H_2O + 12e^- \qquad E^0_{anode} = -0.74\,V \qquad (1.10)$$

$$O_2 + 2H_2O + 4e^- \rightarrow 4OH^- \qquad E^0_{cathode} = 0.40\,V \qquad (1.11)$$

$$CH_3CH_2OH + O_2 + OH^- \rightarrow CH_3COO^- + 2H_2O \qquad E^0_{cell} = 1.14\,V \qquad (1.12)$$

On the other hand, in PEM-DEFCs, the oxidation of ethanol occurs at a relatively low pH (< 5). The commonly used membranes are Nafion 115 and Nafion 117 which allow the movement of protons through it. In this fuel cell, ethanol is supplied to the anode and oxygen to the cathode. The oxygen and ethanol transfer to the cathode catalyst and the anode catalyst through diffusion layers, respectively. At the anode, ethanol will be oxidized to produce CO_2 and 12 electrons (n = 12) according to eq. 1.13. At the cathode, oxygen will be reduced to water (eq. 1.14). By combining the EOR with the ORR, the overall reaction will be as shown in eq. 1.15,

$$CH_3CH_2OH + 3H_2O \rightarrow 2CO_2 + 12H^+ + 12e^- \qquad E^0_{anode} = 0.09\,V \qquad (1.13)$$

$$O_2 + 4H^+ + 4e^- \rightarrow 2H_2O \qquad E^0_{cathode} = 1.23\,V \qquad (1.14)$$

$$CH_3CH_2OH + 3O_2 \rightarrow 2CO_2 + 3H_2O \qquad E^0_{cell} = 1.14\,V \qquad (1.15)$$

Acid fuel cells can give good power density at a low temperature. However, they have a problem with the cost of the noble catalyst (Pt) that is used to oxidize ethanol. Alkaline fuel cells can challenge the problem (pricey noble catalysts) by using a less expensive catalyst (Pd).[49] Also, in the alkaline fuel cell, the amount of ethanol that migrates through the membrane to arrive at the cathode is lower. This is due to the reverse transfer of ions from the cathode to the anode.[49] Unfortunately, the major problem with alkaline fuel cells is the formation of carbonates which decrease the conductivity of the anion exchange membrane. As a result, the overall cell efficiency will be reduced.[50]

1.2.1. Electrochemical oxidation of ethanol

The oxidation of ethanol involves complex multiple electron processes that provide many intermediates and products. In general, the proposed mechanisms for the oxidation of ethanol have two pathways: C_1, and C_2 pathways. As shown in Figure 1.4, the C_1 pathway represents the complete oxidation of ethanol to provide CO_2; and the C_2 pathway represents the incomplete oxidation of ethanol which produces mainly acetic acid and acetaldehyde. When ethanol is completely oxidized to CO_2, 12 electrons will be generated. On the other hand, when ethanol is partially oxidized, 2 electrons (acetaldehyde) and/or 4 electrons (acetic acid) will be generated, resulting in the low efficiency of DEFC.[51,52] During EOR, adsorbed CO (CO_{ad}) have been identified as the major adsorbed intermediate on the catalyst's surface, while acetic acid and acetaldehyde have been detected as the main by-products using techniques like infrared spectroscopy.

The mechanism for ethanol oxidation is affected by several factors including potential, temperature,[53] and the pH of the electrolyte.[54,55] Lai et al. have studied the effect of electrolyte pH on the EOR.[54] They found that in both acidic and basic media, CH_x and CO_{ad} were produced as intermediates. However, they found that the oxidation of these intermediates to CO_2 was faster in alkaline media than in acidic media. Furthermore, in acidic media, they found that ethanol mainly was oxidized to acetaldehyde, then the acetaldehyde might diffuse to the bulk and/or be oxidized to acetic acid. On the other hand, in alkaline media, they found that first the O-H bond in ethanol was broken to produce adsorbed ethoxy. Then, the adsorbed ethoxy was converted to acetaldehyde via the dehydrogenation step. Furthermore, they found that at high pH, acetaldehyde was hydrated to form the geminal diol ($CH_3CH(OH)_2$), and then $CH_3CH(OH)_2$ was dehydrogenated to acetic acid. Guo et al. have also studied the ethanol oxidation mechanism in alkaline media.[55] They also found that acetaldehyde was hydrated first to form the geminal diol ($CH_3CH(OH)_2$), and then $CH_3CH(OH)_2$ was dehydrogenated to acetic acid.[55]

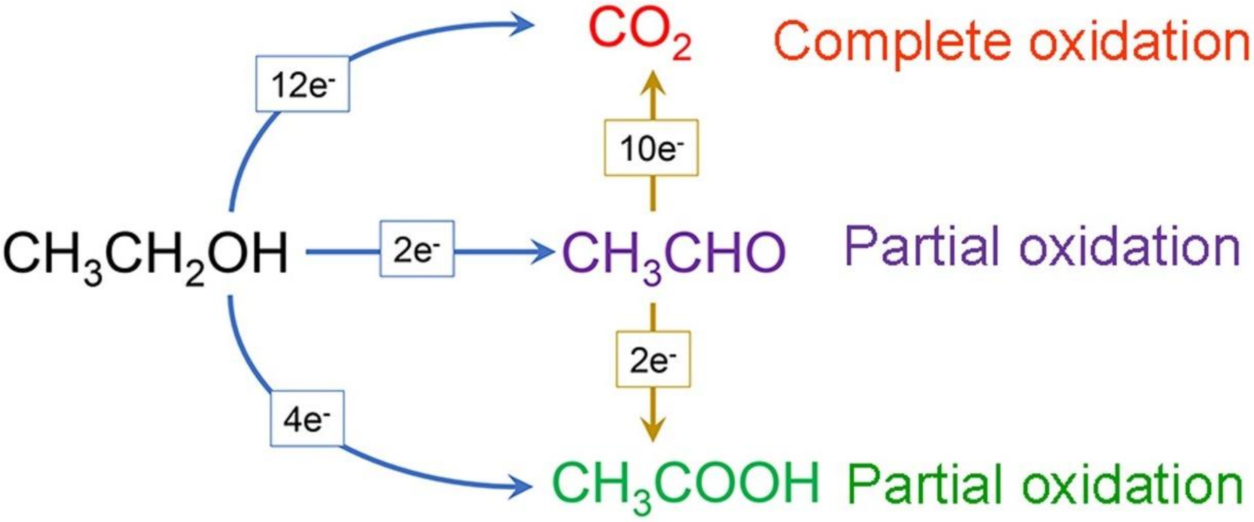

Figure 1.4: The main pathways for electro-oxidation of ethanol. Reprinted from ref.[56]

Many theoretical studies have investigated the oxidation reaction of ethanol.[57,58] These studies have identified the probable reaction pathways and intermediates. Also, they have calculated the reaction barriers and predicted the plausible pathways.[59] Wang et al. studied the oxidation of ethanol on Pt{100} and Pt{111} surfaces.[59] Their calculations were carried out by using the PBE (Perdew–Burke-Ernzerhof) density functional theory (DFT) method. Figure 1.5 shows the calculated reaction barriers on a Pt{111} surface. The initial cleavage of ethanol had five different pathways which depend on the type of bond-breaking that occurred through C-O, C-C, O-H, and C-H bonds. The unfavorable pathway was determined to be the C-C bond-breaking with a relatively high energy barrier of 2.98 eV. In contrast, α-dehydrogenation to CH_3CHOH_{ads} and dehydrogenation to CH_3CHO_{ad} were the most plausible pathways. Moreover, acetaldehyde was dehydrogenated to adsorbed acetyl (CH_3CO_{ad}) via α-dehydrogenation or the cleavage of the O-H bond. When hydroxyl species (OH^-) were present, CH_3CO_{ad} species reacted with OH^- (E_a = 0.31 eV) to produce acetic acid (CH_3COOH). The calculated reaction barriers on a Pt{100} surface showed that ethanol oxidation had the same pathway to produce CH_3CO_{ad} as on Pt{111} surface. However, the oxidation of CH_3CO_{ad} in the presence of OH^- to produce CH_3COOH was inhibited on Pt{100}, while the dehydrogenation of CH_3CO_{ad} was more favorable (0.71 eV). Losing two α-hydrogens from CH_3CO_{ad} to form $CHCO_{ad}$ was the lowest energy pathway of CH_3CO_{ad} oxidation on Pt{100} (0.36 eV), then the C-C bond cleavage in $CHCO_{ad}$ to yield CH_{ad} and CO_{ad} occurred with low energy barrier (0.53 eV). Based on Wang et al., the Pt{100} surface structure was more selective for producing CO_2 in ethanol oxidation than Pt{111} surface.

Moreover, Kavanagh et al. calculated the pathways for acetic acid and CO_{ad} formation for the ethanol oxidation on a Pt(211) surface.[60] All their calculations were carried out using DFT along with Nosé thermostat molecular dynamics (MD) simulations at 353 K in aqueous media. They found that the key steps to produce acetic acid (eq. 1.16) and CO (eq. 1.17) were stimulated by the presence of oxidant species (OH^-). The energy barrier for acetic acid formation was reduced from 0.79 to 0.65 eV in the presence of OH^- species, while it was reduced from 1.07 to 0.86 eV for the C-C cleavage bond to form CO_{ad}.

$$CH_3CO + OH \rightarrow CH_3COOH \tag{1.16}$$

$$CH_2CO \rightarrow CH_2 + CO \tag{1.17}$$

Understanding the reaction pathways for the oxidation of ethanol and the role of catalyst surface structure in the selectivity to produce CO_2 would greatly aid the design of catalysts that can be used for the direct ethanol fuel cell.

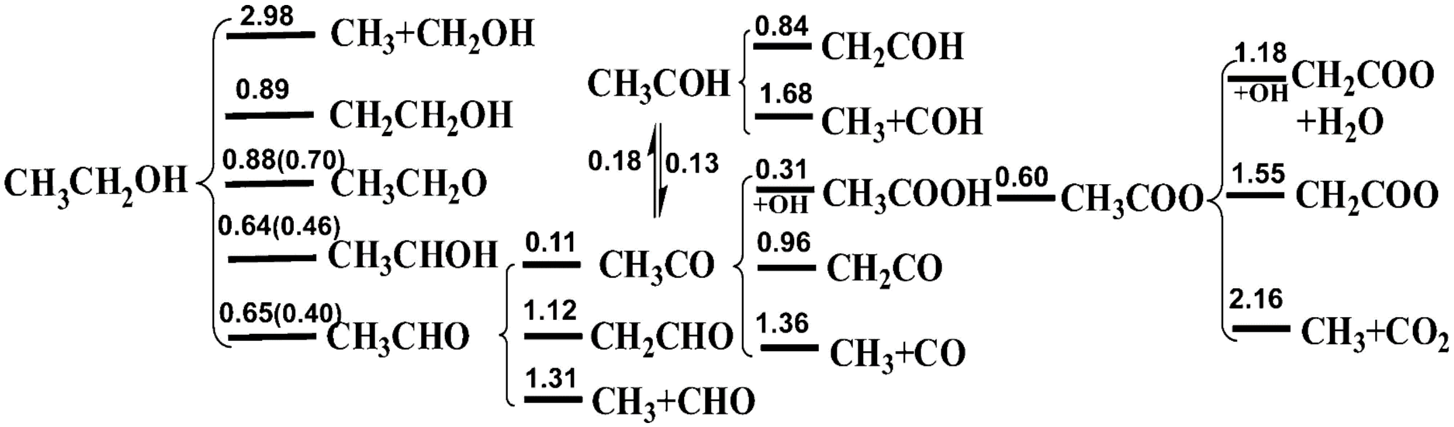

Figure 1.5: The calculated reaction barriers (eV) (after zero-point energy correction) for the oxidation of ethanol on a Pt{100} surface.[59] Reprinted with permission from (*J. Am. Chem. Soc.* 2008, 130, 33, 10996–11004). Copyright (2008) American Chemical Society.

1.2.2. The efficiency of DEFC

Energy-conversion efficiency is an important criterion that can be used to evaluate a fuel cell system. There are three types of efficiency that are commonly used: thermodynamic efficiency (eq. 1.18), potential efficiency (eq. 1.20), and faradaic efficiency (eq. 1.22).[4] The thermodynamic efficiency (it is called also theoretical efficiency) means that the change in the Gibbs free energy of a certain reaction is completely converted into electricity.

$$\varepsilon_{rev} = \frac{\Delta G^\circ}{\Delta H^\circ} \tag{1.18}$$

where ΔG° is the Gibbs free energy of an overall reaction and ΔH° is the enthalpy change of an overall reaction under standard conditions (298.15 K, 1.0 atm). Since the fuel cell works under reversible conditions, the fuel cell is not following Carnot's theorem and all chemical energy is converted to work. However, the internal combustion engine (ICE) follows Carnot's theorem as shown in eq. 1.19,

$$\varepsilon_{rec} = \frac{-W_{cyc}}{\Delta H^{0}} = 1 - \frac{T_C}{T_h} \qquad (1.19)$$

where W_{cyc} is the reversible work, T_C is the cold receiver, and T_h is the hot receiver. Thus, the efficiency of fuel cells is higher than ICE. In DEFC, under standard conditions, $\Delta G° =$ -1325 kJ mol^{-1} and ΔH^{0} = -1.367 kJ mol^{-1}. Hence, the thermodynamic efficiency of DEFC is 97% at ambient temperature.[61] This value (97%) is higher than HFC (83%) and the ICE (43%).[62]

The potential efficiency (ε_E) is caused by the electrode overpotential. It is defined as the ratio between the operation potential (E_{cell}) and the reversible cell potential (E_{rev}),

$$\varepsilon_{\mathrm{E}} = \frac{\mathrm{E}_{cell}}{E_{rev}} \qquad (1.20)$$

When we evaluate the performance of DEFCs, it is crucial to define different concepts of potential. First, the standard cell potential (E^{0}_{cell}) which is defined as the theoretical Nernst potential of the cell under the standard thermodynamic conditions (a = 1). Second, the equilibrium potential (E_{eq}), also called reversible cell potential (E_{rev}), which is defined as the theoretical potential difference between the electrodes (anode and cathode) under thermodynamically reversible conditions (no current flowing); also, it is the highest potential that can be obtained from any fuel cell. Both E^{0}_{cell} and E_{rev} can be calculated from thermodynamic data. Moreover, the actual cell potential (E_{cell}) is the operation potential which can be measured experimentally. Unfortunately, E_{cell} decreases due to the anode (η_{anode}) and cathode ($\eta_{cathode}$) overpotentials, the ohmic resistance of the cell (R), and mass transfer limitations for reactants and products.[63] Thus, the ε_E is redefined as shown in eq. 1.21. The potential efficiency for DEFC is around 44%, while it is around 65% for the HFC.[62]

$$\varepsilon_E = \frac{(E_{rev} - \eta_{anode} - \eta_{cathode} - iR)}{E_{rev}} \tag{1.21}$$

The faradaic efficiency is known as the ratio between the average number of electrons transferred per molecule of ethanol (n_{av}) to the maximum of 12 electrons for the complete oxidation.

$$\varepsilon_F = \frac{n_{av}}{n_t} \tag{1.22}$$

where n_t is the theoretical number of released electrons from the EOR (12). The incomplete oxidation of ethanol causes a loss of faradaic efficiency (ε_F). The n_{av} can be estimated from the product distribution (mainly acetic acid, acetaldehyde, and CO_2) by eq. 1.23,

$$n_{av} = \sum n_i \times f_i \tag{1.23}$$

where f_i is the amount of the product i that is produced from ethanol, while n_i is the number of electrons transferred to make product i. The highest faradaic efficiency that the DEFC might reach is 100% if there are 12 electrons transferred through the reaction (complete oxidation). However, as illustrated above, ethanol oxidation produces acetic acid and acetaldehyde. Thus, the faradaic efficiency will be 16.6% or 33.3% if acetaldehyde or acetic acid are produced, respectively. So, the overall efficiency of a DEFC can be calculated by eq. 1.24,

$$\varepsilon_{DEFC} = \varepsilon_{rev} \times \varepsilon_E \times \varepsilon_F \tag{1.24}$$

Since the theoretical efficiency is constant, the efficiency of the DEFC mainly is affected by the overall potential (the difference between actual potential and reversible potential; $E_{cell} - E_{rev}$)

and the number of electrons transferred per molecule of ethanol. Thus, product analysis is critical in the creation of better anode catalysts because of the relevance of n_{av} in determining the effectiveness of ethanol oxidation methods. Also, it is significant to have an accurate methodology to measure the product distribution and calculate n_{av}.

1.3. Product analysis for the electrochemical oxidation of ethanol

Many different methods have been used to investigate the reaction mechanism of ethanol oxidation and product distribution.[64,65] This section will describe several experiments that aim at studying the ethanol oxidation mechanism, by using high-performance liquid chromatography and nuclear magnetic resonance spectroscopy.[66,67]

1.3.1. High-performance liquid chromatography

High-performance liquid chromatography (HPLC) has been used for the detection and quantification of ethanol oxidation products (acetic acid and acetaldehyde). HPLC consists of an isocratic pump, an autosampler, a high-pressure chromatography column, and a detector. Based on the previous study,[68] suitable columns for this analysis are an Aminex HPX-87H and a C_{18}-NH_2 column. Moreover, a UV detector and a refractive detector are used for the detection of ethanol oxidation products.

Rousseau et al. investigated ethanol oxidation at Pt/C, PtSn/C, and PtSnRu/C catalysts in a DEFC at 80 ℃.[69] Products at the outlet of the anode of a DEFC were trapped as shown in Figure 1.6. Acetic acid, acetaldehyde, and ethanol in the first trap were analyzed directly by HPLC. The nitrogen flowed from the first flask transported the volatile acetaldehyde and CO_2 gas to the second and third traps, respectively. Based on HPLC analysis, only acetic acid, acetaldehyde, and CO_2

were detected as products. Chemical yields of acetic acid were 76.9% on PtSn/C and 75% on PtSnRu/C, while chemical yields of acetaldehyde and CO_2 were 15.4% and 7.7% on PtSn/C, respectively, and 15.2% and 9.8% on PtSnRu/C.

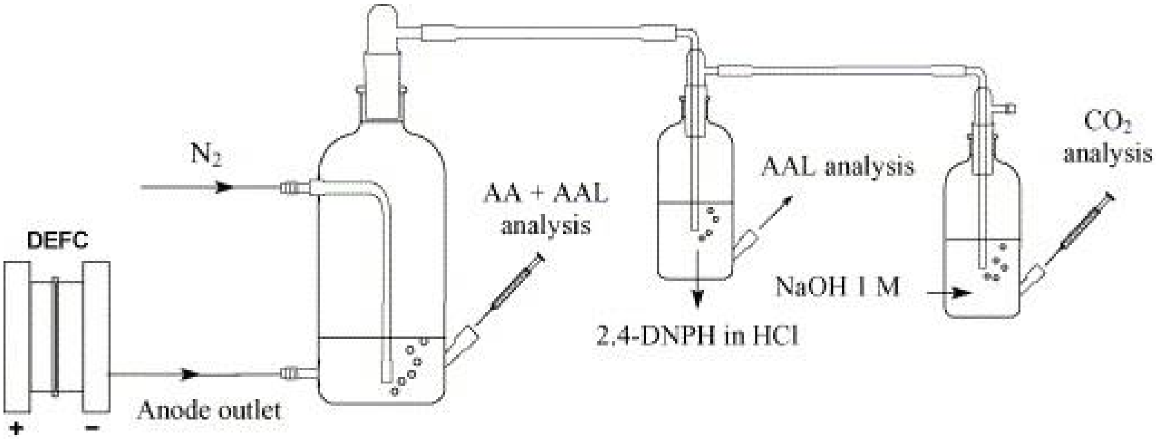

Figure 1.6: The trapping set-up of the EOR products from the outlet of DEFC. Reprinted from ref,[69] Copyright (2006), with permission from Elsevier.

Recently, Corradini et al. studied products of the EOR at the outlet of a DEFC's anode for a commercial PtSn/C (75:25) catalyst and synthesized Pt-Sn-Eu/C catalysts with different atomic ratios: Pt-Sn-Eu/C (50:30:20), Pt-Sn-Eu/C (75:20:05), and Pt-Sn-Eu/C (65:25:10).[70] HPLC was used for analyzing products of ethanol oxidation. The main products were acetic acid, acetaldehyde, and a low amount of CO_2. The average ethanol conversion was around 15%. At 0.008 A cm^{-2}, the highest amount of acetic acid was produced at Pt-Sn-Eu/C (50:30:20), while CO_2 was produced only at Pt-Sn-Eu/C (75:20:5). However, as the current density was increased up to 0.016 A cm^{-2}, the production of CO_2 was high at all Pt-Sn-Eu/C catalysts. Moreover, they found that Pt-Sn-Eu/C catalysts produced a higher amount of CO_2 and acetic acid than the commercial Pt-Sn/C catalyst. These results indicate the effect of europium metal to enhance the presence of OH_{ad}. Thus, acetaldehyde and fragments (CO_{ad} and CH_x) were oxidized in the presence of OH_{ad} to produce acetic acid. In both studies, measurements of products were made by analyzing only the anode outlet of the DEFC. Unfortunately, this provides inaccurate results because the crossover of products from the anode to the cathode occurs. Moreover, ethanol can be oxidized by the oxygen that is supplied to the cathode.

1.3.2. Nuclear magnetic resonance spectroscopy

Recently, nuclear magnetic resonance spectroscopy (NMR) has been also used to identify and quantify acetic acid, acetaldehyde, and residual ethanol produced in ethanol oxidation.[66,67] A Fourier transform (FT) NMR spectrometer is used for this analysis. A FT-NMR spectrometer mainly consists of a frequency synthesizer, a magnet, a sample probe, and a detector. Kim et al. studied the reaction products from Pt/C, PtRu/C, and Pt_3Sn/C in the liquid anode exhaust of a DEFC by ^{13}C NMR.[71] They found that ethane-1,1-diol (ED), acetic acid, and acetaldehyde were the major products detected by NMR spectroscopy for all three catalysts. On the Pt_3Sn/C anode catalyst, the production of acetic acid was dominant over a wider range of potential (at 0.1 V to 0.6 V), while acetic acid production on PtRu/C increased at 0.4 V. Furthermore, Paik et al. analyzed reaction products of ethanol oxidation at a PtRu/C anode in the liquid anode exhaust of a DEFC by ^{13}C NMR, as shown in Figure 1.7.[72]

Additionally, Paik et al. identified species within the PEM using solid-state NMR. The cell was operated at 80 $^{\circ}C$. Figure 1.8 shows the ^{13}C NMR spectrum of DEFC. Only 17 % of the ethanol was consumed during the oxidation. Acetic acid was observed at 177 ppm, acetaldehyde at 206 ppm, and there were peaks for acetaldehyde derivatives, such as ethoxyhydroxyethane (at 94 ppm and 63 ppm), gem-dihydroxyethane at 88 ppm, and methoxyhydroxyethane (at 96 and 54 ppm).

The amount of acetic acid was 17 mM, while acetaldehyde and its derivatives were 23.2 mM. By analyzing the proton exchange membrane using solid-state ^{13}C magic-angle spinning (MAS) NMR, ethanol signal was detected at 58 ppm and there were also signals for acetic acid and ethyl acetate. These species diffused into the membrane from the anode to the cathode during the crossover process. The amount of ethanol detected within the PEM was nine times higher than at the anode exhaust of the DEFC. Paik used both methods (solution and solid-state NMR) for the first time to identify products and intermediates of ethanol oxidation; and their distribution between the polymer membrane and the anode exhaust. Consequently, this might be of critical importance in developing DEFC systems and understanding the mechanism of ethanol oxidation.

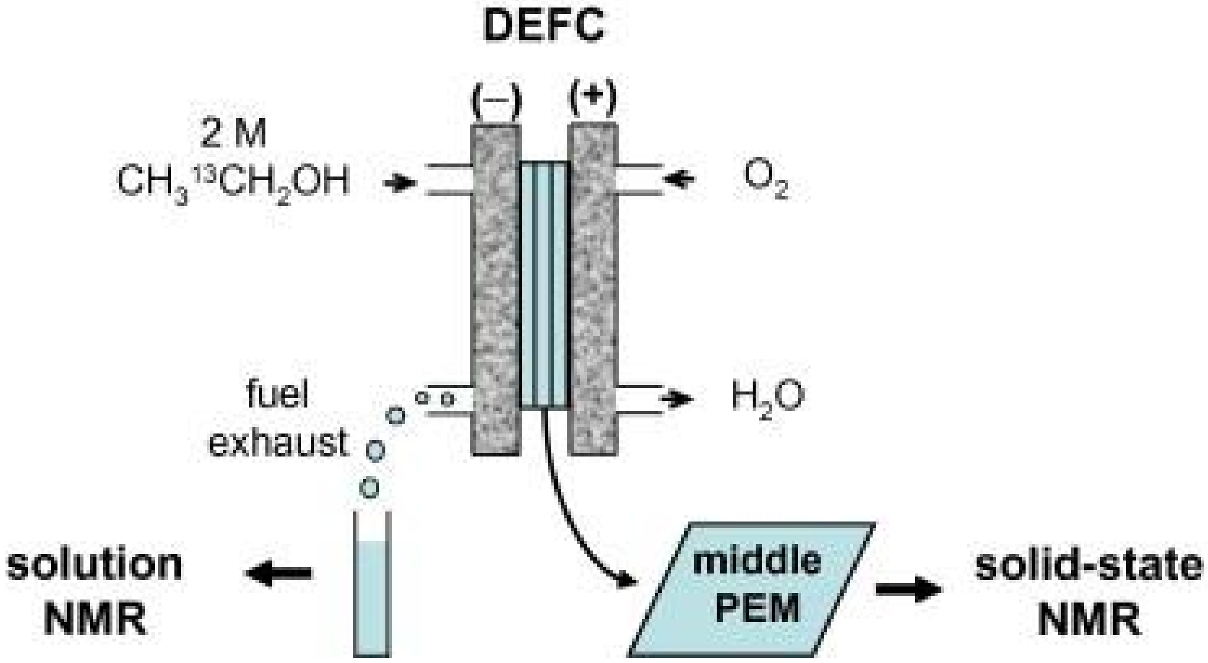

Figure 1.7: A schematic diagram of DEFC and NMR sampling. Reprinted from ref,[72] Copyright (2009), with permission from Elsevier.

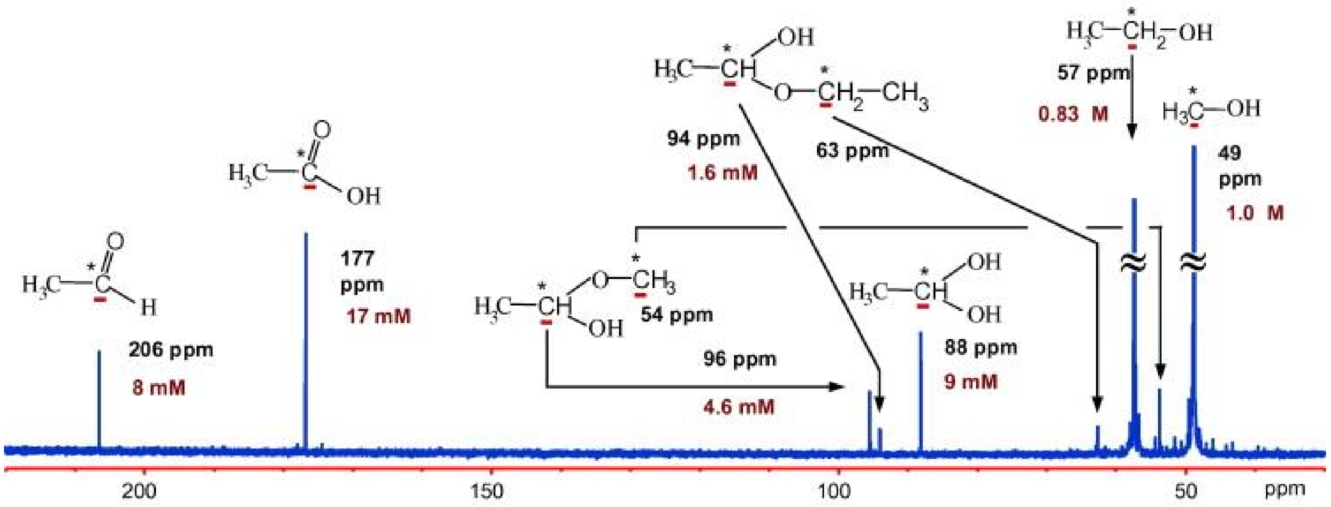

Figure 1.8: The ^{13}C solution NMR of the exhaust solution from a DEFC. Reprinted from ref,[72] Copyright (2009), with permission from Elsevier.

1.3.3. Our methodology for product analysis

In our research group, a proton exchange membrane electrolysis cell (PEMEC) is used to investigate the efficiency, stoichiometry (average number of electrons transferred per ethanol molecule; n_{av}), and product distribution for ethanol oxidation at various catalysts. A PEMEC is like DEFC, but oxygen gas is replaced by nitrogen gas at the cathode. Many researchers have investigated the effect of oxygen on product distributions at ambient and elevated temperatures.[51,73] When oxygen is used at the cathode, a chemical reaction between ethanol and oxygen will occur, as shown in eq. 1.25,

$$CH_3CH_2OH + nO_2 \rightarrow xCO_2 + yCH_3CHO + zCH_3CO_2H + mH_2O \qquad (1.25)$$

However, when nitrogen replaces oxygen, the potential for a chemical reaction at the cathode (eq.1.26) is eliminated. As a result, the product distribution and the measurement of n_{av} values will be accurate,

$$CH_3CH_2OH + 3H_2O \rightarrow 6H_2 + 2CO_2 \quad (1.26)$$

Our group carried out the product analysis experiment over a range of potentials at 80 ºC. The anode was fed directly with 0.100 M ethanol, while the cathode was supplied with nitrogen gas. Residual ethanol and products (acetic acid and acetaldehyde) were collected from both the anode and cathode exhausts to avoid the loss of products and ethanol by the crossover, and measured by ^{1}H NMR spectrometry,[63] as shown in Figure 1.9.

Improving the efficiency, performance, and activity of DEFCs requires understanding the mechanism of ethanol oxidation. This can be achieved by determining the product distribution and n_{av}. Moreover, it can be done by designing new catalysts with different compositions and structures. As a result, the DEFC will be commercially viable.

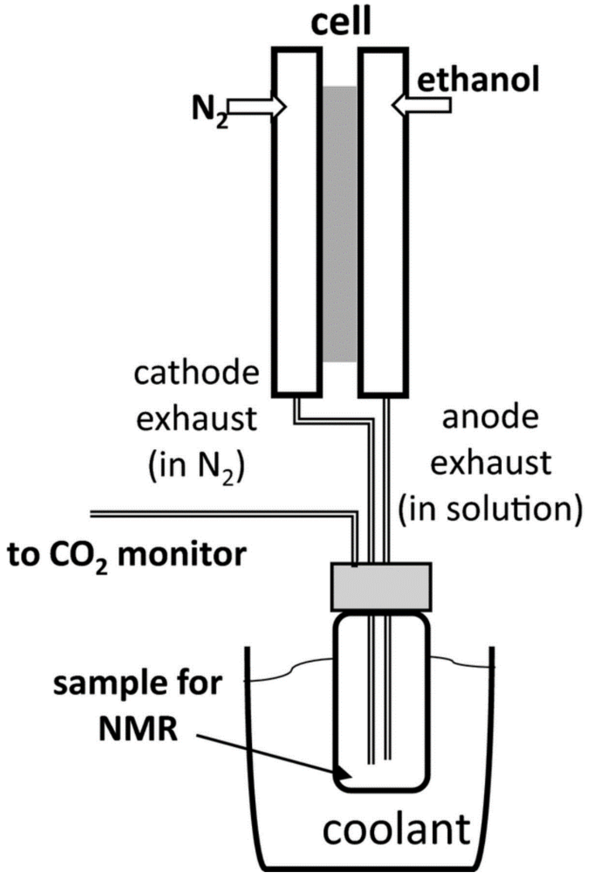

Figure 1.9: A Scheme diagram of product collection. Reprinted from ref.[63]

1.4. Catalysts for the oxidation of ethanol

Catalysts are the main important issue for fuel cells because the reaction is carried out on their surface. Thus, the catalysts are largely responsible for the performance and efficiency of fuel cells. Catalysts for both cathodes and anodes frequently encounter issues such as low conversion efficiency, high cost, and inferior durability.[74] Many researchers have developed catalysts to produce more efficient and commercially practical fuel cells.[74]

For ethanol oxidation and other alcohols, Pt nanoparticles (NPs) are found to be the more suitable single metal catalyst, under acidic conditions, while Pd NPs are used for the EOR under basic conditions.[17] Pt catalysts show higher durability and activity than other noble metal catalysts for fuel cells, although, high loading of Pt is needed to achieve high power density. Using a high concentration of NPs causes an agglomeration, as a result, a decrease in both the surface area and the catalytic activity will take place.[75] Thus, supports material (e.g. carbon) are used with Pt NPs.

Catalyst support materials for fuel cells are categorized into carbon supports and non-carbon supports (e.g. metal oxides).[76,77] In general, ideal support materials should have several properties such as (i) high surface area, (ii) suitable porosity for good mass transport (reactant and products), (iii) high chemical stability, and (iv) good electrical conductivity.[76] Consequently, many carbon support materials have been used (e.g. carbon black (CB), carbon nanofibers (CNFs), carbon nanotubes (CNTs), and graphene) for enhancing the activity of the catalyst, and reducing the amount of Pt.[17] Mainly, carbon materials have a large surface area, a strong corrosion-resistance, and superior electrical conductivity. These features provide high Pt NPs dispersion and rapid electron transport at the electrode-electrolyte interface.

Pt NPs loaded on the carbon support (Pt/C) were found to be the more suitable catalyst for EOR, under acidic conditions.[2,17,78] However, Pt is easily poisoned by intermediates species that are produced during the EOR such as CO_{ad} and CH_x. As a result, CO_{ad} and CH_x will decrease the activity of the Pt catalyst. Also, the cost of Pt is approximately 54% of the total fuel cell cost.[52] These disadvantages of using Pt/C in DEFCs increase the development of PtM/C nanoalloy (binary catalysts; e.g. PtRh, PtRu, and PtNi),[79–82] and PtMZ/C nanoalloy (ternary catalysts; e.g. PtSnNi).[83] Moreover, researchers have improved catalysts by changing the particle shape of Pt NPs (e.g. cubic, tetrahedral, and octahedral).[82,84] Also, Pt nanostructures have been developed to be suitable for the

EOR such as nanowires, nanoparticles, nanosheets, nanopores, and nanoflowers.[85–87] Highly efficient electrocatalysts for complete ethanol oxidation to CO_2 should have several characteristic features. These features include appropriate surface composition for selectivity CO_2 formation and suitable surface-active sites for the cleavage of the C–C bond.[88]

The EOR process follows a complex mechanism and produces mainly acetic acid and acetaldehyde as products. When ethanol is adsorbed at the Pt surface (eq.1.27), a dehydrogenation process occurs to produce acetaldehyde as a product or as adsorbed intermediate, as shown in eq. 1.28 and 1.29,

$$Pt + CH_3CH_2OH \rightarrow Pt(CHOH - CH_3)_{ads} + H^+ + e^- \tag{1.27}$$

$$Pt(CHOH - CH_3)_{ads} \rightarrow Pt + CHO - CH_3 + H^+ + e^- \tag{1.28}$$

$$Pt + CHO - CH_3 \rightarrow Pt(CO - CH_3)_{ads} + H^+ + e^- \tag{1.29}$$

Acetaldehyde, then, will be oxidized to produce acetic acid (eq. 1.30) and/or CO_{ad} intermediate (eq. 1.31). Unfortunately, CO_{ad} intermediate limits the adsorption of the reactants by blocking the active sites of the Pt, as a result, the activity of the catalyst will decrease.[88] At high potentials, water oxidation produces Pt–OH or Pt–O on the Pt surface (eq. 1.32), which then oxidizes CO_{ad} to CO_2, as shown in eq. 1.33,

$$Pt(CO - CH_3)_{ads} + Pt(OH)_{ads} \rightarrow 2Pt + CH_3COOH \tag{1.30}$$

$$Pt(CO - CH_3)_{ads} + Pt \rightarrow Pt(CO)_{ads} + Pt(CH_3)_{ads} \tag{1.31}$$

$$Pt + H_2O \rightarrow Pt - OH + H^+ + e^- \tag{1.32}$$

$$Pt(CO)_{ads} + Pt - OH \rightarrow 2Pt + CO_2 + 2H^+ \tag{1.33}$$

When new binary or ternary catalysts are developed to overcome the disadvantages of Pt/C, electronic (ligand) effects and a bifunctional mechanism are used to explain the improvement in the activity.[86,89] The bifunctional mechanism (ensemble effect or dual active sites effect) follows the Langmuir–Hinshelwood (L–H) principle. When a secondary metal (such as Ru) is alloyed with Pt, the secondary metal will reduce the overpotential for the oxidation of CO_{ad} on the Pt surface. Also, the alloyed metal will enhance the dissociation of water and adsorb the OH_{ad} on its surface, as shown in eq. 1.34. If CO_{ad} and OH_{ad} are closed enough to each other, then, CO_{ad} will be oxidized to CO_2, as shown in eq. 1.35. As a result, the poisoning of the Pt sites will be reduced.[90,91]

$$M + H_2O \rightarrow M - OH + H^+ \tag{1.34}$$

$$Pt - CO + M - OH \rightarrow Pt + M + CO_2 + H^+ + e^- \tag{1.35}$$

On the other hand, the electronic effect (ligand effect) is also an essential effect that plays a major role in enhancing the activity of catalysts. The ligand effect occurs at the interfaces of two atoms with distinct electronegativity (differing d-band center) which allows electronic charge transfer between them.[92] When Pt is alloyed with any metal (such as Ni, Fe, and Co), the bonding between Pt and CO_{ad} will be weakened by changing the electronic structure of the Pt surface. Therefore, the catalytic activity will be increased. However, the ligand effect is limited within the two monolayers of the catalyst near-surface.[92]

Furthermore, the strain effect is another significant factor that tunes the d-band center of the Pt catalyst. Also, it modulates the binding energies of intermediates (e.g. CO_{ad}). In contrast to the ligand effect, the strain effect has an effect within approximately six monolayers of the catalyst near-surface.[93] Generally, there are two types of strain effect (based on the secondary metal size): compressive strain and tensile strain. In compressive strain, the Pt is alloyed with a metal smaller in size than Pt, as a result, the d-band center of the Pt will be downshifted (decreased). Thus, the interaction between Pt active sites and the adsorbate (e.g. CO_{ad}) will be weakened. However, if the Pt is alloyed with metal larger in size than Pt, the d-band center of the Pt will be upshifted (increased). Thus, the interaction between Pt active sites and the adsorbate (e.g. CO_{ad}) will be strong.[92]

1.4.1. Binary nanoalloy catalysts

Many Pt-based binary catalysts have been developed to improve activity for the EOR.[56] So far, PtRu alloy has been widely investigated for the electro-oxidation of ethanol.[94,95] It was found that ruthenium atoms (Ru) enhance the bifunctional effect.[96] Ru activates the dissociation of water at potentials less than Pt and forms $RuOH_{ads}$ sites, as shown in eq. 1.36,

$$Ru + H_2O \rightarrow Ru(OH)_{ads} + H^+ + 1e^- \qquad E^0 \approx 0.2\,V\,NHE \quad (1.36)$$

The formation of $Ru(OH)_{ad}$ sites close to the $Pt(CO)_{ad}$ can oxidize CO_{ad} to CO_2, as shown in eq. 1.37. Also, the Pt sites will be free for a new fuel molecule.

$$Pt(CO)_{ads} + Ru(OH)_{ads} \rightarrow Pt + Ru + CO_2 + H^+ + e^- \quad (1.37)$$

Colmati et al.[97] have studied the behavior of both PtRu and Pt_3Sn catalysts in an acidic solution for ethanol oxidation. As shown in Figure 1.10, Ru provided high activity for ethanol oxidation at low potentials. Moreover, Brueckner and Pickup have studied the activity of a PtRu alloy catalyst at 50°C.[98] They found that PtRu alloy had high activity for methanol and ethanol relative to Pt, as shown in Figure 1.11. Altarawneh et al. have investigated the activity and product analysis for a commercial PtRu/C catalyst.[63] They have found that PtRu/C provided higher currents at low potentials (< 0.50 V) than Pt/C, while 86% of acetic acid was produced at potentials above 0.30 V. However, the activity of PtRu/C was decreased at potentials ≥ 0.5 V and the highest chemical yield of CO_2 was 7% at 0.45 V. Also, Rodríguez-Gómez et al. have studied the influence of the atomic ratio of Pt:Ru on the product distribution of ethanol oxidation in a proton exchange membrane (PEM) cell at 80 °C.[99] They found that a 2:1 PtRu/C anode produced mainly acetic acid (85%) and provided a higher current density (740 mA cm^{-2}) than other ratios.

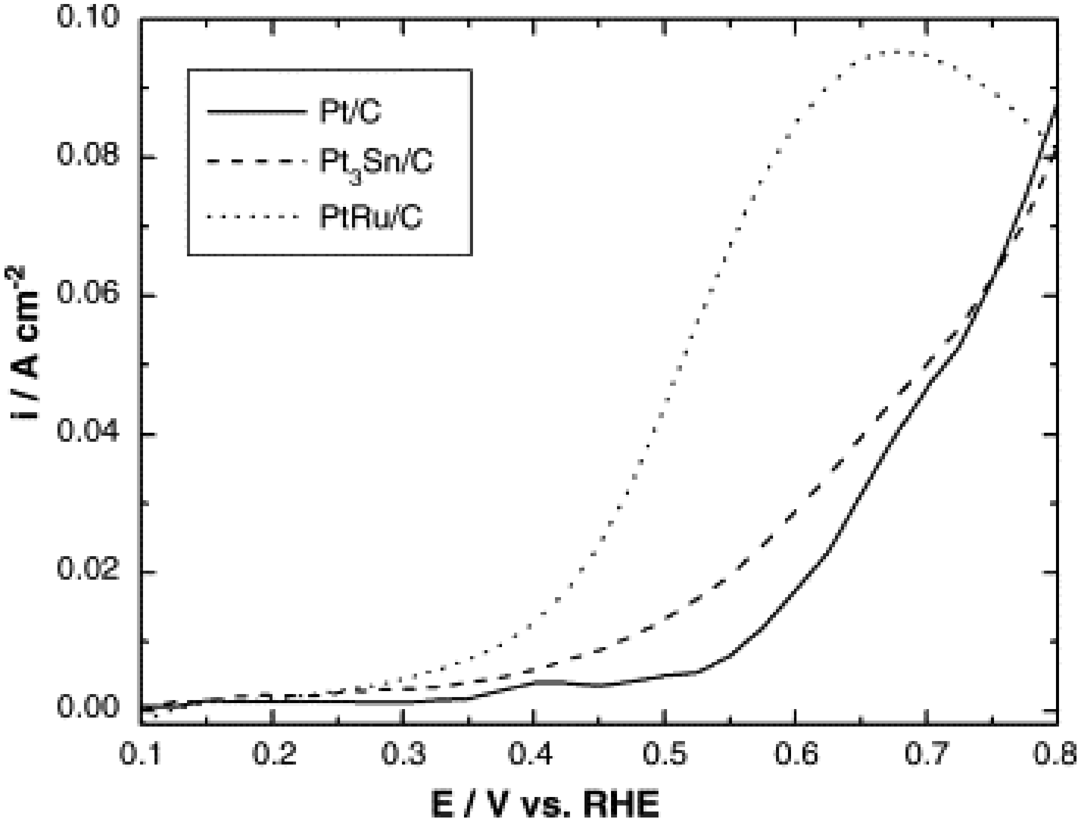

Figure 1.10: Linear sweep voltammograms for ethanol oxidation on Pt/C, Pt_3Sn/C, and PtRu/C electrocatalysts were obtained in the single-cell (1.0 mol L^{-1} ethanol solution and 1 mL min^{-1}). Reprinted from the ref,[97] Copyright (2005), with permission from Elsevier.

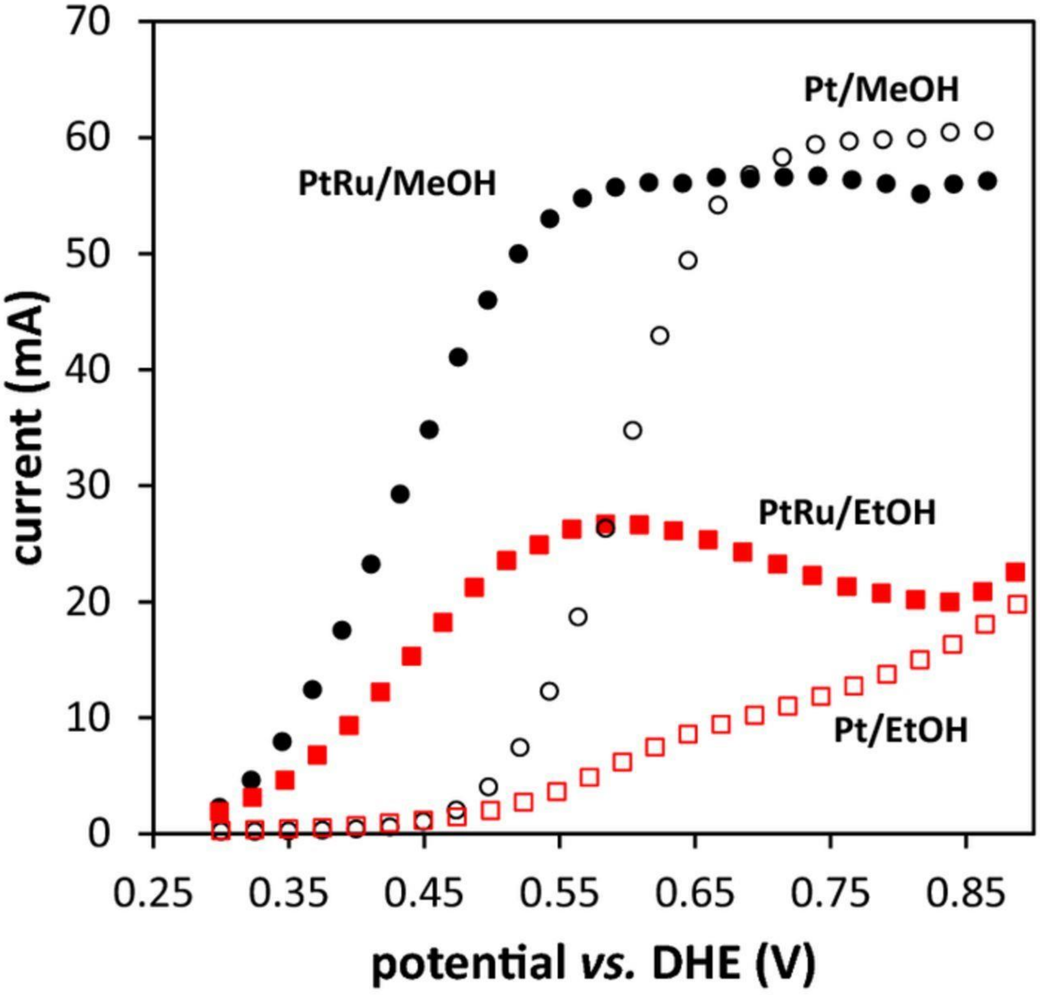

Figure 1.11: A comparison of polarization curves for 1.0 M methanol and 1.0 M ethanol solutions at Pt black and Pt/Ru anodes in a 4 electrodes proton exchange membrane electrolysis cell at 50 ℃. Reprinted from ref.[98]

Also, Rhodium (Rh) has been used as a secondary metal in Pt/C catalysts.[100] Almeida et al. have found that the catalytic activity in the EOR of Pt_3Rh/C was higher 5.2 times than commercial Pt/C.[79] Moreover, they found that the onset potential was shifted negatively (0.11 V) than Pt/C; and more CO_2 was produced at Pt_3Rh/C than Pt/C at low potentials. On the other hand, Bergamaski et al. have reported the effect of Pt:Rh ratio on the faradaic efficiency.[101] They found that $Pt_{47}Rh_{53}/C$ had a faradaic efficiency (50%) higher than Pt/C (8%).[101] El Sawy et al. have studied the activity of both Rh@Pt and Ru@Pt catalysts in the EOR. At ambient temperature, in H_2SO_4(aq), both catalysts showed the same enhancement on the activity for the EOR over Pt.[102] However, in a PEMEC at 80 °C, Ru@Pt enhanced the activity in the EOR more than Rh@Pt.[102]

Another important binary catalyst is PtNi nanoalloy. PtNi nanoalloy catalysts have been used widely for the ORR and methanol oxidation reaction (MOR).[103–106] The development of PtNi alloys has been increased for several reasons: the segregation processes rarely occur in the PtNi alloy and Ni would not be dissolved in the electrolyte over the potential range of fuel oxidation (e.g. oxygen).[107] The resistance of Ni against the dissolution has been attributed to the formation of a nickel hydroxide passivated surface.[108] Also, it has been shown that Ni affects the electronic properties of Pt in PtNi alloys.[109] Antolini et al.[110] have shown that the enhancement in the activity of $Pt_{75}Ni_{25}/C$ could be attributed to an electronic effect.

Since studies of PtNi for the ORR and MOR have proved that incorporating Ni with Pt increases the activity of the catalyst over Pt/C, studying the activity of PtNi for the EOR has been increased.[56,111,112] Unfortunately, there are few reports on the activity of PtNi nanoalloys for ethanol oxidation and the product distribution, in acidic media.[113] Soundararajan et al. have shown that PtNi alloy has a catalytic activity 2 times higher than Pt for the EOR.[114] Sulaiman et al.[82] have prepared an octahedral PtNi catalyst and studied the activity for the EOR at ambient temperature. As shown in Figure 1.12, they found that the octahedral Pt-Ni/C nanoalloy was at least 4.6 and 7.7 times more active than conventional Pt-Ni/C and commercial Pt/C catalysts, respectively. However, based on an in situ infrared spectroscopic study, they found that octahedral Pt-Ni/C nanoalloy produced more acetic acid than CO_2.

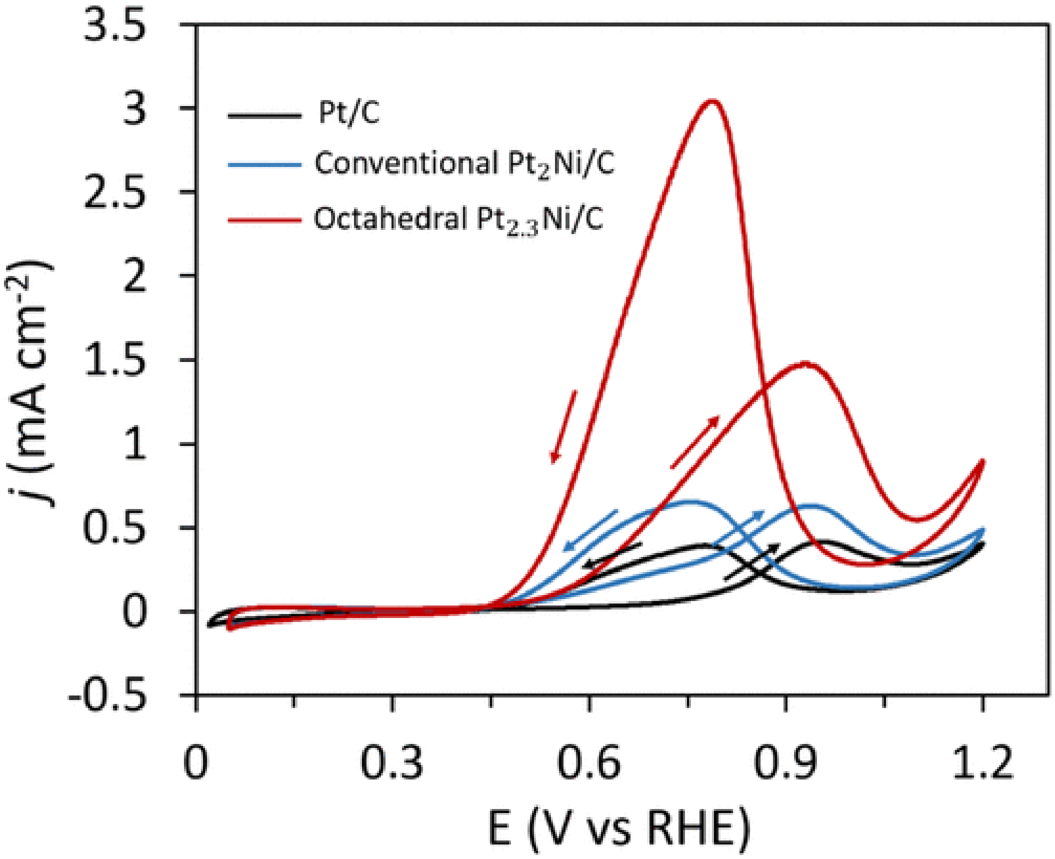

Figure 1.12: Cyclic voltammograms of the Pt/C, conventional Pt_2Ni/C, and octahedral $Pt_{2.3}Ni/C$ electrocatalyst in an Ar-saturated 0.2 M ethanol + 0.1 M $HClO_4$ solution at a scan rate of 50 mV s^{-1}. The currents are normalized to the electrochemical surface areas.[82] Reprinted with permission from (*ACS Catal*. 2017, 7, 8, 5134–5141). Copyright (2017) American Chemical Society.

1.4.2. Ternary nanoalloy catalysts

Since previous studies have shown that PtM/C catalysts have enhanced the activity for EOR, many researchers have prepared ternary PtMN/C alloys (where N is the third metal).[115,116] Preparing ternary catalysts reduce the amount of Pt and might increase the ability to promote the C-C bond cleavage.[117] Many elements have been used as auxiliary components in ternary catalysts to increase current density for the EOR up to date, as shown in Figure 1.13. Several studies have investigated the activity of PtRhM (M is Ni, Cu, Fe, or Co) for EOR.[88] Erini et al. have reported an increase in the activity for a PtRhNi/C catalyst for the EOR.[118] Han et al. have prepared a porous trimetallic PtRhCu cubic nanoboxes (CNBs). They found that the presence of Rh in PtRhCu CNBs increased the activity for the EOR than at PtCu CNBs.[119] Additionally, they found (based on the CO stripping experiment) that the oxidation peak potential of CO at both catalysts (PtRuCu and PtCu CNBs) was the same. Accordingly, they suggested that the presence of Cu in the PtRhCu CNBs improved the anti-poisoning of CO_{ad}.[119] Furthermore, Chen et al. have found that the electroactivity of ultrafine PtCuRh nanowires (NWs) in the EOR was higher compared with a commercial Pt/C catalyst.[120] On the other hand, Liu et al. have investigated the catalytic activity of PtRhNi alloy nano-assemblies (ANAs) for the EOR in alkaline media.[121] They found that the activity of $Pt_3Rh_1Ni_2$ ANAs was higher (1.388.4 A g^{-1}) than of $Pt_5Rh_1Ni_3$ (659.6 A g^{-1}) and $Pt_1Rh_1Ni_1$ (456.61 A g^{-1}) at 0.74 V.[121] Moreover, Wang et al. have found that the presence of Fe in Pt_9RhFe_3/C catalyst enhanced the activity for the EOR relative to Pt_3Fe/C, Pt_9Rh/C, and Pt/C. Also, the onset potential for CO_{ad} oxidation was shifted negatively at Pt_9RhFe_3/C (0.271 V) relative to Pt_3Fe/C (0.346 V), Pt_9Rh/C (0.326 V), and Pt/C (0.462 V).[122]

The activity of PtRu has enhanced the bifunctional effect at low potentials. Thus, researchers have prepared and studied the activity of PtRuM for EOR.[88,123] Wang et al. have investigated the EOR for PtRuNi/C and PtRu/C catalysts. The activity of PtRuNi/C was enhanced 5.4 times at 0.30 V than PtRu/C.[124] Moreover, Gang et al. have studied the effect of the Ru:Sn ratio in PtRuSn/C catalysts on the activity for EOR.[125] Their results indicated that the Ru-rich $Pt_{60}Ru_{30}Sn_{10}$/C catalyst was much active for the EOR at low potentials (the ability of Ru to remove CO_{ad} via bifunctional mechanism), while the Sn-rich $Pt_{60}Ru_{10}Sn_{30}$/C catalyst was favorable for the activation of the C-C bond breaking at high potentials. Furthermore, PtRuMo/C and PtRu/C catalysts were prepared by García et al.[123] They found that PtRuMo/C had higher CO tolerance (removing the CO_{ad}) at low potentials ($< 0.3\,V$) than PtRu/C. Also, they found that catalysts with a high amount of Mo enhanced the production of acetic acid at potentials higher than 0.3 V.[123]

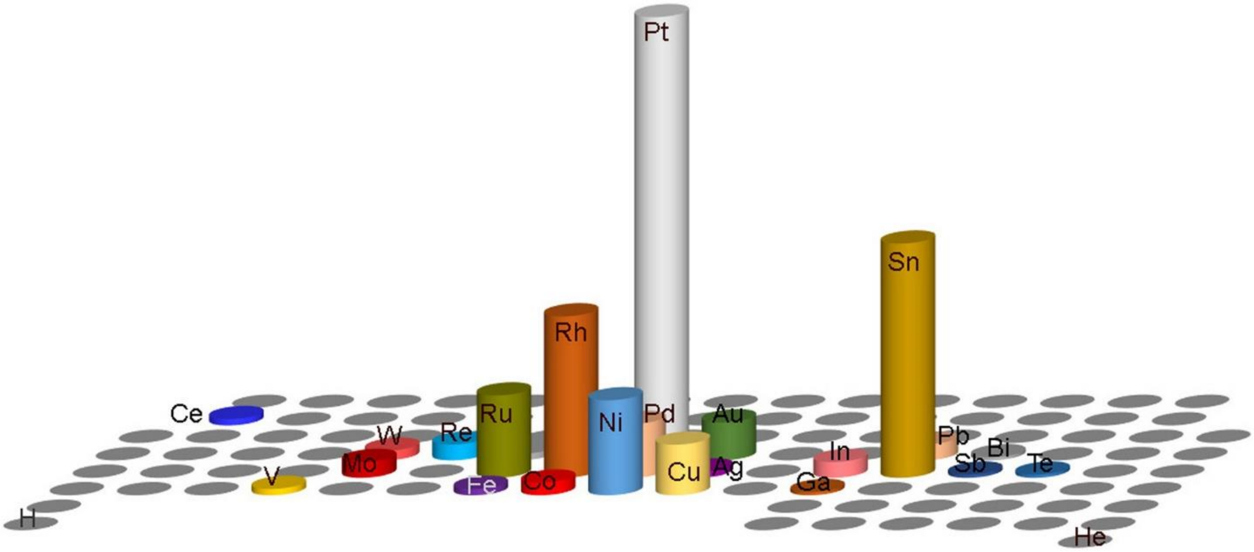

Figure 1.13: Frequency of use of elements acting as components of ternary catalysts for EOR. Reprinted from ref.[56]

On the other hand, Beyhan et al. have investigated the performance of $Pt_{80}Sn_{10}Ni_{10}/C$ and $Pt_{90}Sn_{10}/C$ in a DEFC at 80 °C.[126] They found that the presence of Ni enhanced the performance of $Pt_{80}Sn_{10}Ni_{10}/C$ and CO_2 production over the $Pt_{90}Sn_{10}/C$ catalyst. They confirmed that the presence of Ni promotes the C-C bond cleavage.[126] Furthermore, as shown in Figure 1.14, Beyhan et.al.[127] have shown that both PtSnNi/C and PtSnCo/C had high catalytic activity at low potentials. When these ternary catalysts were examined in a DEFC, the power density was 34 mW cm^{-2} at the PtSnCo/C, and it was 3 and 6 times higher than the PtSn/C and Pt/C catalysts, respectively.[127]

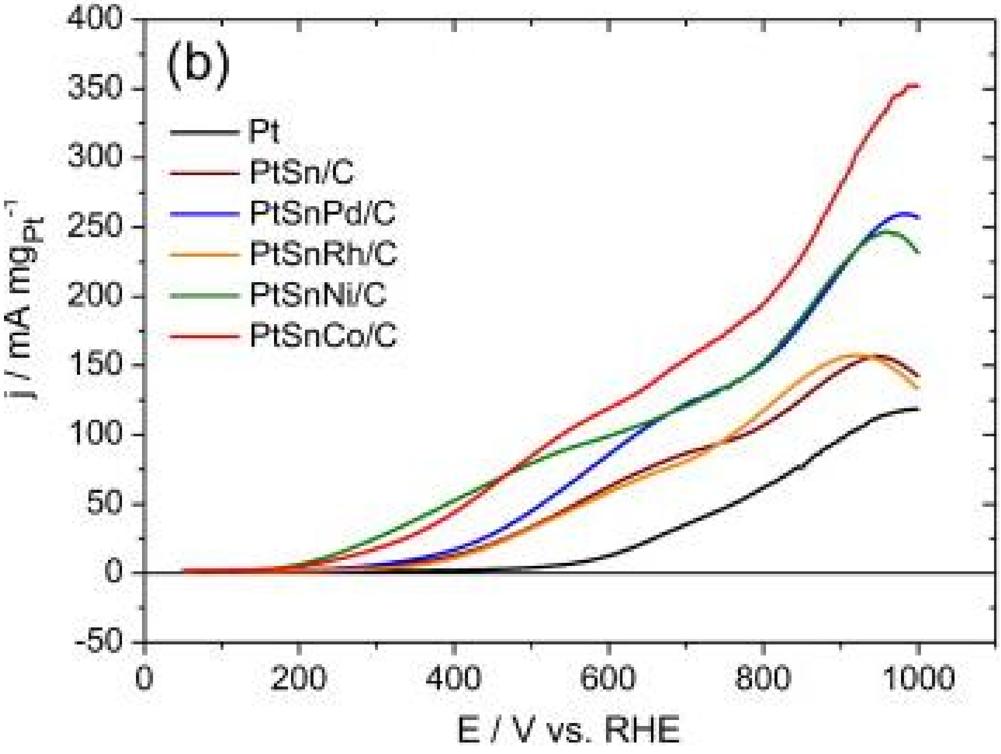

Figure 1.14: Linear sweep voltammograms for electrooxidation of 1 M ethanol in 0.1 M $HClO_4$(aq) on Pt/C and PtSnM/C (M = Ni, Co, Rh, Pd). Reprinted from ref,[127] Copyright (2013), with permission from Elsevier.

Further development and studies are required for ternary catalysts to be suitable for DEFCs. Different structures, compositions, and morphologies of ternary catalysts can increase activity and stability. However, there are still several difficulties during the development process such as the development of high precision control of particle size and high-index crystal synthesis. In contrast, the application of fuel cells to new energy systems has a bright future by continuous improvements in the characterization of materials and theoretical investigation.

1.4.3. Acid treatment of nanoalloy catalysts

The improvement of catalysts for the EOR is not limited to conventional alloy catalysts. Researchers have developed and improved binary and ternary catalysts by modifying their surfaces, changing the particles' shape, and developing other nanostructures such as core-shell structures. Core-shell structures can be prepared via several methods such as a dealloying process.[128,129] The dealloying is defined as a dissolution process of a non-noble metal (M) from the surface of a PtM alloy to form a Pt enriched particle shell (Pt-skeleton surface) with the PtM alloy core (a core-shell or a core-shell like structure), as shown in Figure 1.15.[128,130] In particular, there are two main methods to dealloying PtM: electrochemical dealloying and chemical leaching (acid treatment).[129,131] The electrochemical dealloying is carried out using a potential cycling (e.g. from 0.05 V to 1 V vs. a reversible hydrogen electrode (RHE) in acidic media), as a result, a thick Pt enriched shell can be formed. However, the chemical leaching (acid treatment) is carried out by immersing the PtM alloy in acidic media (e.g. H_2SO_4, acetic acid, or HNO_3) to remove M from the near-surface region of the PtM alloy.[129] Choi et. al. observed an enhancement in the specific activity toward the ORR for an octahedral PtNi/C catalyst after the acid treatment.[39] Wang et al. found that acid treatment improved the ORR activity for a PtNi catalyst.[132]

Many studies have investigated the effect of acid treatment on the EOR activity and breaking the C-C bond. Huang et. al. found that acid treatment enhanced the activity of a Pt_2SnCu nanoalloy for the EOR 3.1 times higher than for Pt/C.[133] Altarawneh et al. studied acid treatment effect on the EOR activity for the PtNi octahedra.[113] They found that the activity and chemical yield of CO_2 (at 0.3 V vs. a dynamic hydrogen electrode (DHE)) improved after treating PtNi with acetic acid.[113]

Also, Guo et.al.. found that acid treatment increased the performance significantly for PtNi compared toward the EOR.[134] Further investigation and studies are required to understand the mechanism of dealloying/acid treatment. As a result, many catalysts can be improved for DEFCs.

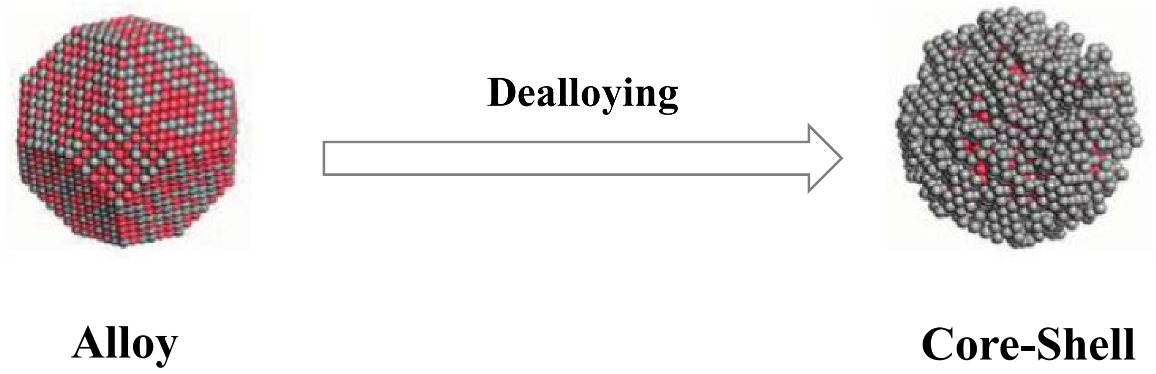

Figure 1.15: Illustration of the dealloying/acid treatment process. Three-dimensional structures of the alloy and core-shell were reprinted with permission from (*J. Am. Chem. Soc*. 2011, 133, 33, 14369–14403). Copyright (2011) American Chemical Society.[132]

1.5. Structures and characterization of binary/ternary nanoparticles

Generally, when a Pt is combined with various metals, in all possible compositions, an alloy system will be formed. As explained above, if the alloy system is prepared of two metals, it is called a binary alloy system. On the other hand, if the alloy system is made up of three metals, it is called a ternary alloy system.[17] However, when a second metal (B) is added to another metal (A), several structures will be formed based on the conditions of the synthesis process. These structures include alloy, intermetallic, and bimetallic structures, as shown in Figure 1.16.[135]

A bimetallic binary catalyst for A and B metals (it can be represented as A/B) is defined as phase segregation of A and B without any substitution of one metal into the lattice of the other metal. A core-shell structure is the best example of a bimetallic structure. It consists of two metals (A@B) where A forms the core and B surrounds the core as a shell, as shown in Figure 1.17.[128] On the other hand, in the alloy (A_xB_{1-x}) structure, one metal can incorporate into the lattice of the other metal. Atoms will have mixed atomic positions in a disordered arrangement. Furthermore, the structure of the alloy will be similar to that of the metals (e.g. both will have fcc). In contrast, in intermetallic structures (which can be represented as A_xB_y), metals B and A produce different ordered structures than the structure of each metal (it is called also ordered alloys). Also, atoms in the intermetallic structure have fixed positions. For example, both Cu and Pd metals have a fcc structure, however, the intermetallic structure of PdCu is body center cubic(bcc) and ordered atoms (Pd atoms were at the body center and Cu atoms at the corners).[136]

When a certain catalyst (binary or ternary) is prepared, characterization is needed to differentiate the structures (alloy from intermetallic or bimetallic) and determine the morphology of the catalyst. Also, characterization is required to estimate the particle size and measure the oxidation states of the metals. Therefore, various characterization techniques are used such as transmission electron microscopy (TEM), X-ray photoelectron spectroscopy (XPS), and X-ray diffraction (XRD).[126]

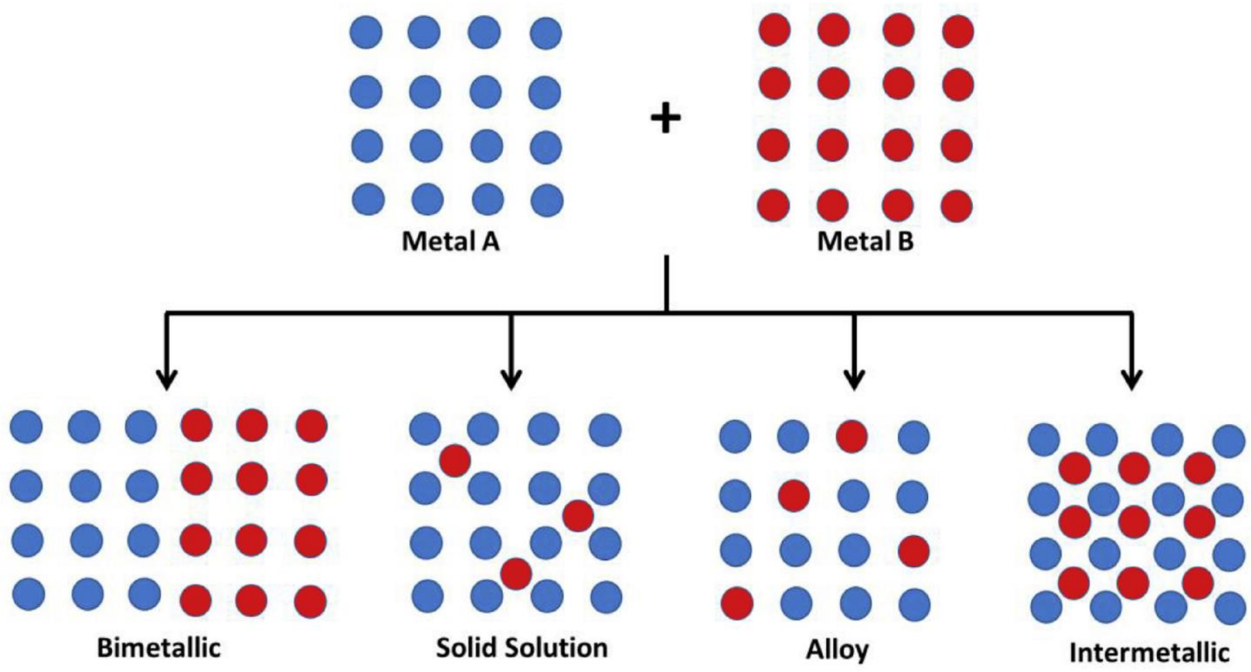

Figure 1.16*:* Schematic structures of bimetallic, solid solution, alloy, and intermetallic compounds at the atomic level. Reprinted from ref,[135] Copyright (2018), with permission from Elsevier.

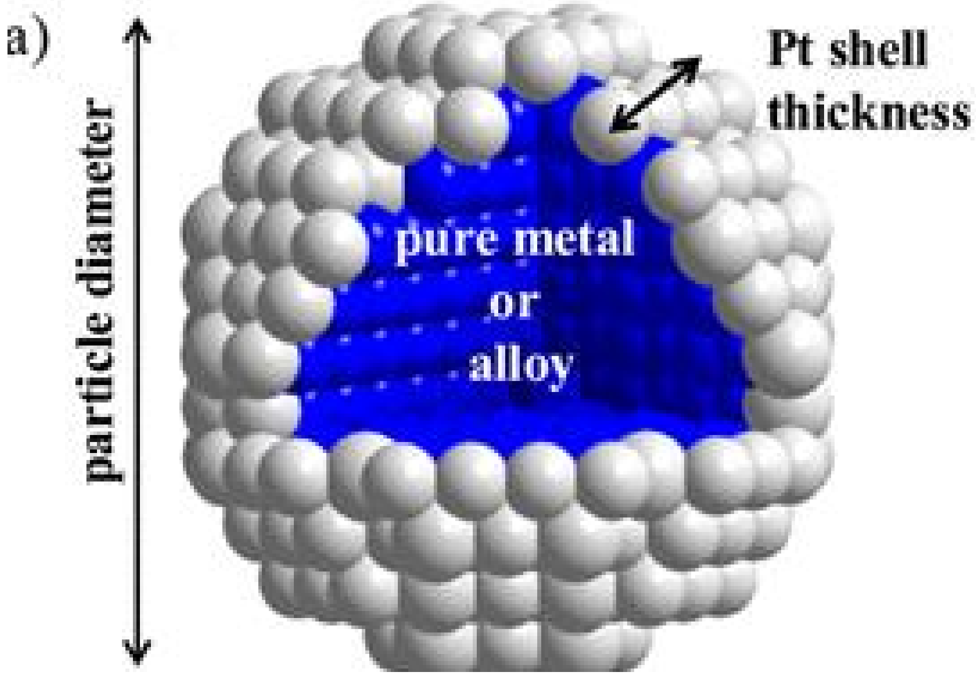

Figure 1.17: A 3D cross-section of a core−shell nanoparticle.[128] Reprinted with permission from (*J. Phys. Chem. Lett*. 2013, 4, 19, 3273–3291). Copyright (2013) American Chemical Society.

1.5.1. Transmission electron microscopy (TEM)

TEM is a technique that is used widely to characterize catalysts. A high-energy beam of electrons penetrates through a very thin layer of the catalyst, then, electrons will be scattered, and a TEM image will be recorded. From the TEM image of a catalyst, the particle size and the size distribution histogram (measuring more than 300 particles in the TEM images) can be obtained. Also, the morphology and the particle shape can be known.[126] The number of average particle size (d_{NA}) can be calculated from eq. 1.38,

$$d_{NA} = \frac{\sum n_i d_i}{\sum n_i} \tag{1.38}$$

where n_i is number of the particles that were used to measure d_{NA}, $d_i$is the size of each particle, and n is the total number of the counted particles. Moreover, TEM provides information about the homogeneous distribution of elements from the dark and bright spots. On the other hand, when high-resolution transmission electron microscopy (HR-TEM) is used, in the case of an intermetallic catalyst, information can be determined about the exposed plane and the presence of an oxide phase on the surface.[137] For example, Friedrich et al. have detected the formation of ZnO on the surface of PdZn by using the HR-TEM.

1.5.2. X-ray diffraction (XRD)

XRD is an analytical technique that is used widely for the determination of crystalline structures in materials science and chemistry. It is a powerful method to provide information about the structure, phases, and structural parameters (e.g. average particle size and lattice constant). In contrast to the TEM, X-rays penetrate through the materials and then the intensity of the scattered X-ray at different scattering angles are measured. From the XRD diffractogram, the presence of an alloy, intermetallic, bimetallic, or pure metal can be detected. It gives a clear difference between these structures. For example, in the case of an AB alloy catalyst, the XRD diffractogram will show a shift in the diffraction peaks between those for pure A and B, as shown in Figure 1.18. However, in the case of intermetallic catalysts, a new XRD diffractogram or additional peaks will be observed.

Furthermore, the average particle size can be measured from the XRD diffraction pattern by using the Scherrer equation (1.39); and the result can be compared with the TEM result.

$$average\ particle\ size = \frac{0.9 \times \lambda}{\beta \times cos\theta} \tag{1.39}$$

where λ is X-ray wavelength, θ is Bragg angle (the angle between the X-ray beam and the diffracting planes; in radians), and β is line broadening at half of the maximum intensity (in radians). Furthermore, lattice constants (a_{hkl}) can be measured by using eq.1.41 when interplanar spacing (d_{hkl}) is measured from eq. 1.40.

$$\frac{1}{d_{hkl}^2} = \frac{h^2 + k^2 + l^2}{a_{hkl}^2} \tag{1.40}$$

$$\lambda = 2d_{hkl}sin\theta_{hkl} \tag{1.41}$$

where λ is the X-ray wavelength, θ is the Bragg angle (in degree), and (hkl) are the Miller indices for the scattering angle.

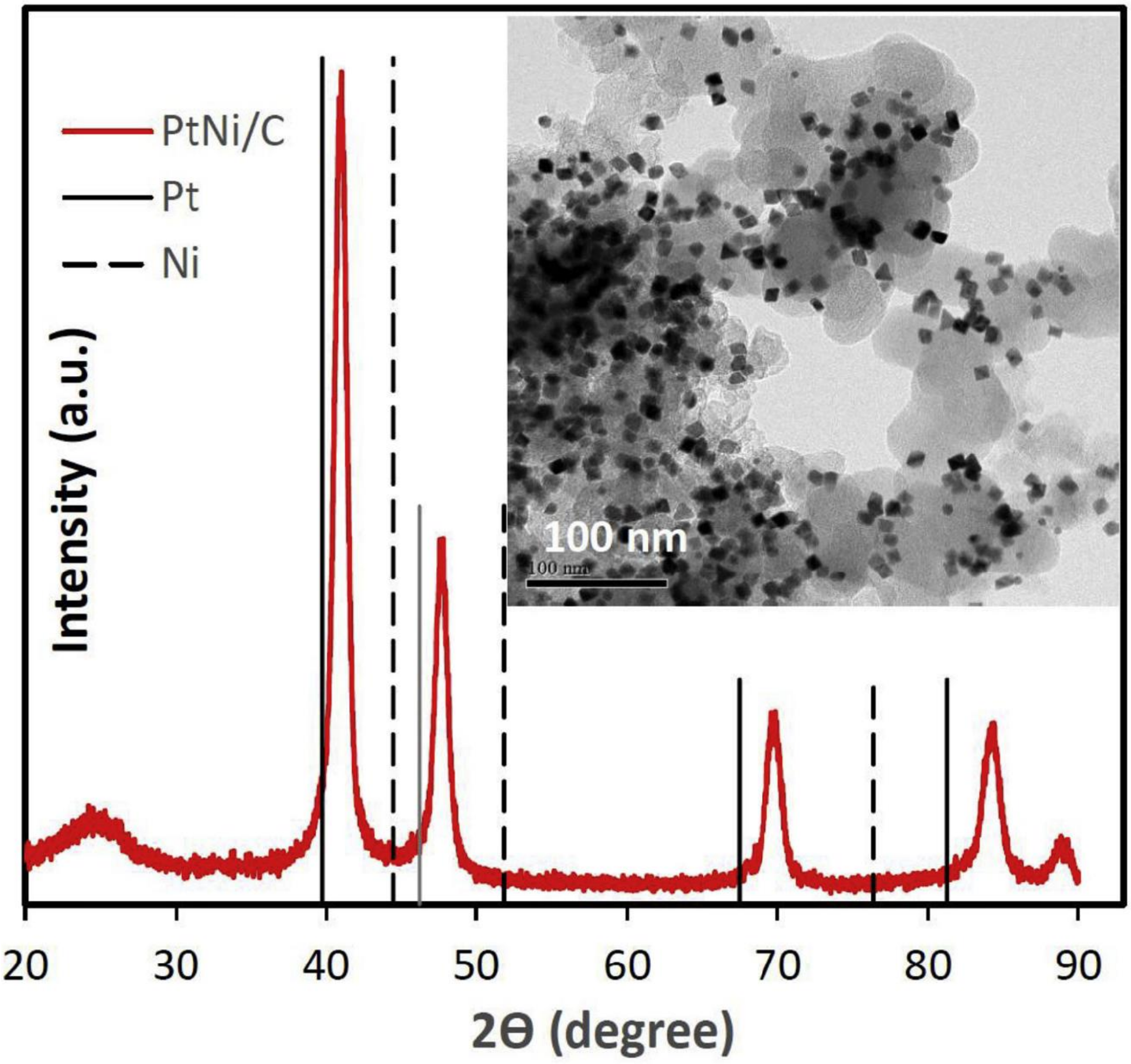

Figure 1.18: X-ray diffraction patterns at the PtNi/C catalyst and TEM image (inset). Reprinted from ref,[113] Copyright (2018), with permission from Elsevier.

Vegard's law (1.42) can be used to estimate the composition of alloys. For a certain ideal random alloy (disordered PtM alloy), Vegard's law assumes that the lattice parameter (a_{PtM}) has a linear relationship with PtM composition.

$$a\,(PtM) = a_{Pt}X + a_M(1 - X) \tag{1.42}$$

where a (PtM) is the lattice constant of PtM alloy, a_{Pt} is the lattice constant of pure Pt, a_M is the lattice constant of pure M, and X is the percentage of Pt in PtM alloy. However, many factors cause a positive deviation from this linearity, such as the chemical disordering effects, excess volume —excess differences in the electron density distribution of the PtM species in comparison to their distribution in the bulk—, and the related atomic level strain.[139] As a result, more order and less stable alloy than the random alloy will be formed.

Petkov et al. have carried out a brief study on the structure of PtCo and PtCoNi in PEMFCs. They have investigated the change in the activity for the ORR and in the structure in PEMFCs. They also studied the deviation of these catalysts from Vegard's law.[140] As shown in Figure 1.19, initially, all alloys (open symbols) have deviated positively from Vegard's law. After 6 h, under PEMFC conditions, they found that the atomic structure and the composition of nanoalloy had changed extremely; also, the nanoalloy catalysts deviated negatively for the Vegard's law. As a result, new stable nanoalloys (closed symbols) were observed with different activities and compositions. For example, as shown in Figure 1.20, a $Pt_{68}Co_{32}$ nanoalloy had initially a chemically ordered structure, then, after 6 h, the $Pt_{68}Co_{32}$ formed a chemically disordered structure. Based on Petkov et al.[140] and other studies,[141–143] for any nanoalloy catalyst, PEMFC conditions should be expected to have an effect on its composition, electrocatalytic activity, and structure.

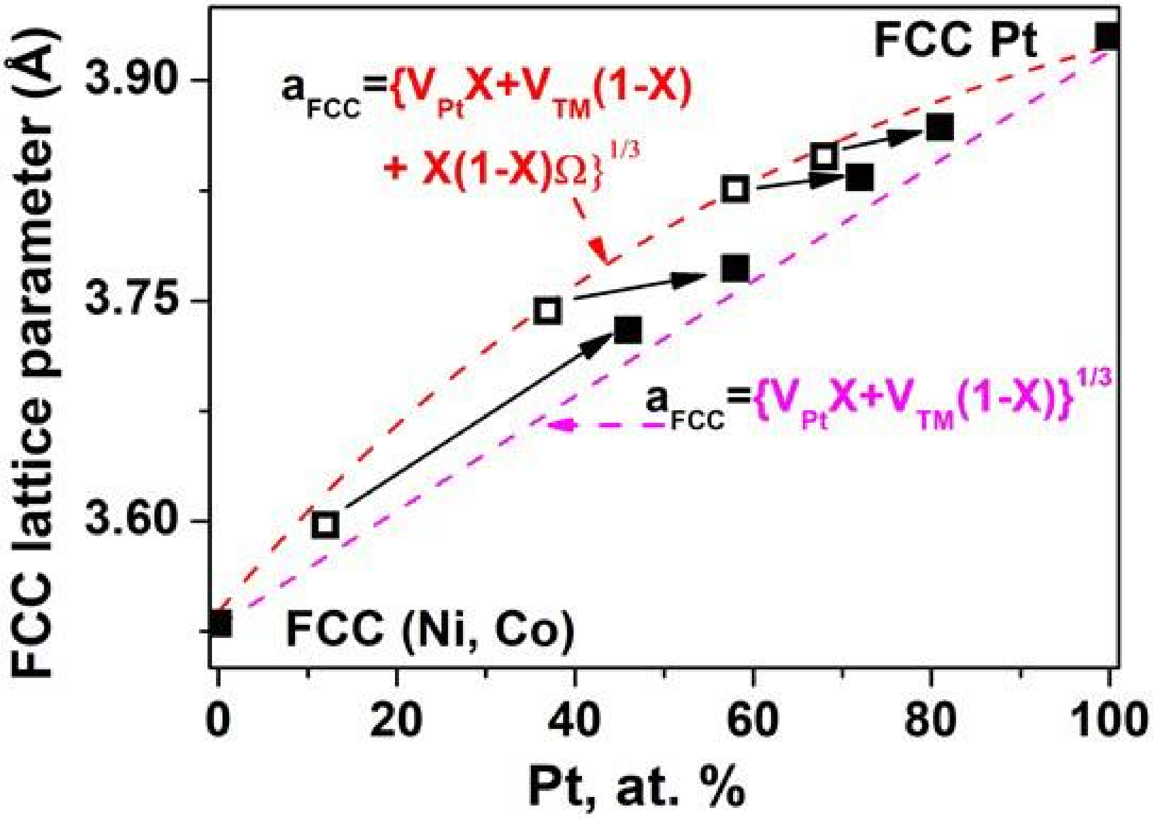

Figure 1.19: Lattice parameters vs. the experimental atomic %Pt for PtM nanoalloys. Closed symbols represent the data for PtM after fuel cell operation and open symbols represent the data for initial PtM. Black arrows linked data for each PtM before and after the cell operation. Reproduced with permission from ref.[140] Copyright 2019, ©Royal Society of Chemistry.

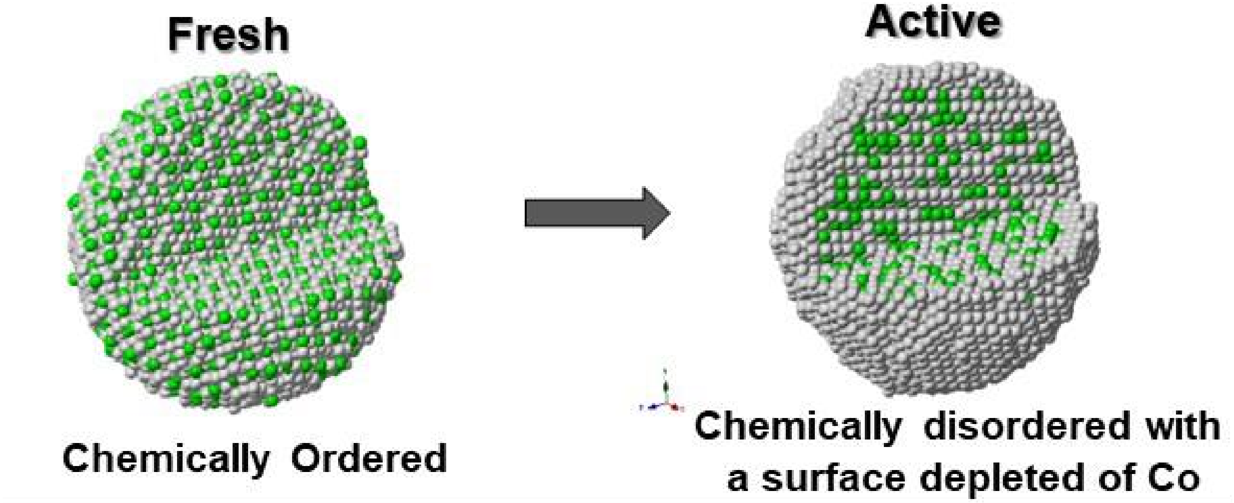

Figure 1.20: 3D structure models for initial (fresh) and active (after fuel cell operation) $Pt_{68}Co_{32}$ nanoalloy. Reproduced with permission from ref.[140] Copyright 2019, ©Royal Society of Chemistry.

1.6. Objectives

Catalysts play an important role in developing the performance and efficiency of DEFCs. Thus, this work aims to develop catalysts that have high activity for the EOR and selectivity for breaking the C-C bond to form CO_2. Based on the literature,[113] PtNi octahedra show high activity for the EOR and CO_2 production, especially when treated with acetic acid. Thus, in Chapter 3 the aim of the work was to prepare spherical PtNi catalysts and treat them with acetic acid. Then, we studied their activity for the EOR when Ni was removed from the catalyst surface with acetic acid (at ambient temperature by using cyclic voltammetry).

In Chapter 4, we investigated the effect of removing Ni from the catalyst surface with acetic acid on the activity of a number of PtNi catalysts for the EOR (in a nine-anode PEM electrolysis cell at 80 °C), the production of CO_2, and n_{av}.

In Chapter 5, our goal was to evaluate PtNi/C, PtFe/C and PtCu/C commercial catalysts in the nine-anode PEM electrolysis cell. Their performance and selectivity toward the C-C bond cleavage (in the EOR) were examined. PtCu/C had the highest production of CO_2.

Based on the literature and the results in Chapter 5, the presence of Cu improved the selectivity for the C-C bond cleavage. Thus, our fourth objective (Chapter 6) was to prepare PtRu/C and PtRuCu/C catalysts and explore the effect of Cu for the EOR (at ambient temperature). Furthermore, the effect of Cu in the PtRuCu/C on the performance and CO_2 yield was investigated at 80 °C in the nine-anode PEM electrolysis cell.

1.7. References

(1) Hannah Ritchie and Max Roser (2020) - “Energy”. Published online at OurWorldInData.org. Retrieved from: ‘https://ourworldindata.org/energy’ [Online Resource].

(2) Akhairi, M. A. F.; Kamarudin, S. K. Catalysts in Direct Ethanol Fuel Cell (DEFC): An Overview. *Int. J. Hydrogen Energy* **2016**, *41*, 4214–4228.

(3) Demirci, U. B. Direct Liquid-Feed Fuel Cells: Thermodynamic and Environmental Concerns. *J. Power Sources* **2007**, *169*, 239–246.

(4) Lamy, C.; Lima, A.; LeRhun, V.; Delime, F.; Coutanceau, C.; Léger, J.-M. Recent Advances in the Development of Direct Alcohol Fuel Cells (DAFC). *J. Power Sources* **2002**, *105*,

283–296.

(5) Chu, S.; Majumdar, A. Opportunities and Challenges for a Sustainable Energy Future. *Nature* **2012**, *488*, 294–303.

(6) Hemmat Esfe, M.; Afrand, M. A Review on Fuel Cell Types and the Application of Nanofluid in Their Cooling. *J. Therm. Anal. Calorim.* **2020**, *140*, 1633–1654.

(7) Lucia, U. Overview on Fuel Cells. *Renew. Sustain. Energy Rev.* **2014**, *30*, 164–169.

(8) Abdelkareem, M. A.; Elsaid, K.; Wilberforce, T.; Kamil, M.; Sayed, E. T.; Olabi, A. Environmental Aspects of Fuel Cells: A Review. *Sci. Total Environ.* **2021**, *752*, 141803.

(9) Wilberforce, T.; Alaswad, A.; Palumbo, A.; Dassisti, M.; Olabi, A. G. Advances in Stationary and Portable Fuel Cell Applications. *Int. J. Hydrogen Energy* **2016**, *41*, 16509–16522.

(10) Arshad, A.; Ali, H. M.; Habib, A.; Bashir, M. A.; Jabbal, M.; Yan, Y. Energy and Exergy Analysis of Fuel Cells: A Review. *Therm. Sci. Eng. Prog.* **2019**, *9*, 308–321.

(11) Lafforgue, C.; Zadick, A.; Dubau, L.; Maillard, F.; Chatenet, M. Selected Review of the Degradation of Pt and Pd-based Carbon-supported Electrocatalysts for Alkaline Fuel Cells: Towards Mechanisms of Degradation. *Fuel Cells* **2018**, *18*, 229–238.

(12) Eapen, D. E.; Suseendiran, S. R.; Rengaswamy, R. Phosphoric Acid Fuel Cells. In *Compendium of Hydrogen Energy*; Elsevier, 2016; pp 57–70.

(13) Lysik, A.; Cwieka, K.; Wejrzanowski, T.; Skibinski, J.; Milewski, J.; Marques, F. M. B.; Norby, T.; Xing, W. Silver Coated Cathode for Molten Carbonate Fuel Cells. *Int. J. Hydrogen Energy* **2020**, *45*, 19847–19857.

(14) Abdalla, A. M.; Hossain, S.; Azad, A. T.; Petra, P. M. I.; Begum, F.; Eriksson, S. G.; Azad, A. K. Nanomaterials for Solid Oxide Fuel Cells: A Review. *Renew. Sustain. Energy Rev.* **2018**, *82*, 353–368.

(15) Abdelkareem, M. A.; Sayed, E. T.; Nakagawa, N. Significance of Diffusion Layers on the Performance of Liquid and Vapor Feed Passive Direct Methanol Fuel Cells. *Energy* **2020**, *209*, 118492.

(16) Fathy, A.; Abdelkareem, M. A.; Olabi, A. G.; Rezk, H. A Novel Strategy Based on Salp Swarm Algorithm for Extracting the Maximum Power of Proton Exchange Membrane Fuel Cell. *Int. J. Hydrogen Energy* **2021**, *46*, 6087–6099.

(17) Ren, X.; Lv, Q.; Liu, L.; Liu, B.; Wang, Y.; Liu, A.; Wu, G. Current Progress of Pt and Pt-Based Electrocatalysts Used for Fuel Cells. *Sustain. Energy Fuels* **2020**, *4*, 15–30.

(18) Altarawneh, R. M. Overview on the Vital Step toward Addressing Platinum Catalyst Poisoning Mechanisms in Acid Media of Direct Ethanol Fuel Cells (DEFCs). *Energy & Fuels* **2021**, *35*, 11594–11612.

(19) Wang, Y.; Ruiz Diaz, D. F.; Chen, K. S.; Wang, Z.; Adroher, X. C. Materials, Technological Status, and Fundamentals of PEM Fuel Cells – A Review. *Mater. Today* **2020**, *32*, 178–203.

(20) Wigmore, J. G.; Langille, R. M. Six Generations of Breath Alcohol Testing Instruments: Changes in the Detection of Breath Alcohol Since 1930. An Historical Overview. *Can. Soc. Forensic Sci. J.* **2009**, *42*, 276–283.

(21) Rahman, M. R.; Allan, J. T. S.; Zamanzad Ghavidel, M.; Prest, L. E.; Saleh, F. S.; Easton, E. B. The Application of Power-Generating Fuel Cell Electrode Materials and Monitoring Methods to Breath Alcohol Sensors. *Sensors Actuators B Chem.* **2016**, *228*, 448–457.

(22) Kundu, P. P.; Dutta, K. Hydrogen Fuel Cells for Portable Applications. In *Compendium of Hydrogen Energy*; Elsevier, 2016; pp 111–131.

(23) Kreuer, K.-D.; Paddison, S. J.; Spohr, E.; Schuster, M. Transport in Proton Conductors for Fuel-Cell Applications: Simulations, Elementary Reactions, and Phenomenology. *Chem. Rev.* **2004**, *104*, 4637–4678.

(24) Daud, W. R. W.; Rosli, R. E.; Majlan, E. H.; Hamid, S. A. A.; Mohamed, R.; Husaini, T. PEM Fuel Cell System Control: A Review. *Renew. Energy* **2017**, *113*, 620–638.

(25) Wang, Y.; Chen, K. S.; Mishler, J.; Cho, S. C.; Adroher, X. C. A Review of Polymer Electrolyte Membrane Fuel Cells: Technology, Applications, and Needs on Fundamental Research. *Appl. Energy* **2011**, *88*, 981–1007.

(26) Acres, G. Recent Advances in Fuel Cell Technology and Its Applications. *J. Power Sources* **2001**, *100*, 60–66.

(27) Choi, W.; Howze, J. W.; Enjeti, P. Fuel-Cell Powered Uninterruptible Power Supply Systems: Design Considerations. *J. Power Sources* **2006**, *157*, 311–317.

(28) Badwal, S. P. S.; Giddey, S.; Kulkarni, A.; Goel, J.; Basu, S. Direct Ethanol Fuel Cells for Transport and Stationary Applications – A Comprehensive Review. *Appl. Energy* **2015**, *145*, 80–103.

(29) Corti, H. R.; Gonzalez, E. R. Introduction to Direct Alcohol Fuel Cells. In *Direct Alcohol Fuel Cells*; Springer Netherlands: Dordrecht, 2014; pp 1–32.

(30) Mauritz, K. A.; Moore, R. B. State of Understanding of Nafion. *Chem. Rev.* **2004**, *104*, 4535–4586.

(31) Dresch, M. A.; Matos, B. R.; Godoi, D. R. M.; Linardi, M.; Fonseca, F. C.; Villullas, H. de las M.; Santiago, E. I. Advancing Direct Ethanol Fuel Cell Operation at Intermediate Temperature by Combining Nafion-Hybrid Electrolyte and Well-Alloyed PtSn/C Electrocatalyst. *Int. J. Hydrogen Energy* **2021**, *46*, 13252–13264.

(32) Mathias, M. F.; Makharia, R.; Gasteiger, H. A.; Conley, J. J.; Fuller, T. J.; Gittleman, C. J.; Kocha, S. S.; Miller, D. P.; Mittelsteadt, C. K.; Xie, T.; Yan, S. G.; Yu, P. T.; S, U.; Hoover, H. Two Fuel Cell Cars In Every Garage ?. *Electrochem Soc Interface* **2005**, 14.

(33) Kim, Y. S.; Dong, L.; Hickner, M. A.; Glass, T. E.; Webb, V.; McGrath, J. E. State of Water in Disulfonated Poly(Arylene Ether Sulfone) Copolymers and a Perfluorosulfonic Acid Copolymer (Nafion) and Its Effect on Physical and Electrochemical Properties. *Macromolecules* **2003**, *36*, 6281–6285.

(34) Kim, H.; Lee, S.; Kim, S.; Oh, C.; Ryu, J.; Kim, J.; Park, E.; Hong, S.; No, K. Membrane Crystallinity and Fuel Crossover in Direct Ethanol Fuel Cells with Nafion Composite Membranes Containing Phosphotungstic Acid. *J. Mater. Sci.* **2017**, *52*, 2400–2412.

(35) Kienitz, B.; Kolde, J.; Priester, S.; Baczkowski, C.; Crum, M. Ultra-Thin Reinforced Ionomer Membranes to Meet Next Generation Fuel Cell Targets. *ECS Trans.* **2019**, *41*, 1521–1530.

(36) Litster, S.; McLean, G. PEM Fuel Cell Electrodes. *J. Power Sources* **2004**, *130*, 61–76.

(37) Shao, Y.; Yin, G.; Wang, Z.; Gao, Y. Proton Exchange Membrane Fuel Cell from Low Temperature to High Temperature: Material Challenges. *J. Power Sources* **2007**, *167*, 235–242.

(38) Kulkarni, A.; Siahrostami, S.; Patel, A.; Nørskov, J. K. Understanding Catalytic Activity

Trends in the Oxygen Reduction Reaction. *Chem. Rev.* **2018**, *118*, 2302–2312.

(39) Choi, S.-I.; Xie, S.; Shao, M.; Odell, J. H.; Lu, N.; Peng, H.-C.; Protsailo, L.; Guerrero, S.; Park, J.; Xia, X.; Wang, J.; Kim, M. J.; Xia, Y. Synthesis and Characterization of 9 Nm Pt–Ni Octahedra with a Record High Activity of 3.3 A/Mg Pt for the Oxygen Reduction Reaction. *Nano Lett.* **2013**, *13*, 3420–3425.

(40) Edwards, P. P.; Kuznetsov, V. L.; David, W. I. F.; Brandon, N. P. Hydrogen and Fuel Cells: Towards a Sustainable Energy Future. *Energy Policy* **2008**, *36*, 4356–4362.

(41) Hua, T.; Ahluwalia, R.; Eudy, L.; Singer, G.; Jermer, B.; Asselin-Miller, N.; Wessel, S.; Patterson, T.; Marcinkoski, J. Status of Hydrogen Fuel Cell Electric Buses Worldwide. *J. Power Sources* **2014**, *269*, 975–993.

(42) de Miranda, P. E. V.; Carreira, E. S.; Icardi, U. A.; Nunes, G. S. Brazilian Hybrid Electric-Hydrogen Fuel Cell Bus: Improved on-Board Energy Management System. *Int. J. Hydrogen Energy* **2017**, *42*, 13949–13959.

(43) An, L.; Zhao, T. S.; Zeng, L. Agar Chemical Hydrogel Electrode Binder for Fuel-Electrolyte-Fed Fuel Cells. *Appl. Energy* **2013**, *109*, 67–71.

(44) Sharaf, O. Z.; Orhan, M. F. An Overview of Fuel Cell Technology: Fundamentals and Applications. *Renew. Sustain. Energy Rev.* **2014**, *32*, 810–853.

(45) Gong, L.; Yang, Z.; Li, K.; Xing, W.; Liu, C.; Ge, J. Recent Development of Methanol Electrooxidation Catalysts for Direct Methanol Fuel Cell. *J. Energy Chem.* **2018**, *27*, 1618–1628.

(46) An, L.; Zhao, T. S. Transport Phenomena in Alkaline Direct Ethanol Fuel Cells for

Sustainable Energy Production. *J. Power Sources* **2017**, *341*, 199–211.

(47) Ramachandran, S.; Stimming, U. Well to Wheel Analysis of Low Carbon Alternatives for Road Traffic. *Energy Environ. Sci.* **2015**, *8*, 3313–3324.

(48) Zakaria, Z.; Kamarudin, S. K.; Timmiati, S. N. Membranes for Direct Ethanol Fuel Cells: An Overview. *Appl. Energy* **2016**, *163*, 334–342.

(49) Ong, B. C.; Kamarudin, S. K.; Basri, S. Direct Liquid Fuel Cells: A Review. *Int. J. Hydrogen Energy* **2017**, *42*, 10142–10157.

(50) Abuin, G. C.; Franceschini, E. A.; Nonjola, P.; Mathe, M. K.; Modibedi, M.; Corti, H. R. A High Selectivity Quaternized Polysulfone Membrane for Alkaline Direct Methanol Fuel Cells. *J. Power Sources* **2015**, *279*, 450–459.

(51) James, D. D.; Bennett, D. V.; Li, G.; Ghumman, A.; Helleur, R. J.; Pickup, P. G. Online Analysis of Products from a Direct Ethanol Fuel Cell. *Electrochem. Commun.* **2009**, *11*, 1877–1880.

(52) Wang, Y.; Zou, S.; Cai, W.-B. Recent Advances on Electro-Oxidation of Ethanol on Pt- and Pd-Based Catalysts: From Reaction Mechanisms to Catalytic Materials. *Catalysts* **2015**, *5*, 1507–1534.

(53) Sun, S.; Halseid, M. C.; Heinen, M.; Jusys, Z.; Behm, R. J. Ethanol Electrooxidation on a Carbon-Supported Pt Catalyst at Elevated Temperature and Pressure: A High-Temperature/High-Pressure DEMS Study. *J. Power Sources* **2009**, *190*, 2–13.

(54) Lai, S. C. S.; Kleijn, S. E. F.; Öztürk, F. T. Z.; van Rees Vellinga, V. C.; Koning, J.; Rodriguez, P.; Koper, M. T. M. Effects of Electrolyte PH and Composition on the Ethanol

Electro-Oxidation Reaction. *Catal. Today* **2010**, *154*, 92–104.

(55) Guo, J.; Chen, R.; Zhu, F.-C.; Sun, S.-G.; Villullas, H. M. New Understandings of Ethanol Oxidation Reaction Mechanism on Pd/C and Pd2Ru/C Catalysts in Alkaline Direct Ethanol Fuel Cells. *Appl. Catal. B Environ.* **2018**, *224*, 602–611.

(56) Yang, G.; Zhang, Q.; Yu, H.; Peng, F. Platinum-Based Ternary Catalysts for the Electrooxidation of Ethanol. *Particuology* **2021**, *58*, 169–186.

(57) Sheng, T.; Lin, W.-F.; Hardacre, C.; Hu, P. Role of Water and Adsorbed Hydroxyls on Ethanol Electrochemistry on Pd: New Mechanism, Active Centers, and Energetics for Direct Ethanol Fuel Cell Running in Alkaline Medium. *J. Phys. Chem. C* **2014**, *118*, 5762–5772.

(58) Hibbitts, D. D.; Neurock, M. Influence of Oxygen and PH on the Selective Oxidation of Ethanol on Pd Catalysts. *J. Catal.* **2013**, *299*, 261–271.

(59) Wang, H.-F.; Liu, Z.-P. Comprehensive Mechanism and Structure-Sensitivity of Ethanol Oxidation on Platinum: New Transition-State Searching Method for Resolving the Complex Reaction Network. *J. Am. Chem. Soc.* **2008**, *130*, 10996–11004.

(60) Kavanagh, R.; Cao, X.-M.; Lin, W.-F.; Hardacre, C.; Hu, P. Origin of Low CO_2 Selectivity on Platinum in the Direct Ethanol Fuel Cell. *Angew. Chemie Int. Ed.* **2012**, *51*, 1572–1575.

(61) An, L.; Zhao, T. S.; Li, Y. S. Carbon-Neutral Sustainable Energy Technology: Direct Ethanol Fuel Cells. *Renew. Sustain. Energy Rev.* **2015**, *50*, 1462–1468.

(62) Lamy, C.; Coutanceau, C.; Leger, J.-M. The Direct Ethanol Fuel Cell: A Challenge to Convert Bioethanol Cleanly into Electric Energy. In *Catalysis for Sustainable Energy Production*; Wiley-VCH Verlag GmbH & Co. KGaA: Weinheim, Germany; pp 1–46.

(63) Altarawneh, R. M.; Pickup, P. G. Product Distributions and Efficiencies for Ethanol Oxidation in a Proton Exchange Membrane Electrolysis Cell. *J. Electrochem. Soc.* **2017**, *164*, F861–F865.

(64) Flórez-Montaño, J.; García, G.; Guillén-Villafuerte, O.; Rodríguez, J. L.; Planes, G. A.; Pastor, E. Mechanism of Ethanol Electrooxidation on Mesoporous Pt Electrode in Acidic Medium Studied by a Novel Electrochemical Mass Spectrometry Set-Up. *Electrochim. Acta* **2016**, *209*, 121–131.

(65) Torrero, J.; Pérez-Alonso, F. J.; Peña, M. A.; Domínguez, C.; Al-Youbi, A. O.; Al-Thabaiti, S. A.; Basahel, S. N.; Alshehri, A. A.; Rojas, S. In Situ Infrared Study of the Electrooxidation of Ethanol and Acetaldehyde in Acid Electrolyte. *ChemElectroChem* **2016**, *3*, 1072–1083.

(66) Zhang, X.; Zwanziger, J. W. Design and Applications of an in Situ Electrochemical NMR Cell. *J. Magn. Reson.* **2011**, *208*, 136–147.

(67) Webster, R. D. In Situ Electrochemical-NMR Spectroscopy. Reduction of Aromatic Halides. *Anal. Chem.* **2004**, *76*, 1603–1610.

(68) Simões, F. C.; dos Anjos, D. M.; Vigier, F.; Léger, J.-M.; Hahn, F.; Coutanceau, C.; Gonzalez, E. R.; Tremiliosi-Filho, G.; de Andrade, A. R.; Olivi, P.; Kokoh, K. B. Electroactivity of Tin Modified Platinum Electrodes for Ethanol Electrooxidation. *J. Power Sources* **2007**, *167*, 1–10.

(69) Rousseau, S.; Coutanceau, C.; Lamy, C.; Léger, J.-M. Direct Ethanol Fuel Cell (DEFC): Electrical Performances and Reaction Products Distribution under Operating Conditions with Different Platinum-Based Anodes. *J. Power Sources* **2006**, *158*, 18–24.

(70) Corradini, P. G.; Santos, N. A.; Perez, J. Pt-Sn-Eu/C Catalysts: Application of Rare Earth

Metals as Anodes in Direct Ethanol Fuel Cells. *Fuel Cells* **2018**, *18*, 73–81.

(71) Kim, I.; Han, O. H.; Chae, S. A.; Paik, Y.; Kwon, S.-H.; Lee, K.-S.; Sung, Y.-E.; Kim, H. Catalytic Reactions in Direct Ethanol Fuel Cells. *Angew. Chem. Int. Ed* **2011**, *123*, 2318–2322.

(72) Paik, Y.; Kim, S.-S.; Han, O. H. Spatial Distribution of Reaction Products in Direct Ethanol Fuel Cell. *Electrochem. Commun.* **2009**, *11*, 302–304.

(73) James, D. D.; Pickup, P. G. Effects of Crossover on Product Yields Measured for Direct Ethanol Fuel Cells. *Electrochim. Acta* **2010**, *55*, 3824–3829.

(74) Zheng, Y.; Wan, X.; Cheng, X.; Cheng, K.; Dai, Z.; Liu, Z. Advanced Catalytic Materials for Ethanol Oxidation in Direct Ethanol Fuel Cells. *Catalysts* **2020**, *10*, 166.

(75) Jung, N.; Chung, D. Y.; Ryu, J.; Yoo, S. J.; Sung, Y.-E. Pt-Based Nanoarchitecture and Catalyst Design for Fuel Cell Applications. *Nano Today* **2014**, *9*, 433–456.

(76) Ozoemena, K. I. Nanostructured Platinum-Free Electrocatalysts in Alkaline Direct Alcohol Fuel Cells: Catalyst Design, Principles and Applications. *RSC Adv.* **2016**, *6*, 89523–89550.

(77) Sharma, S.; Pollet, B. G. Support Materials for PEMFC and DMFC Electrocatalysts—A Review. *J. Power Sources* **2012**, *208*, 96–119.

(78) Friedl, J.; Stimming, U. Model Catalyst Studies on Hydrogen and Ethanol Oxidation for Fuel Cells. *Electrochim. Acta* **2013**, *101*, 41–58.

(79) Almeida, C. V. S.; Ferreira, D. S.; Huang, H.; Gaiotti, A. C.; Camara, G. A.; Russell, A. E.; Eguiluz, K. I. B.; Salazar-Banda, G. R. Highly Active Pt_3Rh/C Nanoparticles towards Ethanol Electrooxidation. Influence of the Catalyst Structure. *Appl. Catal. B Environ.* **2019**,

254, 113–127.

(80) Zhu, Y.; Bu, L.; Shao, Q.; Huang, X. Subnanometer PtRh Nanowire with Alleviated Poisoning Effect and Enhanced C–C Bond Cleavage for Ethanol Oxidation Electrocatalysis. *ACS Catal.* **2019**, *9*, 6607–6612.

(81) Spinacé, E. .; Neto, A. .; Linardi, M. Electro-Oxidation of Methanol and Ethanol Using PtRu/C Electrocatalysts Prepared by Spontaneous Deposition of Platinum on Carbon-Supported Ruthenium Nanoparticles. *J. Power Sources* **2004**, *129*, 121–126.

(82) Sulaiman, J. E.; Zhu, S.; Xing, Z.; Chang, Q.; Shao, M. Pt–Ni Octahedra as Electrocatalysts for the Ethanol Electro-Oxidation Reaction. *ACS Catal.* **2017**, *7*, 5134–5141.

(83) Almeida, T. S.; Van Wassen, A. R.; VanDover, R. B.; de Andrade, A. R.; Abruña, H. D. Combinatorial PtSnM (M = Fe, Ni, Ru and Pd) Nanoparticle Catalyst Library toward Ethanol Electrooxidation. *J. Power Sources* **2015**, *284*, 623–630.

(84) Narayanan, R.; El-Sayed, M. A. Shape-Dependent Catalytic Activity of Platinum Nanoparticles in Colloidal Solution. *Nano Lett.* **2004**, *4*, 1343–1348.

(85) Li, L.; Liu, H.; Qin, C.; Liang, Z.; Scida, A.; Yue, S.; Tong, X.; Adzic, R. R.; Wong, S. S. Ultrathin Pt x Sn 1– x Nanowires for Methanol and Ethanol Oxidation Reactions: Tuning Performance by Varying Chemical Composition. *ACS Appl. Nano Mater.* **2018**, *1*, 1104–1115.

(86) Chen, J.-Y.; Lim, S.-C.; Kuo, C.-H.; Tuan, H.-Y. Sub-1 Nm PtSn Ultrathin Sheet as an Extraordinary Electrocatalyst for Methanol and Ethanol Oxidation Reactions. *J. Colloid Interface Sci.* **2019**, *545*, 54–62.

(87) Huang, D.-B.; Yuan, Q.; He, P.-L.; Wang, K.; Wang, X. A Facile and General Strategy for the Synthesis of Porous Flowerlike Pt-Based Nanocrystals as Effective Electrocatalysts for Alcohol Oxidation. *Nanoscale* **2016**, *8*, 14705–14710.

(88) Yaqoob, L.; Noor, T.; Iqbal, N. A Comprehensive and Critical Review of the Recent Progress in Electrocatalysts for the Ethanol Oxidation Reaction. *RSC Adv.* **2021**, *11*, 16768–16804.

(89) Rizo, R.; Sebastián, D.; Lázaro, M. J.; Pastor, E. On the Design of Pt-Sn Efficient Catalyst for Carbon Monoxide and Ethanol Oxidation in Acid and Alkaline Media. *Appl. Catal. B Environ.* **2017**, *200*, 246–254.

(90) Luo, C.; Xie, H.; Wang, Q.; Luo, G.; Liu, C. A Review of the Application and Performance of Carbon Nanotubes in Fuel Cells. *J. Nanomater.* **2015**, *2015*, 1–10.

(91) Qin, Y.-H.; Li, Y.; Lam, T.; Xing, Y. Nitrogen-Doped Carbon-TiO 2 Composite as Support of Pd Electrocatalyst for Formic Acid Oxidation. *J. Power Sources* **2015**, *284*, 186–193.

(92) Wang, Y.; Wang, D.; Li, Y. A Fundamental Comprehension and Recent Progress in Advanced Pt-based ORR Nanocatalysts. *SmartMat* **2021**, *2*, 56–75.

(93) Strasser, P.; Koh, S.; Anniyev, T.; Greeley, J.; More, K.; Yu, C.; Liu, Z.; Kaya, S.; Nordlund, D.; Ogasawara, H.; Toney, M. F.; Nilsson, A. Lattice-Strain Control of the Activity in Dealloyed Core–Shell Fuel Cell Catalysts. *Nat. Chem.* **2010**, *2*, 454–460.

(94) Camara, G. .; de Lima, R. .; Iwasita, T. Catalysis of Ethanol Electrooxidation by PtRu: The Influence of Catalyst Composition. *Electrochem. commun.* **2004**, *6*, 812–815.

(95) Şen, S.; Şen, F.; Gökağaç, G. Preparation and Characterization of Nano-Sized Pt–Ru/C

Catalysts and Their Superior Catalytic Activities for Methanol and Ethanol Oxidation. *Phys. Chem. Chem. Phys.* **2011**, *13*, 6784.

(96) dos Santos, M. C.; Parreira, L. S.; De Moura Souza, F.; Camargo Junior, J.; Gentil, T. Fuel Cells: Hydrogen and Ethanol Technologies. In *Reference Module in Materials Science and Materials Engineering*; Elsevier, 2017.

(97) Colmati, F.; Antolini, E.; Gonzalez, E. R. Effect of Temperature on the Mechanism of Ethanol Oxidation on Carbon Supported Pt, PtRu and Pt3Sn Electrocatalysts. *J. Power Sources* **2006**, *157*, 98–103.

(98) Brueckner, T. M.; Pickup, P. G. Kinetics and Stoichiometry of Methanol and Ethanol Oxidation in Multi-Anode Proton Exchange Membrane Cells. *J. Electrochem. Soc.* **2017**, *164*, F1172–F1178.

(99) Rodríguez-Gómez, A.; Dorado, F.; de Lucas-Consuegra, A.; de la Osa, A. R. Influence of Pt/Ru Anodic Ratio on the Valorization of Ethanol by PEM Electrocatalytic Reforming towards Value-Added Products. *J. Energy Chem.* **2021**, *56*, 264–275.

(100) Shen, S. Y.; Zhao, T. S.; Xu, J. B. Carbon Supported PtRh Catalysts for Ethanol Oxidation in Alkaline Direct Ethanol Fuel Cell. *Int. J. Hydrogen Energy* **2010**, *35*, 12911–12917.

(101) Bergamaski, K.; Gonzalez, E. R.; Nart, F. C. Ethanol Oxidation on Carbon Supported Platinum-Rhodium Bimetallic Catalysts. *Electrochim. Acta* **2008**, *53*, 4396–4406.

(102) El Sawy, E. N.; Brueckner, T. M.; Pickup, P. G. Electrochemical Oxidation of Methanol and Ethanol at Rh@Pt and Ru@Pt Catalysts. *J. Electrochem. Soc.* **2020**, *167*, 106507.

(103) Sorsa, O.; Romar, H.; Lassi, U.; Kallio, T. Co-Electrodeposited Mesoporous PtM (M=Co,

Ni, Cu) as an Active Catalyst for Oxygen Reduction Reaction in a Polymer Electrolyte Membrane Fuel Cell. *Electrochim. Acta* **2017**, *230*, 49–57.

(104) Gong, W.; Jiang, Z.; Huang, L.; Shen, P. K. Pt Ni Alloy Hyperbranched Nanostructures with Enhanced Catalytic Performance towards Oxygen Reduction Reaction. *Int. J. Hydrogen Energy* **2018**, *43*, 18436–18443.

(105) Travitsky, N.; Ripenbein, T.; Golodnitsky, D.; Rosenberg, Y.; Burshtein, L.; Peled, E. Pt-, PtNi- and PtCo-Supported Catalysts for Oxygen Reduction in PEM Fuel Cells. *J. Power Sources* **2006**, *161*, 782–789.

(106) Wang, Y.; Yang, J.; Sun, S.; Wang, L.; Guo, T.; Zhang, D.; Xue, Z.; Zhou, X. PtNi Nanoparticles Supported on Electrochemically Reduced Porous Graphene Oxide for Methanol Oxidation Reaction. *Chem. Phys. Lett.* **2019**, *730*, 575–581.

(107) Paulus, U. A.; Wokaun, A.; Scherer, G. G.; Schmidt, T. J.; Stamenkovic, V.; Radmilovic, V.; Markovic, N. M.; Ross, P. N. Oxygen Reduction on Carbon-Supported Pt−Ni and Pt−Co Alloy Catalysts. *J. Phys. Chem. B* **2002**, *106*, 4181–4191.

(108) Park, K.-W.; Choi, J.-H.; Kwon, B.-K.; Lee, S.-A.; Sung, Y.-E.; Ha, H.-Y.; Hong, S.-A.; Kim, H.; Wieckowski, A. Chemical and Electronic Effects of Ni in Pt/Ni and Pt/Ru/Ni Alloy Nanoparticles in Methanol Electrooxidation. *J. Phys. Chem. B* **2002**, *106*, 1869–1877.

(109) Antolini, E. Pt-Ni and Pt-M-Ni (M = Ru, Sn) Anode Catalysts for Low-Temperature Acidic Direct Alcohol Fuel Cells: A Review. *Energies* **2017**, *10*, 42.

(110) Antolini, E.; Salgado, J. R. C.; Gonzalez, E. R. Carbon Supported $Pt_{75}M_{25}$ (M=Co, Ni) Alloys as Anode and Cathode Electrocatalysts for Direct Methanol Fuel Cells. *J. Electroanal. Chem.* **2005**, *580*, 145–154.

(111) Zhang, X.; Li, H.; Yang, J.; Lei, Y.; Wang, C.; Wang, J.; Tang, Y.; Mao, Z. Recent Advances in Pt-Based Electrocatalysts for PEMFCs. *RSC Adv.* **2021**, *11*, 13316–13328.

(112) Xing, G.; Wang, L.; Fu, H. Advanced Research Progress on High-Efficient Utilization of Pt Electrocatalysts in Fuel Cells. *Energy Technol.* **2021**, *9*, 2100227.

(113) Altarawneh, R. M.; Brueckner, T. M.; Chen, B.; Pickup, P. G. Product Distributions and Efficiencies for Ethanol Oxidation at PtNi Octahedra. *J. Power Sources* **2018**, *400*, 369–376.

(114) Soundararajan, D.; Park, J. H.; Kim, K. H.; Ko, J. M. Pt–Ni Alloy Nanoparticles Supported on CNF as Catalyst for Direct Ethanol Fuel Cells. *Curr. Appl. Phys.* **2012**, *12*, 854–859.

(115) Antolini, E. Effect of the Structural Characteristics of Binary Pt – Ru and Ternary Pt – Ru – M Fuel Cell Catalysts on the Activity of Ethanol Electrooxidation in Acid Medium. **2013**, 1–9.

(116) Liu, D.; Yang, J.; Chen, Y. Nanocatalysts for Electrocatalytic Oxidation of Ethanol. *ChemSusChem.* **2019**, *12*, 2117-2132.

(117) Almeida, C. V. S.; Galiote, N. A.; Eguiluz, K. I. B.; Salazar-Banda, G. R.; Del Colle, V.; Tremiliosi-Filho, G. Evidence of Surface Restructuration on Pt–Rh/C and Pt–Rh–Ni/C Nanoparticles Applied to Ethanol Electrooxidation Reaction. *Electrochim. Acta* **2020**, *351*, 136223.

(118) Erini, N.; Rudi, S.; Beermann, V.; Krause, P.; Yang, R.; Huang, Y.; Strasser, P. Exceptional Activity of a Pt-Rh-Ni Ternary Nanostructured Catalyst for the Electrochemical Oxidation of Ethanol. *ChemElectroChem* **2015**, *2*, 903–908.

(119) Han, S.; Liu, H.; Chen, P.; Jiang, J.; Chen, Y. Porous Trimetallic PtRhCu Cubic Nanoboxes for Ethanol Electrooxidation. *Adv. Energy Mater.* **2018**, *8*, 1801326.

(120) Chen, C.; Xu, H.; Shang, H.; Jin, L.; Song, T.; Wang, C.; Gao, F.; Zhang, Y.; Du, Y. Ultrafine PtCuRh Nanowire Catalysts with Alleviated Poisoning Effect for Efficient Ethanol Oxidation. *Nanoscale* **2019**, *11*, 20090–20095.

(121) Liu, H.; Li, J.; Wang, L.; Tang, Y.; Xia, B. Y.; Chen, Y. Trimetallic PtRhNi Alloy Nanoassemblies as Highly Active Electrocatalyst for Ethanol Electrooxidation. *Nano Res.* **2017**, *10*, 3324–3332.

(122) Wang, P.; Yin, S.; Wen, Y.; Tian, Z.; Wang, N.; Key, J.; Wang, S.; Shen, P. K. Ternary Pt 9 RhFe x Nanoscale Alloys as Highly Efficient Catalysts with Enhanced Activity and Excellent CO-Poisoning Tolerance for Ethanol Oxidation. *ACS Appl. Mater. Interfaces* **2017**, *9*, 9584–9591.

(123) García, G.; Tsiouvaras, N.; Pastor, E.; Peña, M. A.; Fierro, J. L. G.; Martínez-Huerta, M. V. Ethanol Oxidation on PtRuMo/C Catalysts: In Situ FTIR Spectroscopy and DEMS Studies. *Int. J. Hydrogen Energy* **2012**, *37*, 7131–7140.

(124) Wang, Z.-B.; Yin, G.-P.; Zhang, J.; Sun, Y.-C.; Shi, P.-F. Investigation of Ethanol Electrooxidation on a Pt–Ru–Ni/C Catalyst for a Direct Ethanol Fuel Cell. *J. Power Sources* **2006**, *160*, 37–43.

(125) Wu, G.; Swaidan, R.; Cui, G. Electrooxidations of Ethanol, Acetaldehyde and Acetic Acid Using PtRuSn/C Catalysts Prepared by Modified Alcohol-Reduction Process. *J. Power Sources* **2007**, *172*, 180–188.

(126) Beyhan, S.; Léger, J.-M.; Kadırgan, F. Pronounced Synergetic Effect of the Nano-Sized

PtSnNi/C Catalyst for Ethanol Oxidation in Direct Ethanol Fuel Cell. *Appl. Catal. B Environ.* **2013**, *130–131*, 305–313.

(127) Kadırgan, F. Promising Anode Candidates for Direct Ethanol Fuel Cell : Carbon Supported PtSn-Based Trimetallic Catalysts Prepared by Bo ¨ Nnemann Method. **2013**, *38*, 6830-6841.

(128) Oezaslan, M.; Hasché, F.; Strasser, P. Pt-Based Core–Shell Catalyst Architectures for Oxygen Fuel Cell Electrodes. *J. Phys. Chem. Lett.* **2013**, *4*, 3273–3291.

(129) Luo, M.; Wei, L.; Wang, F.; Han, K.; Zhu, H. Gram-Level Synthesis of Core–Shell Structured Catalysts for the Oxygen Reduction Reaction in Proton Exchange Membrane Fuel Cells. *J. Power Sources* **2014**, *270*, 34–41.

(130) Strasser, P. Dealloyed Core-Shell Fuel Cell Electrocatalysts. *Rev. Chem. Eng.* **2009**, *25*.

(131) Wang, D.; Yu, Y.; Xin, H. L.; Hovden, R.; Ercius, P.; Mundy, J. A.; Chen, H.; Richard, J. H.; Muller, D. A.; DiSalvo, F. J.; Abruña, H. D. Tuning Oxygen Reduction Reaction Activity via Controllable Dealloying: A Model Study of Ordered Cu_3Pt/C Intermetallic Nanocatalysts. *Nano Lett.* **2012**, *12*, 5230–5238.

(132) Wang, C.; Chi, M.; Li, D.; Strmcnik, D.; van der Vliet, D.; Wang, G.; Komanicky, V.; Chang, K.-C.; Paulikas, A. P.; Tripkovic, D.; Pearson, J.; More, K. L.; Markovic, N. M.; Stamenkovic, V. R. Design and Synthesis of Bimetallic Electrocatalyst with Multilayered Pt-Skin Surfaces. *J. Am. Chem. Soc.* **2011**, *133*, 14396–14403.

(133) Huang, M.; Wu, W.; Wu, C.; Guan, L. Pt_2SnCu Nanoalloy with Surface Enrichment of Pt Defects and SnO_2 for Highly Efficient Electrooxidation of Ethanol. *J. Mater. Chem. A* **2015**, *3*, 4777–4781.

(134) Guo, R.; Qian, F.; An, S.; Zhang, J.; Chou, K.; Ye, J.; Zhou, Z. Effect of Acid Treatment on Electrocatalytic Performance of PtNi Catalyst. *Chem. Res. Chinese Univ.* **2020**.

(135) Marakatti, V. S.; Peter, S. C. Synthetically Tuned Electronic and Geometrical Properties of Intermetallic Compounds as Effective Heterogeneous Catalysts. *Prog. Solid State Chem.* **2018**, *52*, 1–30.

(136) Marakatti, V. S.; Sarma, S. C.; Joseph, B.; Banerjee, D.; Peter, S. C. Synthetically Tuned Atomic Ordering in PdCu Nanoparticles with Enhanced Catalytic Activity toward Solvent-Free Benzylamine Oxidation. *ACS Appl. Mater. Interfaces* **2017**, *9*, 3602–3615.

(137) Friedrich, M.; Penner, S.; Heggen, M.; Armbrüster, M. High CO_2 Selectivity in Methanol Steam Reforming through ZnPd/ZnO Teamwork. *Angew. Chemie Int. Ed.* **2013**, *52*, 4389–4392.

(138) Xiong, L.; Yang, X.; Xu, M.; Xu, Y.; Wu, D. Pt–Ni Alloy Nanoparticles Supported on Multiwalled Carbon Nanotubes for Methanol Oxidation in Alkaline Media. *J. Solid State Electrochem.* **2013**, *17*, 805–810.

(139) Lubarda, V. . On the Effective Lattice Parameter of Binary Alloys. *Mech. Mater.* **2003**, *35*, 53–68.

(140) Petkov, V.; Maswadeh, Y.; Vargas, J. A.; Shan, S.; Kareem, H.; Wu, Z.-P.; Luo, J.; Zhong, C.-J.; Shastri, S.; Kenesei, P. Deviations from Vegard's Law and Evolution of the Electrocatalytic Activity and Stability of Pt-Based Nanoalloys inside Fuel Cells by in Operando X-Ray Spectroscopy and Total Scattering. *Nanoscale* **2019**, *11*, 5512–5525.

(141) Petkov, V.; Maswadeh, Y.; Zhao, Y.; Lu, A.; Cronk, H.; Chang, F.; Shan, S.; Kareem, H.; Luo, J.; Zhong, C. J.; Shastri, S.; Kenesei, P. Nanoalloy Catalysts inside Fuel Cells: An

Atomic-Level Perspective on the Functionality by Combined in Operando x-Ray Spectroscopy and Total Scattering. *Nano Energy* **2018**, *49*, 209–220.

(142) Greco, G.; Witkowska, A.; Minicucci, M.; Olivi, L.; Principi, E.; Dsoke, S.; Moretti, A.; Marassi, R.; Di Cicco, A. Local Ordering Changes in Pt–Co Nanocatalyst Induced by Fuel Cell Working Conditions. *J. Phys. Chem. C* **2012**, *116*, 12791–12802.

(143) Principi, E.; Witkowska, A.; Dsoke, S.; Marassi, R.; Di Cicco, A. An XAS Experimental Approach to Study Low Pt Content Electrocatalysts Operating in PEM Fuel Cells. *Phys. Chem. Chem. Phys.* **2009**, *11*, 9987.

Chapter 2

2. Experimental

2.1 Chemicals and materials

All chemicals and materials were used as received. Table A.1, Appendix A, shows all chemicals and materials.

2.1.1 Nafion™ 117 membranes for the PEM electrolysis cells

Nafion™ 117 membranes were cut into pieces (4.5 cm * 4.5 cm). First, all pieces were heated to 80 °C in 3% H_2O_2 for 1 h under stirring. Then, pieces were immersed in 1.0 M aqueous H_2SO_4 at 80 °C for 2 h under stirring. After each step, pieces were rinsed well with deionized water. Finally, the Nafion™ 117 membranes were heated for 3 h in deionized water at 80 °C under stirring; and all pieces were stored in deionized water.[1]

2.2 Working electrodes

2.2.1 Electrode preparation for a nine-anode proton exchange membrane (PEM) electrolysis cell

Catalyst coated electrodes were prepared by suspending the catalyst in 70 µL of Nafion solution (Dupont; 5% Nafion), 120 µL of 1-propanol, 120 µL of 2-propanol, and 100 µL of deionized water. The mixture was sonicated at ambient temperature for 3 h. A 71 µL of the suspension was dropped onto a disk of Toray™ carbon fiber paper (0.236 cm^2) and dried overnight at ambient temperature.

2.2.2 Electrode preparation for a 5 cm^2 PEM electrolysis cell

An anode for a 5 cm^2 PEM electrolysis cell was prepared by suspending the catalyst in a Nafion solution (5%) and 1-propanol, and the mixture was sonicated at ambient temperature. Then, the ink was spread onto Toray carbon fiber paper (5 cm^2) and dried overnight at ambient temperature.[2]

2.2.3 Electrode preparation for cyclic voltammetry

Working electrodes for cyclic voltammetry were prepared by suspending 2 mg of the catalyst in 120 μL of water, 50 μL of 5% Nafion solution, and 30 μL of 2-propanol.[3] The mixture was sonicated for 3 h and pipetted (3 μL) onto a polished glassy carbon disk (0.072 cm^2). The glassy carbon was left to dry overnight at ambient temperature. The catalyst loading was 0.03 mg.[3] For each catalyst, at least three glassy carbon disks were prepared.

2.3 Electrochemical measurements

Electrochemical measurements were carried out by cyclic voltammetry, a nine-anode PEM electrolysis cell (Electro Chem Inc.), and a 5 cm^2 PEM electrolysis cell (Fuel Cell Technology Inc).

2.3.1 Cyclic voltammetry

Cyclic voltammetry measurements were made in a three-compartment glass cell (Figure 2.1). The reference electrode was a saturated calomel electrode (SCE), and the counter electrode was a platinum wire. EC-Lab electrochemical software was used to record the results obtained with a Bio-Logic SP-50 potentiostat/galvanostat. These experiments were carried out in 1.0 M aqueous H_2SO_4 at ambient temperature. The solution was purged with N_2 gas to remove O_2 from the solution for 15 min. First, the working electrodes were cycled from -0.20 V to 0.80 V at 100 mV s^{-1} in 1.0 M aqueous H_2SO_4. Then, they were cycled from -0.20 V to 0.80 V at 10 mV s^{-1} in 0.10 M ethanol and 1.0 M H_2SO_4.

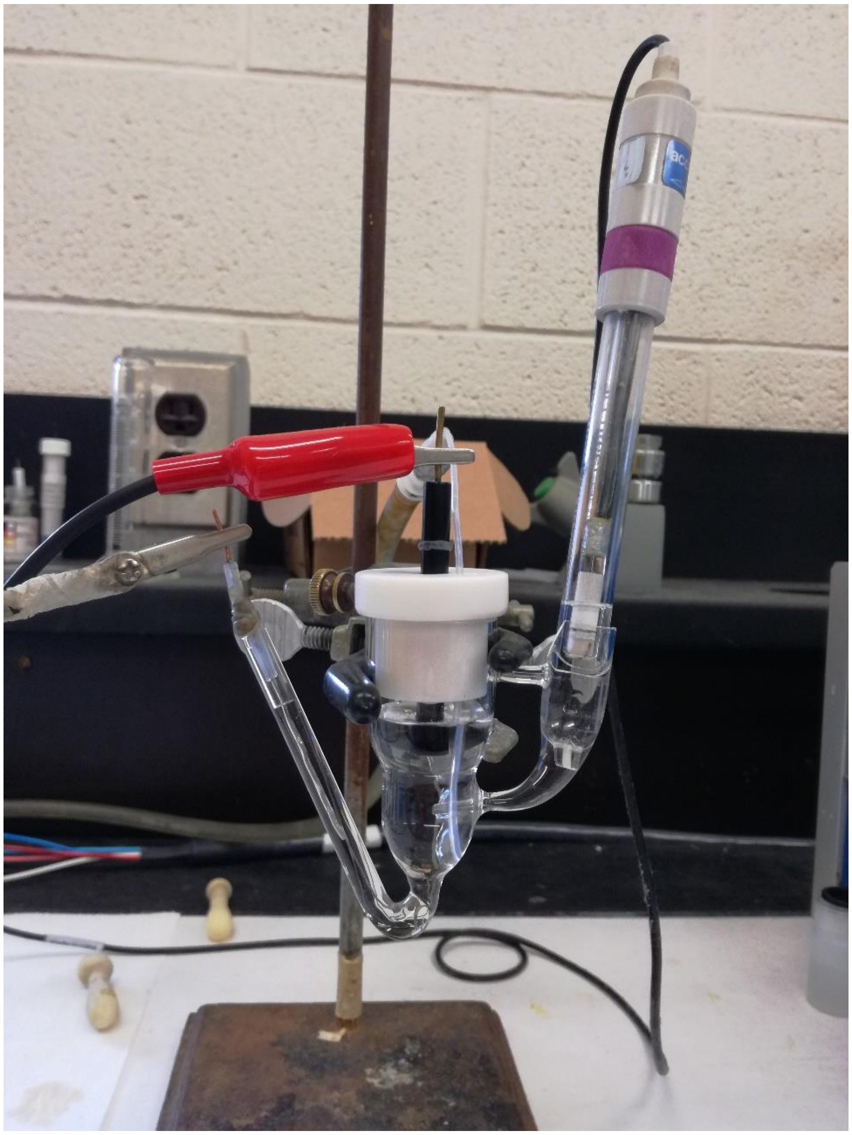

Figure 2.1: The three-compartment glass cell for cyclic voltammetry.

2.3.2 A nine-anode PEM electrolysis cell

The nine-anode PEM electrolysis cell consisted of a cathode (a 5 cm^2 Pt black commercial), nine individual anodes (0.236 cm^2 per anode), a Nafion™ 117 membrane, and a gasket with nine individual holes, as shown in Figure 2.2.[4] An Arbin® Instruments MSTAT multi-channel potentiostat was used to control the potentials. The membrane and electrode assemblies were pressed inside the cell by a torque wrench (ca. 1.5 MPa, ambient temperature). A Cole-Parmer temperature controller (type K thermocouple, model 89810-02) was used to control the temperature of the cell (80 ℃). Also, a mass flow meter was used to control the N_2 flow rate (Omega® Engineering Inc, FMA1806A). A crossover mode was used to operate the cell to control the diffusion of ethanol to the anode. As a result, steady-state polarization curves with mass transport regions were produced. In this mode, the anode is purged with N_2 gas, while the ethanol (0.10 M ethanol at 0.5 mL min^{-1} or 0.2 mL min^{-1}) is pumped at the cathode. As a result, ethanol moves through the membrane to the anode.

When potentials were applied, the ethanol was oxidized, and protons were produced. Then, the protons moved through the membrane to the cathode and hydrogen gas was produced. The production of hydrogen creates a pseudo reference electrode with a stable potential (a dynamic hydrogen reference electrode; DHE). Polarization curves were obtained at 80 ℃ from 0.90 V to 0.00 V in 50 mV steps. Before each polarization curve, the cell was preconditioned at 0.70 V for 1 h. The CO_2 was measured by connecting the outlets of the cathode and anode with a trap. The latter was connected with a non-dispersive infrared (NDIR) carbon dioxide detector (T6615 CO_2 OEM model).

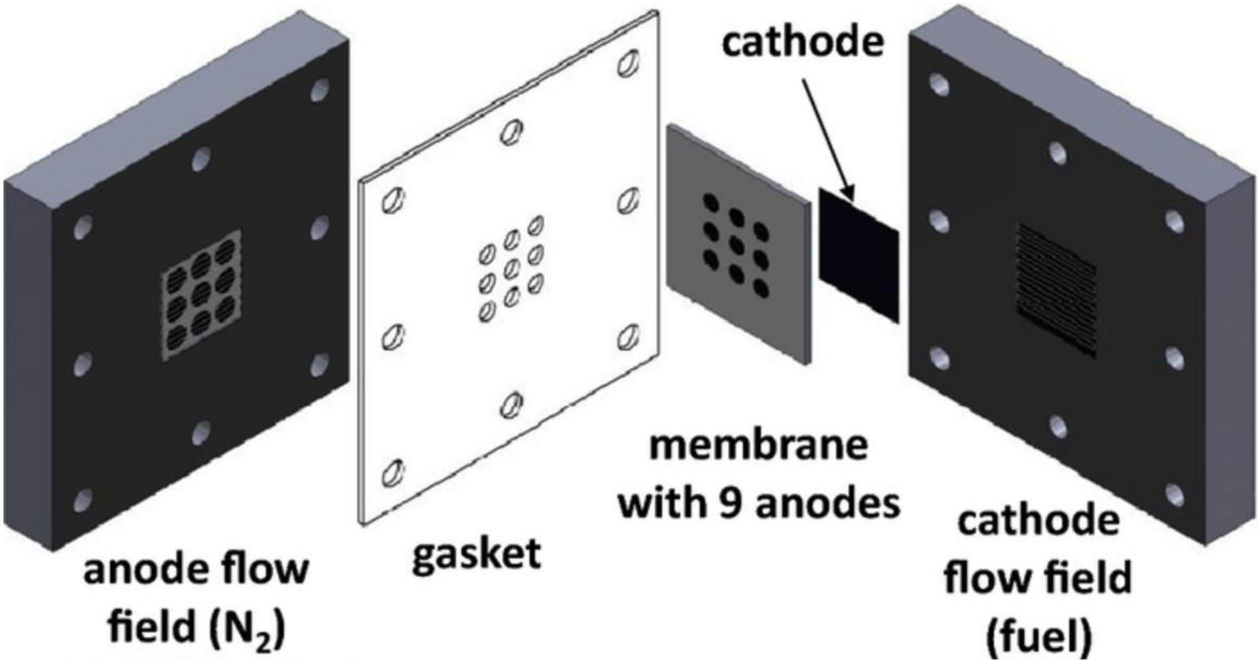

Figure 2.2: A schematic diagram of the nine-anode PEM electrolysis cell. Reprinted from ref.[4]

2.3.3 A 5 cm^2 PEM electrolysis cell

The 5 cm^2 PEM electrolysis cell comprised of a cathode (a 5 cm^2 Pt black commercial cathode), an anode, a Nafion™ 117 membrane, and two gaskets, as shown in Figure 2.3. A Hokuto Denko HA-301 potentiostat was used to operate the cell. The membrane and electrode assembly were prepared by pressing the electrodes onto each side of a Nafion™ 117 membrane at a pressure of ca. 1.5 MPa and ambient temperature. A Cole-Parmer temperature controller was used to control the temperature of this cell at 80 °C. In contrast to the nine-anode PEM electrolysis cell, a polarization mode was used in the 5 cm^2 PEM electrolysis cell. In this mode, ethanol (0.10 M at 0.50 mL min^{-1} or 0.20 mL min^{-1}) was supplied at the anode and oxidized there, while at the cathode, the N_2 gas (30 mL min^{-1}) was supplied, and protons were reduced to produce a DHE.

Figure 2.3: The 5 cm^2 PEM electrolysis cell.

The 5 cm^2 PEM electrolysis was used to measure polarization curves and the product distribution of the ethanol oxidation reaction (EOR).[5] Polarization curves were measured by applying a potential range from 0.0 V to 0.70 V. The current was averaged for at least 100 s and plotted against the potential. The residual ethanol and products (acetic acid, acetaldehyde and CO_2) were collected following a procedure reported by Altarawneh et al.[2] As shown in Figure 2.4, the outlets of the anode and cathode were combined and products were collected in a trap (at different potentials). The trap was cooled with a mixture of dry ice and ice (20:80 ratio). The cooled liquid was taken and a sample for NMR analysis was prepared. The outlet of the trap was connected directly to a NDIR carbon dioxide detector to measure the CO_2.

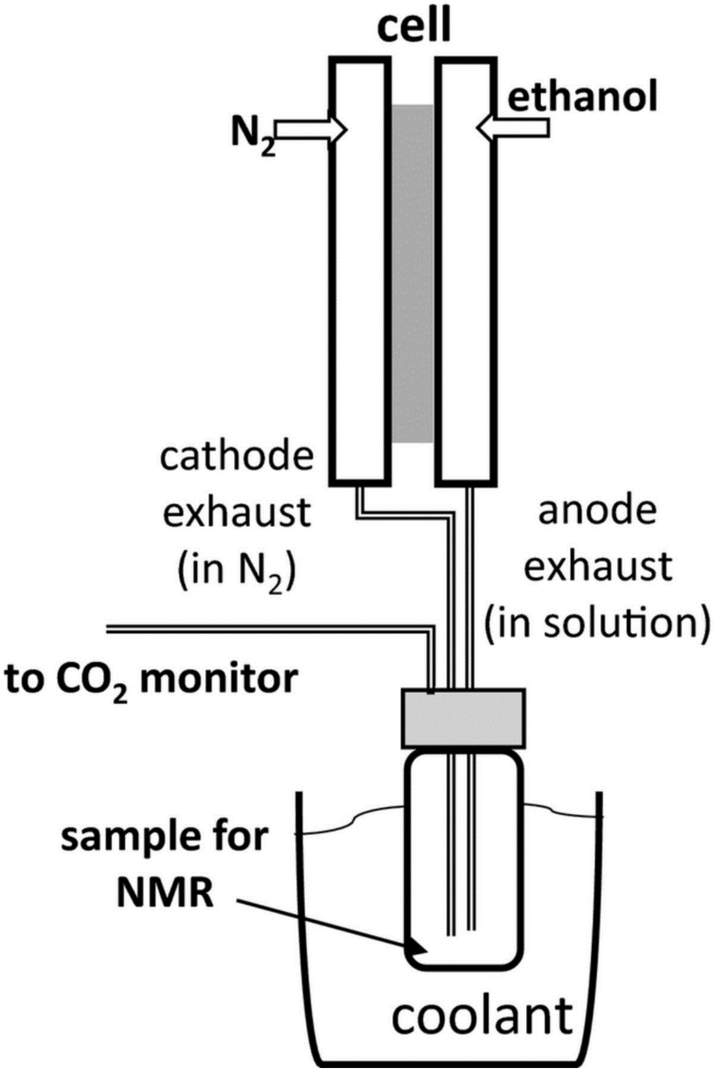

Figure 2.4: The three-compartment glass cell for cyclic voltammetry.

2.4 Measuring the faradaic yield of CO_2

A NDIR carbon dioxide detector with Logger Pro software was used for all CO_2 measurements. For the nine-anode and 5 cm^2 PEM electrolysis cells, the outlets of the cathode and anode were connected to the inlet of the detector. At each potential, CO_2 was produced and recorded over 8 to 10 min; and the measured current was averaged for at least 100 s.

A calibration curve was used to calculate the CO_2 concentration (ppm). The calibration curve, as shown in Figure 2.5, was measured by pumping 0.10 M of methanol to the cell at 0.20 mL min^{-1}, 80 °C, and a potential range from 0.20 V to 0.60 V. At each potential, the measured current was averaged for at least 100 s. Then, the theoretical rate of CO_2 was calculated by eq. 2.1,

$$theoretical\ rate\ of\ CO_2 = \frac{average\ current\ (mA)}{nF} \tag{2.1}$$

where n is the number of electrons transferred to form one molecule of CO_2 and F = 96500 (As mol^{-1}) is the faraday constant. The experimental rate of CO_2 (mole s^{1}) was calculated by eq. 2.2,

$$experimental\ rate\ of\ CO_2 = \frac{CO_2(ppm) \times flow\ rate\ of\ nitrogen\ (Lmin^{-1})}{60 \times 10^6 \times V_m} \tag{2.2}$$

where V_m is the volume of any gas in L mol^{-1}, CO_2 (ppm) is obtained from the detector. Both the theoretical rate of CO_2 and the experimental rate of CO_2 were used to calculate the faradaic CO_2 yield as shown in eq. 2.3,

$$farafaic\ CO_2\ yield = \frac{experimental\ rate\ of\ CO_2}{theoretical\ rate\ of\ CO_2} \tag{2.3}$$

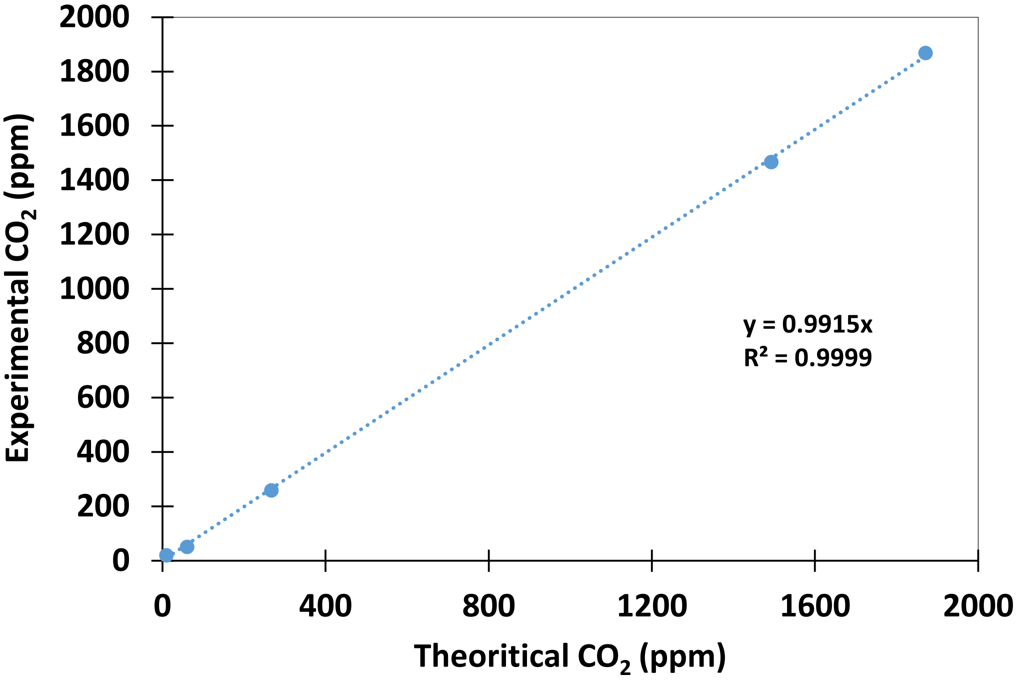

Figure 2.5: A calibration curve of CO_2 for the oxidation of 0.100 M methanol (0.2 mL min^{-1}) at 80 °C and different potentials.

2.5 ^{1}H nuclear magnetic resonance spectrometer (NMR)

For analysis by ^{1}H NMR, 400 μL of cooled sample was taken from the cooled trap and mixed with 400 μL of an internal standard (0.033 g of fumaric acid in 10 mL of D_2O). Moreover, calibration curves were measured for the acetic acid and residual ethanol, as shown in Figure 2.6 and Figure 2.7, respectively. These were used to determine the concentration of ethanol and acetic acid.

A Bruker AVANCE 500 MHz with Topspin 3.0 ICON software was used to quantify the residual ethanol and products (acetic acid and acetaldehyde) from the EOR. The internal standard provides a singlet peak at 6.72 ppm and acetic acid at 2.01 ppm. The residual ethanol has a triplet peak at 1.10 ppm and a quartet peak at 3.6 ppm. All areas under acetic acid and ethanol were normalized against the internal standard. Unfortunately, preparing a calibration curve for acetaldehyde is difficult because the boiling point is 19 °C. Thus, the concentration of acetaldehyde was measured by estimating the area under the doublet peaks at 2.15 ppm and 1.24 ppm. Details about calculating the chemical yield of CO_2 and the faradaic yield of acetic acid and acetaldehyde are shown in Appendix A.

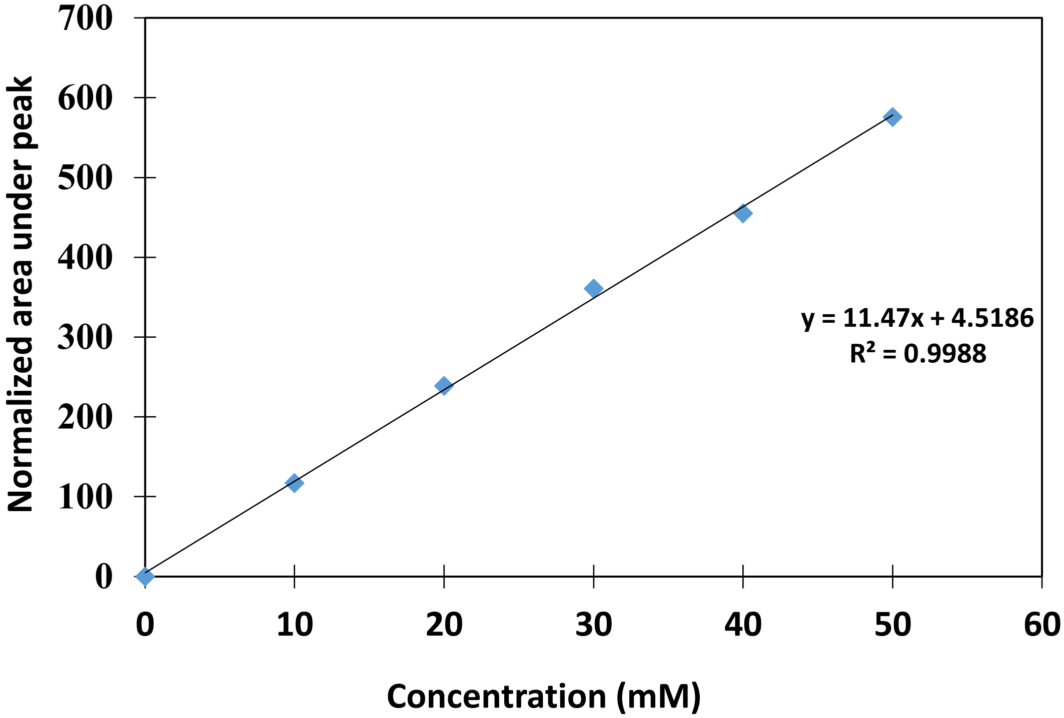

Figure 2.6: The calibration curve of ethanol using NMR method described in section 2.5.

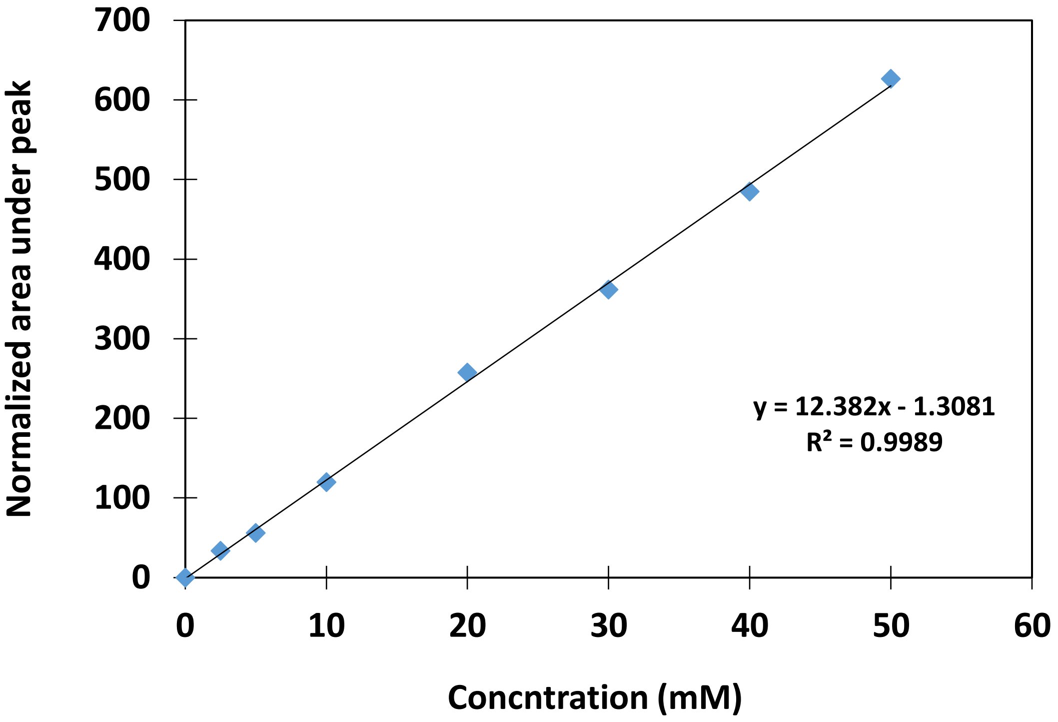

Figure 2.7: The calibration curve of acetic acid using NMR method described in section 2.5.

2.6 Catalyst characterization

2.6.1 X-ray powder diffraction (XRD)

An X-ray diffractometer (Rigaku Ultima IV) with a copper X-ray source (Cu Kα radiation, $\lambda = 1.5406$ Å) and a scintillation counter detector were used to determine X-ray diffraction patterns for the prepared catalysts. These measurements were carried out by Dr. Wanda Aylward of the Core Research Equipment and Instrument Training (CREAIT). The sample was ground by a mortar before the analysis, and the scan range was from 20 degrees to 90 degrees. XRD was used to identify crystalline components of the catalysts, and measure particle sizes and lattice parameters. The mean particle size was measured according to the Scherrer equation (eq. 2.4),

$$\text{mean particle size} = \frac{0.9\lambda}{\beta cos\theta} \qquad (2.4)$$

where λ is X-ray wavelength, θ is Bragg angle (in radians), and β is line broadening at half of the maximum intensity (in radians). Furthermore, the Bragg scattering equation (2.5) was used to calculate the lattice constant (a) for all catalysts,

$$a = \frac{\lambda\sqrt{h^2 + k^2 + l^2}}{2sin\theta} \tag{2.5}$$

where, λ is X-ray wavelength, θ is Bragg angle (in degree), and (hkl) are the Miller indices (111) for the scattering angle.

2.6.2 Thermal gravimetric analysis (TGA)

A TA Instrument Q500 thermogravimetric analyzer with Thermal Advantage software was used for TGA analysis. About 3 mg to 5 mg of catalyst was used for this analysis. All TGA experiments were carried out under an air atmosphere at a temperature range from 25 °C to 1000 °C. Under these conditions, the carbon is completely oxidized, and the residual mass represents the total metal loading of the catalyst.

2.6.3 Scanning electron microscopy (SEM) and the energy dispersive X-ray analysis (EDX)

A Quanta 400 SEM with a Roentec SDD EDX X-ray detector was used to carry out SEM-EDX analysis. The sample was prepared by dispersing about 3 mg of the catalyst in 100 µL of deionized water and 100 µL of 2-propanol. The mixture was sonicated for 3 h. The ink was poured onto an adhesive carbon tab on the specimen stub and left overnight to dry.

2.6.4 Transmission electron microscopy (TEM)

A Tecnai Spirt transmission electron microscopy (FEI), at the Health Sciences Centre, was used by Stephanie Tucker to analyze all catalysts. All measurements were operated at 80 kV. The sample (2 mg) was dispersed in 2-propanol and sonicated for 2 h. A drop of ink was applied onto the 200-carbon mesh Cu grid. The particle size distributions were obtained by analyzing nearly 70 particles randomly from the micrographs.

2.6.5 X-ray photoelectron spectroscopy (XPS)

A VG Micro-tech Multi-lab ESCA 2000 system was used to examine the electronic properties of the catalysts as well as their surface chemical states. Andrew George at Dalhousie University run the experiment.

2.7 References

(1) Napoli, L.; Lavorante, M. J.; Franco, J.; Sanguinetti, A.; Fasoli, H. Effects on Nafion® 117 Membrane Using Different Strong Acids in Various Concentrations. *J. New Mater. Electrochem. Syst.* **2013**, *16*, 151–156.

(2) Altarawneh, R. M.; Majidi, P.; Pickup, P. G. Determination of the Efficiency of Ethanol Oxidation in a Proton Exchange Membrane Electrolysis Cell. *J. Power Sources* **2017**, *351*, 106–114.

(3) Elgrishi, N.; Rountree, K. J.; McCarthy, B. D.; Rountree, E. S.; Eisenhart, T. T.; Dempsey, J. L. A Practical Beginner's Guide to Cyclic Voltammetry. *J. Chem. Educ.* **2018**, *95*, 197–206.

(4) Brueckner, T. M.; Pickup, P. G. Kinetics and Stoichiometry of Methanol and Ethanol Oxidation in Multi-Anode Proton Exchange Membrane Cells. *J. Electrochem. Soc.* **2017**, *164*, F1172–F1178.

(5) Altarawneh, R. M.; Pickup, P. G. Product Distributions and Efficiencies for Ethanol Oxidation in a Proton Exchange Membrane Electrolysis Cell. *J. Electrochem. Soc.* **2017**,

164, F861–F865.

Chapter 3

3. PtNi$_x$/C Catalysts for Improved Activity for Ethanol Oxidation

The first author (Diala A. Alqdeimat) contributed to all parts of this research as the main researcher including literature review, carrying out all the experiments, measuring and analyzing the data, discussing and presenting data, and writing the first draft of the published manuscript.

The corresponding author (Prof. Peter G. Pickup) was the principal investigator and provided the initial ideas for this project. He mentored the principal author (Diala A. Alqdeimat) and supported her throughout the project time. He reviewed all data analysis, finalized, and submitted the manuscript.

Part of this Chapter has been published as: -

(D. A. Alqdeimat and P. G. Pickup, $PtNi_x/C$ Catalysts for Improved Performance in Ethanol Fuel Cells, ECS Trans., 97, 2020).

The raw data are provided in Appendix B.

3.1 Introduction

Direct ethanol fuel cells (DEFC) have been considered as an attractive power source with high potential for vehicles and electronic devices. Ethanol is an important renewable energy resource because it is easy to handle and store, has low toxicity, is produced in large quantities from agricultural waste and biomass, and has a high energy density of 8.0 kWh kg^{-1}.[1–6] However, many problems have impeded the development of commercial DEFC, including low current densities, incomplete ethanol oxidation, low faradic efficiencies, and crossover through the membrane. To overcome these problems, many anode catalysts have been developed to increase the activity, selectivity, and efficiency of DEFC.[7]

Pt nanoparticles (NPs) have been used widely in DEFC due to how highly selective they are when encountering the cleavage of the C-C bond of ethanol and how they provide a high number of low coordination active sites. Thus, they have high activity toward ethanol oxidation. When an ethanol molecule is adsorbed on an active Pt site, two main oxidation reactions occur. The first reaction is the complete oxidation of ethanol to produce carbon dioxide (CO_2), while the second one is the incomplete oxidation of ethanol to produce mainly acetic acid (CH_3COOH) and acetaldehyde (CH_3CHO).[2] However, the reaction intermediates (e.g. CO and CH_x) produced during ethanol oxidation reactions (EOR) cause surface poisoning of Pt/C catalysts, and therefore, the sluggish kinetics of ethanol reactions occur.[8,9]

Studying the effects of alloying Pt catalysts with Ni on the oxidation of ethanol has gained interest.[10–15] Ni is a more electropositive metal (oxophilic metal) than Pt and has been found to enhance its activity toward the EOR.[16,17] Two main factors were found to increase the activity: a bifunctional mechanism and an electronic effect.[7] The presence of a more electropositive metal (e.g. Ni) provides more -OH species on the surface of the catalyst (bifunctional effect) and drives the oxidation of CO_{ad} intermediate to produce CO_2.[16,18] Moreover, the incorporation of Ni into the Pt lattice changes the electronic structure, as a result, the Pt-CO intermediate bonding would be weaker and easy to break.[19,20] The influence of PtNi NPs on oxygen reduction and methanol oxidation reactions has been reported,[21,22] however, few works have studied ethanol oxidation on PtNi catalysts. Soundararaian et al. found that PtNi NPs were more active for the EOR than for Pt.[23] Furthermore, Wang et al. reported that the incorporation of Ni into PtSn alloys increased the peak current density by 1.5 times during the EOR.[17]

Furthermore, there has been growing interest in the use of core-shell NPs for the EOR.[24] Core-shell Pt NP consists of a core (metal or alloy) and one or more monolayers of Pt as a shell, represented as M@Pt. It has been found that M@Pt structures provide more control of the electronic structure, surface reactivity for Pt, and geometric lattice strain.[25] Dealloying is a common method that has been used to prepare core-shell NPs and/or core-shell-like NPs.[26] In general, the dealloying process is the dissolution of one metal (less noble metal) from a uniform alloy to form a thicker Pt-rich surface in an acidic media.[27] Few studies have been conducted concerning the effect of acid treatment (dealloying) on PtNi catalysts for the EOR.[18,28] Furthermore, the detailed mechanism at PtNi for the EOR is still unclear. Altarawneh et al. studied the effect of acid treatment on the activity of PtNi octahedra for the EOR.[18] They found that the activity and the chemical yield of CO_2 (at 0.3 V) were improved after treating PtNi with acetic acid.[18] However, the increased amount of CO_2 that was reported by Altarawneh et al is not fully understood.[18] There are limited studies of the activity and the yield of CO_2 at PtNi for the EOR, in contrast with the ORR and MOR (methanol oxidation reaction). Thus, we first aimed to prepare spherical PtNi catalysts using a polyol method and treated them with acetic acid. Then, we studied their activity for the EOR when

Ni was removed from the catalyst surface with acetic acid at ambient temperature by using cyclic voltammetry.

3.2 Experimental part

3.2.1 Synthesis of $PtNi_x/C$ catalysts

Carbon-supported $PtNi_x$ NPs with a target loading of 40 mass% PtNi in a 1:1 molar ratio were prepared by adapting a method reported for PtRh[29] and PtNi.[30] Carbon black (122 mg) was added to sodium acetate (145 mg) and dissolved in 29 mL of propylene glycol. Then the mixture was sonicated for 1 h. $H_2PtCl_6.6H_2O$ (79 mg) and $NiCl_2.6H_2O$ (40 mg) were dissolved in 27 mL of propylene glycol and 6 mL of 0.5 M NaOH(aq) and added to the mixture, which was then heated to 150 °C under reflux for 1 h. The catalyst was collected by centrifugation at 6000 rpm for 30 min, washed twice with water and acetone, and dried at 80 °C for 3 h. Commercial 40% $PtNi_x/C$ (Fuel Cell Store, nominally 3:1 Pt:Ni) and 70% Pt/C (3.5 nm, HiSPEC™ 13100, Alfa Aesar) catalysts were used for comparison with these catalysts. Table 3.1 summarizes catalysts that were prepared following the same method.

Table 3.1: Summary of $PtNi_x/C$ catalysts (x represent the Ni:Pt atomic ratio) prepared in this work.

Catalyst	Target Metal loading	Target Pt:Ni ratio	Solvent
$PtNi_x/C$(EG)	40%	1:1	Ethylene glycol (EG)
$PtNi_x/C$(PG)	40%	1:1	Propylene glycol (PG)

3.2.2 Treatment of $PtNi_x/C$ catalysts with acid

Both $PtNi_x/C(PG)$ (after the treatment is $PtNi_x/C(PG)^{AA}$) and $PtNi_x/C(EG)$ (after the treatment is $PtNi_x/C(EG)^{AA}$) catalysts were heated at 60 °C in 20 mL of the acetic acid for 4 h to dissolve surface Ni.[21] They were then collected by centrifugation, washed several times with water and ethanol, and dried at 80 °C for 3 h. The commercial $PtNi_x/C$ (after the treatment is $PtNi_x/C^{AA}$) was also heated to compare the different catalysts.

3.2.3 Characterization of catalysts

X-ray powder diffraction (XRD) was used to determine the crystal structure of the $PtNi_x/C$ catalysts. Thermal gravimetric analysis (TGA) and energy-dispersive X-ray spectroscopy (EDX) were used to determine the metal loading and composition of the carbon support. Transmission electron microscopy (TEM) was used to determine the particle size of $PtNi_x/C$ catalysts. X-ray photoelectron spectroscopy (XPS) was used to examine the electronic properties of the catalysts as well as their surface chemical states. Details about these instruments are shown in Chapter 2 (section 2.6).

3.2.4 Electrochemical measurements

Working electrodes for cyclic voltammetry were prepared by suspending 2 mg of the catalyst in 120 μL of water, 50 μL of Nafion solution (5%), and 30 μL of 2-propanol. Then, the mixture was sonicated for 3 h and 3 μL was left onto a glassy carbon disk to dry overnight at ambient temperature. Cyclic voltammetry was carried out in 1.0 M aqueous H_2SO_4 at room temperature under N_2. First, the working electrodes were cycled from -0.20 V to 0.80 V vs. saturated calomel electrode (SCE) at 100 mV s^{-1} in 1.0 M $H_2SO_4(aq)$. Second, they were cycled from -0.20 V to 0.80 V at 10 mV s^{-1} in 0.10 M ethanol and 1.0 M $H_2SO_4(aq)$. Currents were normalized based on the mass of metal (Pt + Ni) in the catalyst applied to the electrode.

3.3 Physical characterization of $PtNi_x/C$ catalysts

3.3.1 Thermogravimetric analysis (TGA) and energy-dispersive X-ray spectroscopy (EDX)

TGA and EDX analysis were carried out to investigate the metal loading and the atomic ratio of metals (Pt:Ni). The Ni to Pt ratios used in the names of the catalysts are the values determined by EDX. A commercial 40% $PtNi_{0.26}/C$ catalyst (nominally 3:1 Pt:Ni mole ratio) was used for comparison with the $PtNi_x/C$ catalysts prepared in this work. Samples are prepared for analysis as described in Chapter 2.

The residue was assumed to be from Pt and Ni metals as both have melting points higher than 1000 °C and are thermally stable at that temperature. As shown in Figure B.3 (Appendix B), there was no significant mass loss before 400 °C for the commercial 40% $PtNi_{0.26}/C$ catalyst, indicating that it was not hydrated. The residual mass was 42.8%, close to the specified metal loading for this commercial catalyst (40%) with a relative error ca. 7.0%. The TGA analysis of the other catalysts also is shown in Appendix B. Residual masses are summarized in Table 3.2. TGA results for these catalysts showed residual masses lower than the target metal loading (40%). It was 36.8% for the $PtNi_{0.50}/C$(EG) catalyst, however, $PtNi_{0.62}/C$(PG) had a significantly lower value 27.7%. This difference can be attributed to the inefficient deposition of PtNi NPs during the synthesis by using PG.

EDX analysis was used to obtain semiquantitative information on the catalyst composition. Three elements were detected for $PtNi_x/C$ and commercial $PtNi_{0.26}/C$ catalysts: Pt, Ni, and C. EDX spectra are shown in Appendix B. Based on semiquantitative EDX results, the Ni to Pt ratio increased from commercial $PtNi_{0.26}/C$ < $PtNi_{0.50}/C$(EG) < $PtNi_{0.62}/C$(PG). Moreover, EDX results for both $PtNi_{0.62}/C$(PG) and $PtNi_{0.50}/C$(EG) showed a small peak for O, which might indicate that some NiO_x was present. The metal loading obtained by EDX for $PtNi_{0.50}$/C(EG) was close to the TGA result. However, it was higher for other catalysts. This is expected from the EDX method since it is not an accurate method to measure the mass% because of the matrix effect.

Table 3.2: TGA and EDX results of $PtNi_x$/C catalysts.

Catalysts	**Atomic ratio Ni:Pt**	**Mass (%) Pt, Ni**	**Mass (%) PtNi**
	EDX		**TGA**
$PtNi_{0.62}$/C(PG)	0.62	27.5, 5.10	27.7
$PtNi_{0.50}$/C(EG)	0.50	32.5, 4.98	36.8
Commercial $PtNi_{0.26}$/C	0.26	48.7, 3.91	42.8
Treated $PtNi_{0.62}$/C(PG)	0.48	28.5, 4.2	24.7
Treated $PtNi_{0.50}$/C(EG)	0.08	30.2, 3.30	29.7
Treated commercial $PtNi_{0.26}$/C	0.22	48.9, 3.30	41.3

The $PtNi_{0.62}$/C(PG), $PtNi_{0.50}$/C(EG), and commercial $PtNi_{0.26}$/C were treated with acetic acid for 4 h and at 60 ℃. TGA and EDX results for treated $PtNi_x$/C are shown in Appendix B. When these catalysts were treated with acetic acid, the residual masses were decreased significantly for both $PtNi_{0.62}$/C(PG) and $PtNi_{0.50}$/C(EG), as shown in Table 3.2, while it was decreased slightly for the commercial $PtNi_{0.26}$/C catalyst. For example, it decreased from 27.7% to 24.7% at the $PtNi_{0.62}$/C(PG). These results were accompanied by a corresponding decrease in the Ni:Pt ratio, measured by EDX analysis. This is consistent with the removal of Ni from the near-surface region as shown in previous work.[18] The Ni to Pt ratio decreased from 0.62 to 0.48 at $PtNi_{0.62}$/C(PG), 0.50 to 0.08 at $PtNi_{0.50}$/C(EG), and 0.26 to 0.22 at commercial $PtNi_{0.26}$/C. The large decrease in the Ni:Pt ratio for the $PtNi_{0.50}$/C(EG) catalyst suggests that most of the Ni may have been present as Ni oxide.

The Ni:Pt ratios from EDX were used to name the catalysts after the treatment. The treated $PtNi_{0.62}/C(PG)$ catalyst is $PtNi_{0.48}/C(PG)^{AA}$, treated $PtNi_{0.50}/C(EG)$ is $PtNi_{0.08}/C(EG)^{AA}$, and treated commercial $PtNi_{0.26}/C$ is $PtNi_{0.22}/C^{AA}$.

3.3.2 X-ray powder diffraction (XRD)

The crystalline structures of the untreated $PtNi_x/C$ catalysts were characterized by XRD, as shown in Figure 3.1. Peak positions were compared with those for pure Pt and pure Ni. The diffraction peak at ca. 25° belongs to the carbon (002) plane. The diffraction patterns for PtNi in these catalysts have four peaks corresponding to the (111), (200), (220), and (311) planes. However, the diffraction peak of the (200) plane was not clear for $PtNi_{0.62}/C(PG)$ and $PtNi_{0.50}/C(EG)$. This can be explained due to the addition of NaOH (aq) as observed in reference.[30] They have found that as pH becomes close to 12, the (200) planes disappeared because of the corrosion of Ni. These four peaks were shifted to higher angles relative to those of pure Pt and lower angles than for pure Ni. This is consistent with the formation of PtNi alloys. Moreover, there was no peak resulting from the formation of intermetallic PtNi NPs[31] (at $2\theta = 54^{\circ}$), NiO, (at $2\theta = 63^{\circ}$), and/or individual metallic Ni, indicating that Ni is present as PtNi alloy and/or as an amorphous oxide.[32] Although the $PtNi_{0.50}/C(EG)$ catalyst has more Ni content than $PtNi_{0.26}/C$, its Bragg angle (θ_{111}) was lower than the $PtNi_{0.26}/C$ catalyst. This might indicate that there was a Ni amorphous oxide of the $PtNi_{0.50}/C(EG)$ catalyst. The average particle size of the PtNi NPs was measured according to the Scherrer equation (3.1) using the most intense peak (111) in the spectrum,

$$\text{average particle size} = \frac{0.9\lambda}{\beta cos\theta} \qquad (3.1)$$

where λ is X-ray wavelength, θ is Bragg angle (in radians), and β is line broadening at half of the maximum intensity (in radians). The mean particle sizes for these catalysts are shown in Table 3.3. Based on the XRD results, the average particle sizes were nearly identical for both $PtNi_{0.62}$/C(PG) and $PtNi_{0.50}$/C(EG), thus the influence of particle size on the catalytic activity and structure could be reduced. However, the particle size of commercial $PtNi_{0.26}$/C was 1.4 times higher than $PtNi_{0.62}$/C(PG) and $PtNi_{0.50}$/C(EG) which would decrease its degree of dispersion and the fraction of atoms at the vertices.[28,33,34]

Moreover, XRD measurement was carried out for treated catalysts, XRD patterns are shown in Appendix B. Treating $PtNi_x$/C catalysts with acetic acid shifted all peaks slightly to lower angles, and the particle sizes were decreased slightly for all catalysts, as shown in Table 3.3. This is consistent with the loss of surface Ni that was indicated by EDX results.[35,33] Moreover, the decrease in Ni:Pt ratio at the $PtNi_{0.50}$/C(EG) after treatment indicates that most Ni was formed an amorphous oxide at the surface.[21].

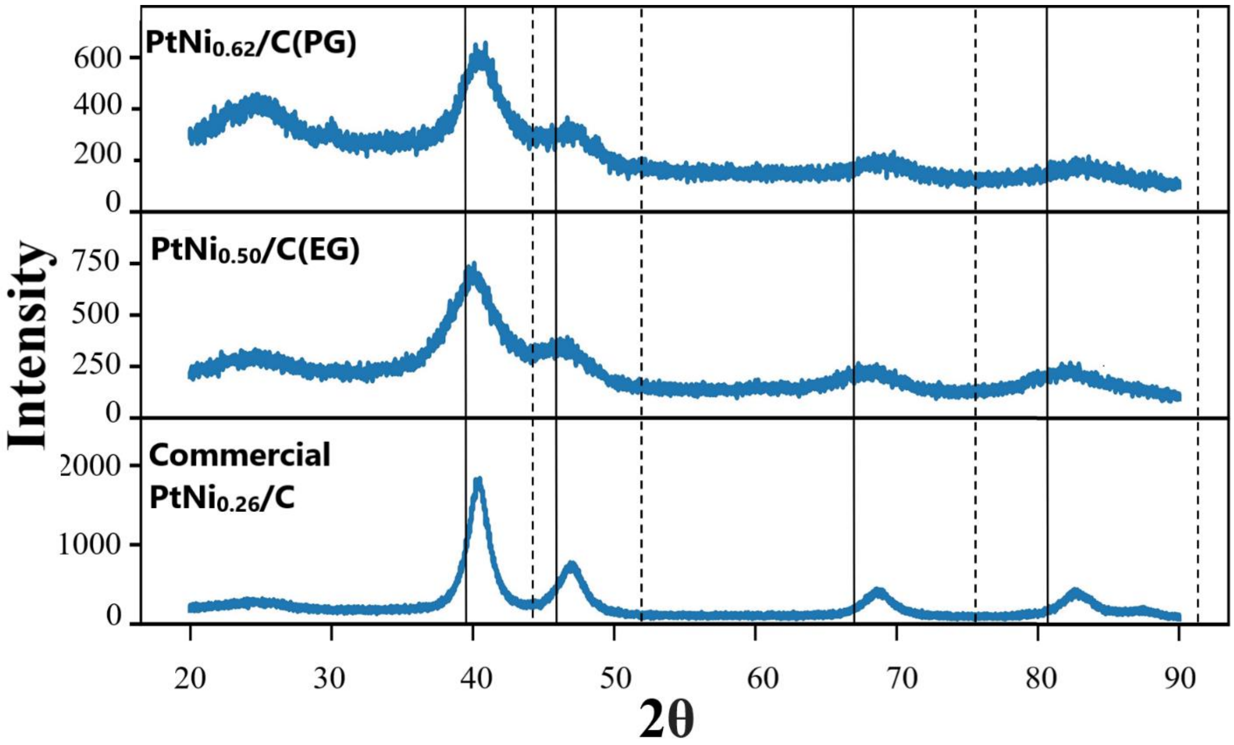

Figure 3.1: X-ray diffraction pattern of $PtNi_x/C$ catalysts and commercial $PtNi_{0.26}/C$. The solid and dashed lines are the standard peak positions for pure Pt and Ni, respectively.

Furthermore, the Bragg scattering equation (3.2) was used to calculate the lattice constant (a) for all catalysts,

$$a = \frac{\lambda\sqrt{h^2 + k^2 + l^2}}{2sin\theta} \tag{3.2}$$

where, λ is X-ray wavelength, θ is Bragg angle (in degree), and (hkl) are the Miller indices (111) for the scattering angle. Lattice constants are listed in Table 3.3. The fcc-lattice parameters for pure Pt and Ni are 3.92 Å and 3.52 Å, respectively.[36] Lattice constants of untreated $PtNi_x/C$ were lower than the lattice constant of pure Pt and higher than pure Ni, indicating that Pt and Ni have formed PtNi single-phase alloys.[35,37] Moreover, it can be seen in Table 3.3 that the lattice constant increased slightly after treating the catalysts with acids.[38] When Ni atoms are dissolved partially by acid treatment, the Pt at the surface is reconstructed, as a result, the surface of the PtNi alloy is strained to form a new surface skin. Based on that, a structure close to a Pt rich alloy, quasi core-shell, and/or a core-shell (PtNi@Pt) might be formed after treatment.[39]

Table 3.3: The average particle sizes and lattice constants for $PtNi_x/C$ and treated $PtNi_x/C$ catalysts.

Catalysts	**Particle size (nm)**		**Lattice constant (nm)**
	XRD	**TEM**	**a**
$PtNi_{0.62}/C(PG)$	3.5	3.4 ± 0.4	0.385
$PtNi_{0.50}/C(EG)$	3.4	3.3 ± 0.4	0.389
Commercial $PtNi_{0.26}/C$	5.0	5.0 ± 0.6	0.386
$PtNi_{0.48}/C(PG)^{AA}$	3.2	3. 0 ± 0.4	0.387
$PtNi_{0.08}/C(EG)^{AA}$	3.1	3.0 ± 0.4	0.391
$PtNi_{0.22}/C^{AA}$	4.9	5.0 ± 0.6	0.388

Vegard's law (e.q 3.3) can be used to estimate the percentage of Pt in the $PtNi_x$ catalysts (before and after treatment), as shown in Figure 3.2 (black line).

$$a(PtNi) = a_{Pt}X + a_{Ni}(1 - X) \tag{3.3}$$

where a(PtNi) is the lattice constant of the PtNi alloy, a_{Pt} is the lattice constant of pure Pt, a_{Ni} is the lattice constant of pure Ni, and X is the percentage of Pt in PtM alloy. Also, the percentage of Pt in $PtNi_x$ obtained from the EDX experiment was plotted against the lattice parameters (Figure 3.2). As shown in Figure 3.2, the commercial $PtNi_{0.26}/C$ catalyst did not deviate from Vegard's law. This might indicate that the commercial catalyst had a random nanoalloy structure. After removing Ni from the surface of the commercial catalyst with acetic acid, a small deviation from Vegard's law was observed. This deviation might imply that the structure of $PtNi_{0.26}/C$ (after the treatment) remained a random alloy. On the other hand, as shown in Figure 3.2, both $PtNi_{0.62}/C(PG)$ and $PtNi_{0.50}/C(EG)$ deviated positively from Vegard's law. This deviation is anticipated as aforementioned in Chapter 1, section 1.5.2. When $PtNi_{0.50}/C(EG)$ was treated in acetic acid, the catalyst deviated negatively toward Vegard's law, however, $PtNi_{0.62}/C(PG)$ deviated slightly toward Vegard's law.

The determination of the exact structure of both $PtNi_{0.50}/C(EG)$ and $PtNi_{0.62}C(PG)$ after the treatment with acetic acid is challenging. However, based on the $Pt_{81}Co_{19}$ catalyst that was reported by Petkov et. al.[36], $PtNi_{0.50}/C(EG)$ and $PtNi_{0.62}/C(PG)$ catalysts might have a core shell-like structure. Based on the EDX results, $PtNi_{0.50}/C(EG)$ lost more Ni from the surface than $PtNi_{0.62}/C(PG)$ during the treatment. Thus, $PtNi_{0.08}/C(EG)^{AA}$ might have a core shell-like structure with low Ni content in the core, while, $PtNi_{0.48}/C(PG)^{AA}$ might have a core shell-like structure with more Ni content in the core.

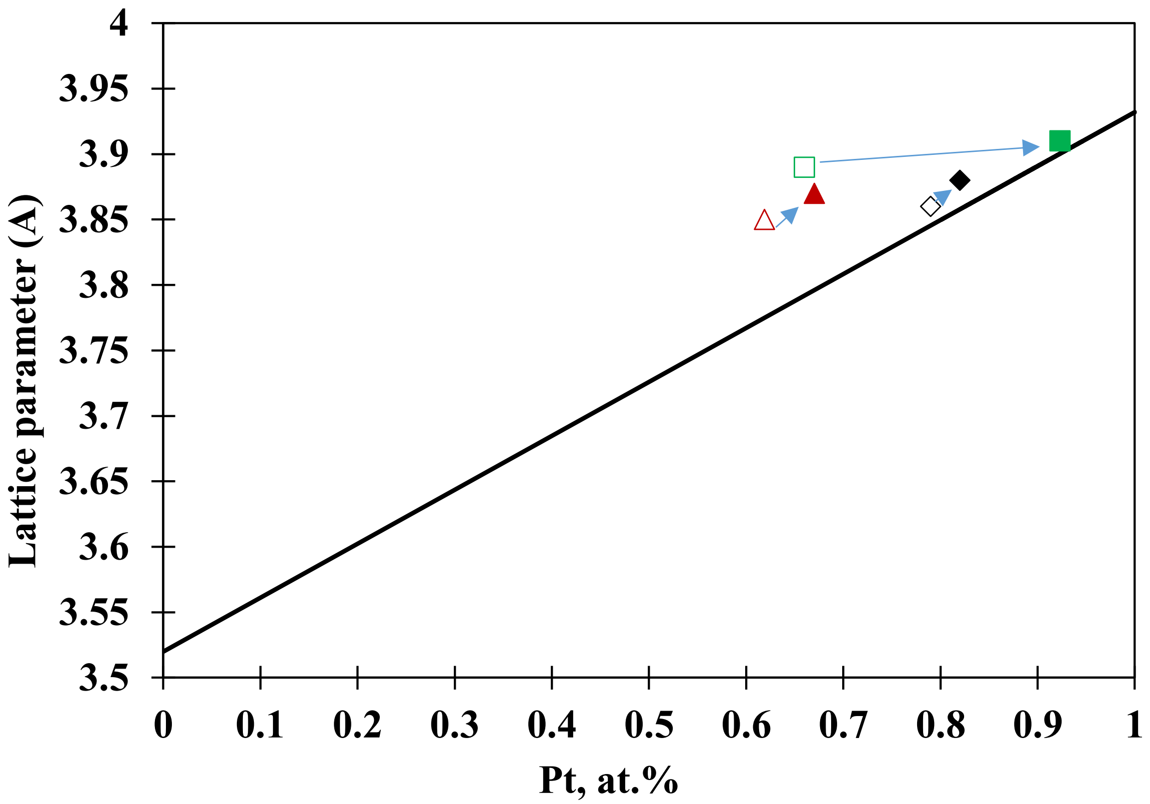

Figure 3.2: Lattice parameters vs. the experimental atomic %Pt for $PtNi_x/C$ catalysts. Closed symbols represent the data for treated $PtNi_x/C$, and open symbols represent the data for untreated $PtNi_x/C$. Blue arrows linked data before and after treatment effect. The black line represents the expected relationship based on Vegard's law. Red: $PtNi_x/(PG)$, green: $PtNi_x/C(EG)$, and black: commercial $PtNi_{0.26}/C$.

3.3.3 Transmission electron microscopy (TEM)

The morphology and the particle size of $PtNi_{0.62}/C(PG)$, $PtNi_{0.50}/C(EG)$, and commercial $PtNi_{0.26}/C$ catalysts were obtained by TEM. Figure 3.3 shows TEM images and corresponding histograms of the particle size distributions of these catalysts. Particle sizes are listed in Table 3.3. TEM images showed that the NPs distribution of both $PtNi_{0.62}/C(PG)$ and $PtNi_{0.50}/C(EG)$ on the carbon support was disorderly, with approximate particle sizes of 3.4 ± 0.4 nm and 3.3 ± 0.4 nm, respectively (over 70 particles were used for these calculations over the whole area). Histograms of these two catalysts showed narrow particle size distributions, which might indicate there was no Pt NPs agglomeration. However, the commercial $PtNi_{0.26}/C$ catalyst was distributed homogeneously with an average particle size of 5.0 ± 0.6 nm.

Furthermore, TEM analysis was carried out for treated $PtNi_x/C$ catalysts. Images and corresponding histograms of the particle size distributions of these catalysts are listed in Appendix B. Particle sizes were lower for treated $PtNi_x/C$ than untreated catalysts, which is consistent with results obtained from XRD analysis. There were no significant changes in the morphology of these catalysts after treatment with acetic acid. The particle size values measured from TEM were in good agreement with those obtained from the XRD measurement. This demonstrates that these catalysts are uniform and crystalline. Moreover, the particle sizes for all the catalysts, except commercial $PtN_{0.26}/C$ and $PtNi_{0.22}/C^{AA}$, are nearly identical and the influence of the particle size of the structures and/or the catalytic activities could be reduced.[33,40]

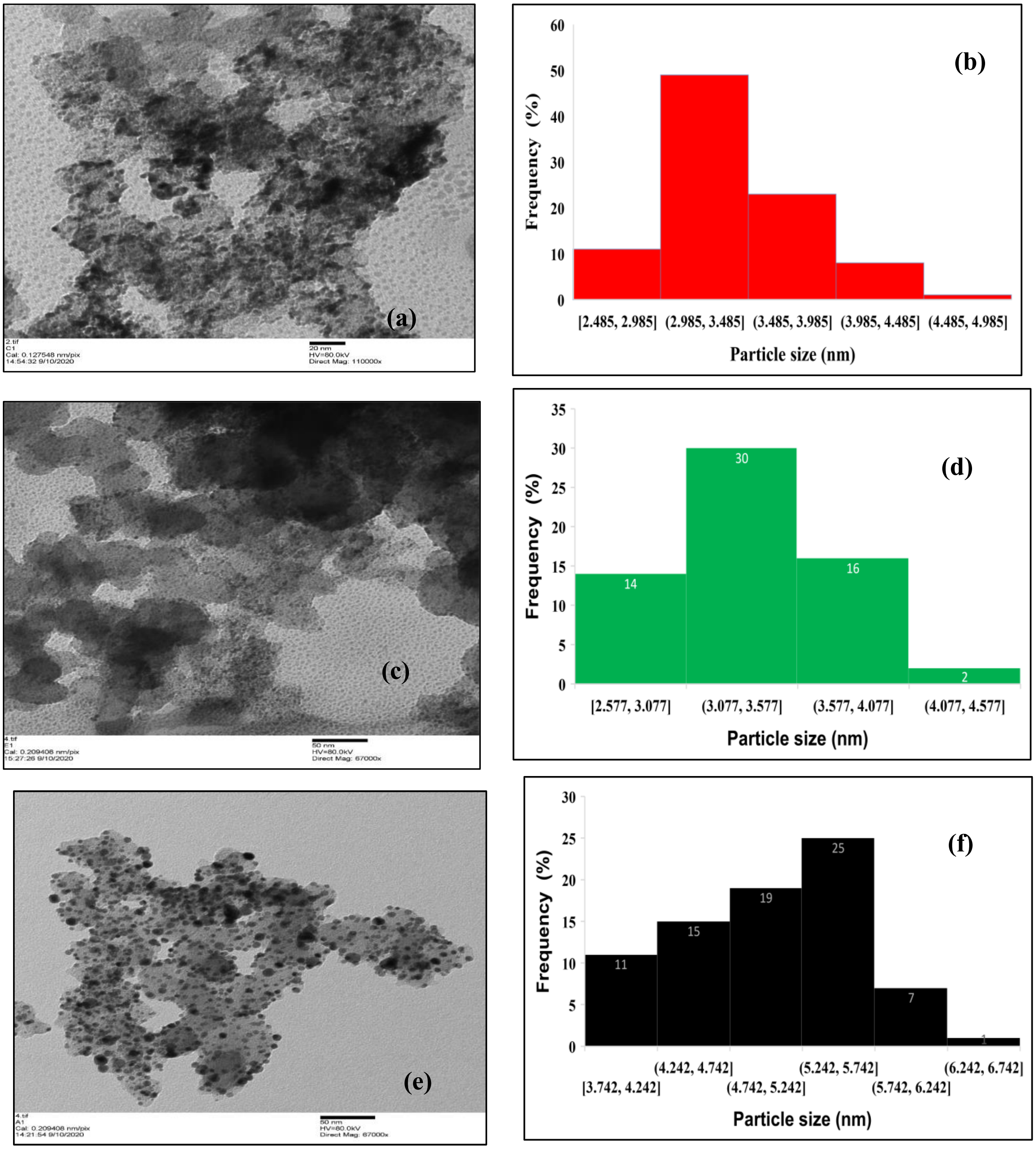

Figure 3.3: TEM images of (a) $PtNi_{0.62}/C(PG)$, (c) $PtNi_{0.50}/C(EG)$, and (e) commercial $PtNi_{0.26}/C$ and histogram of (b) $PtNi_{0.62}/C(PG)$, (d) $PtNi_{0.50}/C(EG)$, and (f) commercial $PtNi_{0.26}/C$.

3.3.4 X-ray photoelectron spectroscopy (XPS)

X-ray photoelectron spectroscopy (XPS) measurements were carried out for the $PtNi_{0.62}/C(PG)$, $PtNi_{0.48}/C(PG)^{AA}$, and commercial $PtNi_{0.26}/C$ catalysts. This technique is more sensitive to the catalysts surface than EDX. Thus, the distribution of Pt/Ni and the formation of oxides on the surface can be detected. Also, XPS can provide information on electronic effects. Figure 3.4 shows the full XPS spectra for the catalysts. The commercial $PtNi_{0.26}/C$ and $PtNi_{0.62}C(PG)$ spectra were similar (except the absence of metal Ni peak at 852 eV), indicating that $PtNi_{0.62}/C(PG)$ was an alloy. However, some peaks were absent from the $PtNi_{0.48}/C(PG)^{AA}$ spectrum (metal Ni and Ni hydroxide at 852 eV and 856 eV, respectively).

Table 3.4 shows the measured atomic ratios of Ni:Pt and the binding energies of the Pt 4f peaks ($4f_{7/2}$ and $4f_{5/2}$) for the commercial $PtNi_{0.26}/C$, $PtNi_{0.62}/C(PG)$, and $PtNi_{0.48}/C(PG)^{AA}$ catalysts. Based on Table 3.4, the atomic ratio of Pt/Ni increased significantly after treating the $PtNi_{0.62}/C(PG)$ catalyst with acetic acid. Since XPS is sensitive to the surface, this indicates that $PtNi_{0.48}/C(PG)^{AA}$ had a core shell-like structure as we expected. As shown in Table 3.4, the Pt 4f peaks for $PtNi_{0.48}/C(PG)^{AA}$ had a slight negative shift of binding energy (approximately 0.04 eV) relative to the $PtNi_{0.62}/C(PG)$. This shift indicates that there was electron transfer from Ni to Pt in $PtNi_{0.48}/C(PG)^{AA}$ relative to pure Pt.[37] This indicates that the acid treatment has a slight effect on the electronic structure of the $PtNi_{0.62}/C(PG)$.

Table 3.4: Ni:Pt atomic ratios and Pt $4f_{5/2}$ binding energies from XPS for commercial $PtNi_{0.26}/C$, $PtNi_{0.62}/C(PG)$, and $PtNi_{0.48}/C(PG)^{AA}$ catalysts.

Catalyst	Ni:Pt atomic ratio	Binding energy (eV) of Pt $4f_{7/2}$ ($4f_{5/2}$)
Commercial $PtNi_{0.26}/C$	0.22	70.78 (74.13)
$PtNi_{0.62}/C(PG)$	0.42	70.90 (74.23)
$PtNi_{0.48}/C(PG)^{AA}$	0.06	70.86 (74.20)

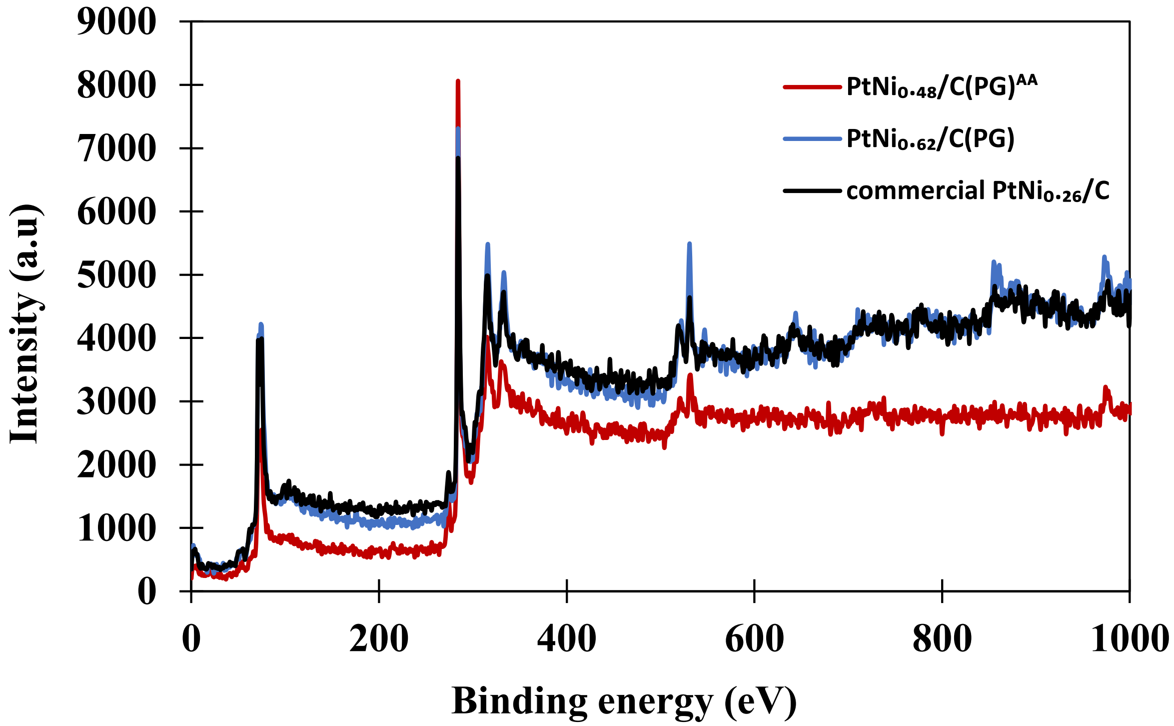

Figure 3.4: XPS spectra for the commercial $PtNi_{0.26}/C$, $PtNi_{0.62}/C(PG)$, and $PtNi_{0.48}/C(PG)^{AA}$ catalysts.

The Ni $2p_{3/2}$ region (NiO and $Ni(OH)_2$) of the XPS, expanded in Figures (B.9, B.10 and B.11) showed a broad peak deconvoluted to peaks. Table 3.5 shows the binding energies obtained from the deconvolution of the peaks. As shown in Figure B.9, the $2p_{3/2}$ region of the commercial $PtNi_{0.26}/C$ catalyst could be deconvoluted into three peaks at 852.59 eV, 855.39 eV, and 860.88 eV which are characteristic of pure Ni, NiO, and $Ni(OH)_2$, respectively.[41] However, there were no peaks detected for $2p_{1/2}$, indicating that these peaks were within the background. When $PtNi_{0.62}/C(PG)$ was treated with acetic acid, only one peak was observed with very low intensity (within the noise background), indicating that the amount of NiO was lower at the $PtNi_{0.48}/C(PG)^{AA}$ surface than the $PtNi_{0.62}/C(PG)$ surface. Furthermore, the $Ni(OH)_2$ peak was absent from the $PtNi_{0.48}/C(PG)^{AA}$ surface. These observations indicate that the surface of $PtNi_{0.48}/C(PG)^{AA}$ was covered with a Pt layer and a core shell-like structure formed after acid treatment.

Table 3.5: Ni 2p binding energies ($2p_{3/2}$) from the deconvoluted spectra (Appendix B) for commercial $PtNi_{0.26}/C$, $PtNi_{0.62}/C(PG)$, and $PtNi_{0.48}/C(PG)^{AA}$ catalysts.

Catalyst	NiO	$Ni(OH)_2$
Commercial $PtNi_{0.26}/C$	855.4	860.9
$PtNi_{0.62}/C(PG)$	855.3	861.2
$PtNi_{0.48}/C(PG)^{AA}$	854.4	Absent

.

3.4 Cyclic voltammetry analysis

Before testing any catalyst using an electrolysis cell, it is essential to evaluate and understand its behavior and activity. The cyclic voltammetry technique is the best way to gain a preliminary idea about the behavior of the catalyst. This technique can be used to measure the active surface area of Pt NPs and the activity of the catalyst toward the oxidation of biofuels (e.g. ethanol) at room temperature. In this section, the results of evaluating $PtNi_x/C$ catalysts in the presence of ethanol and the active surface area of Pt NPs are provided.

3.4.1 Studying the electrochemically active surface area

A cyclic voltammogram of the Pt surface was reported in acidic media.[42] At potentials below ca. 0 V, the voltammogram showed characteristic peaks on the forward and reverse scans for the hydrogen desorption/adsorption. Since H can only be adsorbed at the Pt surface, this area is used as an indication for uncovered Pt surface for Pt-based catalysts.

Cyclic voltammograms for $PtNi_x/C$ catalysts in aqueous 1.0 M H_2SO_4 are shown in Figure 3.5. They were similar for all of the catalysts, although there were significant differences in the mass normalized current densities. The differences in the areas of the hydrogen adsorption-desorption region from -0.20 V to 0.0 V indicate that the electrochemically active surface area increased from commercial $PtNi_{0.26}/C \sim PtNi_{0.62}/C(PG) < PtNi_{0.50}/C(EG)$. This increase in the electrochemical activity can be related to a decrease in Ni:Pt ratio, thus more Pt sites are available for H adsorption. However, the commercial catalyst’s low area of activity can be attributed to its higher particle size (5.0 nm vs ca. 3.5 nm) which results in a reduction in the active site.[38] Heating these catalysts in acetic acid increased the active surface area for all catalysts, as shown in Figure 3.5. This increase could be due to the removal of Ni from the Pt surface.

By comparing voltammograms of the PtNi$_x$/C and catalysts with the commercial 70% Pt/C catalyst (as shown in Appendix B), characteristic peaks of the hydrogen adsorption-desorption region were not as clear for the PtNi$_x$/C catalyst as for the 70% Pt/C, which indicates that the Pt surface was not pure Pt. On the other hand, the cyclic voltammogram of treated PtNi$_{0.50}$/C showed the characteristic peaks of Pt in acidic media. These results are in accord with those from the EDX analysis, which shows the low Ni:Pt ratio (0.08) in this catalyst.

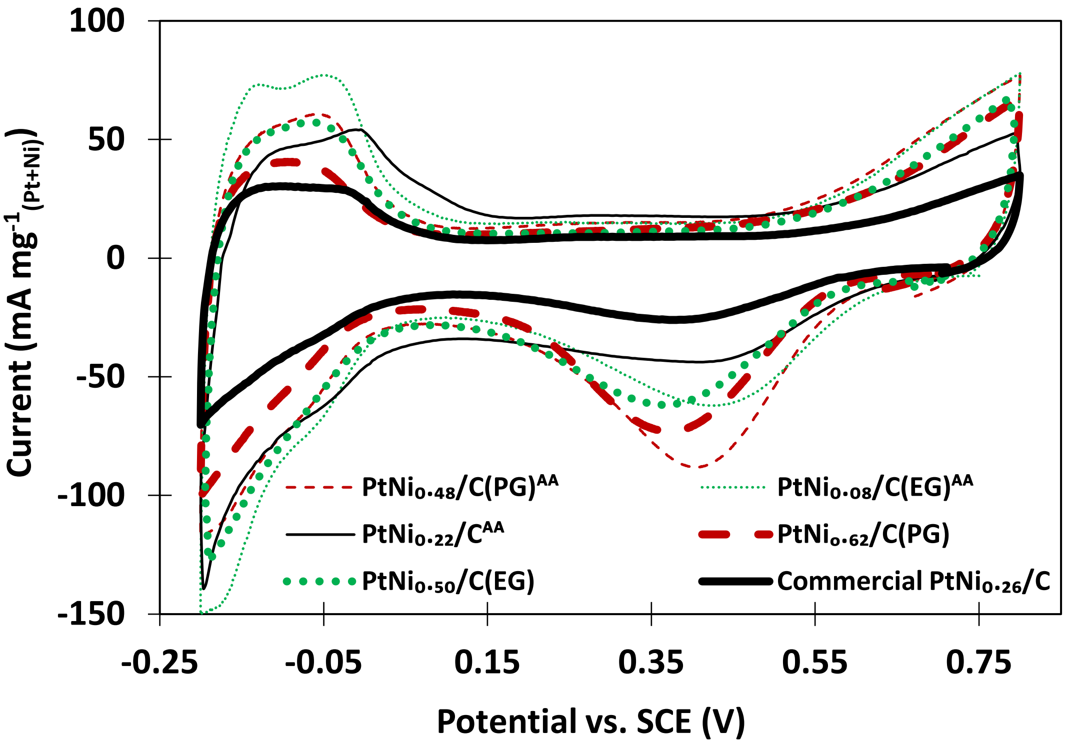

Figure 3.5: Cyclic voltammograms (100 mV s^{-1} ; 1 M H_2SO_4 (aq)) of the PtNi$_{0.62}$/C(PG), PtNi$_{0.50}$/C(EG), commercial PtNi$_{0.26}$/C, PtNi$_{0.48}$/C(PG)^{AA} , PtNi$_{0.08}$/C(EG)^{AA}, and PtNi$_{0.22}$/C^{AA} catalysts.

The evaluation of electrochemically active surface area (ECSA) of Pt and Pt-based NPs was carried out first by measuring the charge associated with the electrochemical oxidation of monolayers of hydrogen adsorption/desorption (Q_H); then normalizing Q_H using the charge for full coverage for clean polycrystalline Pt, 210 μcm^{-2},[43] as shown in equation (3.3),

$$ECSA\ (cm^2) = \frac{Q_{H-desorption}(C)}{210\ (\mu Ccm^{-2})} \tag{3.3}$$

Table 3.6 shows the ECSA, geometric area, and the utilization of the $PtNi_x/C$, treated $PtNi_x/C$, and 70% Pt/C catalysts. The utilization of $PtNi_x/C$ increased from $PtNi_{0.62}/C$(PG) ~ commercial $PtNi_{0.26}/C$ < $PtNi_{0.50}/C$(EG). Heating $PtNi_x/C$ catalysts in acetic acid for 4 h increased the utilization. The higher utilization of $PtNi_{0.08}/C(EG)^{AA}$ relative to that for $PtNi_{0.48}/C(PG)^{AA}$ and $PtNi_{0.22}/C^{AA}$ is attributed to the removal of Ni from the Pt surface,[21] as the TGA and EDX results showed. Moreover, it can be seen that both $PtNi_x/C$ and treated $PtNi_x/C$ catalysts had low ECSA and utilization relative to Pt/C. However, the particle size and shape/structure of the NPs were found to have a significant effect on the performance and activity.[44–46] Moreover, the surface of the $PtNi_x/C$ catalyst is not only Pt, as a result, comparing $PtNi_x/C$ catalysts with Pt/C based on the ECSA is not accurate. Therefore, measuring the utilization of the $PtNi_x/C$ catalysts means how much active surface area in $PtNi_x/C$ catalyst is active relative to its geometric area (an area that is measured based on the particle size and shape of the catalyst) and particle size of PtNi/C. Details of measuring the geometric area and the utilization of $PtNi_x/C$ catalyst are shown in Appendix B.

Table 3.6: Geometric area, electrochemical active surface area, and utilization of the 70% Pt/C and $PtNi_x/C$ catalysts (mass loading 0.03 g) were determined from the hydrogen adsorption charges.

Catalysts	**Geometric area (cm^2)**	**Electrochemical active surface area (cm^2)**	**Utilization (%)**
70% Pt/C	16.3	15.9	98
$PtNi_{0.62}/C(PG)$	7.6	1.8	23
$PtNi_{0.50}/C(EG)$	10.9	4.0	37
Commercial $PtNi_{0.26}/C$	9.1	2.4	26
$PtNi_{0.48}/C(PG)^{AA}$	7.8	2.7	34
$PtNi_{0.08}/C(EG)^{AA}$	10.2	4.5	45
$PtNi_{0.22}/C^{AA}$	10.8	3.8	35

3.4.2 Activity of $PtNi_x/C$ catalysts toward ethanol oxidation

Cyclic voltammetry experiments were carried out to study the activity of these catalysts toward ethanol oxidation. Figure 3.6 shows cyclic voltammograms for the $PtNi_x/C$ catalysts. All the voltammograms were normalized based on (Pt + Ni) metal loading.

The $PtNi_{0.62}/C(PG)$ catalyst was much more active for ethanol oxidation than the $PtNi_{0.50}/C(EG)$ and commercial $PtNi_{0.26}/C$ catalysts. In the forward scan, the current at the $PtNi_{0.62}/C(PG)$ catalyst began to increase at ca. 0.30 V and the maximum current was at 0.63 V. The enhancement of the ethanol oxidation activity of the $PtNi_{0.62}/C(PG)$ can be attributed to an electronic effect.[21,47] The high ratio of Ni to Pt in this catalyst might affect the electronic structure of Pt compared to other catalysts; and result in weak interaction between Pt and CO_{ad}, especially at low overpotentials where Pt is poisoned by CO_{ad}.[10] This result is consistent with $Pt_{25}Ni_{75}$ that was reported by Liu et al.[48] By comparing $PtNi_{0.50}/C(EG)$ with the commercial $PtNi_{0.26}/C$ catalyst, there was a slight increase in the activity at $PtNi_{0.50}/C(EG)$ which might be attributed to the higher Ni:Pt ratio than the commercial $PtNi_{0.26}/C$ catalyst. Furthermore, commercial $PtNi_{0.26}/C$ has a larger particle size ($\sim 5\ nm$) than the other catalysts which might decrease the fraction of atoms at the vertices, edges and surface, and decrease the dispersion of the catalyst. As a result, the catalytic activity would be expected to be lower.[49] Moreover, the $PtNi_{0.62}/C(PG)$ catalyst showed higher activity than the commercial 70% Pt/C catalyst. On the other hand, the $PtNi_{0.50}/C(EG)$ and commercial $PtNi_{0.26}/C$ catalysts were not significantly more active than the 70% Pt/C catalyst, which suggest that the ratio of Pt:Ni and/or the structure of the catalyst has a strong influence on the activity.[49]

When cyclic voltammetry experiments were carried out for treated $PtNi_x/C$ catalysts, as shown in Figure 3.7, the activities of both the $PtNi_{0.62}/C(PG)$ and $PtNi_{0.50}/C(EG)$ catalysts were increased by treatment with acetic acid. In contrast, the activity of the commercial $PtNi_{0.26}/C$ catalyst decreased and this result is reproducible, see Appendix Figure B.13. Moreover, the $PtNi_{0.48}/C(PG)^{AA}$ catalyst activity obtained following the acetic acid treatment was much higher than for the $PtNi_{0.08}/C(EG)^{AA}$ treated catalyst, and both were much more active than the $PtNi_{0.22}/C^{AA}$ catalyst.

The activity of $PtNi_{0.48}/C(PG)^{AA}$ increased significantly relative to the $PtNi_{0.62}/C(PG)$. For example, the treated $PtNi_{0.62}/C(PG)$ activity was 11.6 mA mg^{-1} at 0.27 V while it was 6.7 mA mg^{-1} for the untreated catalyst. This might be attributed to the core shell-like structure with a high Ni to Pt ratio at the core, as a result, a large electronic effect and/or compressive effect from the Ni was generated.[50] On the other hand, for the $PtNi_{0.08}/C(EG)^{AA}$ catalyst, the activity was increased slightly at potentials higher than 0.45 V, although it might have a core sell-like structure. This might be attributed to the low Ni to Pt ratio at the core. In contrast to the $PtNi_{0.62}/C(PG)$ and $PtNi_{0.50}/C(EG)$, the activity of the commercial $PtNi_{0.26}/C$ catalyst was decreased significantly, although only small amounts of Ni were dissolved. Since there was no change in the structure of $PtNi_{0.26}C$ (after the treatment) as predicted for $PtNi_{0.62}/C(PG)$ and $PtNi_{0.50}/C(EG)$, this might be an indication that the structure also plays an important role in the activity toward the EOR. Also, it might be attributed to the loss in Ni at the surface, diminished atomic-level strain, and restructuring of the Pt to Ni in the nanoalloy.[48] Liu et al have observed a 50% drop in the ORR activity at a $Pt_{35}Ni_{65}$ nanoalloy after only a few minutes of electrochemical cycling where a small amount of Ni was dissolved.[48]

The explanation of the $PtNi_x$ behavior after the treatment can not only be considered to be due to the change in Pt to Ni ratio. It is mainly attributed to the surface structure and the geometric structure (number of Pt nearest neighbors). Furthermore, the electronic effect and bifunctional mechanism have an impact on the activity of $PtNi_x$ catalysts. It is difficult to determine which one will have the most impact on the activity of a certain catalyst.

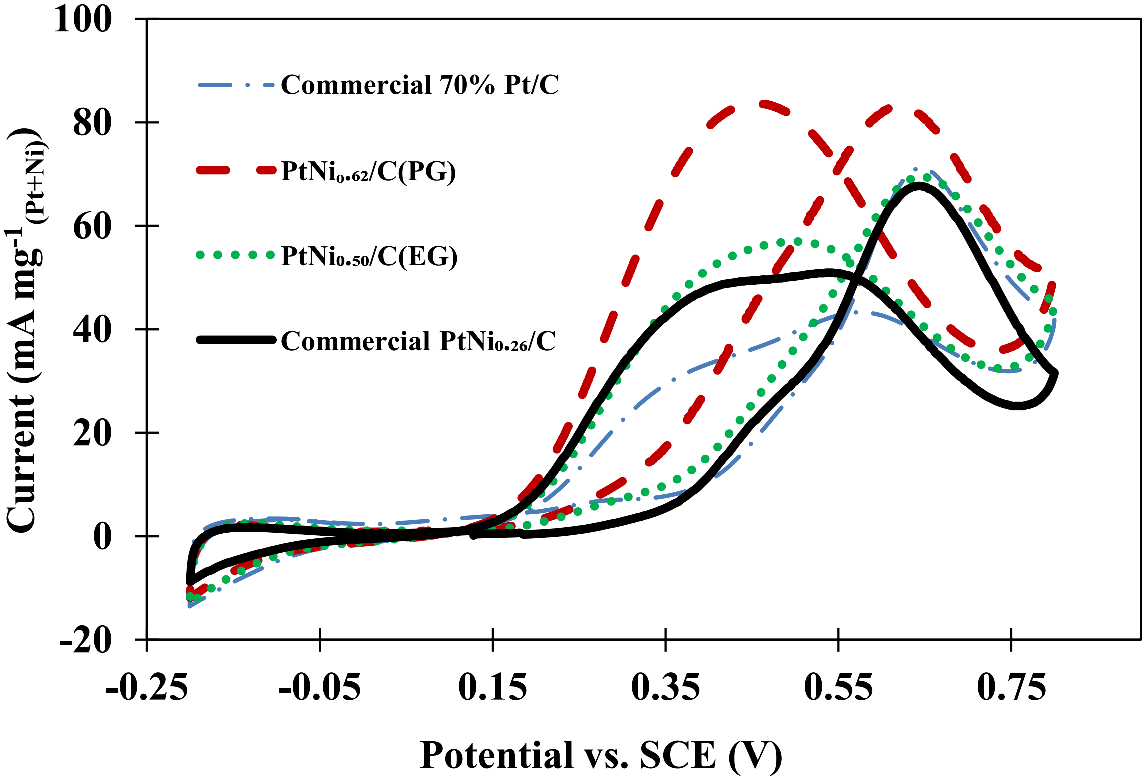

Figure 3.6: Cyclic voltammograms (10 mV s^{-1}) in 1 M H_2SO_4 (aq) containing 0.100 M ethanol of the PtNi$_{0.62}$/C(PG), PtNi$_{0.50}$/C(EG), commercial PtNi$_{0.26}$/C, and commercial 70% Pt/C catalysts.

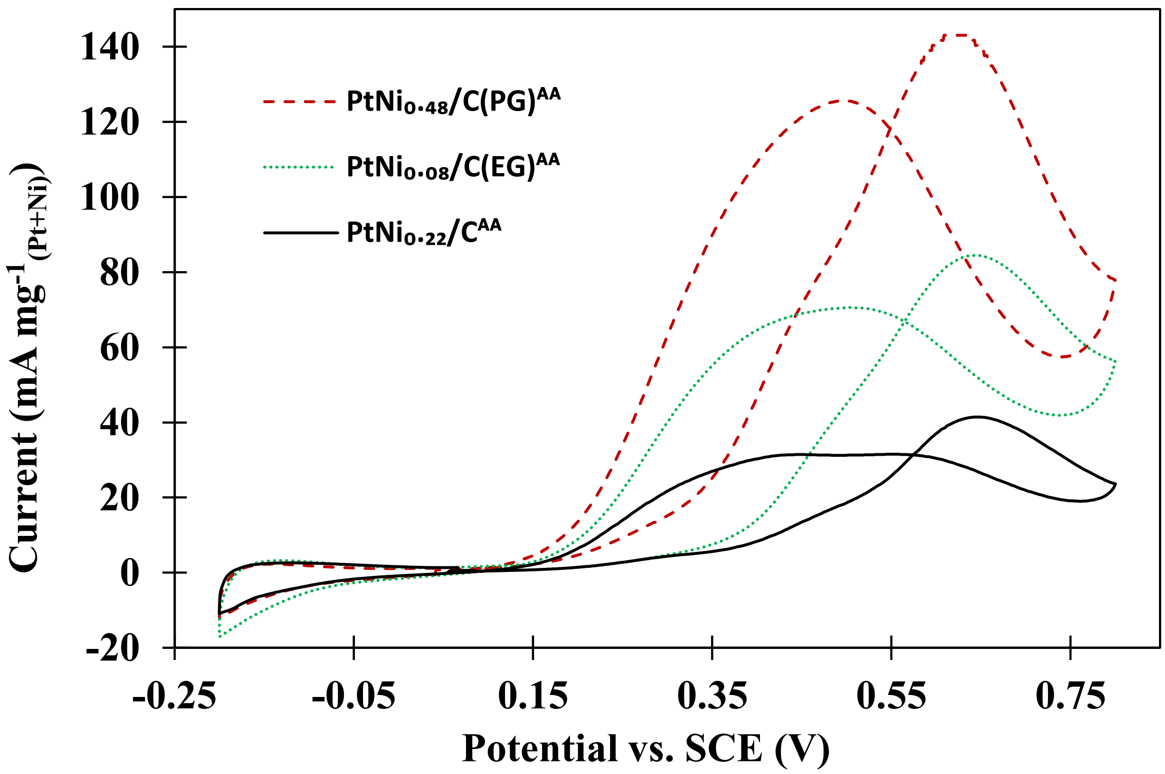

Figure 3.7: Cyclic voltammograms (10 mV s^{-1}) in 1 M H_2SO_4 (aq) containing 0.100 M ethanol of the PtNi$_{0.48}$/C(PG)^{AA}, PtNi$_{0.08}$/C(EG)^{AA}, and PtNi$_{0.22}$/C^{AA} catalysts.

3.5 Conclusion

In summary, the polyol synthesis of PtNi$_x$/C under basic conditions is dependent on the polyol employed, with propylene glycol producing more active catalysts than ethylene glycol. The Ni appears to be present in PtNi alloy nanoparticles, with a higher ratio being incorporated into the alloy in propylene glycol. A PtNi$_{0.62}$/C(PG) catalyst prepared in propylene glycol showed higher activity toward ethanol oxidation than a PtNi$_{0.50}$/C(EG) catalyst prepared in ethylene glycol and a commercial PtNi$_{0.26}$/C catalyst at ambient temperature in an aqueous acid electrolyte (H_2SO_4 (aq)).

Treatment of these catalysts with acetic acid successfully removed Ni from the surface and increased activities at both $PtNi_{0.62}/C(PG)$ and $PtNi_{0.50}/C(EG)$. The exceedingly high activity observed for the treated $PtNi_{0.62}/C(PG)$ catalyst toward ethanol oxidation indicates that it produced the most suitable type of PtNi@Pt core shell-like structure, as shown in Figure 3.8, with the best balance of PtNi core composition, surface composition, and structure. Moreover, controlling the composition and surface structure of PtNi catalysts has a high potential for achieving highly efficient catalysts for ethanol oxidation.[23,18]

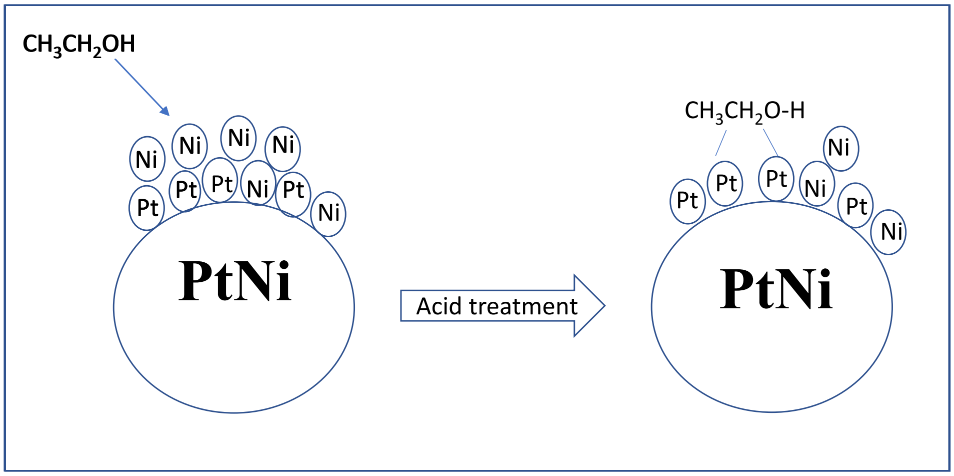

Figure 3.8: Schematic diagram of how treatment affects the PtNi alloy surface.

3.6 References

(1) Chu, S.; Majumdar, A. Opportunities and Challenges for a Sustainable Energy Future. *Nature* **2012**, *488*, 294–303.

(2) Wang, Y.; Zou, S.; Cai, W.-B. Recent Advances on Electro-Oxidation of Ethanol on Pt- and Pd-Based Catalysts: From Reaction Mechanisms to Catalytic Materials. *Catalysts* **2015**, *5*, 1507–1534.

(3) Akhairi, M. A. F.; Kamarudin, S. K. Catalysts in Direct Ethanol Fuel Cell (DEFC): An Overview. *Int. J. Hydrogen Energy* **2016**, *41*, 4214–4228.

(4) Badwal, S. P. S.; Giddey, S.; Kulkarni, A.; Goel, J.; Basu, S. Direct Ethanol Fuel Cells for Transport and Stationary Applications – A Comprehensive Review. *Appl. Energy* **2015**, *145*, 80–103.

(5) An, L.; Zhao, T. S. Transport Phenomena in Alkaline Direct Ethanol Fuel Cells for Sustainable Energy Production. *J. Power Sources* **2017**, *341*, 199–211.

(6) Ramachandran, S.; Stimming, U. Well to Wheel Analysis of Low Carbon Alternatives for Road Traffic. *Energy Environ. Sci.* **2015**, *8*, 3313–3324.

(7) Zheng, Y.; Wan, X.; Cheng, X.; Cheng, K.; Dai, Z.; Liu, Z. Advanced Catalytic Materials for Ethanol Oxidation in Direct Ethanol Fuel Cells. *Catalysts* **2020**, *10*, 166.

(8) Friedl, J.; Stimming, U. Model Catalyst Studies on Hydrogen and Ethanol Oxidation for Fuel Cells. *Electrochim. Acta* **2013**, *101*, 41–58.

(9) Lai, S. C. S.; Kleijn, S. E. F.; Öztürk, F. T. Z.; van Rees Vellinga, V. C.; Koning, J.; Rodriguez, P.; Koper, M. T. M. Effects of Electrolyte PH and Composition on the Ethanol Electro-Oxidation Reaction. *Catal. Today* **2010**, *154*, 92–104.

(10) Antolini, E. Pt-Ni and Pt-M-Ni (M = Ru, Sn) Anode Catalysts for Low-Temperature Acidic Direct Alcohol Fuel Cells: A Review. *Energies* **2017**, *10*, 42.

(11) Comignani, V.; Sieben, J. M.; Brigante, M. E.; Duarte, M. M. E. Carbon Supported Pt–NiO Nanoparticles for Ethanol Electro-Oxidation in Acid Media. *J. Power Sources* **2015**, *278*, 119–127.

(12) Kuriganova, A. B.; Leontyeva, D. V.; Ivanov, S.; Bund, A.; Smirnova, N. V. Electrochemical Dispersion Technique for Preparation of Hybrid MO_x–C Supports and Pt/MO_x–C Electrocatalysts for Low-Temperature Fuel Cells. *J. Appl. Electrochem.* **2016**, *4*, 1245–1260.

(13) Beyhan, S.; Léger, J.-M.; Kadırgan, F. Understanding the Influence of Ni, Co, Rh and Pd Addition to PtSn/C Catalyst for the Oxidation of Ethanol by in Situ Fourier Transform Infrared Spectroscopy. *Appl. Catal. B Environ.* **2014**, *144*, 66–74.

(14) Erini, N.; Beermann, V.; Gocyla, M.; Gliech, M.; Heggen, M.; Dunin-Borkowski, R. E.; Strasser, P. The Effect of Surface Site Ensembles on the Activity and Selectivity of Ethanol Electrooxidation by Octahedral PtNiRh Nanoparticles. *Angew. Chemie Int. Ed.* **2017**, *56*, 6533–6538.

(15) Beyhan, S.; Léger, J.-M.; Kadırgan, F. Pronounced Synergetic Effect of the Nano-Sized PtSnNi/C Catalyst for Ethanol Oxidation in Direct Ethanol Fuel Cell. *Appl. Catal. B Environ.* **2013**, *130–131*, 305–313.

(16) Soundararajan, D.; Park, J. H.; Kim, K. H.; Ko, J. M. Pt–Ni Alloy Nanoparticles Supported on CNF as Catalyst for Direct Ethanol Fuel Cells. *Curr. Appl. Phys.* **2012**, *12*, 854–859.

(17) Wang, Z.-B.; Yin, G.-P.; Zhang, J.; Sun, Y.-C.; Shi, P.-F. Investigation of Ethanol Electrooxidation on a Pt–Ru–Ni/C Catalyst for a Direct Ethanol Fuel Cell. *J. Power Sources* **2006**, *160*, 37–43.

(18) Altarawneh, R. M.; Brueckner, T. M.; Chen, B.; Pickup, P. G. Product Distributions and Efficiencies for Ethanol Oxidation at PtNi Octahedra. *J. Power Sources* **2018**, *400*, 369–376.

(19) Neto, A. O.; Dias, R. R.; Tusi, M. M.; Linardi, M.; Spinacé, E. V. Electro-Oxidation of Methanol and Ethanol Using PtRu/C, PtSn/C and PtSnRu/C Electrocatalysts Prepared by an Alcohol-Reduction Process. *J. Power Sources* **2007**, *166*, 87–91.

(20) Simões, F. C.; dos Anjos, D. M.; Vigier, F.; Léger, J.-M.; Hahn, F.; Coutanceau, C.; Gonzalez, E. R.; Tremiliosi-Filho, G.; de Andrade, A. R.; Olivi, P.; Kokoh, K. B. Electroactivity of Tin Modified Platinum Electrodes for Ethanol Electrooxidation. *J. Power Sources* **2007**, *167*, 1–10.

(21) Choi, S.-I.; Xie, S.; Shao, M.; Odell, J. H.; Lu, N.; Peng, H.-C.; Protsailo, L.; Guerrero, S.; Park, J.; Xia, X.; Wang, J.; Kim, M. J.; Xia, Y. Synthesis and Characterization of 9 Nm Pt–Ni Octahedra with a Record High Activity of 3.3 A/Mg Pt for the Oxygen Reduction Reaction. *Nano Lett.* **2013**, *13*, 3420–3425.

(22) Park, K.-W.; Choi, J.-H.; Kwon, B.-K.; Lee, S.-A.; Sung, Y.-E.; Ha, H.-Y.; Hong, S.-A.; Kim, H.; Wieckowski, A. Chemical and Electronic Effects of Ni in Pt/Ni and Pt/Ru/Ni Alloy Nanoparticles in Methanol Electrooxidation. *J. Phys. Chem. B* **2002**, *106*, 1869–1877.

(23) Sulaiman, J. E.; Zhu, S.; Xing, Z.; Chang, Q.; Shao, M. Pt–Ni Octahedra as Electrocatalysts for the Ethanol Electro-Oxidation Reaction. *ACS Catal.* **2017**, *7*, 5134–5141.

(24) Gawande, M. B.; Goswami, A.; Asefa, T.; Guo, H.; Biradar, A. V.; Peng, D.-L.; Zboril, R.; Varma, R. S. Core–Shell Nanoparticles: Synthesis and Applications in Catalysis and Electrocatalysis. *Chem. Soc. Rev.* **2015**, *44*, 7540–7590.

(25) Oezaslan, M.; Hasché, F.; Strasser, P. Pt-Based Core–Shell Catalyst Architectures for Oxygen Fuel Cell Electrodes. *J. Phys. Chem. Lett.* **2013**, *4*, 3273–3291.

(26) El Sawy, E. N.; Pickup, P. G. Carbon Monoxide and Formic Acid Oxidation at Rh@Pt

Nanoparticles. *Electrochim. Acta* **2019**, *302*, 234–240.

(27) Oezaslan, M.; Strasser, P. Activity of Dealloyed $PtCo_3$ and $PtCu_3$ Nanoparticle Electrocatalyst for Oxygen Reduction Reaction in Polymer Electrolyte Membrane Fuel Cell. *J. Power Sources* **2011**, *196*, 5240–5249.

(28) Guo, R.; Qian, F.; An, S.; Zhang, J.; Chou, K.; Ye, J.; Zhou, Z. Effect of Acid Treatment on Electrocatalytic Performance of PtNi Catalyst. *Chem. Res. Chinese Univ.* **2021**, *37*, 686–695.

(29) Soares, L. A.; Morais, C.; Napporn, T. W.; Kokoh, K. B.; Olivi, P. Beneficial Effects of Rhodium and Tin Oxide on Carbon Supported Platinum Catalysts for Ethanol Electrooxidation. *J. Power Sources* **2016**, *315*, 47–55.

(30) Rusnaeni, N.; Purwanto, W. W.; Nasikin, M.; Hendrajaya, L. The Effect of NaOH in The Formation PtNi/C Nanocatalyst for Cathode of PEMFC. *J. Appl. Sci.* **2010**, *10*, 2899–2904.

(31) Leonard, B. M.; Zhou, Q.; Wu, D.; DiSalvo, F. J. Facile Synthesis of PtNi Intermetallic Nanoparticles: Influence of Reducing Agent and Precursors on Electrocatalytic Activity. *Chem. Mater.* **2011**, *23*, 1136–1146.

(32) Lu, Q.; Mellinger, Z. J.; Wang, W.; Li, W.; Chen, Y.; Chen, J. G.; Xiao, J. Q. Differentiation of Bulk and Surface Contribution to Supercapacitance in Amorphous and Crystalline NiO. *ChemSusChem* **2010**, *3*, 1367–1370.

(33) Bao, H.; Li, J.; Jiang, L.; Shang, M.; Zhang, S.; Jiang, Z.; Wei, X.; Huang, Y.; Sun, G.; Wang, J.-Q. Structure of Pt n Ni Nanoparticles Electrocatalysts Investigated by X-Ray Absorption Spectroscopy. *J. Phys. Chem. C* **2013**, *117*, 20584–20591.

(34) Kim, H.; Park, J.-N.; Lee, W.-H. Preparation of Platinum-Based Electrode Catalysts for Low Temperature Fuel Cell. *Catal. Today* **2003**, *87*, 237–245.

(35) Jiang, Q.; Jiang, L.; Hou, H.; Qi, J.; Wang, S.; Sun, G. Promoting Effect of Ni in PtNi Bimetallic Electrocatalysts for the Methanol Oxidation Reaction in Alkaline Media: Experimental and Density Functional Theory Studies. *J. Phys. Chem. C* **2010**, *114*, 19714–19722.

(36) Petkov, V.; Maswadeh, Y.; Vargas, J. A.; Shan, S.; Kareem, H.; Wu, Z.-P.; Luo, J.; Zhong, C.-J.; Shastri, S.; Kenesei, P. Deviations from Vegard's Law and Evolution of the Electrocatalytic Activity and Stability of Pt-Based Nanoalloys inside Fuel Cells by in Operando X-Ray Spectroscopy and Total Scattering. *Nanoscale* **2019**, *11*, 5512–5525.

(37) Xiong, L.; Yang, X.; Xu, M.; Xu, Y.; Wu, D. Pt–Ni Alloy Nanoparticles Supported on Multiwalled Carbon Nanotubes for Methanol Oxidation in Alkaline Media. *J. Solid State Electrochem.* **2013**, *17*, 805–810.

(38) Guo, R.; Qian, F.; An, S.; Zhang, J.; Chou, K.; Ye, J.; Zhou, Z. Effect of Acid Treatment on Electrocatalytic Performance of PtNi Catalyst. *Chem. Res. Chinese Univ.* **2020**, 37,686-695.

(39) Wang, C.; Chi, M.; Li, D.; Strmcnik, D.; van der Vliet, D.; Wang, G.; Komanicky, V.; Chang, K.-C.; Paulikas, A. P.; Tripkovic, D.; Pearson, J.; More, K. L.; Markovic, N. M.; Stamenkovic, V. R. Design and Synthesis of Bimetallic Electrocatalyst with Multilayered Pt-Skin Surfaces. *J. Am. Chem. Soc.* **2011**, *133*, 14396–14403.

(40) Perez, J.; Paganin, V. A.; Antolini, E. Particle Size Effect for Ethanol Electro-Oxidation on Pt/C Catalysts in Half-Cell and in a Single Direct Ethanol Fuel Cell. *J. Electroanal. Chem.* **2011**, *654*, 108–115.

(41) Zhao, Y.; E, Y.; Fan, L.; Qiu, Y.; Yang, S. A New Route for the Electrodeposition of Platinum–Nickel Alloy Nanoparticles on Multi-Walled Carbon Nanotubes. *Electrochim. Acta* **2007**, *52*, 5873–5878.

(42) Shen, Y.; Xiao, K.; Xi, J.; Qiu, X. Comparison Study of Few-Layered Graphene Supported Platinum and Platinum Alloys for Methanol and Ethanol Electro-Oxidation. *J. Power Sources* **2015**, *278*, 235–244.

(43) Garsany, Y.; Baturina, O. A.; Swider-Lyons, K. E.; Kocha, S. S. Experimental Methods for Quantifying the Activity of Platinum Electrocatalysts for the Oxygen Reduction Reaction. *Anal. Chem.* **2010**, *82*, 6321–6328.

(44) Rudi, S.; Cui, C.; Gan, L.; Strasser, P. Comparative Study of the Electrocatalytically Active Surface Areas (ECSAs) of Pt Alloy Nanoparticles Evaluated by Hupd and CO-Stripping Voltammetry. *Electrocatalysis* **2014**, *5*, 408–418.

(45) Gasteiger, H. A.; Kocha, S. S.; Sompalli, B.; Wagner, F. T. Activity Benchmarks and Requirements for Pt, Pt-Alloy, and Non-Pt Oxygen Reduction Catalysts for PEMFCs. *Appl. Catal. B Environ.* **2005**, *56*, 9–35.

(46) Shao, M.; Odell, J. H.; Choi, S.-I.; Xia, Y. Electrochemical Surface Area Measurements of Platinum- and Palladium-Based Nanoparticles. *Electrochem. commun.* **2013**, *31*, 46–48.

(47) Choi, S.-I.; Lee, S.-U.; Kim, W. Y.; Choi, R.; Hong, K.; Nam, K. M.; Han, S. W.; Park, J. T. Composition-Controlled PtCo Alloy Nanocubes with Tuned Electrocatalytic Activity for Oxygen Reduction. *ACS Appl. Mater. Interfaces* **2012**, *4*, 6228–6234.

(48) Chih-Kang Liu, G.; Stevens, D. A.; Burns, J. C.; Sanderson, R. J.; Vernstrom, G.; Atanasoski, R. T.; Debe, M. K.; Dahn, J. R. Oxygen Reduction Activity of Dealloyed Pt_{1-}

$_{X}$Ni$_x$ Catalysts. *J. Electrochem. Soc.* **2011**, *158*, B919.

(49) Wang, X.; Kariuki, N.; Vaughey, J. T.; Goodpaster, J.; Kumar, R.; Myers, D. J. Bimetallic Pd–Cu Oxygen Reduction Electrocatalysts. *J. Electrochem. Soc.* **2008**, *155*, B602.

(50) Gan, L.; Heggen, M.; Rudi, S.; Strasser, P. Core–Shell Compositional Fine Structures of Dealloyed Pt$_x$Ni$_{1-x}$ Nanoparticles and Their Impact on Oxygen Reduction Catalysis. *Nano Lett.* **2012**, *12*, 5423–5430.

Chapter 4

4. Studying the Performance and CO_2 Production at $PtNi_x/C$ Catalysts in Proton Exchange Membrane Electrolysis Cells

The first author (Diala A. Alqdeimat) contributed to all parts of this research as the main researcher including literature review, carrying out all the experiments, measuring and analyzing the data, and discussing and presenting the data.

Prof. Peter G. Pickup was the principal investigator and provided the initial ideas for this project. He mentored the principal author (Diala A. Alqdeimat) and supported her during the project. He reviewed all data analysis.

The raw data is provided in Appendix C.

4.1 Introduction

Direct ethanol fuel cells (DEFCs) have been considered an attractive power source with low greenhouse emissions. Researchers have developed DEFCs to be used in electronic devices and transportation.[1–6] The importance of DEFCs has resulted in broad studies about the ethanol oxidation reaction (EOR).[7–9] The complete electrochemical oxidation of ethanol yields CO_2 as a product (eq. 4.1) and the highest faradaic efficiency ($\varepsilon_F = \frac{n_{av}}{12}$; n_{av} is the average number of electrons transferred) will be achieved. However, the incomplete EOR generates two major products (acetaldehyde; eq. 4.2 and acetic acid; eq. 4.3), and ε_F will be decreased.

$$CH_3CH_2OH + 3H_2O \rightarrow 2CO_2 + 12e^- + 12H^+ \tag{4.1}$$

$$CH_3CH_2OH \rightarrow CH_3CHO + 2e^- + 2H^+ \tag{4.2}$$

$$CH_3CH_2OH + H_2O \rightarrow CH_3CO_2H + 4e^- + 4H^+ \tag{4.3}$$

To achieve high ε_F, many different anode catalysts have been developed. Commonly, catalysts are evaluated in liquid electrolytes at ambient temperature by cyclic voltammetry (CV).[10] This can give information about the catalytic activity for the EOR. Also, the reaction mechanism (that occurs at the surface of the catalyst) can be investigated. However, CV can not provide information about the product distribution, the stoichiometry of the EOR (n_{av}), or the total efficiency. Moreover, the different conditions between CV and DEFCs affect the behavior and the activity of a certain catalyst. Colmati et al. studied the effect of temperature on the activity of PtRu and Pt_3Sn catalysts by CV and in a DEFC.[11] They reported that for CV at ambient temperature, the activity at low potentials was higher at the PtRu catalyst than at the Pt_3Sn catalyst. However, in the DEFC at high temperatures (70 °C), the performance of Pt_3Sn was higher than for PtRu.[11] Furthermore, El Sawy et al. studied the activity of Ru@Pt and Rh@Pt catalysts by CV at ambient temperature and in a proton exchange membrane (PEM) electrolysis cell at 80 °C. They found that the activity at the Ru@Pt catalyst was higher than at the Rh@Pt catalyst in the PEM electrolysis cell, although, their activities were similar in CV.[12] The difference between the activities may indicate that the temperature and the conditions of the experiment cause a change in the ligand effect and other effects (e.g strain and bifunctional effects). Therefore, studying only the activity of catalysts by CV will not give a clear indication of their activity in PEM electrolysis and fuel cells.

Many studies have measured the products from PEM fuel cells by using instruments such as FTIR spectroscopy and high-performance liquid chromatography.[13–18] However, these measurements were carried out by only analyzing the anode exhaust solution and using O_2 at the cathode. Thus, measurements of products were inaccurate due to the chemical oxidation of ethanol by O_2. A full understanding of the EOR requires knowledge about the product distribution and n_{av}, so it is essential to evaluate catalysts and measure the EOR products correctly. Altarawneh et al. investigated a method to measure n_{av} and the potential dependence of product distributions for ethanol oxidation at Pt/C, PtRu/C, and PtSn/C catalysts at 80 ℃ in a 5 cm^2 PEM electrolysis cell.[19] In their method, the diffusion of ethanol and products from the anode to the cathode (crossover) and the chemical oxidation of ethanol by O_2 were avoided. Moreover, Brueckner et al. reported a method for determining n_{av} and kinetic information from a polarization curve (current vs. cell potential) at 80 ℃ using a multi-anode PEM electrolysis cell. They examined its use to compare and evaluate different catalysts under the same conditions.[20] By measuring the product distribution and n_{av} accurately, an estimation of the efficiency and the activity for catalysts can be reached.

Thus, in this Chapter, a nine-anode PEM electrolysis cell (at 80 ℃) was used for preliminary evaluation of the performance and faradaic yield of CO_2 for $PtNi_x/C$ catalysts. Also, it was used to study the effect of removing Ni from the $PtNi_x/C$ surface with acetic acid (acid treatment) on the performance and faradaic yield of CO_2. Our results are compared with commercial Pt/C and PtNi octahedra catalysts reported by Altarawneh et al.[21] Moreover, a 5 cm^2 PEM electrolysis cell was used to measure the product distribution.

4.2 Experimental

$PtNi_{0.62}/C(PG)$ and $PtNi_{0.50}/C(EG)$ catalysts (Figure 4.1) were prepared using a polyol method and treated with acetic acid following a procedure reported by Alqdeimat and Pickup.[22] The commercial $PtNi_{0.26}/C$ was also treated with acetic acid following the same procedure.

$$\begin{array}{rcl}
\boxed{PtNi_x/C} & & \boxed{Treated\ PtNi_x/C} \\
PtNi_{0.62}/C(PG) & \xrightarrow{\text{acetic acid, 60 }^{\circ}\text{C, 4 h}} & PtNi_{0.48}/C(PG)^{\mathrm{AA}} \\
PtNi_{0.50}/C(EG) & \xrightarrow{\text{acetic acid, 60 }^{\circ}\text{C, 4 h}} & PtNi_{0.08}/C(EG)^{\mathrm{AA}} \\
Commercial\ PtNi_{0.26}/C & \xrightarrow{\text{acetic acid, 60 }^{\circ}\text{C, 4 h}} & PtNi_{0.22}/C^{\mathrm{AA}}
\end{array}$$

Figure 4.1: Summary of $PtNi_x/C$ and treated $PtNi_x/C$ catalysts studied in this work.

4.2.1 Electrode preparation for $PtNi_x/C$ and treated $PtNi_x/C$ catalysts

The preparation of electrodes is described in Chapter 2 (section 2.2.1). For each catalyst, three electrodes were made to study reproducibility. The metal loading (Pt + Ni) for all catalysts was 2 mg cm^{-2} and the Nafion loading was ca. 30 mass%.

4.2.2 Electrochemical measurements

A nine-anode PEM electrolysis cell was used to measure the performance and average faradaic yield of CO_2. The cell was operated at 80 °C in the crossover mode (the anode is purged with N_2, while 0.100 M of ethanol is pumped to the cathode). Polarization curves were obtained from 0.90 V to 0.00 V vs. DHE (dynamic hydrogen electrode) in 50 mV steps. Before each polarization curve, the cell was preconditioned at 0.70 V for 1 h. For each catalyst, three polarization curves were obtained to measure the standard deviation, as shown in Appendix C. The faradaic yield of CO_2 was measured by a non-dispersive infrared (NDIR) carbon dioxide detector. More details about the nine-anode PEM cell and the measurements are described in Chapter 2 (sections 2.3.2 and 2.4).

A 5 cm^2 PEM electrolysis cell was used to measure the product distribution at $PtNi_{0.48}/C(PG)^{AA}$ and $PtNi_{0.08}/C(EG)^{AA}$ anodes. The cell was operated at 80 ℃ in a polarization mode (the cathode is purged with N_2, while 0.100 M of ethanol is pumped to the anode). The outlets of the cathode and anode were connected to a cold trap to collect the residual ethanol and products (acetic acid and acetaldehyde). The outlet of the trap was connected to the NDIR carbon dioxide detector to measure the CO_2. The product distribution was measured by using a 500 MHz ^1H NMR spectrometer. A fumaric acid in D_2O was used as an internal standard.[19] More details about the 5 cm^2 PEM electrolysis cell, product distribution measurements, and the chemical yields are described in Chapter 2 (sections 2.3.3 and 2.5).

4.3 Ethanol oxidation in a nine-anode PEM electrolysis cell at 80 °C

4.3.1 Studying the performances of $PtNi_x/C$ and treated $PtNi_x/C$ catalysts

In general, there are three characteristic potentials in the polarization curve: the onset potential (it is a potential where the current starts to rise from zero), the half-wave potential (the potential at 50% of the maximum current ($E_{1/2}$)), and peak potential (a potential at which the current reaches the maximum).

Figure 4.2 shows polarization curves for the oxidation of 0.100 M ethanol at $PtNi_{0.62}/C(PG)$, $PtNi_{0.50}/C(EG)$, and commercial $PtNi_{0.26}/C$ anodes. The current for the EOR began to increase slightly (0.44 mA) at 0.3 V at all $PtNi_x/C$ catalysts. Furthermore, there was no significant difference in the $E_{1/2}$ for the three $PtNi_x/C$ catalysts, suggesting that the kinetics are similar at 80 ℃.[20] However, at potentials ≥ 0.55 V, the current increased in the order $PtNi_{0.62}/C(PG) > PtNi_{0.50}/C(EG) >$ commercial $PtNi_{0.26}/C$.

Figure 4.3 shows polarization curves for the $PtNi_{0.48}/C(PG)^{AA}$, $PtNi_{0.08}/C(EG)^{AA}$, and $PtNi_{0.22}/C^{AA}$ catalysts. When the $PtNi_{0.62}/C(PG)$ and $PtNi_{0.50}C(EG)$ catalysts were heated in acetic acid to remove Ni from the surface, the activity increased, as shown in Appendix C. Furthermore, there was a slight shift in the $E_{1/2}$ for $PtNi_{0.48}/C(PG)^{AA}$ and $PtNi_{0.08}/C(EG)^{AA}$. This is consistent with results obtained from the CV experiment, as shown in Chapter 3 (3.4). However, the increase in the activity was not significant at the $PtNi_{0.48}/C(PG)^{AA}$ anode as observed in the CV experiment. This observation suggests that the catalyst surfaces were changed during the start-up and conditioning of the PEM cell. Altarawneh et al. have also reported that the significant difference in the activity for PtNi octahedra (before and after heating in acetic acid) decreased under the PEM conditions compared to CV conditions.[21] Unlike the CV result, after treating commercial $PtNi_{0.26}C$ with acetic acid, the activity began to increase slightly at 0.4 V. Also, there was a negative shift of the $E_{1/2}$ at the $PtNi_{0.22}/C^{AA}$ anode. This may indicate that at 80 ℃ more Ni was dissolved from the surface of commercial $PtNi_{0.26}/C$.

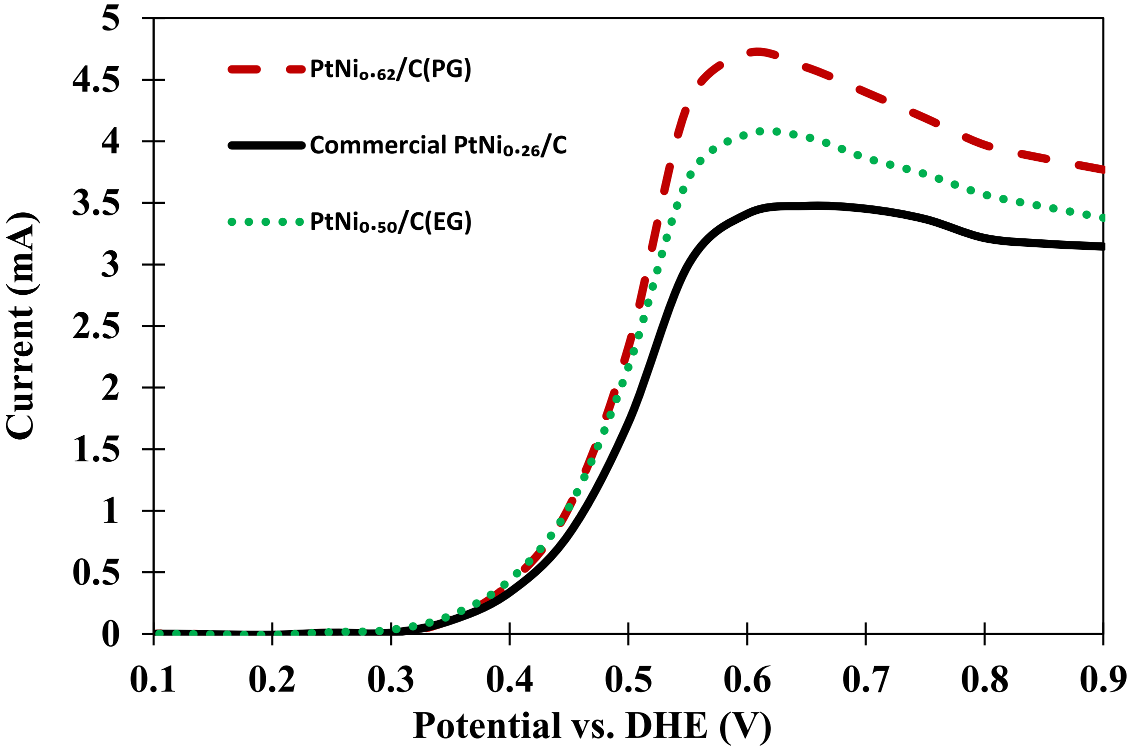

Figure 4.2: Polarization curves for the oxidation of 0.100 M ethanol (0.5 mL min^{-1}) at 80 °C in a nine-anode PEM electrolysis cell in crossover mode at $PtNi_{0.62}/C(PG)$, $PtNi_{0.50}/C(EG)$, and commercial $PtNi_{0.26}/C$ anodes.

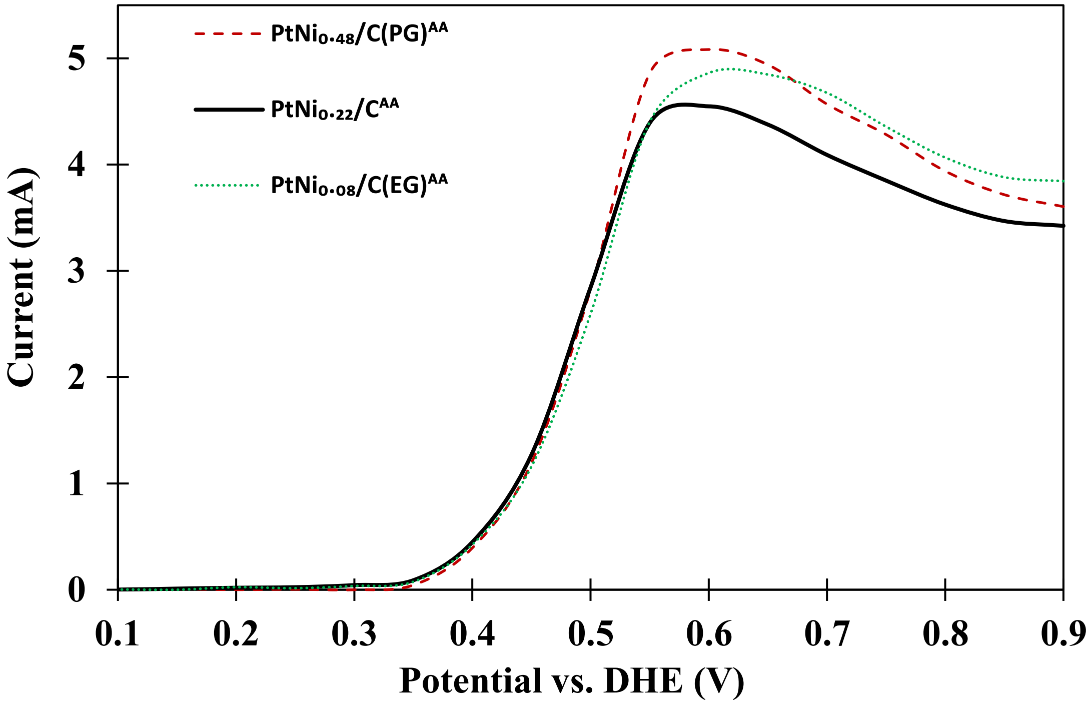

Figure 4.3: Polarization curves for the oxidation of 0.100 M ethanol (0.5 mL min^{-1}) at 80 °C in a nine-anode PEM electrolysis cell in crossover mode at $PtNi_{0.48}/C(PG)^{AA}$, $PtNi_{0.08}/C(EG)^{AA}$, and $PtNi_{0.22}/C^{AA}$ anodes.

At high potentials, currents peaked between 0.55 V and 0.6 V at $PtNi_x/C$ anodes (before and after acid treatment). Then, currents decreased at potentials higher than 0.6 V. As reported in the literature, the limiting current is proportional to the n_{av}, as shown in eq. 4.4,[21,12]

$$I_{lim} = n_{av}FmC \tag{4.4}$$

where F is the Faraday constant, m is the mass transport coefficient, and C is the bulk concentration of ethanol. Based on eq. 4.4, current is proportional to n_{av}. Also, it is known that n_{av} is the average number of transferred electrons per ethanol molecule, as shown in eq. 4.5,[12]

$$n_{av} = \sum n_i f_i \tag{4.5}$$

where f_i is the fraction of ethanol converted to a product i and n_i is the number of electrons transferred to form product i. As a result, any changes in the product distribution will change n_{av}. For example, if the acetic acid to CO_2 ratio was increased, n_{av} will be decreased.[23–25]

By using eq. 4.4, n_{av} values were calculated and listed in Table 4.1. It can be seen from Table 4.1 that n_{av} increased in the order $PtNi_{0.62}/C(PG) > PtNi_{0.50}/C(EG) >$ commercial $PtNi_{0.26}/C$. Based on eq. 4.4 and 4.5, the decrease in the current at $PtNi_x/C$ anodes, after 0.6 V, is due to a change in n_{av}.[7] As known from the EOR mechanism,[7] 4 electrons transfer to produce acetic acid, while production of CO_2 needs 12 electrons to be transferred. Therefore, the acetic acid to CO_2 ratio was higher at potentials > 0.6 V. Since the current for $PtNi_{0.62}/C(PG)$ was higher than for $PtNi_{0.50}/C(EG)$ and commercial $PtNi_{0.26}/C$, the CO_2 to acetic acid ratio might be higher for $PtNi_{0.62}/C(PG)$ than for $PtNi_{0.50}/C(EG)$ and commercial $PtNi_{0.26}/C$. When Ni was removed from the catalyst surface with acetic acid, n_{av} increased for treated PtNi/C catalysts. This indicates that the production of CO_2 was enhanced by treating $PtNi_x/C$ catalysts with acetic acid.

4.3.2 Measuring the faradaic yield of CO_2

The nine-anode PEM electrolysis cell was also used to measure the faradaic yield of CO_2. Figure 4.4 shows CO_2 concentration traces recorded over 500 s at 0.5 V. In this experiment, three anodes of each catalyst were run at the same time to provide an average value of CO_2 over the last 100 s.

Table 4.1 shows the average faradaic yield of CO_2 and average current. The average faradaic yield of CO_2 was slightly higher for $PtNi_{0.62}/C(PG)$ (39%) and $PtNi_{0.50}C(EG)$ (38%) than for commercial $PtNi_{0.26}/C$ (36%). This is consistent with the slightly higher current that was observed in Figure 4.2. When Ni was removed from the $PtNi_x/C$ surface with acetic acid, the average CO_2 yields increased. After acid treatment, the faradaic yield of CO_2 was slightly higher at the $PtNi_{0.50}/C(EG)$ and commercial $PtNi_{0.26}/C$ anodes, 41% and 37%, respectively. Acetic acid treatment of $PtNi_x/C$ catalysts removed most of the surface Ni atoms,[26] as a result, more adjacent Pt atoms would be available to break the C-C bond (at least three sites of Pt are required to adsorb an ethanol molecule) and produce CO_2.[27] Interestingly, the faradaic yield of CO_2 increased significantly at the $PtNi_{0.62}/C(PG)$ anode (after acid treatment) from 39 % to 56 %. This observation suggests that the selectivity toward CO_2 production is not only sensitive to the surface coverage of Ni,[21] but also to the catalyst structure. When Ni was removed from the $PtNi_{0.62}/C(PG)$ surface with acetic acid, a core shell-like structure was formed with a high Ni to Pt ratio at the core. As a result, a large electronic effect and/or compressive effect was generated from the Ni at the core. Although current at the commercial $PtNi_{0.26}/C$ anode increased significantly from 1.7 to 2.9 mA, after acid treatment, the faradaic yield of CO_2 increased only by 1%. On the other hand, the current increased only from 2.3 to 2.8 mA at $PtNi_{0.48}/C(PG)$, but the faradaic yield of CO_2 increased significantly from 39 % to 56 %. These results indicate that the production of CO_2 is more sensitive to the Pt surface and the catalyst structure than the current. This observation is consistent with the results reported by Altarawneh et al for PtNi octahedra.[21] They found that the CO_2 yield was lower at a octahedral PtNi catalyst before acid treatment than after acid treatment, although the current was higher.

The CO_2 yields at $PtNi_x/C$ anodes were higher than the reported value by Altarawneh et al for the octahedral PtNi (ca. 21%).[21] Furthermore, $PtNi_{0.48}/C(PG)^{AA}$ provided more CO_2 (56%) than the octahedral PtNi with acid treatment (ca. 28 %). This may indicate that the structure of the catalyst (core-shell like in the case of $PtNi_{0.48}/C(PG)^{AA}$) has more effect for breaking the C-C bond than the shape of the PtNi nanoparticles (octahedral) and Pt to Ni ratio at 0.5 V. When the $PtNi_x/C$

catalysts (before and after treatment) are compared with the commercial PtRu catalyst reported by Altarawneh et al,[19] it is clear that Ni can enhance C-C bond cleavage to produce CO_2 (36% to 56%) relative to PtRu (18%).[19] As a result, $PtNi_x/C$ catalysts will provide higher faradaic efficiency in DEFCs. Unfortunately, all $PtNi_x/C$ catalysts showed lower CO_2 yields than the reported value for a commercial 70% Pt/C catalyst at 0.50 V (79%), under the same conditions.[21]

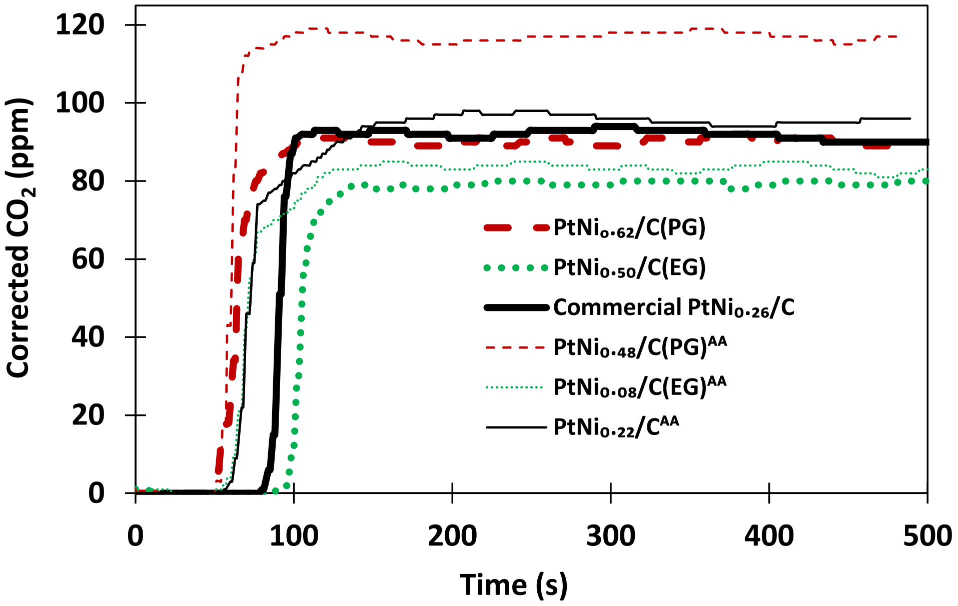

Figure 4.4: CO_2 concentrations for the oxidation of 0.100 M ethanol (0.2 mL min^{-1}) at 0.5 V and 80 °C at $PtNi_{0.62}/C(PG)$, $PtNi_{0.50}/C(EG)$, $PtNi_{0.48}/C(PG)^{AA}$, $PtNi_{0.08}/C(EG)^{AA}$, commercial $PtNi_{0.26}/C$, and $PtNi_{0.22}/C^{AA}$ anodes.

Table 4.1: Average faradaic yields of CO_2, currents for the oxidation of 0.100 M ethanol (0.2 mL min^{-1}, 80 °C, 0.5 V), and nav for $PtNi_x/C$ and treated $PtNi_x/C$ catalysts.

Catalysts	**CO_2 yield %**	**I_{av} (mA)**	**n_{av} (0.60 V)**
$PtNi_{0.62}/C(PG)$	39%	2.3	6.8
$PtNi_{0.50}/C(EG)$	38%	2.2	5.9
Commercial $PtNi_{0.26}/C$	36%	1.7	5.0
$PtNi_{0.48}/C(PG)^{AA}$	56%	2.8	7.4
$PtNi_{0.08}/C(EG)^{AA}$	41%	2.6	7.1
$PtNi_{0.22}/C^{AA}$	37%	2.9	6.7

4.4 Ethanol oxidation in a 5 cm^2 PEM electrolysis cell

4.4.1 Polarization curves

The $PtNi_{0.48}/C(PG)^{AA}$ and $PtNi_{0.08}/C(EG)^{AA}$ catalysts were tested in a 5 cm^2 PEM electrolysis cell. Currents were measured from 0.0 to 0.7 V for the oxidation of 0.100 M ethanol at 80 ℃. Figure 4.5 shows polarization curves for the EOR at the $PtNi_{0.48}/C(PG)^{AA}$ and $PtNi_{0.08}/C(EG)^{AA}$ anodes. Results are compared with data reported by Altarawneh et al. for Pt/C, PtRu, and octahedral PtNi catalysts.[21]

At potentials < 0.4 V, there were higher currents for $PtNi_{0.48}/C(PG)^{AA}$ than for $PtNi_{0.08}/C(EG)^{AA}$. Between 0.4 and 0.5 V, there was a negative shift in the half-wave potential at the $PtNi_{0.48}/C(PG)^{AA}$ anode. At the $PtNi_{0.48}/C(PG)^{AA}$ anode, the current peaked at 0.65 V, while it peaked at 0.55 V at the $PtNi_{0.08}/C(EG)^{AA}$ anode. At high potentials, currents for $PtNi_{0.48}/C(PG)^{AA}$ were higher than for $PtNi_{0.08}/C(EG)^{AA}$. As shown in eq. 4.4, the limiting current is proportional to n_{av}, therefore, higher currents at the $PtNi_{0.48}/C(PG)^{AA}$ anode indicate that n_{av} was higher for

$PtNi_{0.48}/C(PG)^{AA}$ than for $PtNi_{0.08}/C(EG)^{AA}$. Also, it indicates that more CO_2 was produced at the $PtNi_{0.48}/C(PG)^{AA}$ anode than at the $PtNi_{0.08}/C(EG)^{AA}$ anode.

In contrast to the octahedral PtNi catalyst reported by Altarawneh, currents for $PtNi_{0.48}/C(PG)^{AA}$ and $PtNi_{0.08}/C(EG)^{AA}$ at potentials < 0.45 V were low. However, currents at the $PtNi_{0.48}/C(PG)^{AA}$ and $PtNi_{0.08}/C(EG)^{AA}$ anodes were higher at potentials ≥ 0.45 V than at the octahedral PtNi catalyst. This indicates that fewer electrons were transferred per ethanol molecule (low acetic acid to CO_2 ratio) at the octahedral PtNi catalyst than at the $PtNi_{0.48}/C(PG)^{AA}$ or $PtNi_{0.08}/C(EG)^{AA}$ catalysts.[21] Conversely, currents for the 70% Pt/C catalyst were higher than for $PtNi_{0.48}/C(PG)^{AA}$ and $PtNi_{0.08}/C(EG)^{AA}$ over the whole potential range (0.1 to 0.7 V). At high potentials, the high current at the 70% Pt/C catalyst indicates that more electrons were transferred per ethanol molecule than at the $PtNi_{0.48}/C(PG)^{AA}$ and $PtNi_{0.08}/C(EG)^{AA}$ anodes. Furthermore, $PtNi_{0.48}/C(PG)^{AA}$ and $PtNi_{0.08}/C(EG)^{AA}$ had lower activity than the reported PtRu/Ccatalyst,[19,20] which suggests that the role of Ni in the PtNi catalyst is different from that for Ru.[19]

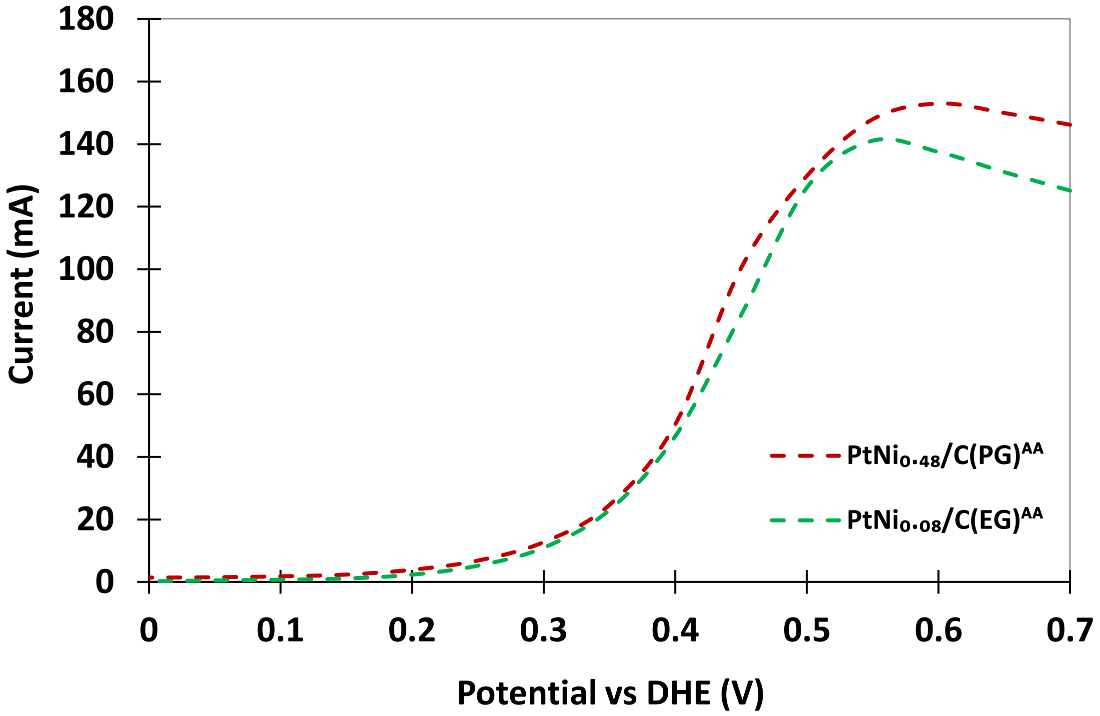

Figure 4.5: Polarization curves for the oxidation of 0.100 M ethanol (0.50 mL min^{-1}) at 80 °C at $PtNi_{0.48}/C(PG)^{AA}$ (2 mg cm^{-2}) and $PtNi_{0.08}/C(EG)^{AA}$ (2 mg cm^{-2}) anodes.

4.4.2 Stoichiometry (n_{av}) and product distribution

Measuring n_{av} is important to determine the faradaic efficiency of a DEFC, therefore, n_{av} values were calculated from the acetic acid, acetaldehyde, and CO_2 yields by using eq. 4.5. Results of n_{av} for $PtNi_{0.48}/C(PG)^{AA}$ and $PtNi_{0.08}/C(EG)^{AA}$ were plotted as a function of potential, as shown in Figure 4.6. Moreover, if we suppose that there were no losses of ethanol during the product collection in the exhausts, n_{av} can also be obtained from eq. 4.6.[19]

$$n_{av} = i/uF(C_{in} - C_{out}) \tag{4.6}$$

where i is the average current, u is the flow rate (mL min^{-1}), C_{in} is the concentration of ethanol entering the cell (0.100 M in our experiment), and C_{out} is the concentration of residual ethanol.

Results are shown in Figure C.7 in the Appendix. These two ways of measuring n_{av} gave close values, as shown in Table C.1 and C.2. The small difference can be attributed to the uncertainty in the experiments. It is clear from Figure 4.6 that n_{av} values varied between 2.5 to 6.6 and 2.9 to 6.8 for PtNi$_{0.48}$/C(PG)^{AA} and PtNi$_{0.8}$/C(EG)^{AA}, respectively. At the PtNi$_{0.08}$/C(PG)^{AA} anode, a decrease in n_{av} was observed at 0.4 V, which suggests that the surface of Pt was blocked either by CO$_{ad}$ and/or CH$_3$CHO$_{ads}$. However, at 0.6 V, the n_{av} was around 6.6 for PtNi$_{0.08}$/C(EG)^{AA}, while it was 5.6 for PtNi$_{0.48}$/C(PG)^{AA}, indicating that the production of CO$_2$ was high at the PtNi$_{0.08}$/C(EG)^{AA} anode. Since the current was lower at 0.6 V for PtNi$_{0.08}$/C(EG)^{AA} than for PtNi$_{0.48}$/C(PG)^{AA}, as shown in Figure 4.3, this indicates that there is another factor that affects the selectivity of the catalyst besides the current (e.g. third body effect).

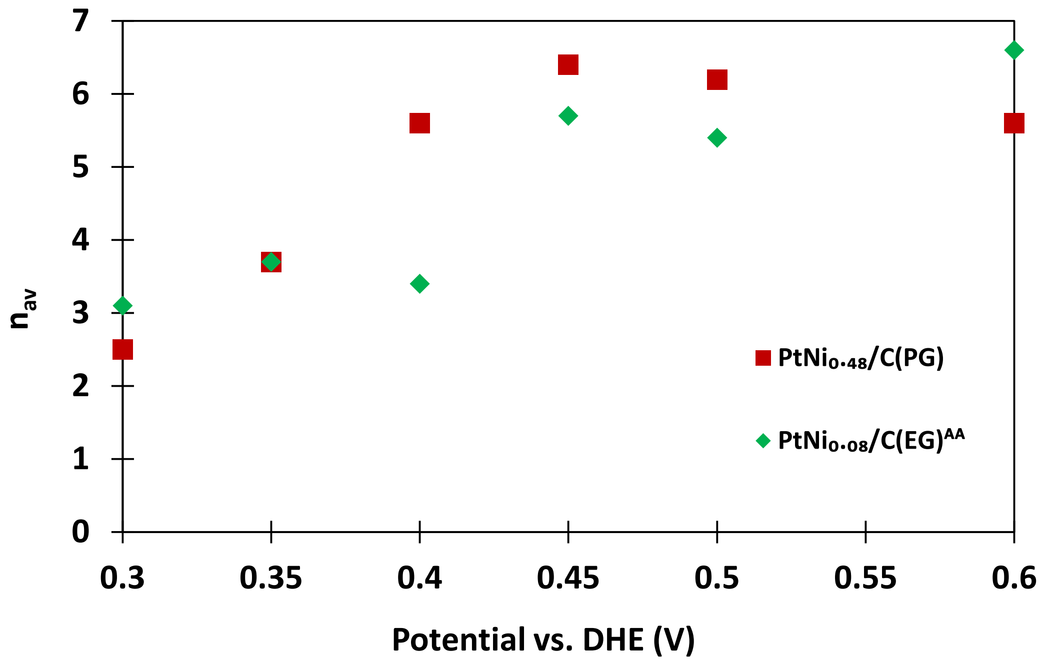

Figure 4.6: n_{av} vs. the potential for the oxidation of 0.100 M ethanol (0.2 mL min^{-1}) at PtNi$_{0.48}$/C(PG)^{AA} and PtNi$_{0.08}$/C(EG)^{AA} anodes at 80 °C. These results were obtained from the acetic acid, acetaldehyde, and CO$_2$ yields by using eq. 4.5.

An accurate analysis of products (acetaldehyde and acetic acid) is essential to calculate the faradic efficiency and understand the mechanism of the EOR.[27] Here, product analysis was carried out for ethanol oxidation at $PtNi_{0.48}/C(PG)^{AA}$ and $PtNi_{0.08}/C(EG)^{AA}$ anodes by using the NMR and NDIR methods reported by Altarawneh et al.[28] Figures 4.7 and 4.8 show the chemical yields of acetic acid, acetaldehyde, and CO_2 as a function of potential. No other products (such as ethyl acetate and ethane-1,1-diol) were detected in this work.[29] An example of a ^1H NMR spectrum is shown in Appendix C. It can be seen from these data that the highest chemical yields of CO_2 were 36% at 0.45 V for $PtNi_{0.48}/C(PG)^{AA}$ and 29% for $PtNi_{0.08}/C(EG)^{AA}$. This indicates that $PtNi_{0.48}/C(PG)^{AA}$ had more ability to oxidize CO_{ad} to produce CO_2 at 0.45 V than $PtNi_{0.08}/C(EG)^{AA}$. At high potentials (0.5 V to 0.6 V), 59% of ethanol was oxidized at the $PtNi_{0.48}/C(PG)^{AA}$ anode to acetic acid, 25-32% was converted to CO_2, and 9-17% was oxidized to acetaldehyde. On the other hand, at the $PtNi_{0.08}/C(EG)^{AA}$ anode, 40-68% was oxidized to acetic acid, 12-23% to acetaldehyde, and around 20-38% to CO_2. The superior production of acetic acid at high potentials can be explained based on the dissociation of water. It has been shown that at high potentials, the presence of OH species enhances the oxidation of the acetaldehyde intermediate to produce acetic acid.[13] Interestingly, at 0.4 V, the chemical yield of CO_2 was higher for $Ni_{0.48}/C(PG)^{AA}$ than $PtNi_{0.08}/C(EG)$. This indicates that $PtNi_{0.48}/C(PG)^{AA}$ was more selective than $PtNi_{0.08}/C(EG)^{AA}$ for breaking the C-C bond at 0.4 V.[30] At low potentials, around 95% of ethanol, at both the $PtNi_{0.48}/C(PG)^{AA}$ and $PtNi_{0.08}/C(EG)^{AA}$ anodes, was converted to acetaldehyde, which is consistent with the proposed mechanism for the EOR at low potentials in acidic media.[31,32]

In contrast to data reported for a octahedral PtNi catalyst,[21] $PtNi_{0.48}/C(PG)^{AA}$ and $PtNi_{0.08}/C(EG)^{AA}$ produced more CO_2 at high potentials (≥ 0.45 V) under the same conditions. For example, at 0.45 V, the chemical yield of CO_2 was 21% for octahedral PtNi, while it was 36% and

29% for $PtNi_{0.48}/C(PG)^{AA}$ and $PtNi_{0.08}/C(EG)^{AA}$, respectively. However, at low potentials, the chemical yields of CO_2 were low for $PtNi_{0.48}/C(PG)^{AA}$ and $PtNi_{0.08}/C(EG)^{AA}$, while they were around 40% for octahedral PtNi. Furthermore, the CO_2 yields for $PtNi_{0.48}/C(PG)^{AA}$ and $PtNi_{0.08}/C(EG)^{AA}$ were less than for 70% Pt/C from 0.3 to 0.6 V.[21] However, chemical yields of CO_2 (at the overall potential range) for $PtNi_{0.48}/C(PG)^{AA}$ and $PtNi_{0.08}/C(EG)^{AA}$ were higher than for the PtRu catalyst reported by Altarawneh et al,[19] So, when the PtRu catalyst is compared with $PtNi_{0.48}/C(PG)^{AA}$ and $PtNi_{0.08}/C(EG)^{AA}$, PtNi showed higher chemical yields at potentials ≥ 0.35 V. In conclusion, this may confirm that the effect of Ni differs significantly from the effect of Ru, as previously reported.[21] Whereas Ru increases ethanol oxidation predominantly through the bifunctional effect, the electronic effect in PtNi enhances the C-C bond cleavage. Furthermore, since $PtNi_{0.48}/C(PG)^{AA}$ and $PtNi_{0.08}/C(EG)^{AA}$ catalysts have Ni as a secondary metal and probably a core-shell like structure (PtNi@Pt), it is clear that the Ni to Pt core ratio and the surface geometry may have an impact on the product distribution and CO_2 yield.

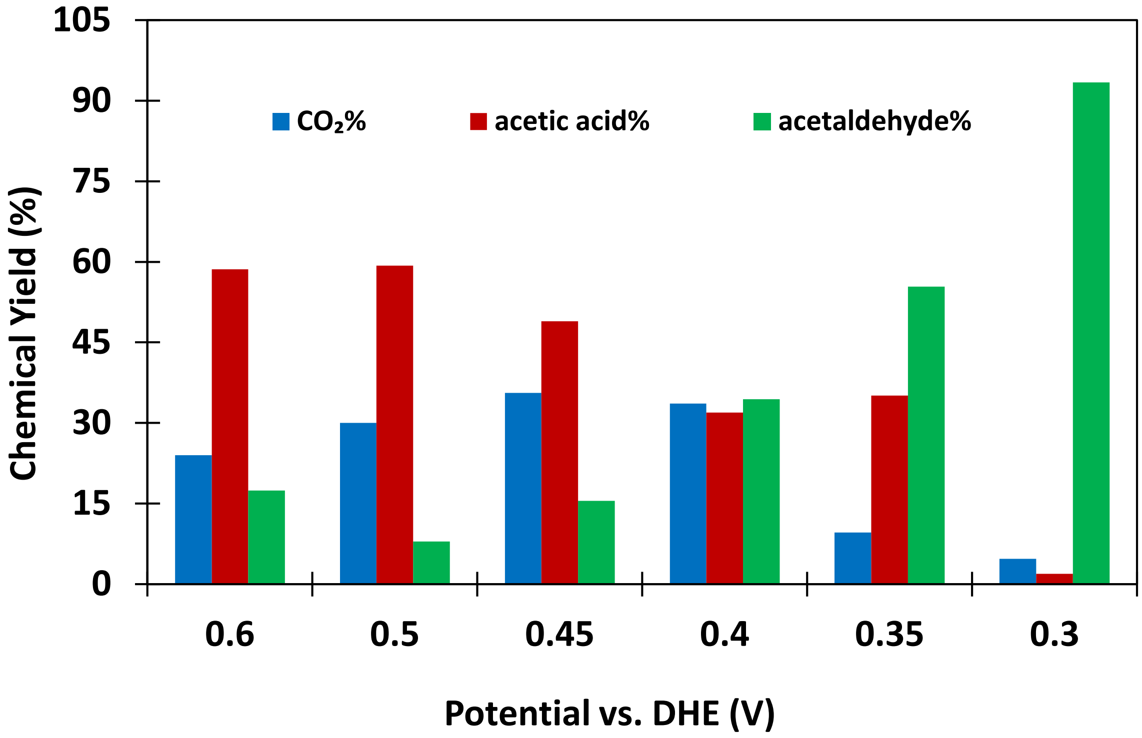

Figure 4.7: Chemical yields of CO_2, acetic acid, and acetaldehyde as a function of potential for 0.100 M ethanol oxidation (0.2 mL min^{-1}) at a $PtNi_{0.48}/C(PG)^{AA}$ anode in a 5 cm^2 PEM electrolysis cell at 80 °C.

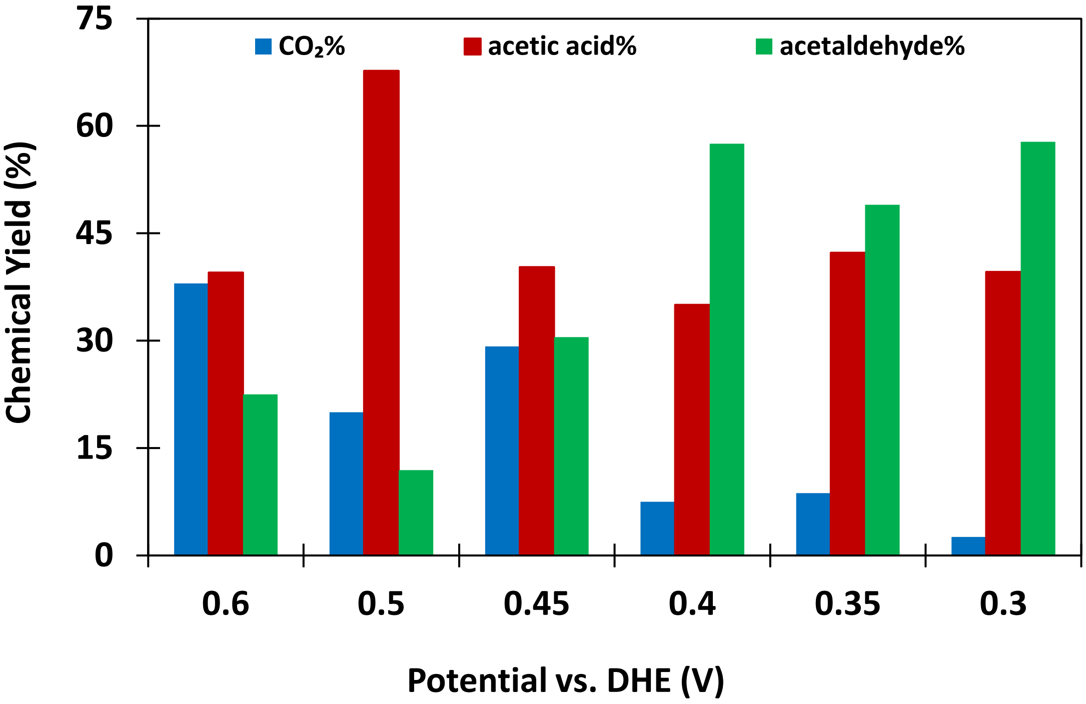

Figure 4.8: Chemical yields of CO_2, acetic acid, and acetaldehyde as a function of potential for 0.100 M ethanol oxidation (0.2 mL min^{-1}) at the $PtNi_{0.08}/C(EG)^{AA}$ anode in a 5 cm^2 PEM electrolysis cell at 80 °C.

4.5 Conclusion

$PtNi_{0.62}/C(PG)$, $PtNi_{0.50}/C(EG)$, and commercial $PtNi_{0.26}/C$ catalysts were tested in a nine-anode PEM electrolysis cell at 80 °C. At high potentials, $PtNi_{0.62}/C(PG)$ had more activity toward the oxidation of ethanol than $PtNi_{0.50}/C(EG)$ and commercial $PtNi_{0.26}/C$. When Ni was removed from the catalyst surface with acetic acid ($PtNi_{0.48}/C(PG)^{AA}$, $PtNi_{0.08}/C(EG)^{AA}$, and $PtNi_{0.22}/C^{AA}$), the activity increased slightly for $PtNi_{0.62}/C(PG)$ and $PtNi_{0.50}/C(EG)$. On the other hand, it was enhanced significantly at the treated commercial $PtNi_{0.26}/C$ catalyst ($PtNi_{0.22}/C^{AA}$). When these results were compared with the results obtained from cyclic voltammetry (at ambient temperature and H_2SO_4(aq)) in reference,[22] it is clear that cyclic voltammetry is not a good indicator of performance in the PEM electrolysis cell. Interestingly, the acid treatment of $PtNi_{0.62}/C(PG)$ and $PtNi_{0.50}/C(EG)$ enhanced the production of CO_2 more than for commercial $PtNi_{0.26}/C$, which indicates that the structure of the catalyst (core-shell like structure in the case of $PtNi_{0.48}/C(PG)^{AA}$ and $PtNi_{0.08}/C(EG)^{AA}$) has more effect for breaking the C-C bond in ethanol.

A 5 cm^2 PEM electrolysis cell was used to measure the product distribution for $PtNi_{0.48}/C(PG)^{AA}$ and $PtNi_{0.08}/C(EG)^{AA}$. The results showed that $PtNi_{0.48}/C(PG)^{AA}$ had high activity at high potentials and was more selective in producing CO_2 than $PtNi_{0.08}/C(EG)^{AA}$, particularly at 0.45 V vs DHE. On the other hand, $PtNi_{0.08}/C(EG)^{AA}$ was more selective in producing acetic acid than $PtNi_{0.48}/C(PG)^{AA}$. $PtNi_{0.48}/C(PG)^{AA}$ and $PtNi_{0.08}/C(EG)^{AA}$ can be improved to increase the performance of DEFCs, especially at low potentials. For example, preparing PtNi@Pt or PtNiRu may enhance the performance at low potentials and/or the selectivity to produce CO_2.[33,34]

4.6 References

(1) Badwal, S. P. S.; Giddey, S.; Kulkarni, A.; Goel, J.; Basu, S. Direct Ethanol Fuel Cells for Transport and Stationary Applications – A Comprehensive Review. *Appl. Energy* **2015**, *145*, 80–103.

(2) Bambagioni, V.; Bevilacqua, M.; Bianchini, C.; Filippi, J.; Lavacchi, A.; Marchionni, A.; Vizza, F.; Shen, P. K. Self-Sustainable Production of Hydrogen, Chemicals, and Energy from Renewable Alcohols by Electrocatalysis. *ChemSusChem* **2010**, *3*, 851–855.

(3) An, L.; Zhao, T. S.; Li, Y. S. Carbon-Neutral Sustainable Energy Technology: Direct Ethanol Fuel Cells. *Renew. Sustain. Energy Rev.* **2015**, *50*, 1462–1468.

(4) Rahman, M. R.; Allan, J. T. S.; Zamanzad Ghavidel, M.; Prest, L. E.; Saleh, F. S.; Easton, E. B. The Application of Power-Generating Fuel Cell Electrode Materials and Monitoring

Methods to Breath Alcohol Sensors. *Sensors Actuators B Chem.* **2016**, *228*, 448–457.

(5) Wigmore, J. G.; Langille, R. M. Six Generations of Breath Alcohol Testing Instruments: Changes in the Detection of Breath Alcohol Since 1930. An Historical Overview. *Can. Soc. Forensic Sci. J.* **2009**, *42*, 276–283.

(6) Lamy, C.; Jaubert, T.; Baranton, S.; Coutanceau, C. Clean Hydrogen Generation through the Electrocatalytic Oxidation of Ethanol in a Proton Exchange Membrane Electrolysis Cell (PEMEC): Effect of the Nature and Structure of the Catalytic Anode. *J. Power Sources* **2014**, *245*, 927–936.

(7) Wang, Y.; Zou, S.; Cai, W.-B. Recent Advances on Electro-Oxidation of Ethanol on Pt- and Pd-Based Catalysts: From Reaction Mechanisms to Catalytic Materials. *Catalysts* **2015**, *5*, 1507–1534.

(8) Tayal, J.; Rawat, B.; Basu, S. Bi-Metallic and Tri-Metallic Pt–Sn/C, Pt–Ir/C, Pt–Ir–Sn/C Catalysts for Electro-Oxidation of Ethanol in Direct Ethanol Fuel Cell. *Int. J. Hydrogen Energy* **2011**, *36*, 14884–14897.

(9) Akhairi, M. A. F.; Kamarudin, S. K. Catalysts in Direct Ethanol Fuel Cell (DEFC): An Overview. *Int. J. Hydrogen Energy* **2016**, *41*, 4214–4228.

(10) Wang, Q.; Lu, X.; Xin, Q.; Sun, G. Polyol-Synthesized $Pt_{2.6}Sn_1Ru_{0.4}/C$ as a High-Performance Anode Catalyst for Direct Ethanol Fuel Cells. *Chinese J. Catal.* **2014**, *35*, 1394–1401.

(11) Colmati, F.; Antolini, E.; Gonzalez, E. R. Effect of Temperature on the Mechanism of Ethanol Oxidation on Carbon Supported Pt, PtRu and Pt_3Sn Electrocatalysts. *J. Power Sources* **2006**, *157*, 98–103.

(12) El Sawy, E. N.; Brueckner, T. M.; Pickup, P. G. Electrochemical Oxidation of Methanol and Ethanol at Rh@Pt and Ru@Pt Catalysts. *J. Electrochem. Soc.* **2020**, *167*, 106507.

(13) Rousseau, S.; Coutanceau, C.; Lamy, C.; Léger, J.-M. Direct Ethanol Fuel Cell (DEFC): Electrical Performances and Reaction Products Distribution under Operating Conditions with Different Platinum-Based Anodes. *J. Power Sources* **2006**, *158*, 18–24.

(14) Torrero, J.; Pérez-Alonso, F. J.; Peña, M. A.; Domínguez, C.; Al-Youbi, A. O.; Al-Thabaiti, S. A.; Basahel, S. N.; Alshehri, A. A.; Rojas, S. In Situ Infrared Study of the Electrooxidation of Ethanol and Acetaldehyde in Acid Electrolyte. *ChemElectroChem* **2016**, *3*, 1072–1083.

(15) Almeida, T. S.; Kokoh, K. B.; De Andrade, A. R. Effect of Ni on Pt/C and PtSn/C Prepared by the Pechini Method. *Int. J. Hydrogen Energy* **2011**, *36*, 3803–3810.

(16) Hernandez-Fernandez, P.; Lund, P. B.; Kallesøe, C.; Clausen, H. F.; Christensen, L. H. Supported Pt-Based Nanoparticulate Catalysts for the Electro-Oxidation of Methanol: An Experimental Protocol for Quantifying Its Activity. *Int. J. Hydrogen Energy* **2015**, *40*, 284–291.

(17) Sayadi, A.; Pickup, P. G. Evaluation of Ethanol Oxidation Catalysts by Rotating Disc Voltammetry. *Electrochim. Acta* **2016**, *215*, 84–92.

(18) Bach Delpeuch, A.; Jacquot, M.; Chatenet, M.; Cremers, C. The Influence of Mass-Transport Conditions on the Ethanol Oxidation Reaction (EOR) Mechanism of Pt/C Electrocatalysts. *Phys. Chem. Chem. Phys.* **2016**, *18*, 25169–25175.

(19) Altarawneh, R. M.; Pickup, P. G. Product Distributions and Efficiencies for Ethanol Oxidation in a Proton Exchange Membrane Electrolysis Cell. *J. Electrochem. Soc.* **2017**, *164*, F861–F865.

(20) Brueckner, T. M.; Pickup, P. G. Kinetics and Stoichiometry of Methanol and Ethanol Oxidation in Multi-Anode Proton Exchange Membrane Cells. *J. Electrochem. Soc.* **2017**, *164*, F1172–F1178.

(21) Altarawneh, R. M.; Brueckner, T. M.; Chen, B.; Pickup, P. G. Product Distributions and

Efficiencies for Ethanol Oxidation at PtNi Octahedra. *J. Power Sources* **2018**, *400*, 369–376.

(22) Alqdeimat, D.; Pickup, P. G. $PtNi_x$/C Catalysts for Improved Performance in Ethanol Fuel Cells. *ECS Trans.* **2020**, *97*, 893–900.

(23) Corradini, P. G.; Santos, N. A.; Perez, J. Pt-Sn-Eu/C Catalysts: Application of Rare Earth Metals as Anodes in Direct Ethanol Fuel Cells. *Fuel Cells* **2018**, *18*, 73–81.

(24) Friedl, J.; Stimming, U. Model Catalyst Studies on Hydrogen and Ethanol Oxidation for Fuel Cells. *Electrochim. Acta* **2013**, *101*, 41–58.

(25) Song, S.; He, C.; Liu, J.; Wang, Y.; Brouzgou, A.; Tsiakaras, P. Two-Step Sequence for Synthesis of Efficient PtSn@Rh/C Catalyst for Oxidizing Ethanol and Intermediate Products. *Appl. Catal. B Environ.* **2012**, *119–120*, 227–233.

(26) Choi, S.-I.; Xie, S.; Shao, M.; Odell, J. H.; Lu, N.; Peng, H.-C.; Protsailo, L.; Guerrero, S.; Park, J.; Xia, X.; Wang, J.; Kim, M. J.; Xia, Y. Synthesis and Characterization of 9 Nm Pt–Ni Octahedra with a Record High Activity of 3.3 A/Mg Pt for the Oxygen Reduction Reaction. *Nano Lett.* **2013**, *13*, 3420–3425.

(27) Evarts, S. E.; Kendrick, I.; Wallstrom, B. L.; Mion, T.; Abedi, M.; Dimakis, N.; Smotkin, E. S. Ensemble Site Requirements for Oxidative Adsorption of Methanol and Ethanol on Pt Membrane Electrode Assemblies. *ACS Catal.* **2012**, *2*, 701–707.

(28) Altarawneh, R. M.; Majidi, P.; Pickup, P. G. Determination of the Efficiency of Ethanol Oxidation in a Proton Exchange Membrane Electrolysis Cell. *J. Power Sources* **2017**, *351*, 106–114.

(29) Kim, I.; Han, O. H.; Chae, S. A.; Paik, Y.; Kwon, S.-H.; Lee, K.-S.; Sung, Y.-E.; Kim, H. Catalytic Reactions in Direct Ethanol Fuel Cells. *Angew. Chem. Int. Ed* **2011**, *123*, 2318–2322.

(30) Antolini, E. Pt-Ni and Pt-M-Ni (M = Ru, Sn) Anode Catalysts for Low-Temperature Acidic Direct Alcohol Fuel Cells: A Review. *Energies* **2017**, *10*, 42.

(31) Paik, Y.; Kim, S.-S.; Han, O. H. Spatial Distribution of Reaction Products in Direct Ethanol Fuel Cell. *Electrochem. commun.* **2009**, *11*, 302–304.

(32) Maab, H.; Nunes, S. P. Modified SPEEK Membranes for Direct Ethanol Fuel Cell. *J. Power Sources* **2010**, *195*, 4036–4042.

(33) Lu, Y.; Wang, W.; Chen, X.; Zhang, Y.; Han, Y.; Cheng, Y.; Chen, X.-J.; Liu, K.; Wang, Y.; Zhang, Q.; Xie, S. Composition Optimized Trimetallic PtNiRu Dendritic Nanostructures as Versatile and Active Electrocatalysts for Alcohol Oxidation. *Nano Res.* **2019**, *12*, 651–657.

(34) Erini, N.; Beermann, V.; Gocyla, M.; Gliech, M.; Heggen, M.; Dunin-Borkowski, R. E.; Strasser, P. The Effect of Surface Site Ensembles on the Activity and Selectivity of Ethanol Electrooxidation by Octahedral PtNiRh Nanoparticles. *Angew. Chemie Int. Ed.* **2017**, *56*, 6533–6538.

Chapter 5

5. Screening of Commercial Catalysts in a Nine-Anode Proton Exchange Membrane Electrolysis Cell for the Ethanol Oxidation Reaction

The first author (Diala A. Alqdeimat) contributed to all parts of this research as the main researcher including literature review, carrying out all the experiments, measuring and analyzing the data, and discussing and presenting the data.

Prof. Peter G. Pickup was the principal investigator and provided the initial ideas for this project. He mentored the principal author (Diala A. Alqdeimat) and supported her during the project time. He reviewed all data analyses and edited the text.

The raw data is provided in Appendix D.

5.1 Introduction

Direct alcohol fuel cells (DAFCs) have been utilized in vehicles, sensors and electronic devices.[1,2] The use of liquid fuels like ethanol and methanol in fuel cells would eliminate the need for completely new infrastructure, which is required when using hydrogen as a fuel source. Ethanol has higher specific energy (8.0 kWh kg^{-1}) than methanol (6.09 kWh kg^{-1}).[3–5] Also, it has a higher volumetric density (6.28 kWh L^{-1}) than both hydrogen (0.18 kWh L^{-1}) and methanol (4.82 kWh L^{-1}).[4,6] Moreover, ethanol can be produced in large quantities from biomass (e.g. corn, sugarcane, etc.). Thus, studies have been started to develop direct ethanol fuel cells (DEFCs).[5]

There are two main pathways for the EOR: a C_1 pathway (complete oxidation reaction) and a C_2 pathway (incomplete oxidation reaction), as shown in Figure 5.1.[7] The complete oxidation reaction generates 12 electrons by producing CO_2.[3] However, the incomplete oxidation reaction produces acetic acid (4 electrons) and acetaldehyde (2 electrons). Therefore, the faradaic efficiency ($n_F = \frac{n_{av}}{n_t}$; n_{av} is the average number of transferred electrons per ethanol molecule) will be decreased.[8] Furthermore, during the EOR, adsorbed CO (CO_{ad}) is generated as an intermediate, which poisons the catalyst surface. As a result, the activity of the catalyst to oxidize ethanol will decrease.[3,7]

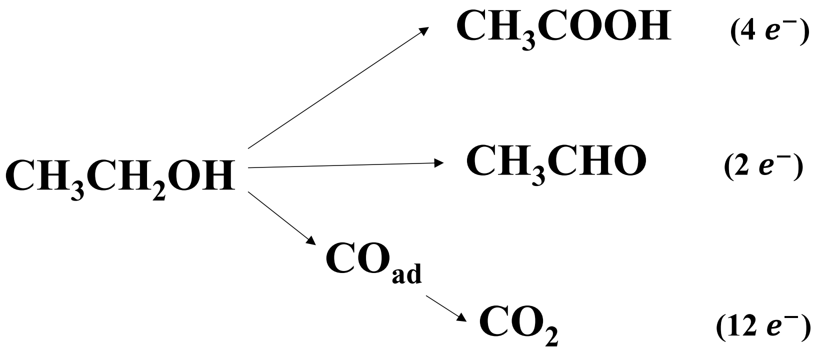

Figure 5.1: Pathways for electro-oxidation of ethanol in acidic media.

Many Pt-based catalysts have been developed to improve performance and efficiency for DEFCs.[9–15] Beyhan et al. investigated the performance of $Pt_{80}Sn_{10}Ni_{10}/C$ and $Pt_{90}Sn_{10}/C$ in a DEFC at 80 °C.[15] Colmati et al. studied the effect of temperature on the activity of PtRu and Pt_3Sn catalysts in a DEFC.[16] Furthermore, Paik et al. analyzed reaction products of ethanol oxidation at a PtRu/C anode in the liquid anode exhaust of a DEFC.[17] Kim et al. examined the reaction products from Pt/C, PtRu/C, and Pt_3Sn/C in the liquid anode exhaust of a DEFC.[18]

However, because of the various DEFC designs and operating conditions that have been used, it is difficult to compare catalysts based on their reported performances. Furthermore, the crossover of the fuel and products (acetic acid and acetaldehyde) from the anode to the cathode impacts the cathode potential. These problems have been avoided by using an electrolysis cell.[8] An ethanol electrolysis cell is similar to a DEFC, but oxygen gas is replaced by nitrogen gas at the cathode. In this cell, hydrogen evolution at the cathode generates a reference electrode with almost constant potential (dynamic hydrogen electrode).[19,20] Few studies have used electrolysis cells to evaluate catalysts for the EOR.[19–22] Brueckner et al.[20] reported a method for determining n_{av} and kinetic information from a polarization curve (current vs. cell potential) using a multi-anode PEM electrolysis cell. They examined its use to compare and evaluate Pt/C and PtRu/C catalysts under the same conditions.[20] Polarization curves were compared for the EOR at 80 ℃ at 70% Pt/C, 20% Pt/C, and PtRu black.[23]

In this work, we aimed to evaluate different commercial PtM/C catalysts (M: Ni, Cu, and Fe) using a nine-anode ethanol electrolysis cell (chapter 2, section 2.3.2). In particular, the performance and selectivity for breaking the C-C bond were examined in the EOR. Furthermore, these commercial catalysts are compared with the results reported for other catalysts under the same conditions. It is important to study the behavior of a variety of PtM/C catalysts optimize ethanol electrolysis cell (EEC) and DEFC performance and understand how the secondary metal influences selectivity for the complete oxidation of ethanol to CO_2.

5.2 Experimental

5.2.1 Electrode preparation for the nine-anode PEM electrolysis cell

Catalyst electrodes were prepared by suspending 8 mg of the catalyst in 70 μL of Nafion solution (Dupont; 5% Nafion), 120 μL of 1-propanol, 120 μL of 2-propanol, and 100 μL of deionized water. The mixture was sonicated at ambient temperature for 3 h. A 71 μL sample of the suspension was dropped onto a Toray™ carbon fiber paper disk (0.236 cm^2) and dried overnight at ambient temperature. The metal loading (Pt+M) for all catalysts was 2 mg cm^{-2} and the Nafion loading was ca. 30 mass%. Three electrodes were prepared for each catalyst. Table 5.1 summarizes the commercial catalysts (Premetek Co.) studied in this work.

Table 5.1: Summary of the commercial catalysts studied in this work.

Commercial catalysts	**PtM% (M: Ni, Cu, Fe)**	**Atomic ratio (Pt:M)**
Carbon supported PtNi alloy catalyst (PtNi/C)	40%	1:1
Carbon supported PtFe alloy catalyst (PtFe/C)	40%	1:1
Carbon supported PtCu alloy catalyst (PtCu/C)	20%	1:1

5.2.2 Electrochemical measurements

A nine-anode PEM electrolysis cell (Chapter 2, section 2.3.2) was used to obtain polarization curves for three electrodes of each catalyst (40% PtNi/C, 40% PtFe/C, and 20% PtCu/C) at the same time. The cell was operated at 80 ℃ in crossover mode (the anode is purged with N_2, while 0.100 M of ethanol is pumped to the cathode). This mode was used to operate the cell to control the diffusion of ethanol to the anode.[20] As a result, steady-state polarization curves with mass transport regions were produced. Polarization curves were obtained from 0.90 V to 0.00 V vs. DHE (dynamic hydrogen electrode) in 50 mV steps. At each potential, the current was averaged over the last 120 s. Before each polarization curve, the cell was preconditioned at 0.70 V for 1 h. For each catalyst, three polarization curves were obtained to measure the standard deviation, as shown in Appendix D. The faradaic yield of CO_2 was measured by a non-dispersive infrared (NDIR) carbon dioxide detector.[24] More details about the nine-anode PEM electrolysis cell and the measurements are described in Chapter 2 (sections 2.3.2 and 2.4).

5.3 Ethanol oxidation in a nine-anode PEM electrolysis cell

Figure 5.2 shows polarization curves for the oxidation of 0.100 M ethanol at 40% PtNi/C, 40% PtFe/C, and 20% PtCu/C anodes. There was no significant difference in the onset or half-wave ($E_{1/2}$) potentials between these catalysts. Also, the $E_{1/2}$ for these catalysts (0.5 V for PtNi, 0.45 V for PtFe and PtCu) was close to that for 70% Pt/C (0.5 V) reported previously[20] under the same conditions, suggesting that the presence of Cu, Ni, or Fe metals does not affect the kinetics. Also, they were higher than the value (0.35 V) reported for PtRu/C by Brueckner et al.[20,23] The low performance of these catalysts at low potentials indicates that the ability of PtNi, PtFe, or PtCu to oxidize the CO_{ad} (the poisoning intermediate) is lower than the PtRu catalyst.

At potentials ≥ 0.55 V, the current was higher for 20% PtCu/C than for 40% PtNi/C and 40% PtFe/C. Furthermore, at high potentials, currents peaked (I_{max}) at 0.6 V for all catalysts instead of rising to a plateau, and then decreased at potentials higher than 0.6 V. This behavior is consistent with literature results for 70% PtC and PtRu black where currents peaked and then decreased.[23] As shown in eq. 5.1,[19,20] the limiting current is proportional to the n_{av},

$$I_{lim} = n_{av}FmC \tag{5.1}$$

where F is the Faraday constant, m is the mass transport coefficient, and C is the bulk concentration of ethanol. Also, as reported previously, n_{av} values depend on the potential at the limiting current region.[20] Therefore, the decrease in currents is due to a potential dependence of n_{av}. Furthermore, based on eq. 5.2, n_{av} values are affected by changes in the product distribution. Since CO_2 production produces 12 electrons, acetic acid production requires 4 electrons to be transferred, and acetaldehyde requires 2 electrons.[5]

$$n_{av} = \sum n_i f_i \tag{5.2}$$

where f_i is the fraction of ethanol converted to a product i and n_i is the number of electrons transferred to form product *i.*

By using eq. 5.1 and the polarization curves in Figure 5.2, n_{av} values were estimated at different potentials (Figure 5.3). It can be seen from Figure 5.3 that n_{av} decreased at all anodes when the potential was increased from 0.65 V to 0.9 V. At the 40% PtFe/C anode, n_{av} was around 4 at high potentials, indicating that the production of acetic acid was high. However, 20% PtCu/C provided a higher n_{av} than 40% PtNi/C and 40% PtFe/C. Since faradaic efficiency is defined as the ratio between the average number of electrons transferred per molecule of ethanol (n_{av}) to the maximum of 12 electrons for the complete oxidation, 20% PtCu/C provides higher faradaic efficiency than 40% PtNi/C and 40% PtFe/C.

When these catalysts are compared with other reported catalysts based on n_{av}, 40% PtFe/C and 40% PtNi/C have n_{av} ranges close to those for the Ru@Pt (4.8 to 4.1)[21] and PtRu[20] (4.0 to 3.9) catalysts reported by El Sawy et al[21] and Brueckner et al[20], respectively. This indicates that the presence of Fe and Ni has a similar effect on the stoichiometry (n_{av}) as Ru at high potentials. Nevertheless, n_{av} values were higher for the 20% PtCu/C anodes than for the Ru@Pt and PtRu catalysts. However, all catalysts provided n_{av} values lower than the 70% Pt/C catalyst.[20]

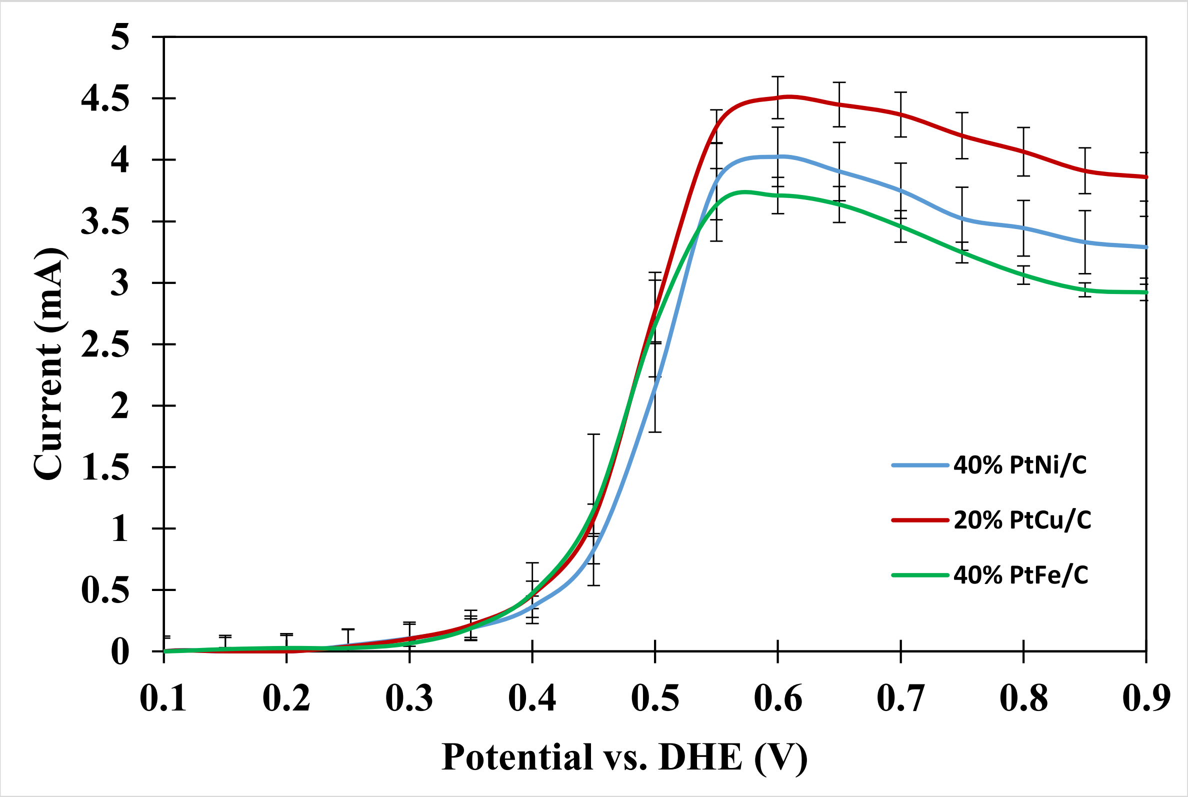

Figure 5.2: Polarization curves for the oxidation of 0.100 M ethanol (0.5 mL min^{-1}) at 80 °C in a nine-anode PEM electrolysis cell in crossover mode at 40% PtNi/C (2 mg cm^{-2}), 40% PtFe/C (2 mg cm^{-2}), and 20% PtCu/C (2 mg cm^{-2}) anodes. Error bars represent standard. Error bars represent standard deviations for each set of three electrodes.

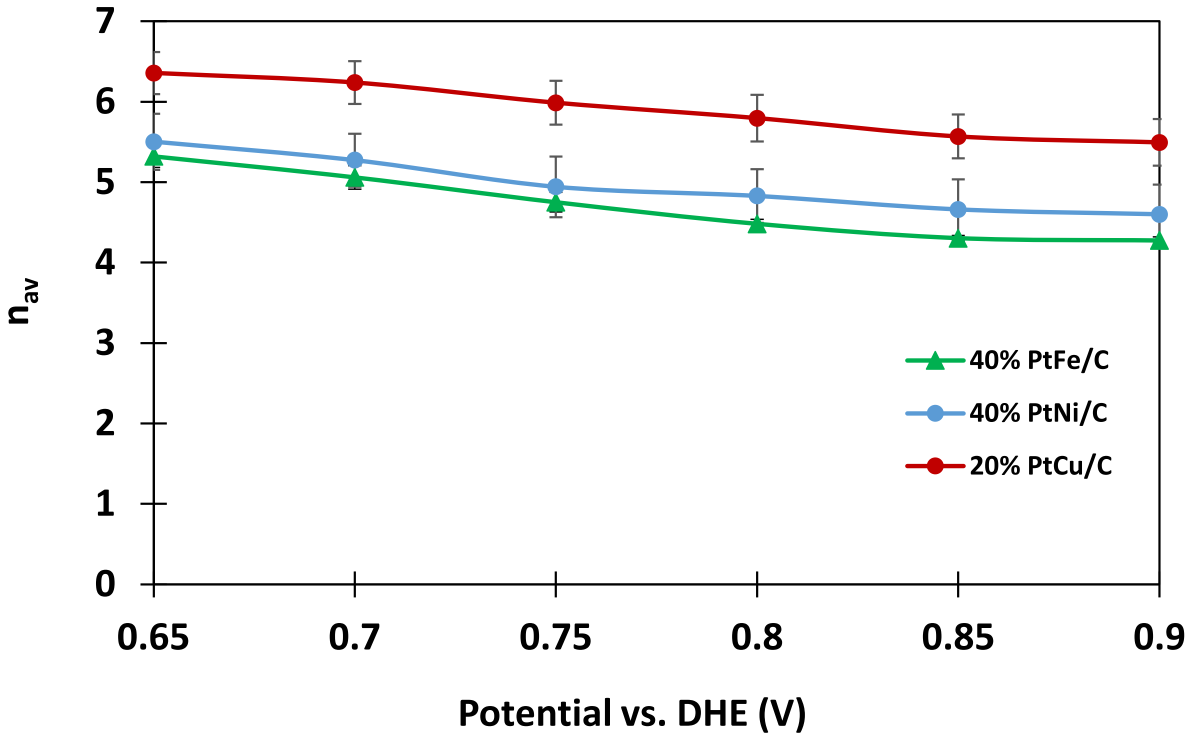

Figure 5.3: n_{av} values from figure 5.2 (eq. 5.1) vs. potential for the oxidation of 0.100 M ethanol at 40% PtNi/C, 40% PtFe/C, and 20% PtCu/C anodes at 80 °C. Error bars represent standard deviations for each set of three electrodes.

5.4 Measurement of faradaic yields of CO_2

The nine-anode PEM electrolysis cell was also used to measure faradaic yields of CO_2 (F_{CO_2}). Table 5.2 shows faradaic yields of CO_2 at 0.5 V. In this experiment, three anodes of each catalyst were run to provide an average value of CO_2 over the last 100 s, at the same time. The average faradaic yield of CO_2 increased in the order 40% PtNi/C < 40% PtFe/C < 20% PtCu/C. Interestingly, 20% PtCu provided a high CO_2 yield (66%). This high value suggests that Cu decreased poisoning by CO_{ad} and promoted C-C bond cleavage. Although the average current at the 40% PtFe/C anodes (4.4 mA) was lower than at the 40% PtNi/C anodes (5.3 mA), the faradaic yield of CO_2 was higher for 40% PtFe/C than for 40% PtNi/C. These results indicate that the production of CO_2 is more sensitive to the Pt surface and the catalyst structure than the current.

When these catalysts are compared with the commercial PtRu catalyst reported by Altarawneh et al,[19] it is clear that Ni, Fe, and Cu can enhance the C-C bond cleavage to produce CO_2 relative to PtRu (18%). As a result, these catalysts will provide higher faradaic efficiency than the PtRu catalyst in DEFCs. Also, the CO_2 yield at the 20% PtCu/C anode was higher than the reported value by Altarawneh et al. for a PtSn/C catalyst (ca. 50%).[19] Unfortunately, these catalysts showed lower CO_2 yields than the reported value for a commercial 70% Pt/C catalyst at 0.50 V (79%), under the same conditions.

Furthermore, n_{av} and the faradaic yield of CO_2 can be used to calculate the faradaic yield of acetic acid ($F_{\text{acetic acid}}$) and acetaldehyde ($F_{\text{acetaldehyde}}$) at 0.5 V using eq. 5.3 and 5.4,

$$n_{av} = 12/(F_{CO_2} + 3F_{acetic\ acid} + 6F_{acetaldehyde}) \tag{5.3}$$

$$100 = F_{CO_2} + F_{acetic\ acid} + F_{acetaldehyde} \tag{5.4}$$

Table 5.2 summarizes all faradaic yields at 0.5 V. The negligible yield of acetaldehyde (1%) at the PtNi/C catalyst is consistent with reported data for PtNi by Altarawneh et al.[25] This can be attributed to the oxidation of acetaldehyde to produce acetic acid (54%). Thus, this result indicates that the PtNi/C catalyst is good for acetic acid production. However, both PtFe/C and PtCu/C showed more acetaldehyde production than PtNi/C, indicating that the selectivity is affected by the electronic effect generated by the second metal.

Table 5.2: Faradaic yields of CO_2, acetic acid, and acetaldehyde for the oxidation of 0.100 M ethanol at 0.5 V and 80 °C at 40% PtNi/C, 40% PtFe/C, and 20% PtCu/C anodes.

Catalyst	CO_2%	acetic acid %	acetaldehyde %
40% PtNi/C	46%	53%	1%
40% PtFe/C	57%	10%	33%
20% PtCu/C	67%	17%	16%

5.5 Conclusion

The commercial catalysts (20% PtCu/C, 40% PtNi/C, and 40% PtFe/C) were evaluated in a nine-anode PEM electrolysis cell at 80 ℃. At high potentials, 20% PtCu/C had more activity toward the oxidation of ethanol than 40% PtNi/C, and 40% PtFe/C. However, based on polarization curves, none of these catalysts decreased the onset or half-wave potentials relative to Pt reported in the literature. This can be attributed to the inability of these metals (Cu, Ni and Fe) to facilitate the bifunctional mechanism (at low potentials) relative to Ru, which does shift the potential relative to Pt. Interestingly, the faradaic yield of CO_2 was higher for 20% PtCu/C (66%) than for 40% PtNi/C (45%) and 40% PtFe/C (55%), indicating that the presence of Cu enhances the breakage of the C-C bond in ethanol to produce CO_2.

The results for the commercial catalysts evaluated here show that 20% PtCu/C would increase the faradaic efficiency of an electrolysis cell, due to the higher stoichiometry (n_{av}) of the EOR, relative to 40% PtNi/C, and 40% PtFe/C. However, these commercial catalysts would suppress the performance of the electrolysis cell due to the slow kinetics at low potentials. Unfortunately, none of these catalysts provided higher selectivity or performance than Pt/C. It should be considered here that the metal loading was higher for the Pt/C catalyst (4 mg cm^{-2}) than these commercial catalysts (2 mg cm^{-2}) which might affect the comparison. Further investigation for these catalysts is needed to understand how Cu, Ni, and Fe in alloys affect the product distribution and efficiencies of a DEFC.

5.6 References

(1) Badwal, S. P. S.; Giddey, S.; Kulkarni, A.; Goel, J.; Basu, S. Direct Ethanol Fuel Cells for Transport and Stationary Applications – A Comprehensive Review. *Appl. Energy* **2015**, *145*, 80–103.

(2) Sharaf, O. Z.; Orhan, M. F. An Overview of Fuel Cell Technology: Fundamentals and Applications. *Renew. Sustain. Energy Rev.* **2014**, *32*, 810–853.

(3) Altarawneh, R. M. Overview on the Vital Step toward Addressing Platinum Catalyst Poisoning Mechanisms in Acid Media of Direct Ethanol Fuel Cells (DEFCs). *Energy & Fuels* **2021**, *35*, 11594–11612.

(4) Azam, A. M. I. N.; Lee, S. H.; Masdar, M. S.; Zainoodin, A. M.; Kamarudin, S. K. Parametric Study on Direct Ethanol Fuel Cell (DEFC) Performance and Fuel Crossover. *Int. J. Hydrogen Energy* **2019**, *44*, 8566–8574.

(5) Zheng, Y.; Wan, X.; Cheng, X.; Cheng, K.; Dai, Z.; Liu, Z. Advanced Catalytic Materials for Ethanol Oxidation in Direct Ethanol Fuel Cells. *Catalysts* **2020**, *10*, 166.

(6) Ramachandran, S.; Stimming, U. Well to Wheel Analysis of Low Carbon Alternatives for Road Traffic. *Energy Environ. Sci.* **2015**, *8*, 3313–3324.

(7) Wang, Y.; Zou, S.; Cai, W.-B. Recent Advances on Electro-Oxidation of Ethanol on Pt- and Pd-Based Catalysts: From Reaction Mechanisms to Catalytic Materials. *Catalysts* **2015**, *5*, 1507–1534.

(8) Altarawneh, R. M.; Majidi, P.; Pickup, P. G. Determination of the Efficiency of Ethanol Oxidation in a Proton Exchange Membrane Electrolysis Cell. *J. Power Sources* **2017**, *351*, 106–114.

(9) Yang, G.; Zhang, Q.; Yu, H.; Peng, F. Platinum-Based Ternary Catalysts for the Electrooxidation of Ethanol. *Particuology* **2021**, *58*, 169–186.

(10) Ren, X.; Lv, Q.; Liu, L.; Liu, B.; Wang, Y.; Liu, A.; Wu, G. Current Progress of Pt and Pt-Based Electrocatalysts Used for Fuel Cells. *Sustain. Energy Fuels* **2020**, *4*, 15–30.

(11) Antolini, E. Catalysts for Direct Ethanol Fuel Cells. *J. Power Sources* **2007**, *170*, 1–12.

(12) Ammam, M.; Easton, E. B. PtCu/C and Pt(Cu)/C Catalysts: Synthesis, Characterization and Catalytic Activity towards Ethanol Electrooxidation. *J. Power Sources* **2013**, *222*, 79–87.

(13) Huang, M.; Jiang, Y.; Jin, C.; Ren, J.; Zhou, Z.; Guan, L. Pt–Cu Alloy with High Density of Surface Pt Defects for Efficient Catalysis of Breaking C–C Bond in Ethanol. *Electrochim. Acta* **2014**, *125*, 29–37.

(14) Wang, P.; Yin, S.; Wen, Y.; Tian, Z.; Wang, N.; Key, J.; Wang, S.; Shen, P. K. Ternary Pt_9RhFe Nanoscale Alloys as Highly Efficient Catalysts with Enhanced Activity and Excellent CO-Poisoning Tolerance for Ethanol Oxidation. *ACS Appl. Mater. Interfaces* **2017**, *9*, 9584–9591.

(15) Beyhan, S.; Léger, J.-M.; Kadırgan, F. Pronounced Synergetic Effect of the Nano-Sized PtSnNi/C Catalyst for Ethanol Oxidation in Direct Ethanol Fuel Cell. *Appl. Catal. B Environ.* **2013**, *130–131*, 305–313.

(16) Colmati, F.; Antolini, E.; Gonzalez, E. R. Effect of Temperature on the Mechanism of Ethanol Oxidation on Carbon Supported Pt, PtRu and Pt_3Sn Electrocatalysts. *J. Power Sources* **2006**, *157*, 98–103.

(17) Paik, Y.; Kim, S.-S.; Han, O. H. Spatial Distribution of Reaction Products in Direct Ethanol

Fuel Cell. *Electrochem. commun.* **2009**, *11*, 302–304.

(18) Kim, I.; Han, O. H.; Chae, S. A.; Paik, Y.; Kwon, S.-H.; Lee, K.-S.; Sung, Y.-E.; Kim, H. Catalytic Reactions in Direct Ethanol Fuel Cells. *Angew. Chem. Int. Ed* **2011**, *123*, 2318–2322.

(19) Altarawneh, R. M.; Pickup, P. G. Product Distributions and Efficiencies for Ethanol Oxidation in a Proton Exchange Membrane Electrolysis Cell. *J. Electrochem. Soc.* **2017**, *164*, F861–F865.

(20) Brueckner, T. M.; Pickup, P. G. Kinetics and Stoichiometry of Methanol and Ethanol Oxidation in Multi-Anode Proton Exchange Membrane Cells. *J. Electrochem. Soc.* **2017**, *164*, F1172–F1178.

(21) El Sawy, E. N.; Brueckner, T. M.; Pickup, P. G. Electrochemical Oxidation of Methanol and Ethanol at Rh@Pt and Ru@Pt Catalysts. *J. Electrochem. Soc.* **2020**, *167*, 106507.

(22) Lamy, C.; Jaubert, T.; Baranton, S.; Coutanceau, C. Clean Hydrogen Generation through the Electrocatalytic Oxidation of Ethanol in a Proton Exchange Membrane Electrolysis Cell (PEMEC): Effect of the Nature and Structure of the Catalytic Anode. *J. Power Sources* **2014**, *245*, 927–936.

(23) Brueckner, T. M.; Wheeler, E.; Chen, B.; Sawy, E. N. El; Pickup, P. G. Screening of Catalysts for the Electrochemical Oxidation of Organic Fuels in A Multi-Anode Proton Exchange Membrane Cell. *J. Electrochem. Soc.* **2019**, *166*, F942–F948.

(24) Altarawneh, R. M.; Brueckner, T. M.; Chen, B.; Pickup, P. G. Product Distributions and Efficiencies for Ethanol Oxidation at PtNi Octahedra. *J. Power Sources* **2018**, *400*, 369–376.

(25) Altarawneh, R. M.; Brueckner, T. M.; Chen, B.; Pickup, P. G. Product Distributions and Efficiencies for Ethanol Oxidation at PtNi Octahedra. *J. Power Sources* **2018**, *400*, 369–

376.

Chapter 6

6. Ethanol Electro-Oxidation on a Carbon-Supported PtRuCu/C Catalyst in a Nine-anode Proton Exchange Membrane Electrolysis Cell

The first author (Diala A. Alqdeimat) contributed to all parts of this research as the main researcher including literature review, carrying out all the experiments, measuring and analyzing the data, and discussing and presenting the data.

Prof. Peter G. Pickup was the principal investigator and provided the initial ideas for this project. He mentored the principal author (Diala A. Alqdeimat) and supported her during the project time. He reviewed all data analysis and edited the text.

The raw data is provided in Appendix E.

6.1 Introduction

Fossil energy has been widely used in transportation and other applications. However, the production of a huge amount of greenhouse gases (CH_4, CO_2, and CO) causes many environmental problems including global warming, ocean pollution, and air pollution.[1] Therefore, it is essential to improve and increase the use of renewable energy sources such as biomass energy.[2]

Direct ethanol fuel cells (DEFCs) can be represented as one of the most promising technologies for a renewable source of power.[3] Ethanol is a renewable energy source because it can be produced in large quantities via the fermentation process. Ethanol is also a promising fuel source because it has lower toxicity than methanol and can be handled and stored easily. Moreover, ethanol has high specific energy (8.0 kWh kg^{-1}). On the other hand, ethanol has a higher volumetric density (6.28 kWh L^{-1}) than both hydrogen and methanol.[4–6]

The oxidation of ethanol involves complex multiple electron processes which provide many intermediates (CO_{ad} and CH_x) and products (acetic acid and acetaldehyde).[7–9] Twelve electrons will be generated if ethanol is completely oxidized to CO_2. However, when ethanol is partially oxidized, 4 electrons (acetic acid) and/or 2 electrons (acetaldehyde) will be generated, resulting in the low efficiency of DEFC.[10–14] Thus, incomplete oxidation of ethanol has become the major constraint for DEFCs.

In the ethanol oxidation reaction (EOR) process, most studies have developed anodes for DEFCs.[15,16] Under acidic conditions, Pt is used as a catalyst to promote the adsorption and dissociation of ethanol molecules.[17–19] Unfortunately, Pt is easily poisoned by intermediates species such as CH_x and CO_{ad}. As a result, these intermediates will decrease the efficiency of the Pt catalyst.[14,20]Also, the cost of Pt is high.[21,22] These disadvantages of using Pt in DEFCs increase the development of binary nanoalloys (PtM).[16,23,24] Alloying Pt with a second metal such as Ru, Sn, and Cu enhances the activity toward the EOR via a bifunctional mechanism and/or the electronic interaction between these alloyed metals and Pt.[16,25–28]

So far, PtRu alloys have been most widely investigated for the electro-oxidation of ethanol.[29–31] It was found that Ru enhances the bifunctional effect when it alloys with Pt.[32–35] Rodríguez-Gómez et al. examined the effect of the atomic ratio of Pt:Ru on the product distribution of ethanol oxidation in a proton exchange membrane (PEM) cell at 80 °C.[30] They found that a PtRu/C 2:1 anode produced mainly acetic acid (85%) and provided the highest current density (740 mA cm^{-2}). Moreover, Altarawneh et al. investigated the activity and product analysis for a PtRu/C catalyst.[36] They found that PtRu/C provided higher currents at potentials below 0.50 V than Pt/C. However, product analysis has shown that the main product from the oxidation of ethanol at PtRu is acetic acid and only a small CO_2 yield is produced (7%).

Since increasing the production of CO_2 is the major point to enhancing the efficiency of DEFCs, it is necessary and crucial to develop and modify PtRu/C. Many researchers have introduced a third transition metal (ternary catalyst) to improve the activity and performance of PtRu/C at high potentials and also to increase the production of CO_2.[37–42] Previous studies showed that alloying Cu with PtM/C enhanced the breaking of the C-C bond.[43,44] Han et al. prepared porous trimetallic PtRhCu cubic nanoboxes (CNBs). They found that the presence of Cu in the PtRhCu CNBs decreased poisoning by CO_{ad}.[44] Furthermore, Chen et al. found that the electroactivity of ultrafine PtCuRh nanowires (NWs) in the EOR was higher compared with a commercial Pt/C catalyst.[45] Few studies have investigated the effect of alloying Cu with PtRu/C on the electro-oxidation of alcohol.[46]

In this work, we prepared PtRu/C and PtRuCu/C catalysts and studied the effect of Cu for the EOR (at ambient temperature). Furthermore, the effect of Cu in the PtRuCu/C on the performance and CO_2 yield was investigated for the EOR at 80 °C in a nine-anode PEM electrolysis cell.

6.2 Experimental

6.2.1 Synthesis of PtRu/C and PtRuCu/C catalysts

Carbon-supported PtRu (2:1 Pt:Ru atomic ratio) NPs with a target loading of 40 mass% PtRu was prepared by adapting a method reported for ruthenium-tin oxide carbon supported platinum catalysts (chemical reduction).[47] Carbon black (0.1049 g) was sonicated in 15 mL of H_2O for 30 min (suspension). $H_2PtCl_6.6H_2O$ (0.0507 g) and $RuCl_3.3H_2O$ (0.0164 g) were dissolved in 10 mL of H_2O. The mixture was added to the suspension and left for 30 min under stirring. Sodium citrate (0.1757 g in 12 mL of H_2O) was added to the mixture and kept under stirring for 1 h. Slowly, sodium borohydride (0.0913 g in 20 mL of H_2O) was added to the mixture and kept under stirring for 3 h at ambient temperature. The catalyst was collected by centrifugation at 6000 rpm for 30 min, washed twice with water and acetone, and dried at 80 °C for 3 h. The same procedure was used to prepare PtRuCu (8:1:6 Pt:Ru:Cu atomic ratio) with a target loading of 40 mass% PtRuCu.

6.2.2 Characterization of catalysts

Scanning electron microscopy (SEM) and energy-dispersive X-ray spectroscopy (EDX) was used to study the distribution of elements and determine the atomic ratio and composition of the PtRu/C and PtRuCu/C catalysts. X-ray powder diffraction (XRD) was used to determine the crystal structures of the catalysts. Details about these instruments are shown in Chapter 2 (section 2.6).

6.2.3 Electrochemical measurements

Working electrodes for cyclic voltammetry were prepared by suspending 2 mg of the catalyst in 50 μL of Nafion solution (5%), 120 μL of water, and 30 μL of 2-propanol. Then, the mixture was sonicated for 3 h. A 3 μL of the suspension was left onto a glassy carbon disk to dry overnight at ambient temperature. The experiment was carried out at ambient temperature. Each working electrode was cycled from -0.20 V to 0.80 V vs. a saturated calomel electrode (SCE) in 1.0 M aqueous H_2SO_4 at 100 mV s^{-1}. Then, it was cycled from -0.20 V to 0.80 V in 0.10 M ethanol and 1.0 M aqueous H_2SO_4 at 10 mV s^{-1}. Currents were normalized based on the mass of Pt in the catalyst applied to the electrode.

6.2.4 A nine-anode PEM electrolysis cell

Catalyst electrodes were prepared by suspending 8 mg of the catalyst in 100 μL of deionized water, 120 μL of 1-propanol, 120 μL of 2-propanol, and 70 μL of Nafion solution (Dupont; 5% Nafion). The mixture was sonicated for 3 h at ambient temperature. A 71 μL of the suspension was dropped onto a Toray™ carbon fiber paper (0.236 cm^2). They were left to dry overnight at ambient temperature. On each carbon fiber paper, the Nafion loading was ca. 30 mass% and the metal loading was 2 mg cm^{-2}. As shown in Appendix E, three electrodes were prepared for each catalyst.

A nine-anode PEM electrolysis cell was used to obtain polarization curves for three electrodes of each catalyst at the same time. The cell was operated in the crossover mode (the anode is purged with N_2, while 0.100 M of ethanol is pumped to the cathode) at 80 °C. Polarization curves were obtained from 0.90 V to 0.00 V vs. DHE (dynamic hydrogen electrode) in 50 mV steps. At each potential, the current was averaged over the last 120 s. The cell was preconditioned at 0.70 V for 1 h before each polarization curve. The faradaic yield of CO_2 was measured by a non-dispersive infrared (NDIR) carbon dioxide detector. More details about the nine-anode PEM electrolysis cell and the measurements are described in Chapter 2 (sections 2.3.2 and 2.4).

6.3 Physical characterization of PtRu/C and PtRuCu/C catalysts

Energy-dispersion X-ray spectroscopy (EDX) was used to obtain the atomic ratio of metals and compositions of the catalysts. Figures 6.1 and 6.2 show X-ray spectra for PtRu/C and PtRuCu/C catalysts with SEM images. It can be seen from the X-ray spectra that all three metals (Pt, Ru, and Cu) were presence, and there was ca. 2% O for both catalysts. The target atomic ratio was 2:1 Pt:Ru for the PtRu/C catalyst and 8:1:6 Pt:Ru:Cu for the PtRuCu/C catalyst. Atomic ratios (target and EDX results) for the PtRu/C and PtRuCu/C catalysts are summarized in Table 6.1. For the PtRu/C catalyst, the target atomic ratio and the detected ratio were similar (2:1). Also, the detected atomic ratio was closed to the target ratio for the PtRuCu/C catalyst. Although the quantitative analysis of mass% may not be accurate by EDX because an electron beam is focused on a thin layer of the sample and the mass% does not reflect the whole sample, masses% obtained are listed in Table 6.1.

Table 6.1: mass% and atomic ratio (Pt:Ru and Pt:Ru:Cu) for PtRu/C and PtRuCu/C catalysts by EDX analysis.

Catalyst	**Target mass%** **Pt Ru Cu**	**EDX mass%** **Pt Ru Cu**	**Target atomic ratio**	**EDX atomic ratio**
PtRu/C	30% 10% 0%	27% 9% 0%	2:1 (Pt:Ru)	1.6:1.0 (Pt:Ru)
PtRuCu/C	30% 2% 8%	21% 2% 8%	8:1:6 (Pt:Ru:Cu)	7.2:1.0:5.3 (Pt:Ru:Cu)

As shown in SEM images, there were gray areas with white spots for both catalysts. Normally, Pt is a heavier element than other elements (Ru, Cu, and C). Thus, it will show brighter spots than other elements. For the PtRu/C catalyst, there was a gray area mainly consisting of C and white spots with a high percentage of Pt. Some white spots were larger than other, which suggest an agglomeration of Pt occurred. However, for the PtRuCu/C, the white spots were much brighter than PtRu/C, suggesting that the agglomeration of Pt was high in PtRuCu/C.

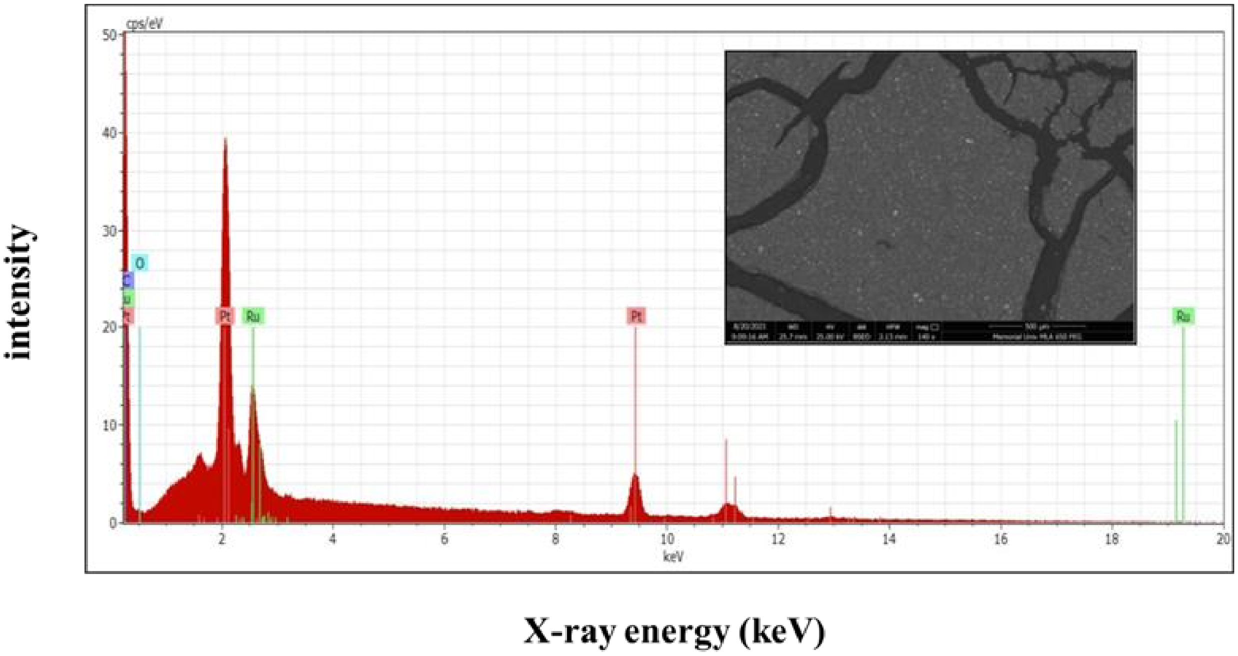

Figure 6.1: X-ray emission spectrum of the PtRu/C catalyst with an SEM image (inset).

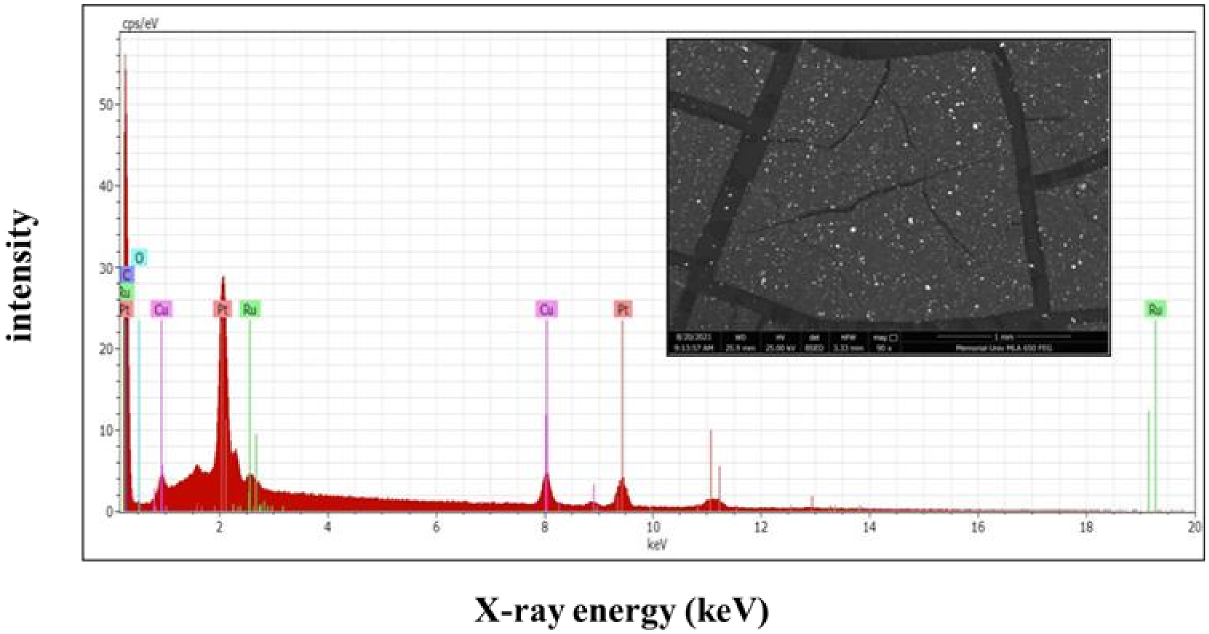

Figure 6.2: X-ray emission spectrum of the PtRuCu/C catalyst with an SEM image (inset).

X-ray powder diffraction (XRD) was used to determine the crystal structures and average particle sizes for the PtRu/C and PtRuCu/C catalysts. Figure 6.3 shows the XRD patterns of the PtRu/C and PtRuCu/C catalysts. The first peak ($2\theta = 24.8^{\circ}$) in the XRD patterns is for the carbon support. The other four peaks are characteristic of face-centered cubic (fcc) crystalline Pt. These peaks matched to the (111), (200), (220), and (311) planes. They are shifted to higher angles relative to those for pure Pt, indicating alloy formation for both catalysts. It is important to mention that no peaks were detected for Ru oxide (55°, 35°)[48], pure Ru (58°, 44°)[49], Cu oxide (38°, 61°), or pure Cu (51°, 74°).[49] Although there were no peaks for pure Cu and/or Ru or their oxides, the presence of such materials cannot be ruled out because they could be present in trace amounts or in amorphous states.

The average particle size was measured for PtRu/C and PtRuCu/C catalysts using the Scherrer equation (6.1),

$$\text{average particle size} = \frac{0.9\lambda}{\beta cos\theta} \tag{6.1}$$

where λ is X-ray wavelength, β is line broadening at half of the maximum intensity (in radians), and θ is Bragg angle (in radians). Particle sizes are summarized in Table 6.2. The average particle size for PtRuCu/C was slightly lower than for PtRu/C. The Bragg scattering equation (6.2) was used to calculate lattice constants (a) for catalysts,

$$a = \frac{\lambda\sqrt{h^2 + k^2 + l^2}}{2sin\theta} \tag{6.2}$$

where, λ is X-ray wavelength (0.15418 nm), (hkl) are the Miller indices (111) for the scattering angle, and θ is Bragg angle (in degree). Lattice constants are listed in Table 6.2. The Lattice constant for pure Pt is 0.3921 nm.[50] Lattice constants of both catalysts were lower than the lattice constant of pure Pt, indicating single-phase alloys were formed.

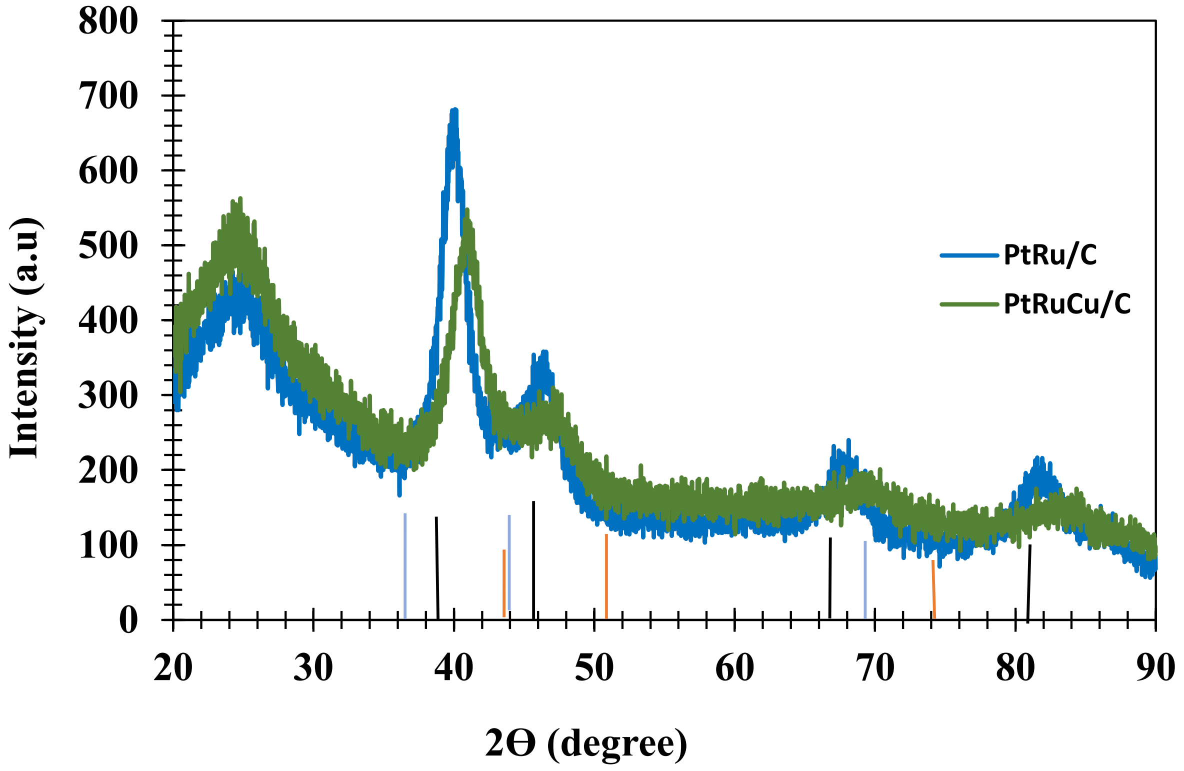

Figure 6.3: X-ray diffraction pattern of PtRu/C (blue) and PtRuCu/C (green) catalysts. The solid lines are the standard peak positions for Pt (black), Ru(blue), and Cu (orange).[49]

Table 6.2: The average particle size and lattice parameter of PtRu/C and PtRuCu/C catalysts.

Catalyst	$2\Theta_{111}$	average particle size (nm)	lattice parameter (nm)
PtRu/C	40.16	4.9	0.3896
PtRuCu/C	40.94	4.0	0.3818

6.4 The electrochemical activity of the catalysts

Figure 6.4 shows the cyclic voltammograms of PtRu/C and PtRuCu/C catalysts in 1.0 M H_2SO_4(aq) at 25 °C. In the hydrogen adsorption/desorption region (potential < 0 V vs SCE), no characteristic peaks for the pure Pt surface appeared for PtRu/C and PtRuCu/C, indicating that the Pt surface was not a pure Pt. In addition, at potentials > 0 V vs SCE, a pseudo-capacitance was observed at the PtRu/C catalyst due to surface Ru oxide.[35] However, the pseudo-capacitance was low at the PtRuCu/C catalyst which is consistent with the low amount of Ru (as shown by EDX analysis).

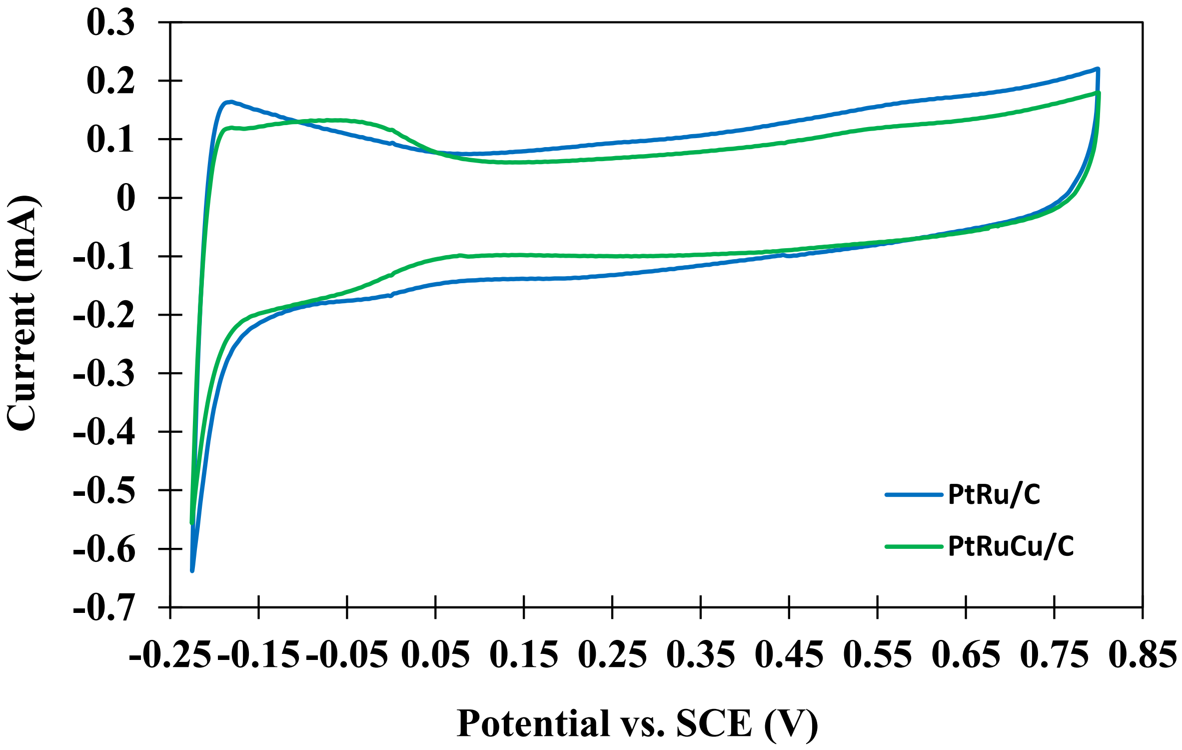

Figure 6.4: Cyclic voltammograms of the PtRu/C and PtRuCu/C catalysts in 1.0 M H_2SO_4(aq) (100 mV s^{-1}) at ambient temperature.

Cyclic voltammetry experiments were carried out to study the activity of PtRu/C and PtRuCu/C catalysts toward ethanol oxidation. Figure 6.5 shows cyclic voltammograms for the PtRu/C and PtRuCu/C catalysts. Since these catalysts were compared with the commercial 70% Pt/C catalyst, all the voltammograms were normalized based on Pt loading.

The PtRu/C catalyst was more active for ethanol oxidation than the 70% Pt/C catalyst. The current at the PtRu/C catalyst began to increase at ca. 0.30 V, while it was at ca. 0.4 V at the 70% Pt/C catalyst. The enhancement of the ethanol oxidation activity at the PtRu/C catalyst can be attributed to a bifunctional mechanism.[33] At low potentials, Ru activates the dissociation of water, and $RuOH_{ads}$ sites are formed. As a result, $Ru(OH)_{ad}$ sites can oxidize CO_{ad} ($Pt(CO)_{ad}$) to CO_2.[51] However, the peak current was much lower for PtRu/C relative to 70% Pt/C. This is consistent with the result reported by Ali and Pickup which show that the activity of PtRu/C is low at high potentials.[35]

When a cyclic voltammetry experiment was carried out for the PtRuCu/C catalyst, the onset potential was close to that for PtRu/C, indicating that alloying Cu with Pt and Ru does not affect ethanol oxidation at low potentials. Interestingly, at potential > 0.5 V, the activity of PtRuCu/C increased significantly relative to the PtRu/C. This indicates that the incorporation of Cu in PtRuCu/C catalyst affects the Pt electronic structure by the electronic effect.[43] Unfortunately, at high potentials, there was no enhancement of the activity at the PtRuCu/C catalyst toward ethanol oxidation relative to the 70% Pt/C catalyst.

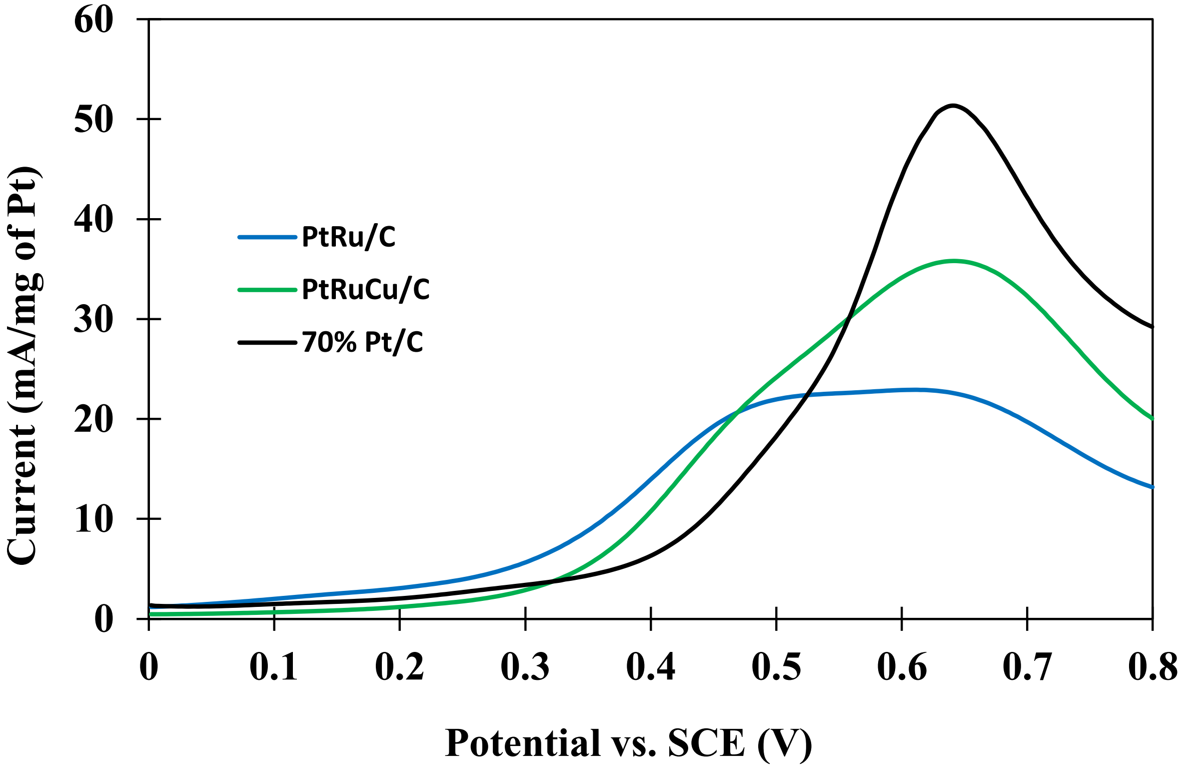

Figure 6.5: Cyclic voltammograms (a 10th forward scan) of the PtRu/C (0.17 mg cm^{-2} metal loading), PtRuCu/C (0.17 mg cm^{-2} metal loading), and 70% Pt/C (0.29 mg cm^{-2} metal loading) catalysts in 1.0 M H_2SO_4(aq) + 0.100 M ethanol (10 mV s^{-1}) at ambient temperature.

6.5 Ethanol electro-oxidation in a nine-anode PEM electrolysis cell

The EOR was studied at the PtRu/C and PtRuCu/C catalysts using a nine-anode PEM electrolysis cell. In this experiment, ethanol is oxidized to acetic acid, acetaldehyde, and CO_2 at the anode, while hydrogen is produced at the cathode. Since using a high concentration of ethanol decreases the production of CO_2,[52,53] a low concentration (0.1 M) of ethanol was used in this study to increase the stoichiometry for ethanol oxidation.

Figure 6.6 shows polarization curves for the oxidation of 0.100 M ethanol at PtRu/C and PtRuCu/C anodes. The half-wave ($E_{1/2}$) was shifted from 0.38 V for PtRu/C to 0.32 V for PtRuCu/C. This indicates that the incorporation of Cu with Ru (PtRuCu/C) influenced the kinetics at low potentials. The $E_{1/2}$ for PtRu/C (0.38 V) and PtRuCu/C (0.32 V) was shifted to a lower potential relative to a 70% Pt/C catalyst (0.5 V) reported previously under the same conditions.[54] This indicates that PtRu/C and PtRuCu/C are more efficient to oxidize the CO_{ad} (the poisoning intermediate) than the Pt/C catalyst.

At potentials ≥ 0.55 V, the current was higher for PtRuCu/C than for PtRu/C. However, at high potentials, currents peaked (I_{max}) at 0.55 V and then decreased. The decrease in currents is due to a potential dependence of n_{av} in eq.6.1,[54]

$$I_{lim} = n_{av}FmC \tag{6.1}$$

where *F* is the Faraday constant, *m* is the mass transport coefficient, and *C* is the bulk concentration of ethanol. This dependence arises from changes in product distribution.[36] As known, the main products are CO_2 (n = 12), acetic acid (*n* = 4), and acetaldehyde (*n* = 2). As shown in eq. 6.2,

$$n_{av} = \sum n_i f_i \tag{6.2}$$

where n_{av} is the average number of transferred electrons per ethanol molecule, f_i is the fraction of ethanol converted to a product *I*, and n_i is the number of electrons transferred to form product *i*. This behavior is consistent with literature results for 70% Pt/C and PtRu black where currents peaked and then decreased.[53,54]

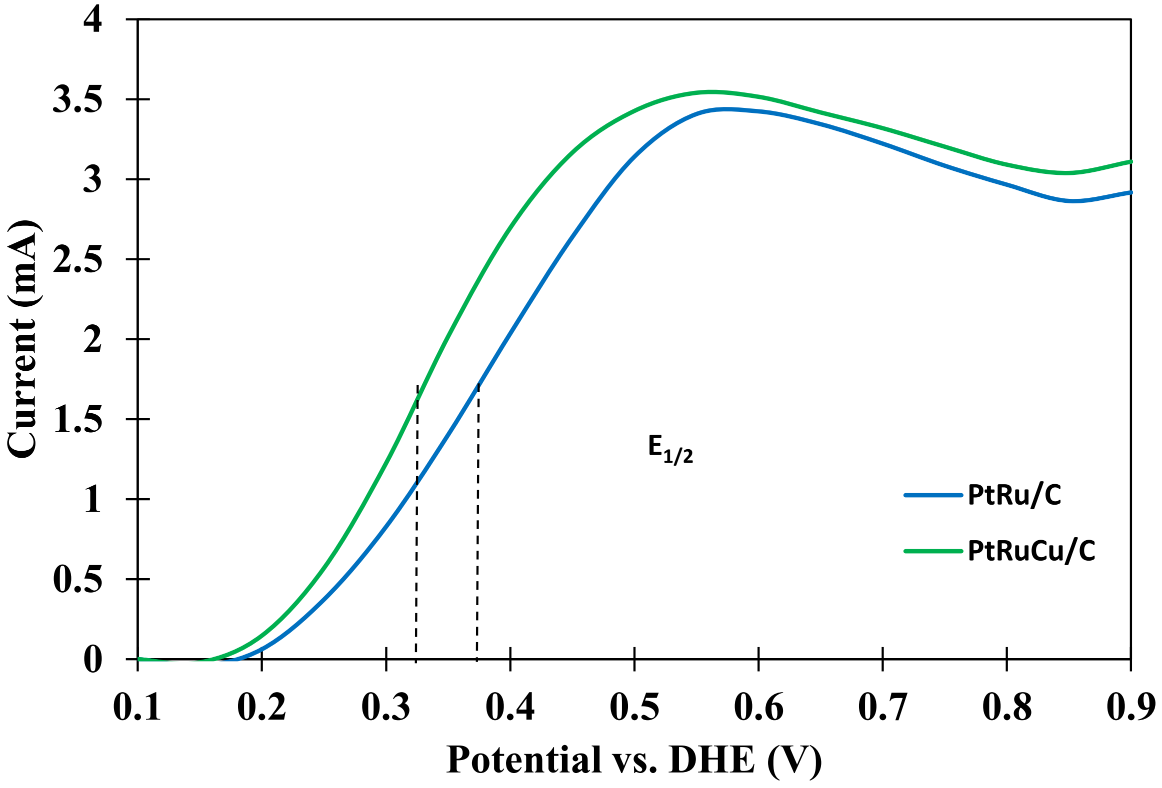

Figure 6.6: Polarization curves for the oxidation of 0.100 M ethanol (0.5 mL min^{-1}) at 80 °C in a nine-anode PEM electrolysis cell in crossover mode at PtRu/C (2 mg cm^{-2}) and PtRuCu/C (2 mg cm^{-2}) anodes.

n_{av} is important to determine the faradaic efficiency of a DEFC. Therefore, by using eq. 6.1 and current from Figure 6.1, n_{av} values were calculated from 0.45 V to 0.9 V. Figure 6.2 shows n_{av} values for PtRu/C and PtRuCu/C. It can be seen that n_{av} decreased at all anodes when the potential was increased from 0.6 V to 0.9 V. At the PtRu/C and PtRuCu/C anodes, n_{av} was between 4.5 to 5.4 at potentials $>$ 0.5 V. PtRuCu/C provided slightly a higher n_{av} relative to the PtRu/C anodes. Since faradaic efficiency is defined as the ratio between the average number of electrons transferred per molecule of ethanol (n_{av}) to the maximum of 12 electrons for the complete oxidation, PtRuCu/C provides higher faradaic efficiency than PtRu/C.

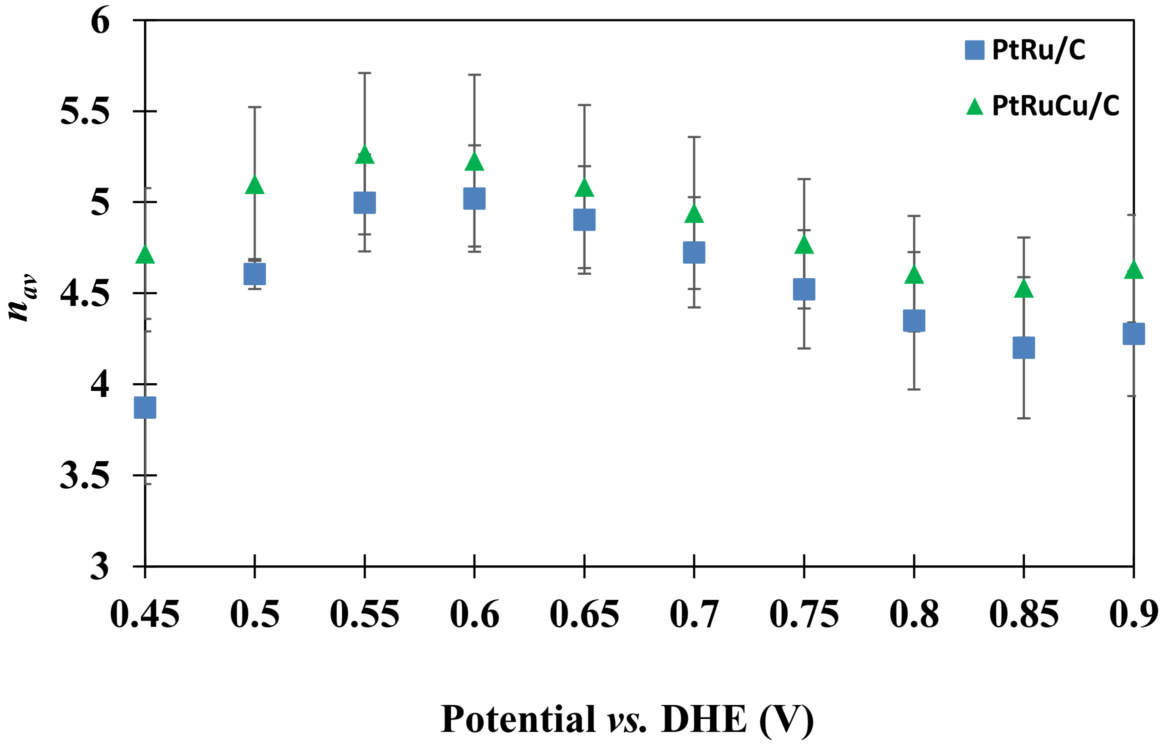

Figure 6.7: n_{av} values from figure 6.5 (eq. 6.1) vs. the potential for the oxidation of 0.100 M ethanol at PtRu/C and PtRuCu/C anodes at 80 °C. Error bars represent standard deviations for each set of three electrodes.

The nine-anode PEM electrolysis cell was also used to measure the faradaic yield of CO_2, as shown in Table 6.3. Three anodes of each catalyst were run at the same time to provide an average value of CO_2 over the last 100 s. As shown in Table 6.3, the faradaic yield of CO_2 was 13% at the PtRu/C anodes. This low amount of CO_2 is consistent with the commercial PtRu catalyst reported by previous studies,[36] indicating that Ru does not have a high ability to break the C-C bond and produce CO_2. Interestingly, PtRuCu/C provided a higher CO_2 yield (26%) relative to PtRu/C. This suggests that Cu decreased poisoning by CO_{ad}.[43,44]

The faradaic yield of acetic acid ($F_{\text{acetic acid}}$) and acetaldehyde ($F_{\text{acetaldehyde}}$) was calculated (eq. 6.3 and 6.4) and listed in Table 6.3.

$$n_{av} = 12/(F_{CO_2} + 3F_{acetic\ acid} + 6F_{acetaldehyde}) \tag{6.3}$$

$$100 = F_{CO_2} + F_{acetic\ acid} + F_{acetaldehyde} \tag{6.4}$$

The negligible faradaic yield of acetaldehyde (6%) at the PtRu/C catalyst is consistent with reported data for PtRu by Altarawneh et al.[36] This can be attributed to the oxidation of acetaldehyde to produce acetic acid (81%). Thus, this result indicates that the PtRu/C catalyst is good for acetic acid production. Furthermore, PtRuCu/C showed lower acetaldehyde production than PtRu/C, indicating that the selectivity is affected by the electronic effect generated by the incorporation of Ru and Cu in the PtRuCu/C catalyst.

Table 6.3: Stoichiometries (n_{av}) and faradaic yields of products (CO_2, acetic acid (AA), acetaldehyde (AAL)) for oxidation of 0.100 M ethanol at 0.5 V in a nine-anode PEM electrolysis cell at 80 °C.

Catalyst	n_{av} (figure 6.7)	CO_2	AA	AAL
PtRu/C	4.6 ± 0.1	13%	81.%	6%
PtRuCu/C	5.1 ± 0.4	26%	72%	2%

6.6 Conclusion

PtRu/C and PtRuCu/C catalysts were prepared by chemical reduction. The PtRuCu/C catalyst showed higher activity toward ethanol oxidation (at high potentials) than the PtRu/C catalyst at ambient temperature in an aqueous acid electrolyte (H_2SO_4 (aq)). When these catalysts were evaluated in a nine-anode proton exchange membrane (PEM) electrolysis cell at 80 ℃, the performance of the PtRuCu/C was slightly higher than PtRu/C at high potentials. This indicates that cyclic voltammetry (CV) is not a good indicator of performance in the PEM electrolysis cell. PtRu/C and PtRuCu/C catalysts decreased the half-wave potentials relative to a commercial 70% Pt/C catalyst reported in the literature.[54] This can be attributed to the ability of Ru to facilitate the bifunctional mechanism (at low potentials) relative to Pt. Interestingly, the faradaic yield of CO_2 was higher for PtRuCu/C (26%) than for PtRu/C (14%), indicating that the presence of Cu enhances the breakage of the C-C bond in ethanol to produce CO_2.

6.7 References

(1) Badwal, S. P. S.; Giddey, S.; Kulkarni, A.; Goel, J.; Basu, S. Direct Ethanol Fuel Cells for Transport and Stationary Applications – A Comprehensive Review. *Appl. Energy* **2015**, *145*, 80–103.

(2) Chu, S.; Majumdar, A. Opportunities and Challenges for a Sustainable Energy Future. *Nature* **2012**, *488*, 294–303.

(3) Ong, B. C.; Kamarudin, S. K.; Basri, S. Direct Liquid Fuel Cells: A Review. *Int. J. Hydrogen Energy* **2017**, *42*, 10142–10157.

(4) Akhairi, M. A. F.; Kamarudin, S. K. Catalysts in Direct Ethanol Fuel Cell (DEFC): An

Overview. *Int. J. Hydrogen Energy* **2016**, *41*, 4214–4228.

(5) Ramachandran, S.; Stimming, U. Well to Wheel Analysis of Low Carbon Alternatives for Road Traffic. *Energy Environ. Sci.* **2015**, *8*, 3313–3324.

(6) Wang, Y.; Zou, S.; Cai, W.-B. Recent Advances on Electro-Oxidation of Ethanol on Pt- and Pd-Based Catalysts: From Reaction Mechanisms to Catalytic Materials. *Catalysts* **2015**, *5*, 1507–1534.

(7) Lai, S. C. S.; Kleijn, S. E. F.; Öztürk, F. T. Z.; van Rees Vellinga, V. C.; Koning, J.; Rodriguez, P.; Koper, M. T. M. Effects of Electrolyte PH and Composition on the Ethanol Electro-Oxidation Reaction. *Catal. Today* **2010**, *154*, 92–104.

(8) Rousseau, S.; Coutanceau, C.; Lamy, C.; Léger, J.-M. Direct Ethanol Fuel Cell (DEFC): Electrical Performances and Reaction Products Distribution under Operating Conditions with Different Platinum-Based Anodes. *J. Power Sources* **2006**, *158*, 18–24.

(9) Friedl, J.; Stimming, U. Model Catalyst Studies on Hydrogen and Ethanol Oxidation for Fuel Cells. *Electrochim. Acta* **2013**, *101*, 41–58.

(10) Richter, J. B.; Eßbach, C.; Senkovska, I.; Kaskel, S.; Brunner, E. Quantitative in Situ 13 C NMR Studies of the Electro-Catalytic Oxidation of Ethanol. *Chem. Commun.* **2019**, *55*, 6042–6045.

(11) Altarawneh, R. M.; Majidi, P.; Pickup, P. G. Determination of the Efficiency of Ethanol Oxidation in a Proton Exchange Membrane Electrolysis Cell. *J. Power Sources* **2017**, *351*, 106–114.

(12) Almeida, T. S.; Kokoh, K. B.; De Andrade, A. R. Effect of Ni on Pt/C and PtSn/C Prepared by the Pechini Method. *Int. J. Hydrogen Energy* **2011**, *36*, 3803–3810.

(13) Corradini, P. G.; Santos, N. A.; Perez, J. Pt-Sn-Eu/C Catalysts: Application of Rare Earth Metals as Anodes in Direct Ethanol Fuel Cells. *Fuel Cells* **2018**, *18*, 73–81.

(14) Kavanagh, R.; Cao, X.-M.; Lin, W.-F.; Hardacre, C.; Hu, P. Origin of Low CO_2 Selectivity on Platinum in the Direct Ethanol Fuel Cell. *Angew. Chemie Int. Ed.* **2012**, *51*, 1572–1575.

(15) Zheng, Y.; Wan, X.; Cheng, X.; Cheng, K.; Dai, Z.; Liu, Z. Advanced Catalytic Materials for Ethanol Oxidation in Direct Ethanol Fuel Cells. *Catalysts* **2020**, *10*, 166.

(16) Ren, X.; Lv, Q.; Liu, L.; Liu, B.; Wang, Y.; Liu, A.; Wu, G. Current Progress of Pt and Pt-Based Electrocatalysts Used for Fuel Cells. *Sustain. Energy Fuels* **2020**, *4*, 15–30.

(17) Beyhan, S.; Léger, J.-M.; Kadırgan, F. Pronounced Synergetic Effect of the Nano-Sized PtSnNi/C Catalyst for Ethanol Oxidation in Direct Ethanol Fuel Cell. *Appl. Catal. B Environ.* **2013**, *130–131*, 305–313.

(18) Soundararajan, D.; Park, J. H.; Kim, K. H.; Ko, J. M. Pt–Ni Alloy Nanoparticles Supported on CNF as Catalyst for Direct Ethanol Fuel Cells. *Curr. Appl. Phys.* **2012**, *12*, 854–859.

(19) Sulaiman, J. E.; Zhu, S.; Xing, Z.; Chang, Q.; Shao, M. Pt–Ni Octahedra as Electrocatalysts for the Ethanol Electro-Oxidation Reaction. *ACS Catal.* **2017**, *7*, 5134–5141.

(20) Wang, H.-F.; Liu, Z.-P. Comprehensive Mechanism and Structure-Sensitivity of Ethanol Oxidation on Platinum: New Transition-State Searching Method for Resolving the Complex Reaction Network. *J. Am. Chem. Soc.* **2008**, *130*, 10996–11004.

(21) Li, D.; Wang, C.; Strmcnik, D. S.; Tripkovic, D. V.; Sun, X.; Kang, Y.; Chi, M.; Snyder, J. D.; van der Vliet, D.; Tsai, Y.; Stamenkovic, V. R.; Sun, S.; Markovic, N. M. Functional Links between Pt Single Crystal Morphology and Nanoparticles with Different Size and Shape: The Oxygen Reduction Reaction Case. *Energy Environ. Sci.* **2014**, *7*, 4061–4069.

(22) Hao, Y.; Wang, X.; Shen, J.; Yuan, J.; Wang, A.-J.; Niu, L.; Huang, S. One-Pot Synthesis of Single-Crystal Pt Nanoplates Uniformly Deposited on Reduced Graphene Oxide, and Their High Activity and Stability on the Electrocalalytic Oxidation of Methanol. *Nanotechnology* **2016**, *27*, 145602.

(23) Huang, M.; Jiang, Y.; Jin, C.; Ren, J.; Zhou, Z.; Guan, L. Pt–Cu Alloy with High Density of Surface Pt Defects for Efficient Catalysis of Breaking C–C Bond in Ethanol. *Electrochim. Acta* **2014**, *125*, 29–37.

(24) Ammam, M.; Easton, E. B. PtCu/C and Pt(Cu)/C Catalysts: Synthesis, Characterization and Catalytic Activity towards Ethanol Electrooxidation. *J. Power Sources* **2013**, *222*, 79–87.

(25) Altarawneh, R. M.; Brueckner, T. M.; Chen, B.; Pickup, P. G. Product Distributions and Efficiencies for Ethanol Oxidation at PtNi Octahedra. *J. Power Sources* **2018**, *400*, 369–376.

(26) Nakamura, M.; Imai, R.; Otsuka, N.; Hoshi, N.; Sakata, O. Ethanol Oxidation on Well-Ordered PtSn Surface Alloy on Pt(111) Electrode. *J. Phys. Chem. C* **2013**, *117* (35), 18139–18143.

(27) Antolini, E. Pt-Ni and Pt-M-Ni (M = Ru, Sn) Anode Catalysts for Low-Temperature Acidic Direct Alcohol Fuel Cells: A Review. *Energies* **2017**, *10*, 42.

(28) Alqdeimat, D.; Pickup, P. G. $PtNi_x/C$ Catalysts for Improved Performance in Ethanol Fuel Cells. *ECS Trans.* **2020**, *97*, 893–900.

(29) Fujiwara, N.; Friedrich, K. A.; Stimming, U. Ethanol Oxidation on PtRu Electrodes Studied by Differential Electrochemical Mass Spectrometry. *J. Electroanal. Chem.* **1999**, *472*, 120–125.

(30) Rodríguez-Gómez, A.; Dorado, F.; de Lucas-Consuegra, A.; de la Osa, A. R. Influence of Pt/Ru Anodic Ratio on the Valorization of Ethanol by PEM Electrocatalytic Reforming towards Value-Added Products. *J. Energy Chem.* **2021**, *56*, 264–275.

(31) Spinacé, E. .; Neto, A. .; Linardi, M. Electro-Oxidation of Methanol and Ethanol Using PtRu/C Electrocatalysts Prepared by Spontaneous Deposition of Platinum on Carbon-Supported Ruthenium Nanoparticles. *J. Power Sources* **2004**, *129*, 121–126.

(32) Colmati, F.; Antolini, E.; Gonzalez, E. R. Effect of Temperature on the Mechanism of Ethanol Oxidation on Carbon Supported Pt, PtRu and Pt_3Sn Electrocatalysts. *J. Power Sources* **2006**, *157*, 98–103.

(33) El Sawy, E. N.; Brueckner, T. M.; Pickup, P. G. Electrochemical Oxidation of Methanol and Ethanol at Rh@Pt and Ru@Pt Catalysts. *J. Electrochem. Soc.* **2020**, *167*, 106507.

(34) Camara, G. ; de Lima, R. ; Iwasita, T. Catalysis of Ethanol Electrooxidation by PtRu: The Influence of Catalyst Composition. *Electrochem. Commun.* **2004**, *6*, 812–815.

(35) Ali, A. H.; Pickup, P. G. Electrolysis of Ethanol and Methanol at PtRu@Pt Catalysts. *J. Electrochem. Soc.* **2022**, *169*, 034523.

(36) Altarawneh, R. M.; Pickup, P. G. Product Distributions and Efficiencies for Ethanol Oxidation in a Proton Exchange Membrane Electrolysis Cell. *J. Electrochem. Soc.* **2017**, *164*, F861–F865.

(37) Zhou, W. Pt Based Anode Catalysts for Direct Ethanol Fuel Cells. *Appl. Catal. B Environ.* **2003**, *46*, 273–285.

(38) Zhou, W. J.; Li, W. Z.; Song, S. Q.; Zhou, Z. H.; Jiang, L. H.; Sun, G. Q.; Xin, Q.; Poulianitis, K.; Kontou, S.; Tsiakaras, P. Bi- and Tri-Metallic Pt-Based Anode Catalysts for Direct Ethanol Fuel Cells. *J. Power Sources* **2004**, *131*, 217–223.

(39) Oliveira Neto, A.; Franco, E. G.; Aricó, E.; Linardi, M.; Gonzalez, E. R. Electro-Oxidation of Methanol and Ethanol on Pt–Ru/C and Pt–Ru–Mo/C Electrocatalysts Prepared by Bönnemann's Method. *J. Eur. Ceram. Soc.* **2003**, *23*, 2987–2992.

(40) Zhao, L.; Mitsushima, S.; Ishihara, A.; Matsuzawa, K.; Ota, K. Pt-Ir-SnO_2/C Electrocatalysts for Ethanol Oxidation in Acidic Media. *Chinese J. Catal.* **2011**, *32*, 1856–1863.

(41) Li, G.; Pickup, P. G. The Promoting Effect of Pb on Carbon Supported Pt and Pt/Ru

Catalysts for Electro-Oxidation of Ethanol. *Electrochim. Acta* **2006**, *52*, 1033–1037.

(42) Ribadeneira, E.; Hoyos, B. A. Evaluation of Pt–Ru–Ni and Pt–Sn–Ni Catalysts as Anodes in Direct Ethanol Fuel Cells. *J. Power Sources* **2008**, *180*, 238–242.

(43) Magalhães, M. M.; Gomes, J. F.; Tremiliosi-Filho, G.; de Figueiredo, P. B. S.; de Lima, R. B.; Colmati, F. Ethanol Electro-Oxidation on Carbon-Supported Pt_3Sn/C, Pt_3Cu/C and PtSnCu/C Catalysts: CV and in Situ FTIR Study. *J. Appl. Electrochem.* **2021**, *51*, 173–181.

(44) Han, S.; Liu, H.; Chen, P.; Jiang, J.; Chen, Y. Porous Trimetallic PtRhCu Cubic Nanoboxes for Ethanol Electrooxidation. *Adv. Energy Mater.* **2018**, *8*, 1801326.

(45) Chen, C.; Xu, H.; Shang, H.; Jin, L.; Song, T.; Wang, C.; Gao, F.; Zhang, Y.; Du, Y. Ultrafine PtCuRh Nanowire Catalysts with Alleviated Poisoning Effect for Efficient Ethanol Oxidation. *Nanoscale* **2019**, *11*, 20090–20095.

(46) Barroso, J.; Pierna, A. R.; Blanco, T. C.; Ruiz, N. Trimetallic Amorphous Catalyst with Low Amount of Platinum: Comparative Study for Ethanol, Bioethanol and CO Electrooxidation. *Int. J. Hydrogen Energy* **2014**, *39*, 3984–3990.

(47) Chen, B.; Brueckner, T. M.; Altarawneh, R. M.; Pickup, P. G. Composition Dependence of Ethanol Oxidation at Ruthenium-Tin Oxide/Carbon Supported Platinum Catalysts. *J. Electrochem. Soc.* **2018**, *165*, J3019–J3025.

(48) Pickup, P. G.; Hang, H. (Invited) Pt/Metal Oxide/Ti and Pt/Metal Oxide/Carbon Composite Films for Ethanol Oxidation. *ECS Trans.* **2020**, *97*, 837–844.

(49) Xue, S.; Deng, W.; Yang, F.; Yang, J.; Amiinu, I. S.; He, D.; Tang, H.; Mu, S. Hexapod PtRuCu Nanocrystalline Alloy for Highly Efficient and Stable Methanol Oxidation. *ACS Catal.* **2018**, *8*, 7578–7584.

(50) Petkov, V.; Maswadeh, Y.; Vargas, J. A.; Shan, S.; Kareem, H.; Wu, Z.-P.; Luo, J.; Zhong, C.-J.; Shastri, S.; Kenesei, P. Deviations from Vegard’s Law and Evolution of the

Electrocatalytic Activity and Stability of Pt-Based Nanoalloys inside Fuel Cells by in Operando X-Ray Spectroscopy and Total Scattering. *Nanoscale* **2019**, *11*, 5512–5525.

(51) dos Santos, M. C.; Parreira, L. S.; De Moura Souza, F.; Camargo Junior, J.; Gentil, T. Fuel Cells: Hydrogen and Ethanol Technologies. In *Reference Module in Materials Science and Materials Engineering*; Elsevier, 2017.

(52) Sun, S.; Halseid, M. C.; Heinen, M.; Jusys, Z.; Behm, R. J. Ethanol Electrooxidation on a Carbon-Supported Pt Catalyst at Elevated Temperature and Pressure: A High-Temperature/High-Pressure DEMS Study. *J. Power Sources* **2009**, *190*, 2–13.

(53) Brueckner, T. M.; Wheeler, E.; Chen, B.; Sawy, E. N. El; Pickup, P. G. Screening of Catalysts for the Electrochemical Oxidation of Organic Fuels in A Multi-Anode Proton Exchange Membrane Cell. *J. Electrochem. Soc.* **2019**, *166*, F942–F948.

(54) Brueckner, T. M.; Pickup, P. G. Kinetics and Stoichiometry of Methanol and Ethanol Oxidation in Multi-Anode Proton Exchange Membrane Cells. *J. Electrochem. Soc.* **2017**, *164*, F1172–F1178.

Chapter 7

7. Summary and Future Work

7.1 $PtNi_x/C$ catalysts for the ethanol oxidation reaction

Based on cyclic voltammetry at ambient temperature, a PtNi catalyst prepared in the presence of propylene glycol ($PtNi_{0.62}/C$(PG)) was more active toward the ethanol oxidation reaction (EOR) than one prepared in ethylene glycol ($PtNi_{0.50}/C$(EG)). Also, it was found that removing the Ni from the catalyst surface with acid treatment affects the activity of catalysts toward the EOR at ambient temperature. It increased the activity of $PtNi_{0.62}/C$(PG) significantly, while the activity of the $PtNi_{0.50}/C$(EG) was enhanced slightly. It was revealed that treatment of these catalysts with acetic acid not only removed Ni from the surface but also produced a core shell-like structure (PtNi@Pt). Based on the literature, the activity of a core-shell catalyst is affected by the Pt shell thickness and the metal core ratio.[1] Therefore, the difference in the activity at $PtNi_{0.62}/C$(PG) and $PtNi_{0.50}/C$(EG) catalysts after the treatment can be attributed to the differences in the Ni to Pt ratio at the core for both catalysts. The $PtNi_{0.62}/C$(PG) catalyst had a higher Ni to Pt ratio at the core than the $PtNi_{0.50}/C$(EG) catalyst. As a result, a larger electronic effect and/or compressive effect from the Ni was generated.

Furthermore, the effect of removing Ni from the catalyst surface with acid treatment on the catalyst performance was investigated at 80 °C for the EOR. A nine-anode PEM electrolysis cell was used to evaluate the performance and the production of CO_2 at the PtNi catalysts. It was noticed that when Ni was removed from the catalyst surface with acetic acid, the activity increased slightly for all of the $PtNi_{0.62}/C$(PG) and $PtNi_{0.50}/C$(EG) catalysts. Cyclic voltammetry revealed a considerable increase in activity at the $PtNi_{0.62}/C$(PG) catalyst following treatment, however, this was not seen in the PEM experiment. This indicates that cyclic voltammetry is not a good indicator of performance in the PEM electrolysis cell.[1] Interestingly, the acid treatment of $PtNi_{0.62}/C$(PG) and $PtNi_{0.50}/C$(EG) enhanced the production of CO_2, which indicates that the structure of the catalyst (core-shell-like structure) affects the breaking of the C-C bond in ethanol. Unfortunately, our study showed that Ni as a second metal does not impact the performance at low potentials.

Based on the literature, PtNi catalysts can be developed by several methods. First, the preparation of ternary PtNiM catalysts (where M is Ru, Cu, or Rh) could be a good way to study how the incorporation of M into PtNi would affect the performance and selectivity of the catalyst.[2,3] In addition, the deposition of Pt onto the PtNi surface to prepare a core-shell catalyst (PtNi@Pt) would enhance the performance and the breaking of the C-C bond.[1]

7.2 Screening of commercial catalysts in a nine-anode proton exchange membrane electrolysis cell for the ethanol oxidation reaction

Understanding the effect of alloying Pt with a second metal is a significant step because we can know how to develop an anode catalyst for DEFCs. Therefore, we evaluated commercial catalysts (20% PtCu/C, 40% PtNi/C, and 40% PtFe/C) in a nine-anode PEM electrolysis cell at 80 ℃. We found that 20% PtCu/C had more activity toward the oxidation of ethanol than 40% PtNi/C and 40% PtFe/C, at high potentials. However, none of these catalysts showed high performance at low potentials relative to Pt, indicating the slow kinetics of these catalysts. On the other hand, the faradaic yield of CO_2 was higher for 20% PtCu/C (66%) than for 40% PtNi/C (45%) and 40% PtFe/C (55%), suggesting that the presence of Cu enhances the breakage of the C-C bond in ethanol to produce CO_2.

As a next step, we should prepare binary and ternary catalysts with Cu and study the effect of the incorporation of Cu on the EOR and the production of CO_2. Also, it would be interesting to carry out a computational study to investigate how each metal (Cu, Ni, and Fe) would affect the breaking of the C-C bond.[41]

7.3 Ethanol electro-oxidation on a carbon-supported PtRuCu/C catalyst in a nine-anode proton exchange membrane electrolysis cell

The incorporation of Cu with Pt and Ru (PtRuCu/C) showed higher activity toward ethanol oxidation (at high potentials) than PtRu/C at ambient temperature in an aqueous acid electrolyte (H_2SO_4 (aq)). In a nine-anode PEM electrolysis cell at 80 ℃, the performance of PtRuCu/C (at high potentials) was slightly higher than PtRu/C. PtRu/C and PtRuCu/C catalysts decreased the half-wave potentials relative to a commercial 70% Pt/C catalyst reported in the literature. This decrease can be attributed to the ability of Ru to facilitate the bifunctional mechanism (at low potentials) relative to Pt. The faradaic yield of CO_2 was higher for PtRuCu/C (26%) than for PtRu/C (14%), indicating that the presence of Cu with Ru in PtRuCu/C enhances the breakage of the C-C bond in ethanol to produce CO_2. As shown in the literature, PtRu produces mainly acetic acid at all potentials, so by incorporating Cu with Ru the production of acetic acid will decrease and the PtRuCu catalyst will be more suitable for a DEFC.

In future work, further characterization is needed for PtRu/C and PtRuCu/C such as XPS and TEM analysis. Also, a 5 cm^2 PEM electrolysis cell should be used to study the product distribution and efficiency for PtRu/C and PtRuCu/C catalysts. Studying the product distribution is very important because in some cases two catalysts might have similar performance at low potentials but they have different CO_2 production.[5] Moreover, it is important to prepare ternary $PtRu_xCu_y/C$ alloy catalysts and core-shell structures (PtRuCu@Pt) with different Ru:Cu atomic ratios, and investigate the effect of Cu amount on the performance and selectivity of CO_2 production. Also, we can explore the effect of Ru:Cu ratios on the stoichiometry (n_{av}) of ethanol oxidation.

In conclusion, the preparation of anode catalysts is challenging because it is not easy to find a catalyst that can increase both the faradaic and potential efficiencies. But based on our results and previous studies, we can confirm that Ru is the best metal that can enhance the potential efficiency of the DEFC, and Cu is a good metal to break the C-C bond.

7.4 References

(1) El Sawy, E. N.; Brueckner, T. M.; Pickup, P. G. Electrochemical Oxidation of Methanol and Ethanol at Rh@Pt and Ru@Pt Catalysts. *J. Electrochem. Soc.* **2020**, *167*, 106507.

(2) Yaqoob, L.; Noor, T.; Iqbal, N. A Comprehensive and Critical Review of the Recent Progress in Electrocatalysts for the Ethanol Oxidation Reaction. *RSC Adv.* **2021**, *11*, 16768–16804.

(3) Erini, N.; Rudi, S.; Beermann, V.; Krause, P.; Yang, R.; Huang, Y.; Strasser, P. Exceptional Activity of a Pt-Rh-Ni Ternary Nanostructured Catalyst for the Electrochemical Oxidation of Ethanol. *ChemElectroChem* **2015**, *2*, 903–908.

(4) Yan, S.-Y.; Huang, Y.-R.; Yang, C.-Y.; Liu, C.-W.; Wang, J.-H.; Wang, K.-W. Enhanced Activity of Ethanol Oxidation Reaction on PtM (M=Au, Ag and Sn): The Importance of Oxophilicity and Surface Oxygen Containing Species. *Electrochim. Acta* **2018**, *259*, 733–741.

(5) Altarawneh, R. M.; Brueckner, T. M.; Chen, B.; Pickup, P. G. Product Distributions and

Efficiencies for Ethanol Oxidation at PtNi Octahedra. *J. Power Sources* **2018**, *400*, 369–376.

Appendix

Appendix A

Table A.1: Chemicals and materials were used.

Chemical/Material	Description	Company
Propylene glycol	99.5%	Sigma-Aldrich
Ethylene glycol	90%-100%	Sigma-Aldrich
Dihydrogen hexachloroplatinate(IV) hexahydrate	$H_2PtCl_6 \cdot 6\ H_2O$	Pressure Chemical Co.
Nickel chloride	$NiCl_2$	Fisher Scientific
Carbon black	Vulcan XC-72	Cabot
Acetone	------	Caledon Laboratory Chemicals
Sodium hydroxide	NaOH	BDH chemicals
Acetic acid	CH_3COOH, 99.7%	Caledon Lab. Chemicals
Ruthenium(III) chloride trihydrate	$RuCl_3.3H_2O$, 99%	Sigma-Aldrich
Copper sulfate pentahydrate	$CuSO_4.5H_2O$	Fisher Scientific
Sodium borohydride	$NaBH_4$	BDH Chemicals
Sodium acetate	C_2H_3NaO	BDH Chemicals
Carbon supported 40% PtNi	nominally 3:1 Pt:Ni	Fuel Cell Store
Carbon supported 40% PtNi	1:1 atomic ratio	Premetek Co.
Carbon supported 40% PtFe	1:1 atomic ratio	Premetek Co.
Carbon supported 20% PtCu	1:1 atomic ratio	Premetek Co.
Carbon supported Pt	70%, HiSPEC™ 13100, 3.5 nm	Alfa Aesar
Nafion solution	5%	DuPont
Anhydrous ethanol	100%	Commercial Alcohols Inc.
2-Propanol	------	Caledon
1-Propanol	99.9%	Caledon
Sulfuric acid	------	Fisher Scientific

Nafion™ 117 membranes	7 mL thick	Ion Power, Inc.
Commercial Pt cathodes	4 mg cm^{-2} of Pt black on non-wet-proofed Toray^{TM} CFP	Ballard Power Systems
Industrial grade nitrogen	Ultra high purity	Air Liquide
Hydrogen peroxide	30%	ACP Chemicals Inc
Alumina polishing suspension	0.3 Micron	Sturbridge Metallurgical Services, Ltd.
Micro cloth polishing	--------	BUEHLER

I. Chemical yield of CO_2

The chemical yield of CO_2 is calculated as shown in eq. A1,

$$\text{the chemical yield of } CO_2 = \frac{(exoperimental\ rate\ of\ CO_2 \times time\ (s))/2}{mole\ of\ ethanol\ consumed} \qquad (A1)$$

where the mole of ethanol consumed is obtained from NMR.

II. Concentration of acetaldehyde

The concentration of acetaldehyde (AAL) was determined by its NMR according to eq. A2,

$$AAL\ concentration = \frac{normalized\ area\ for\ AAL \times standard\ concentration}{normalized\ are\ for\ standard} \qquad (A2)$$

III. Faradaic yield of acetic acid and acetaldehyde

The faradaic yield of acetic acid and acetaldehyde are calculated by eq. A3,

$$faradaic\ yield = \frac{C_A u}{IFn} \tag{A3}$$

where C_A is the concentration in mM obtained from NMR, u is the flow rate of ethanol (mL s^{-1}), I is the measured current (mA), F is the Faraday constant, and *n* is the number of electrons transferred to form acetic acid ($n = 4$) and acetaldehyde ($n = 2$).

Appendix B

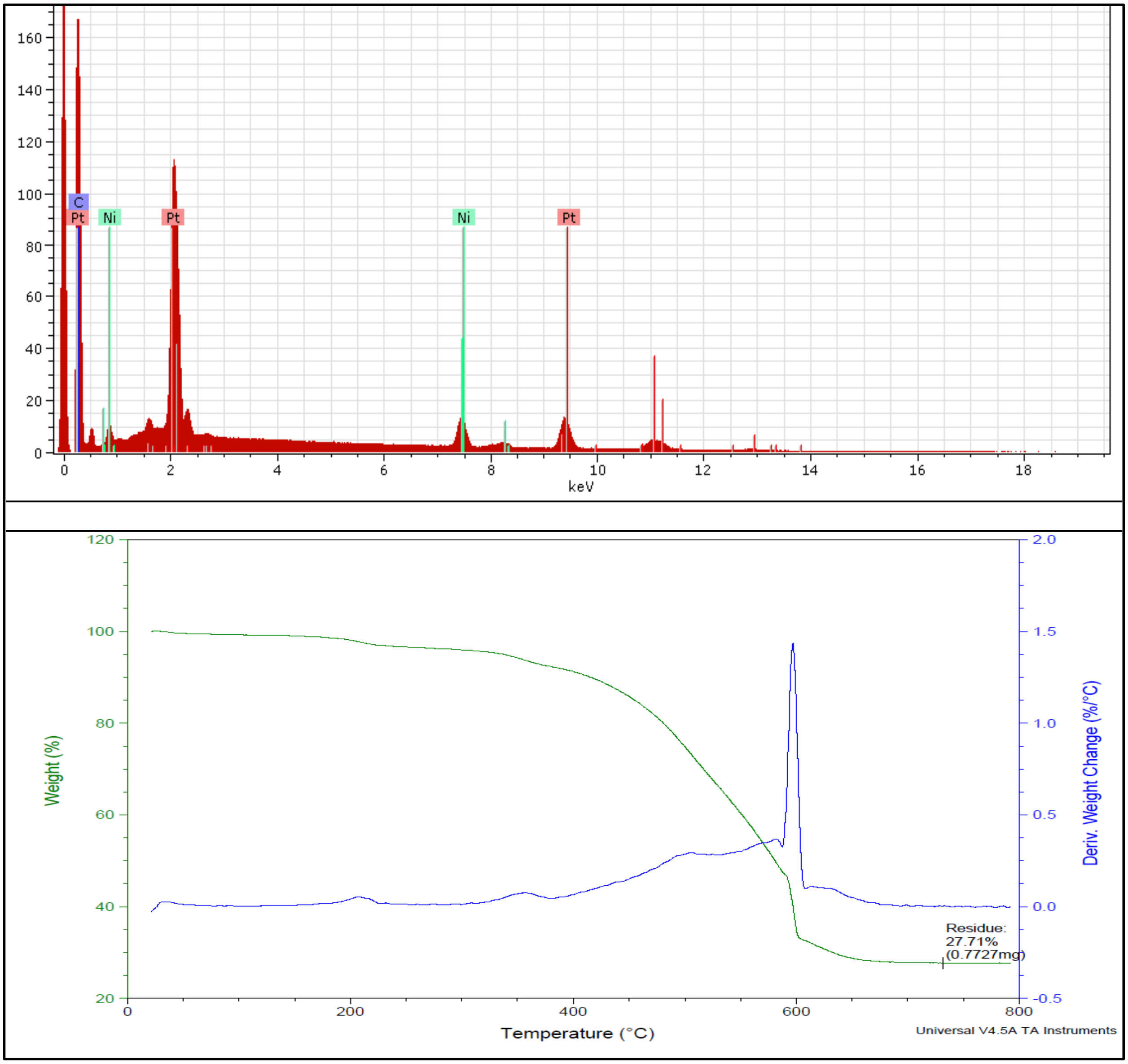

Figure B.1: TGA and EDX analysis for $PtNi_{0.62}/C(PG)$.

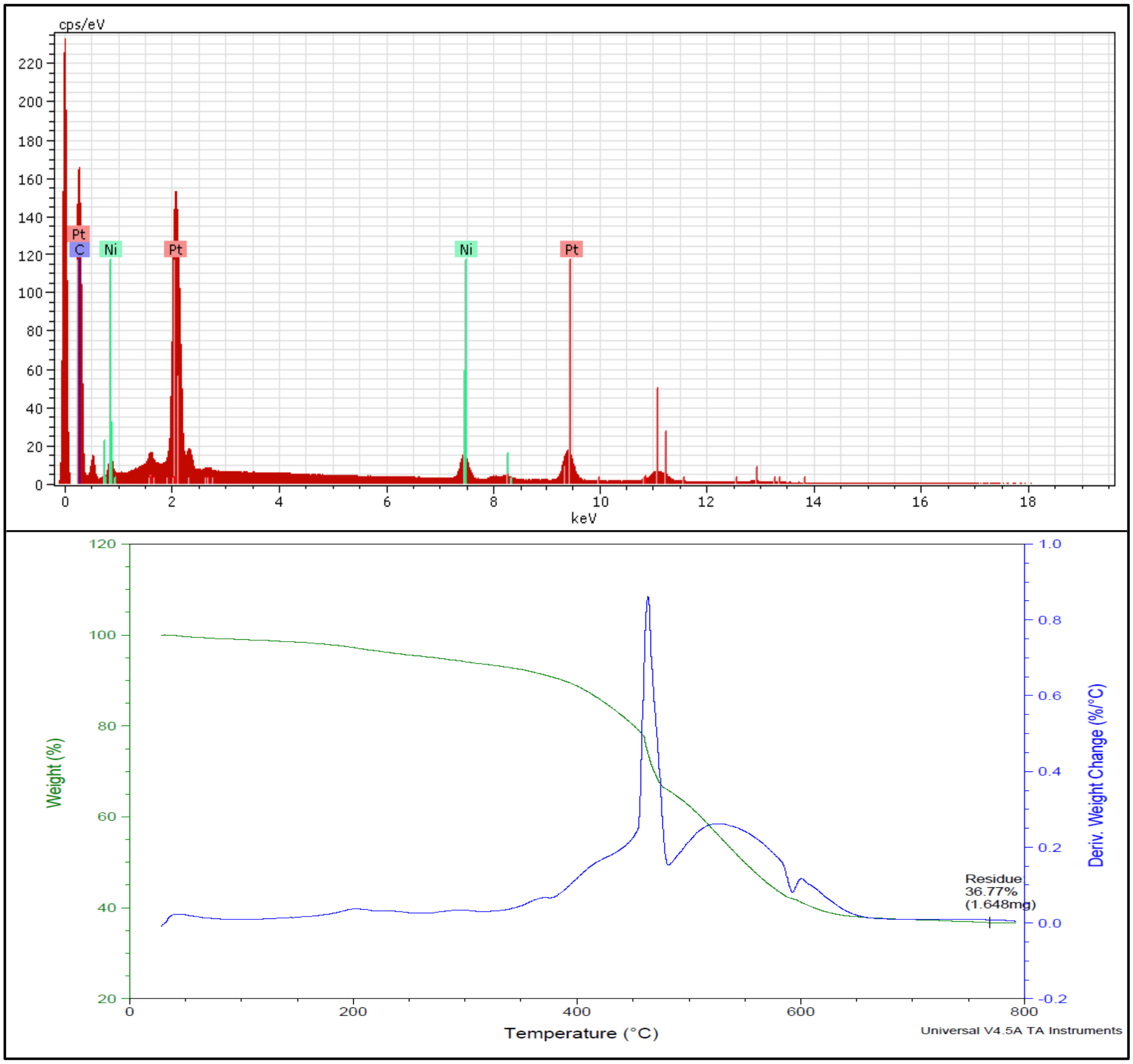

Figure B.2: TGA and EDX analysis for $PtNi_{0.50}/C(EG)$.

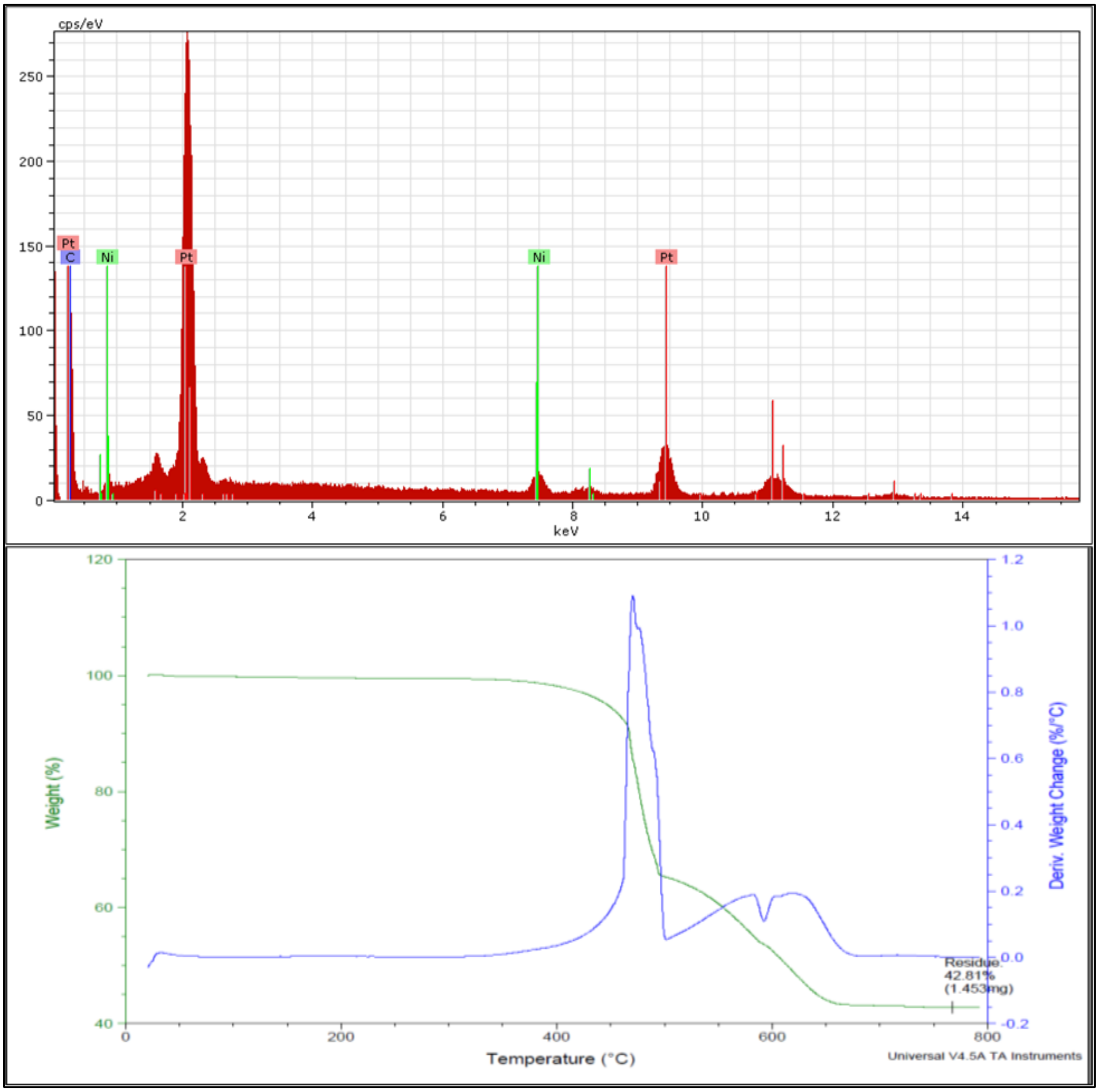

Figure B.3: TGA and EDX analysis for commercial $PtNi_{0.26}/C$.

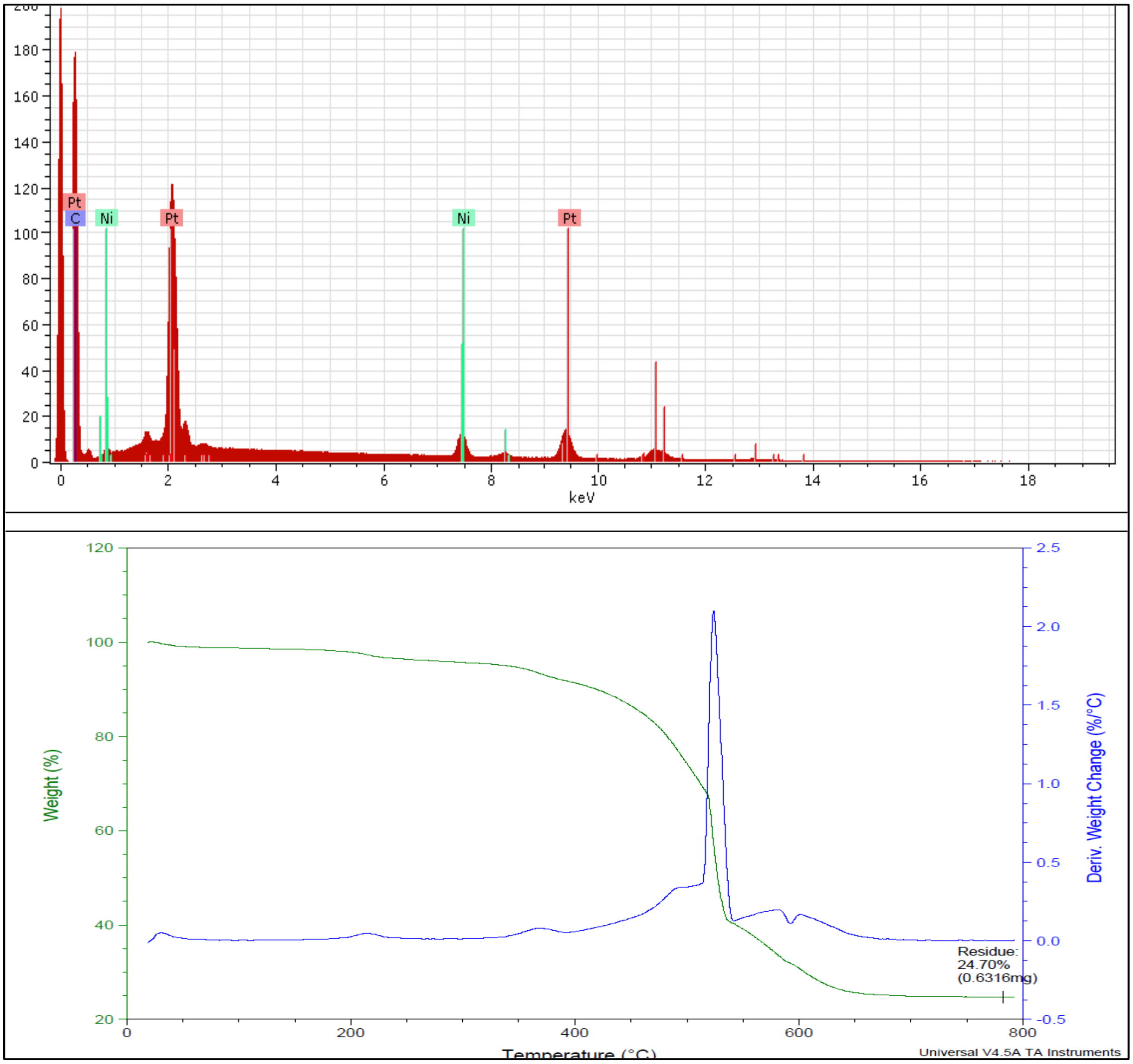

Figure B.4: TGA and EDX analysis for $PtNi_{0.48}/C(PG)^{AA}$.

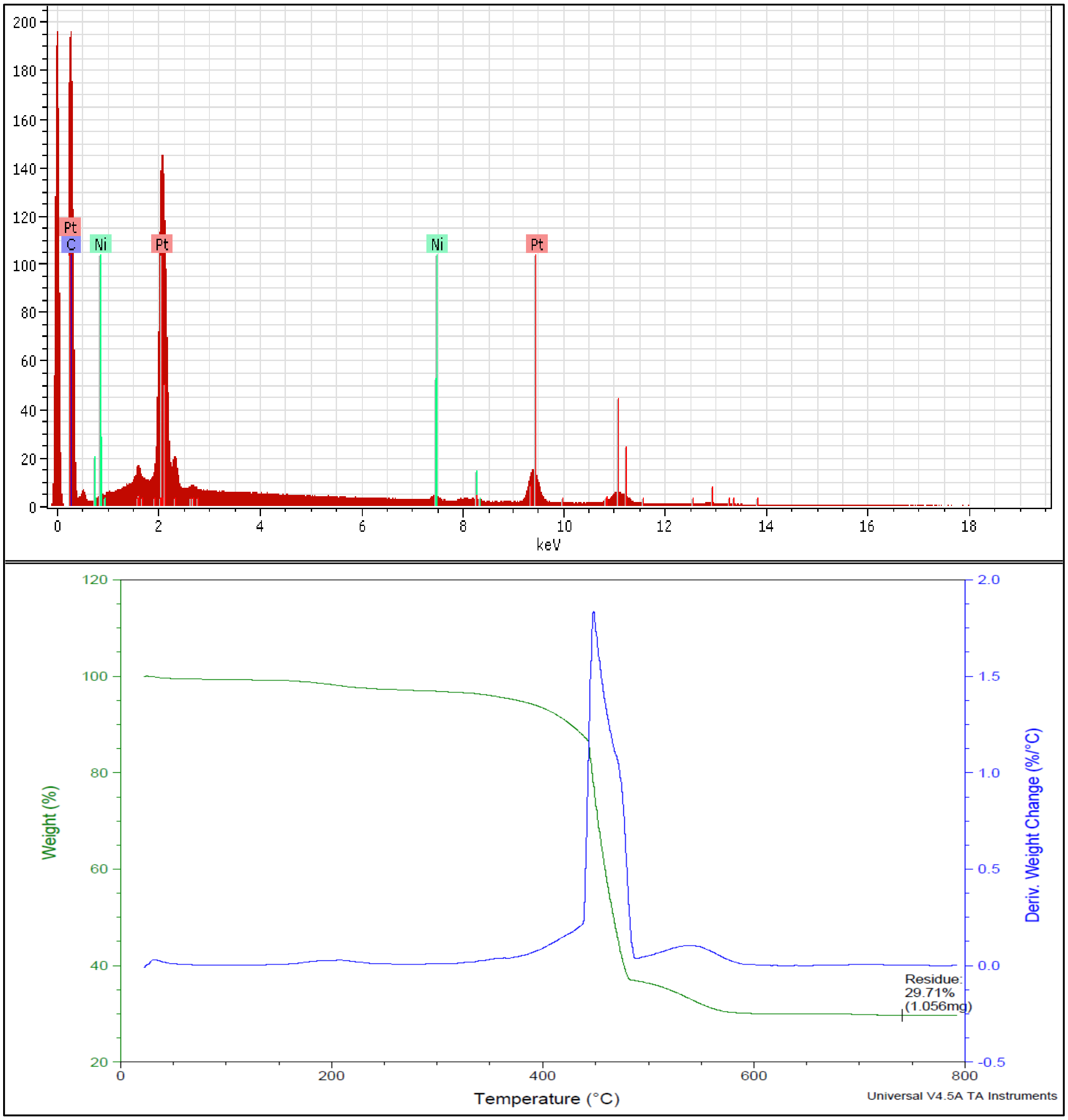

Figure B.5: TGA and EDX analysis for PtNi$_{0.08}$/C(EG)^{AA}.

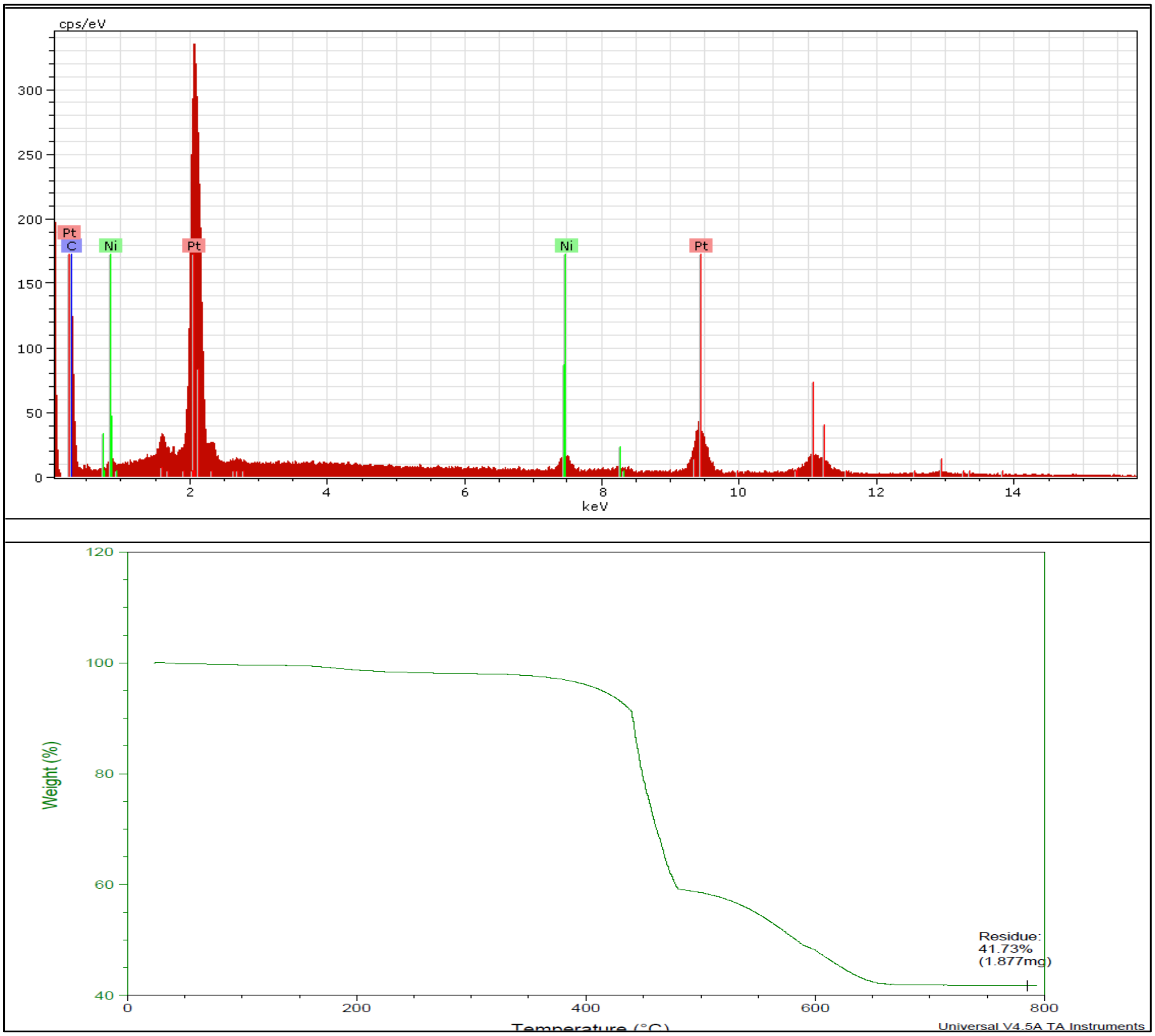

Figure B.6: TGA and EDX analysis for $PtNi_{0.22}/C^{AA}$.

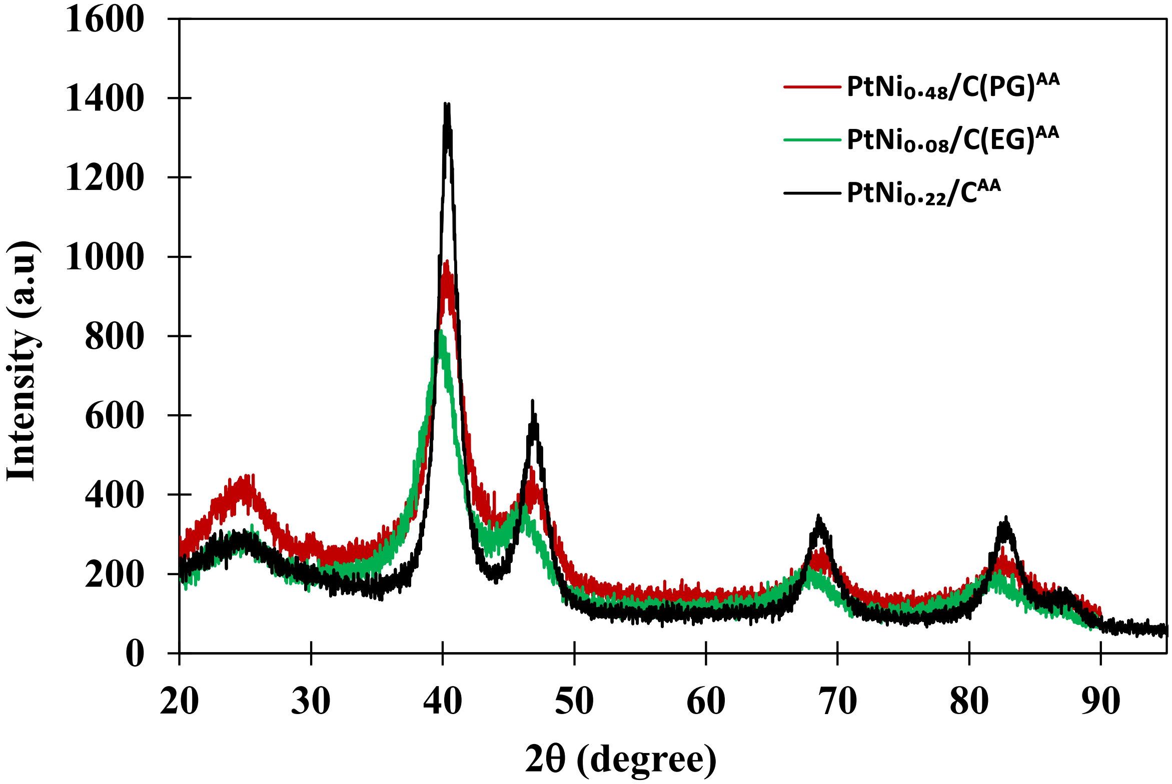

Figure B.7: The X-ray diffraction pattern of $PtNi_{0.48}/C(PG)^{AA}$, $PtNi_{0.08}/C(EG)^{AA}$, and $PtNi_{0.22}/C^{AA}$ catalysts.

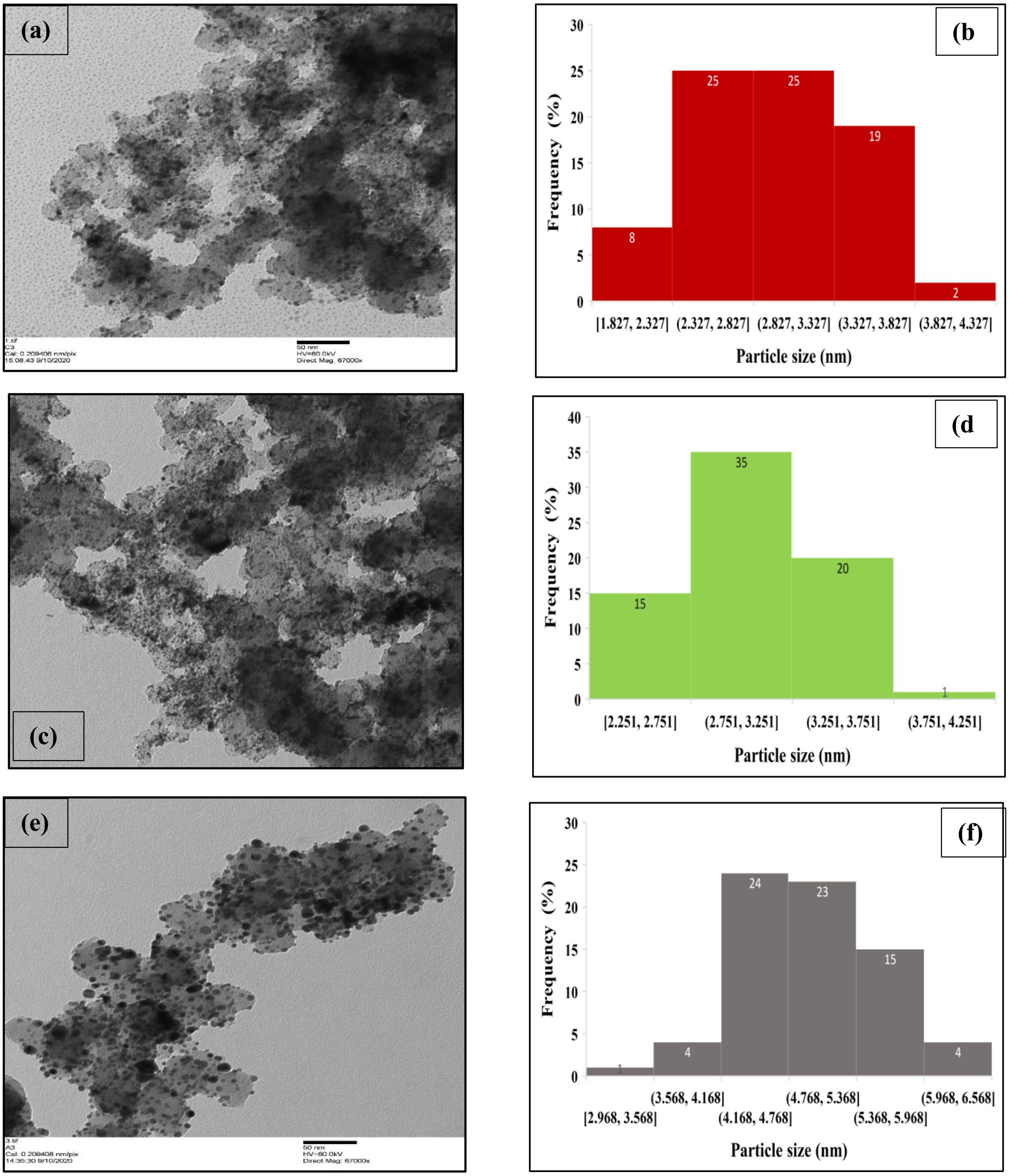

Figure B.8: TEM images of (a) $PtNi_{0.48}/C(PG)^{AA}$, (c) $PtNi_{0.08}/C(EG)^{AA}$, and (e) $PtNi_{0.22}/C^{AA}$ and histogram of (b) $PtNi_{0.48}/C(PG)^{AA}$, (d) $PtNi_{0.08}/C(EG)^{AA}$, and (f) $PtNi_{0.22}/C^{AA}$.

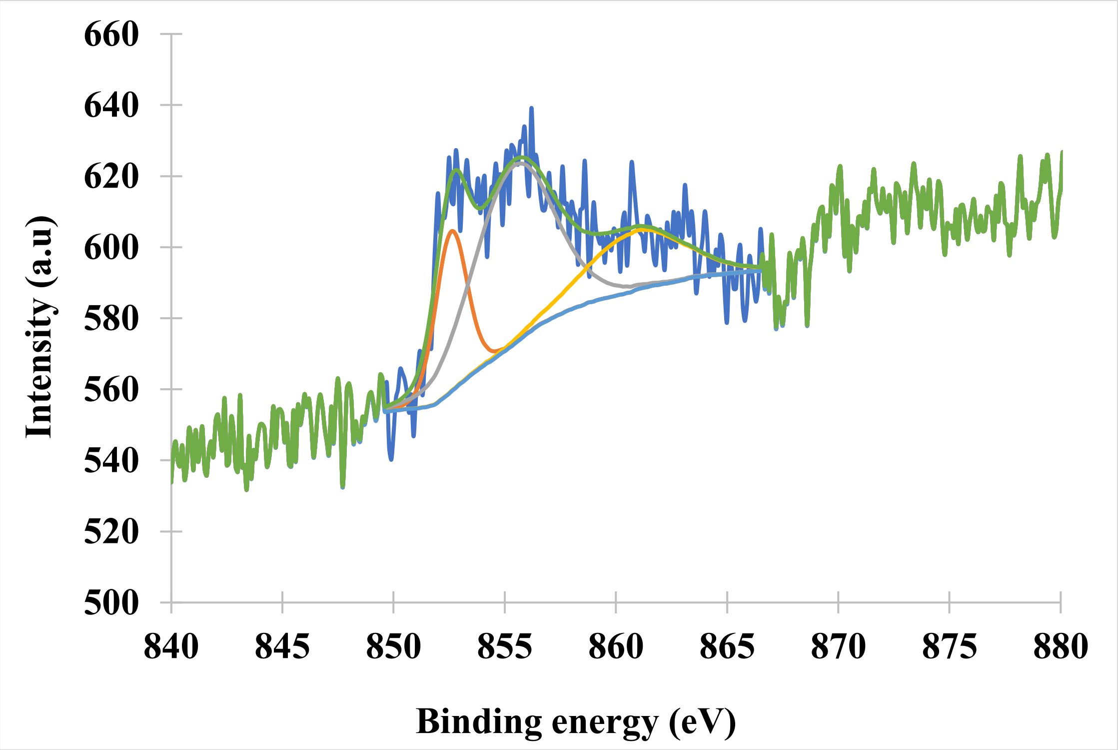

Figure B.9: The deconvolution of Ni $2p_{3/2}$ peak for the commercial $PtNi_{0.26}/C$ catalyst.

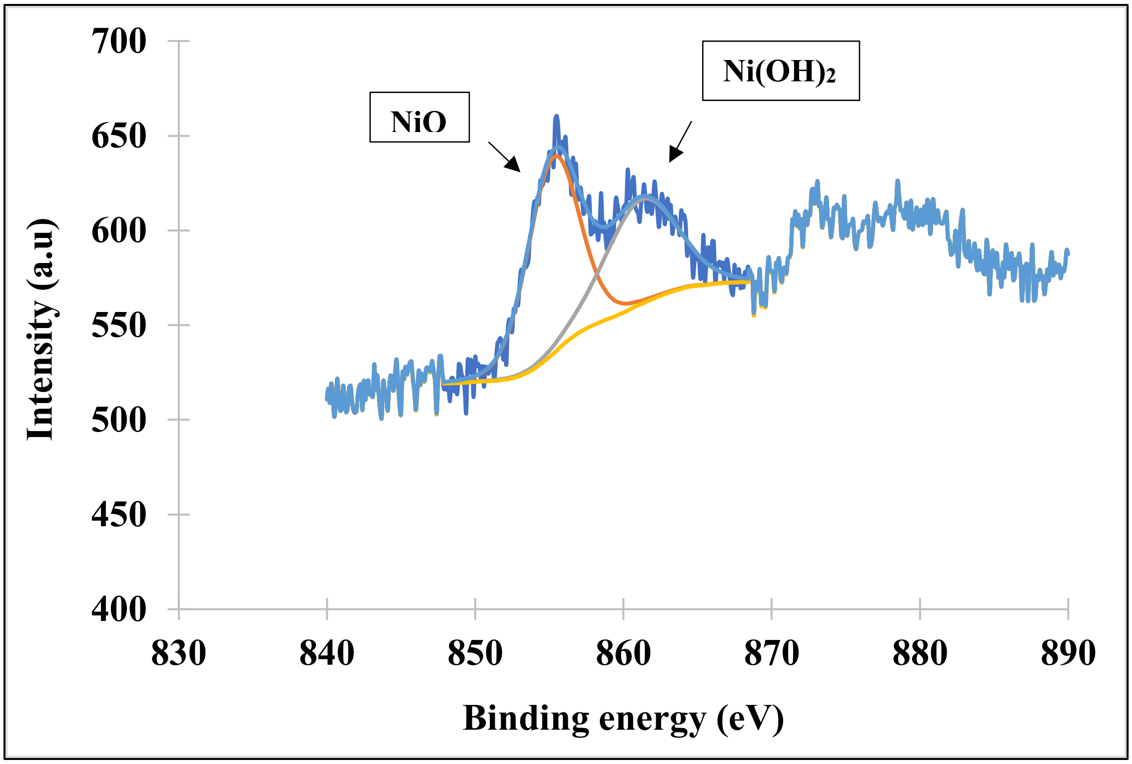

Figure B.10: The deconvolution of Ni $2p_{3/2}$ peak for the $PtNi_{0.62}/C(PG)$ catalyst.

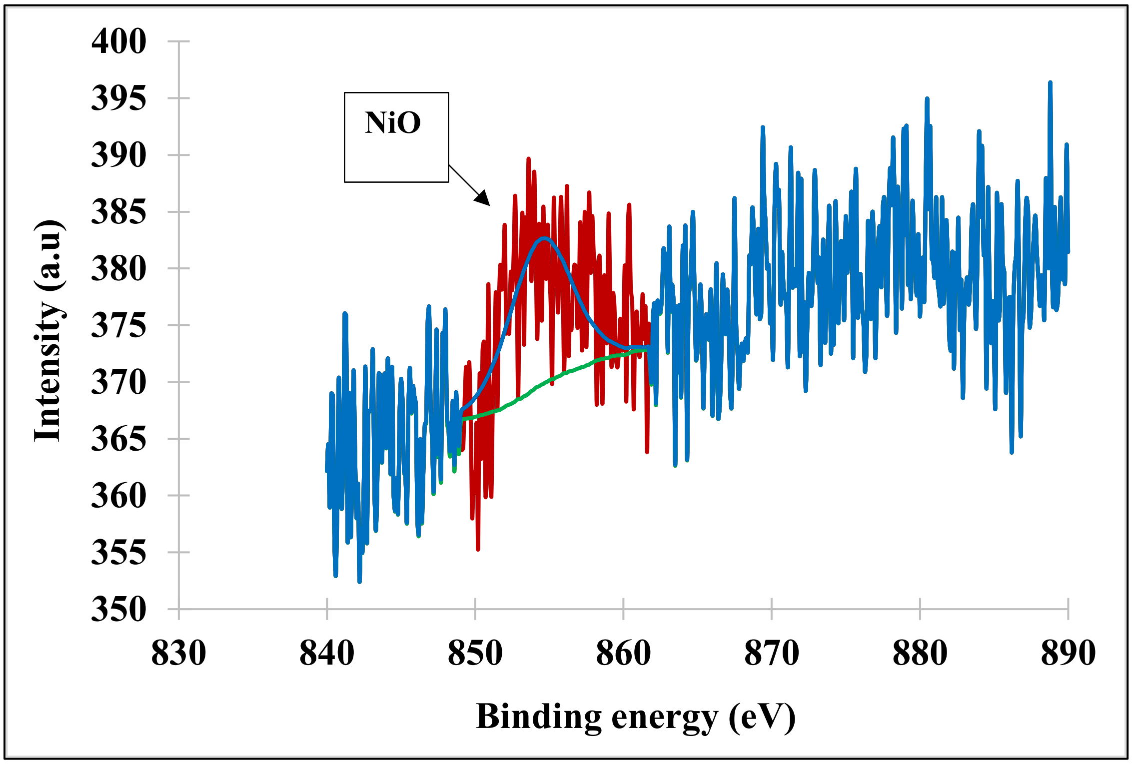

Figure B.11: The deconvolution of Ni $2p_{3/2}$ peak for the $PtNi_{0.48}/C(PG)^{AA}$ catalyst.

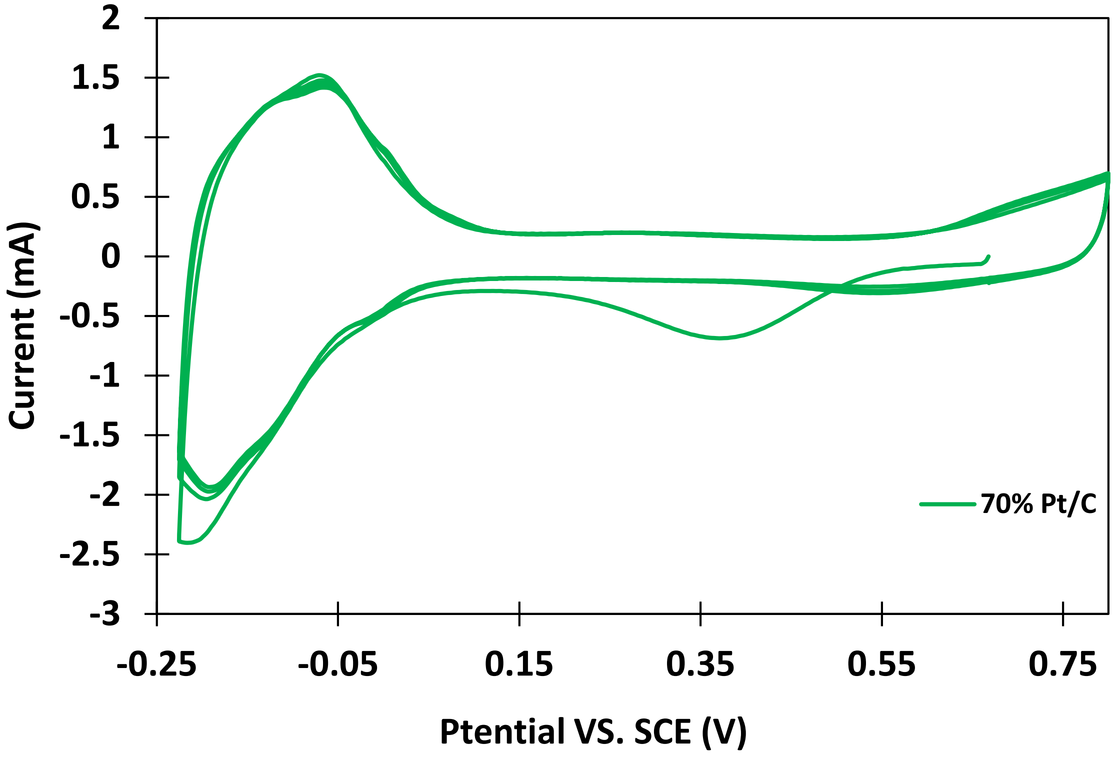

Figure B.12: The Cyclic voltammogram (100 mV s^{-1}; 1 M H_2SO_4(aq)) of the commercial 70% Pt/C catalyst.

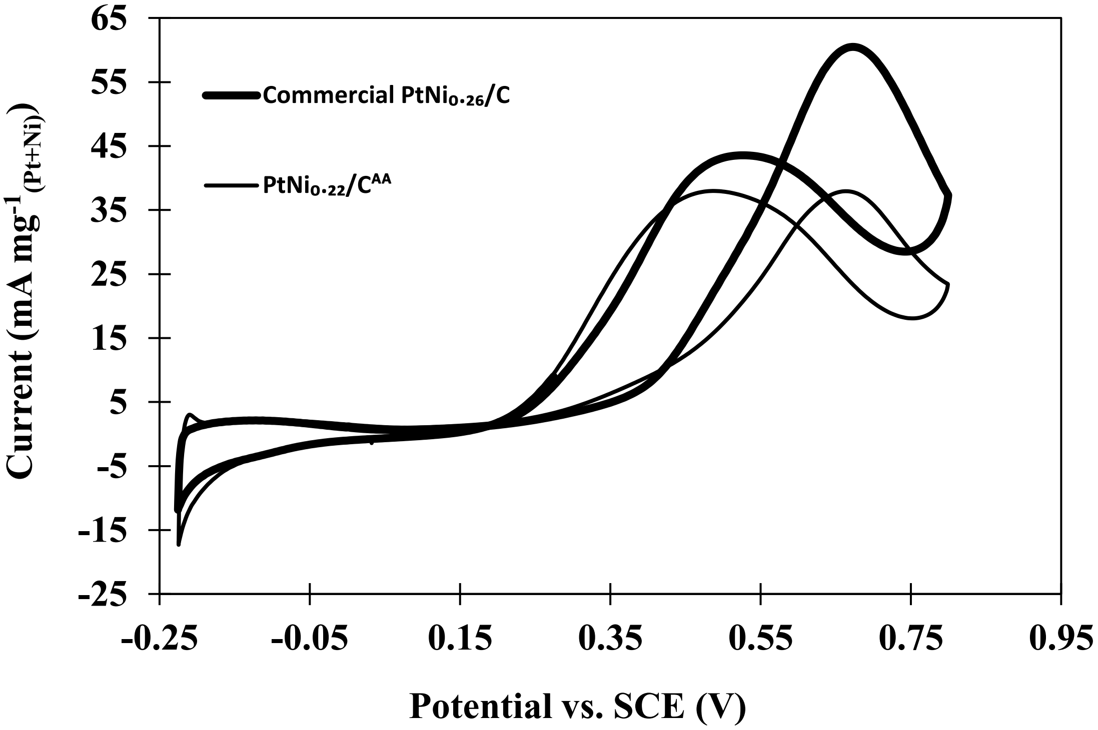

Figure B.13: Cyclic voltammograms (10 mV s^{-1}) in 1 M H_2SO_4 (aq) containing 0.100 M ethanol of the commercial $PtNi_{0.26}/C$ and $PtNi_{0.22}/C^{AA}$ catalysts.

I. Calculated geometric area and the utilization

Geometric area = $N * 4 * \pi * r^2$ $\quad (B1)$

where N is the number of particles and $4\pi r^2$ is the surface of particles

Utilization = $\frac{electroactice\ surface\ area\ (ESCA)}{geometric\ area} * 100\%$ $\quad (B2)$

where the electroactive surface area was measured from the adsorption region in blank CV.

Appendix C

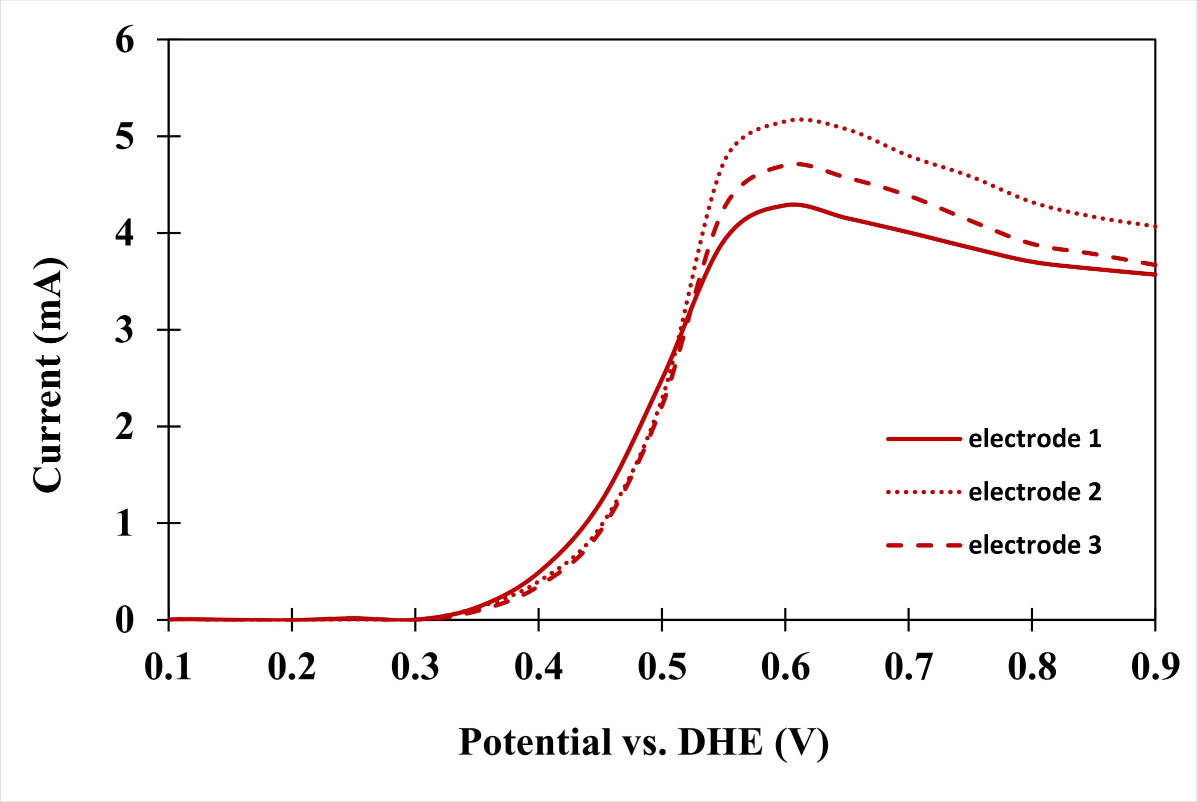

Figure C.1: Polarization curves for the oxidation of 0.100 M ethanol (0.5 mL min^{-1}) at 80 ℃ in a nine-anode PEM cell at three PtNi$_{0.62}$/C(PG) anodes.

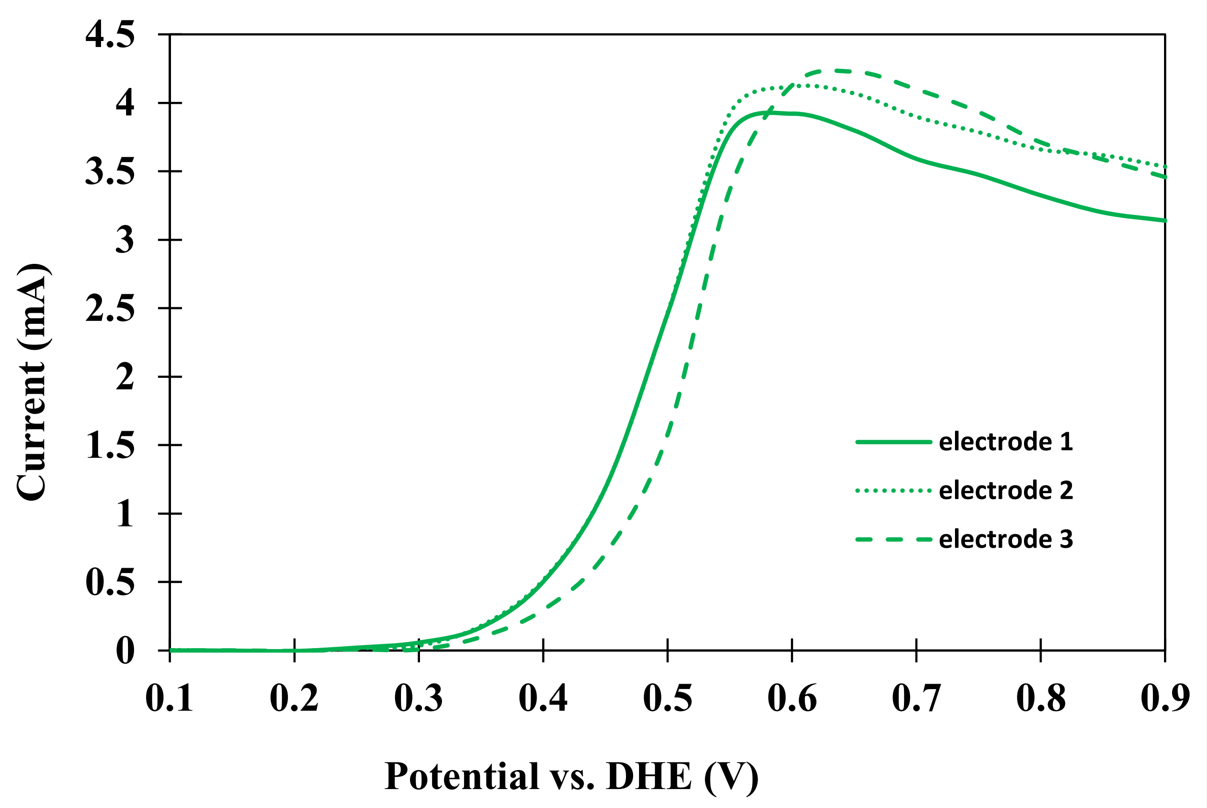

Figure C.2: Polarization curves for the oxidation of 0.100 M ethanol (0.5 mL min^{-1}) at 80 ℃ in a nine-anode PEM cell at three PtNi$_{0.50}$/C(EG) anodes.

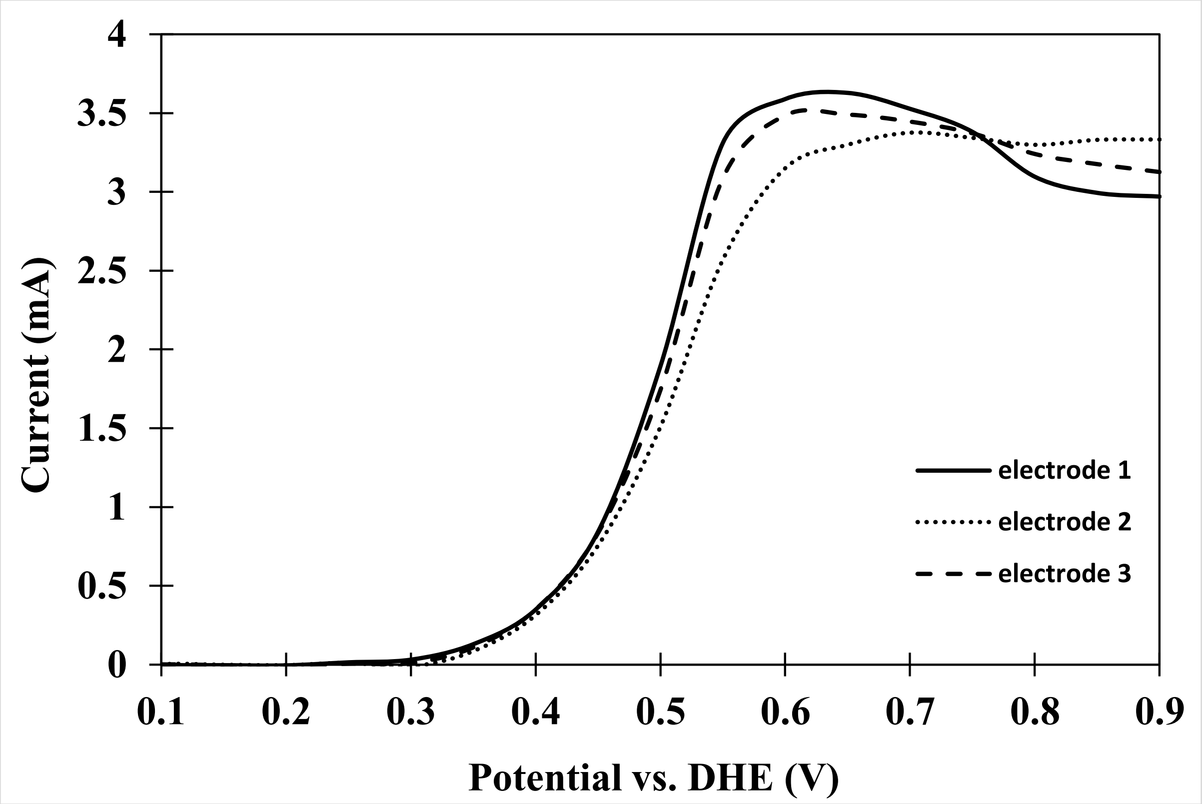

Figure C.3: Polarization curves for the oxidation of 0.100 M ethanol (0.5 mL min^{-1}) at 80 °C in a nine-anode PEM cell at three commercial $PtNi_{0.26}/C$ anodes.

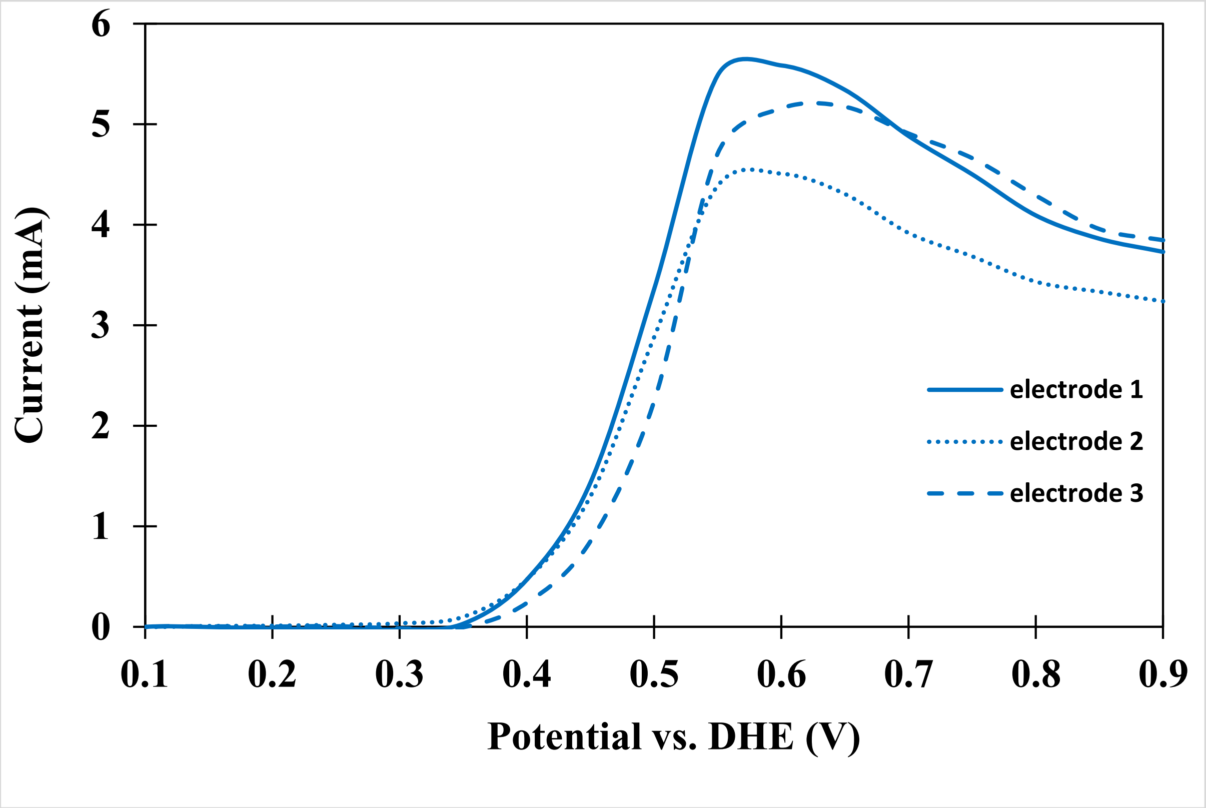

Figure C.4: Polarization curves for the oxidation of 0.100 M ethanol (0.5 mL min^{-1}) at 80 °C in a nine-anode PEM cell at three PtNi$_{0.48}$/C(PG)^{AA} anodes.

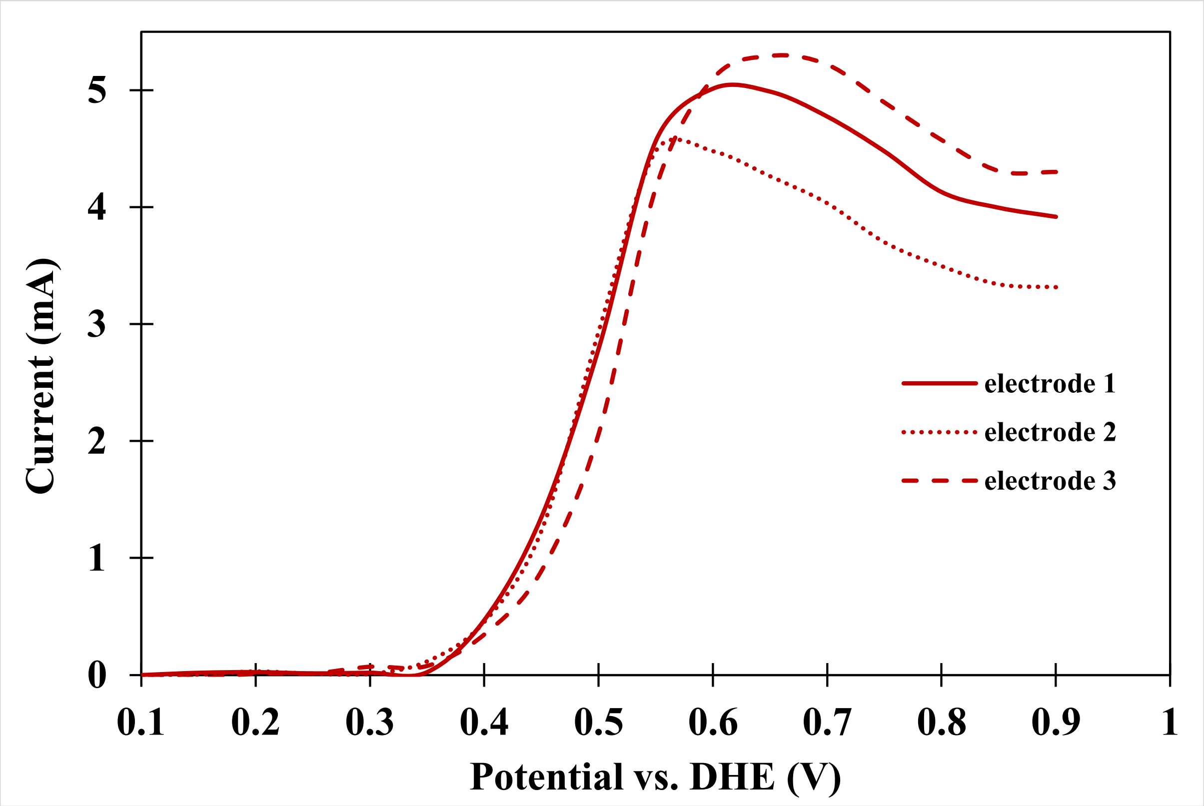

Figure C.5: Polarization curves for the oxidation of 0.100 M ethanol (0.5 mL min^{-1}) at 80 ℃ in a nine-anode PEM cell at three PtNi$_{0.08}$/C(EG)^{AA} anodes.

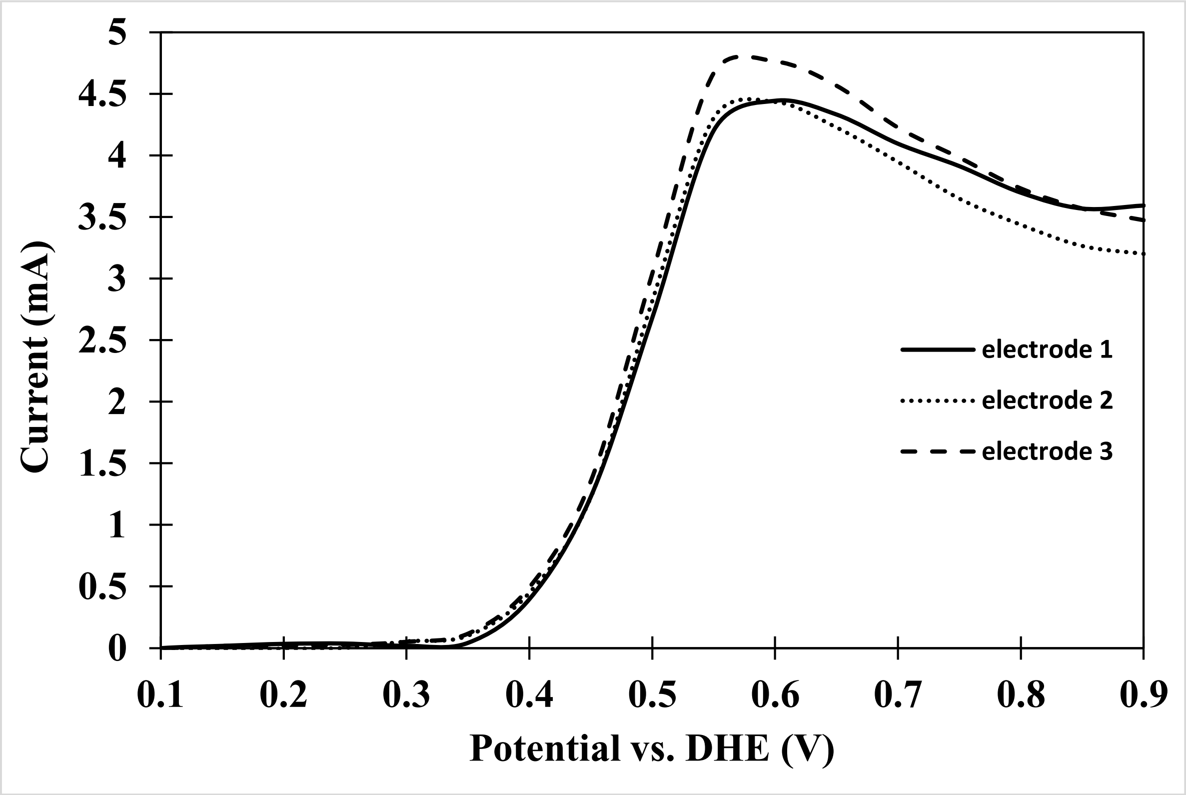

Figure C.6: Polarization curves for the oxidation of 0.100 M ethanol (0.5 mL min^{-1}) at 80 ℃ in a nine-anode PEM cell at three PtNi$_{0.22}$/C^{AA} anodes.

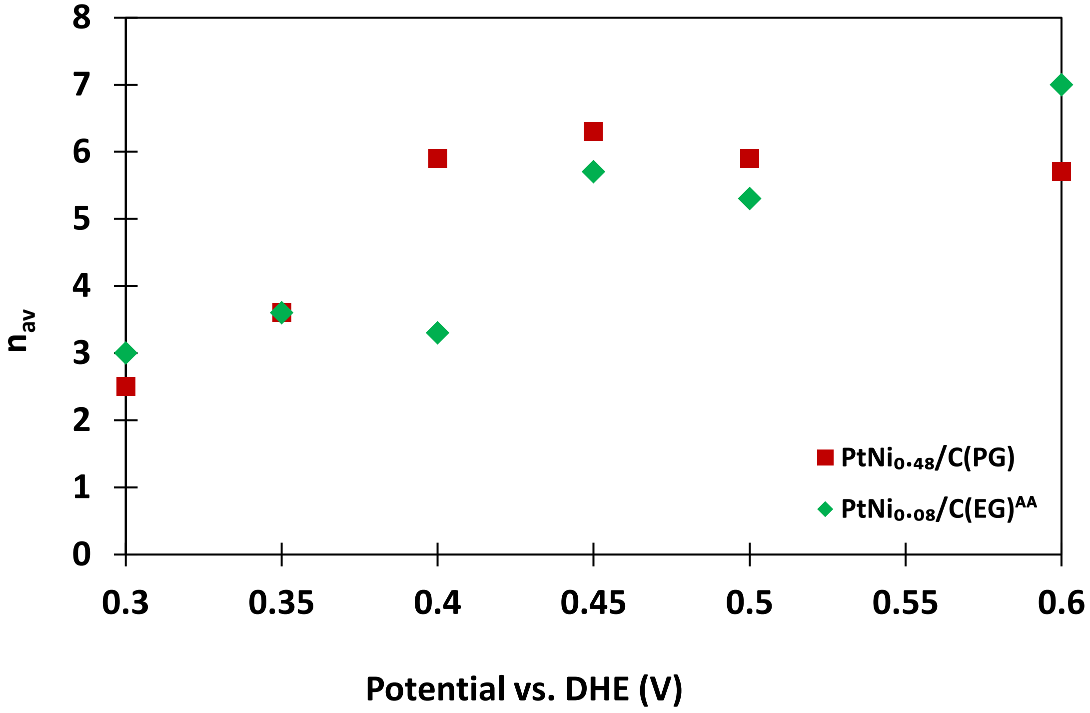

Figure C.7: n_{av} vs. the potential for the oxidation of 0.100 M ethanol (0.2 mL min^{-1}) at PtNi$_{0.48}$/C(PG)^{AA} and PtNi$_{0.08}$/C(EG)^{AA} anodes at 80 °C. Values were calculated from the ethanol consumed by using eq. 4.6.

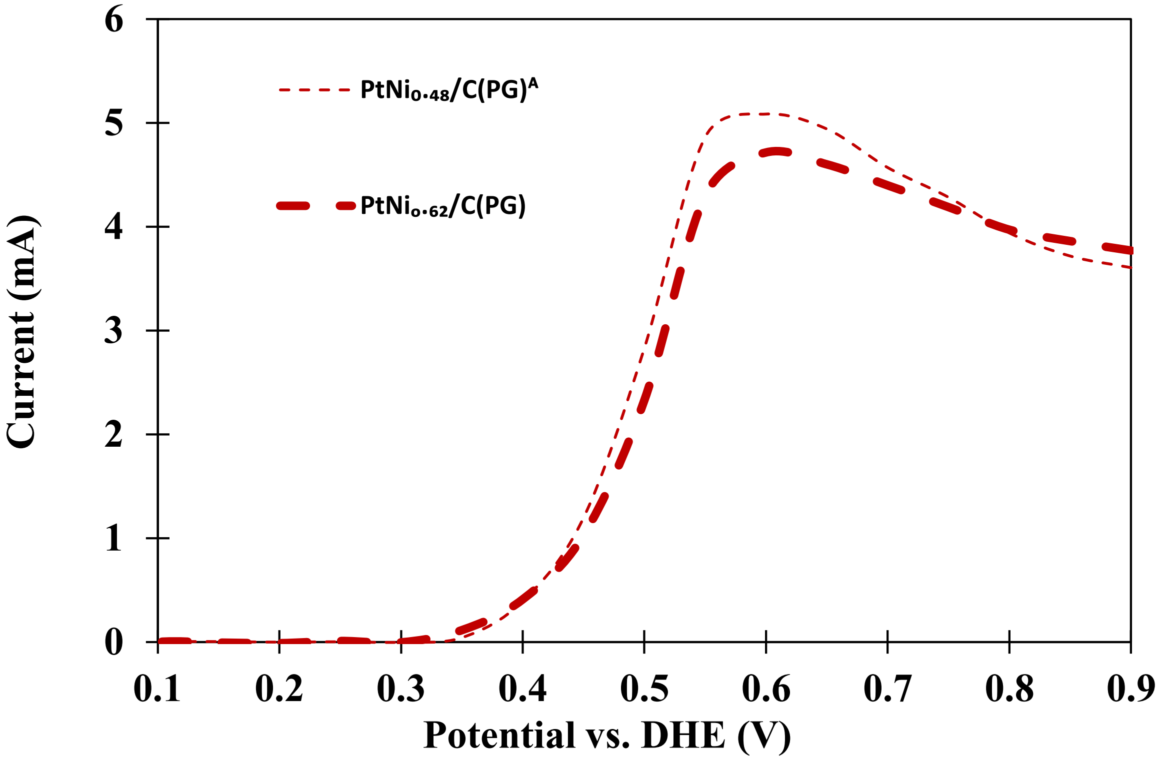

Figure C.8: Polarization curves for the oxidation of 0.100 M ethanol (0.5 mL min^{-1}) at 80 ℃ in a nine-anode PEM cell at PtNi$_{0.62}$/C(PG) and PtNi$_{0.48}$/C(PG)^{AA} anodes.

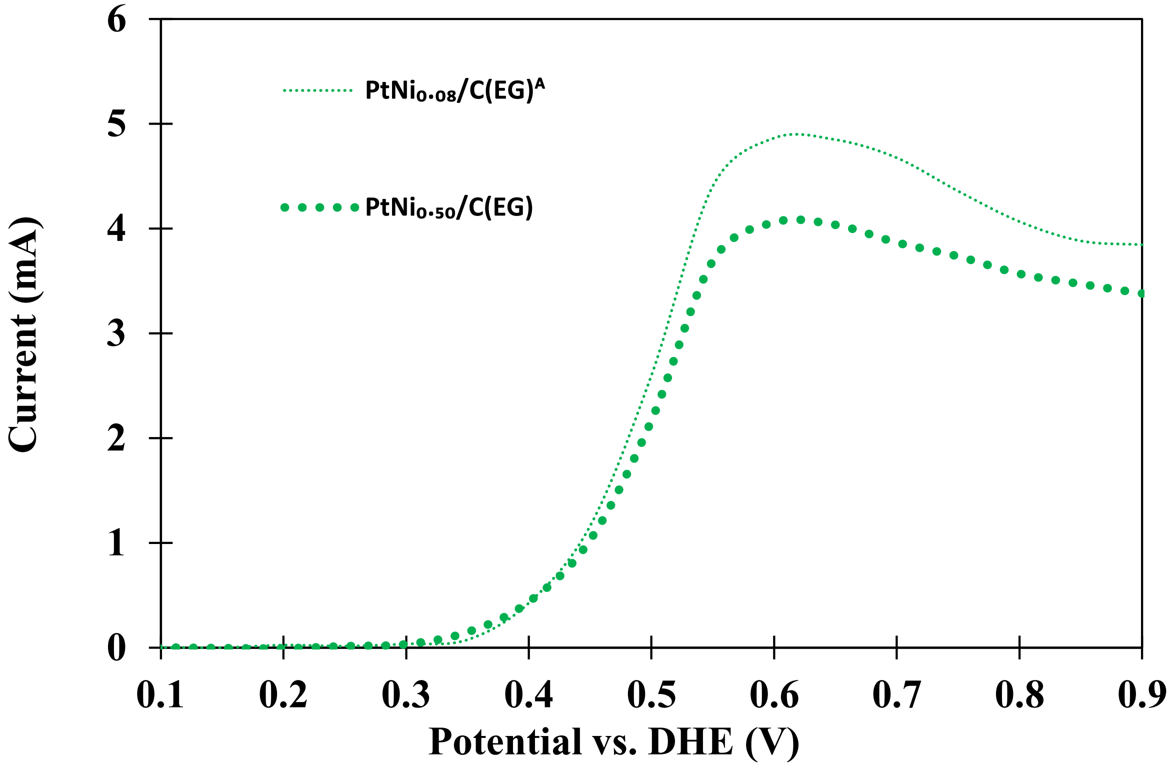

Figure C.9: Polarization curves for the oxidation of 0.100 M ethanol (0.5 mL min^{-1}) at 80 °C in a nine-anode PEM cell at PtNi$_{0.50}$/C(EG) and PtNi$_{0.08}$/C(EG)^{AA} anodes.

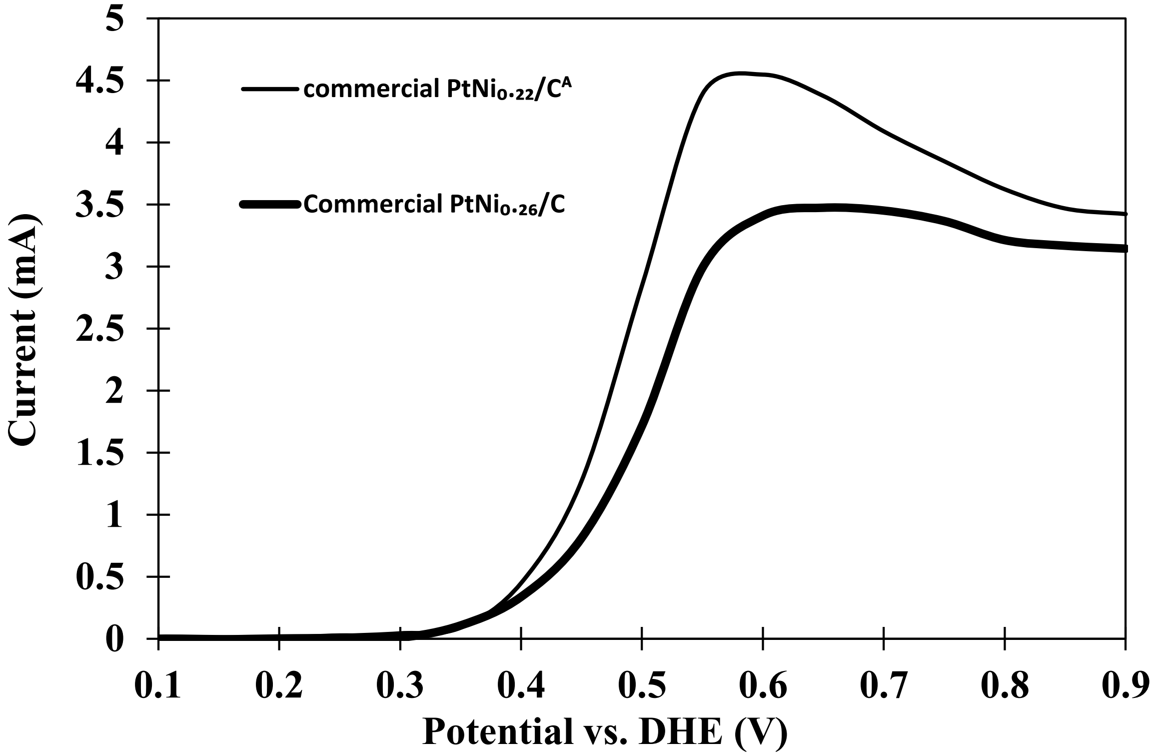

Figure C.10: Polarization curves for the oxidation of 0.100 M ethanol (0.5 mL min^{-1}) at 80 °C in a nine-anode PEM cell at commercial PtNi$_{0.26}$/C and PtNi$_{0.22}$/C^{AA} anodes.

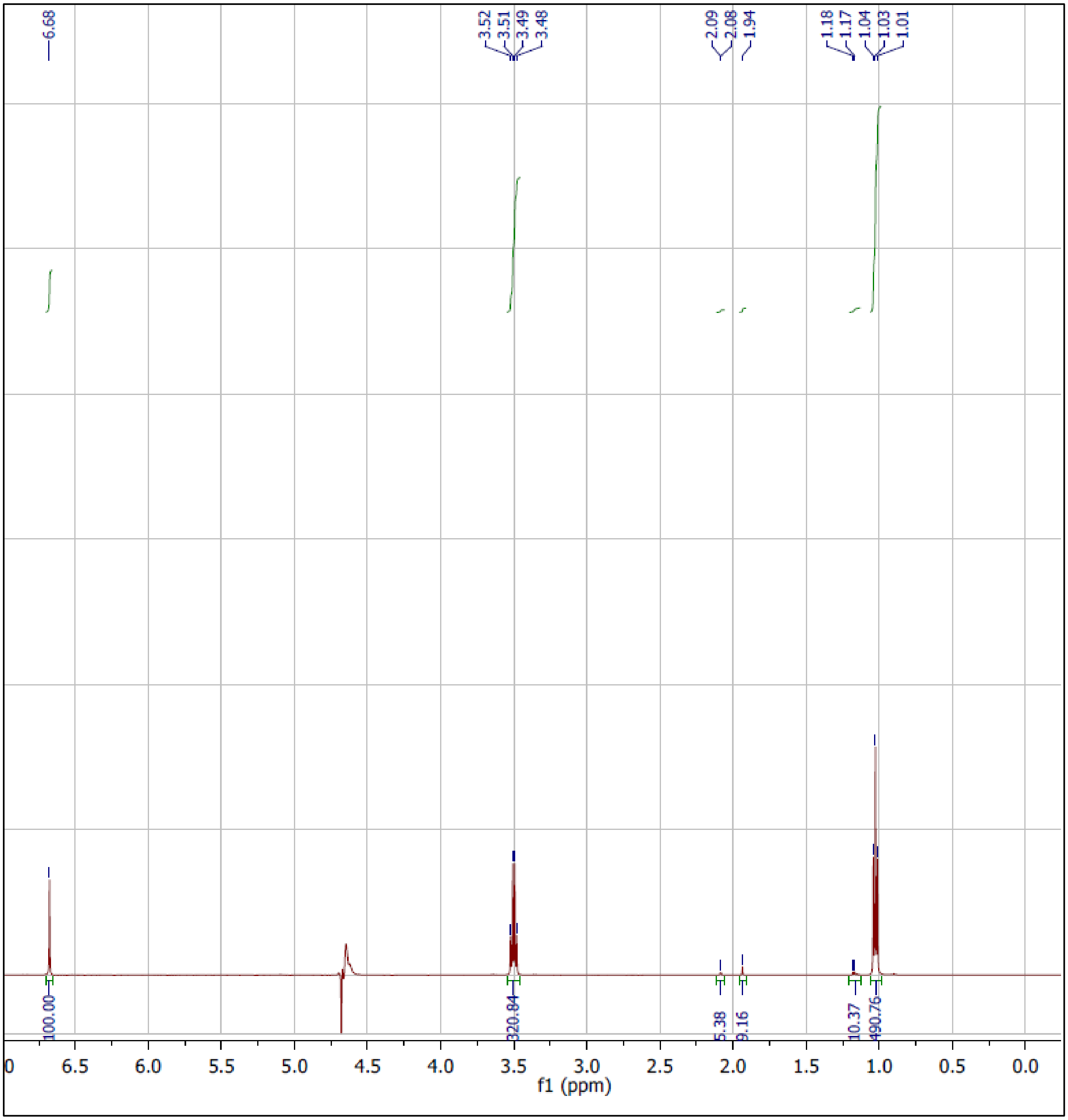

Figure C.11: A ^{1}H NMR spectrum.

Table C.1: n_{av} for the oxidation of 0.100 M ethanol at the $PtNi_{0.48}/C(PG)^{AA}$ anode.

Potentials	n_{av}obtained from eq. 4.5	n_{av} obtained from eq. 4.6
0.6	5.6	5.7
0.5	6.2	5.9
0.45	6.4	6.3
0.4	5.6	5.9
0.35	3.7	3.6
0.3	2.5	2.5

Table C.2: n_{av} for the oxidation of 0.100 M ethanol at the $PtNi_{0.08}/C(EG)^{AA}$ anode

Potentials	$\boldsymbol{n_{av}}$**obtained from eq. 4.5**	$\boldsymbol{n_{av}}$ **obtained from eq. 4.6**
0.6	6.6	7.0
0.5	5.4	5.3
0.45	5.7	5.7
0.4	3.4	3.3
0.35	3.7	3.6
0.3	3.1	3.0

Appendix D

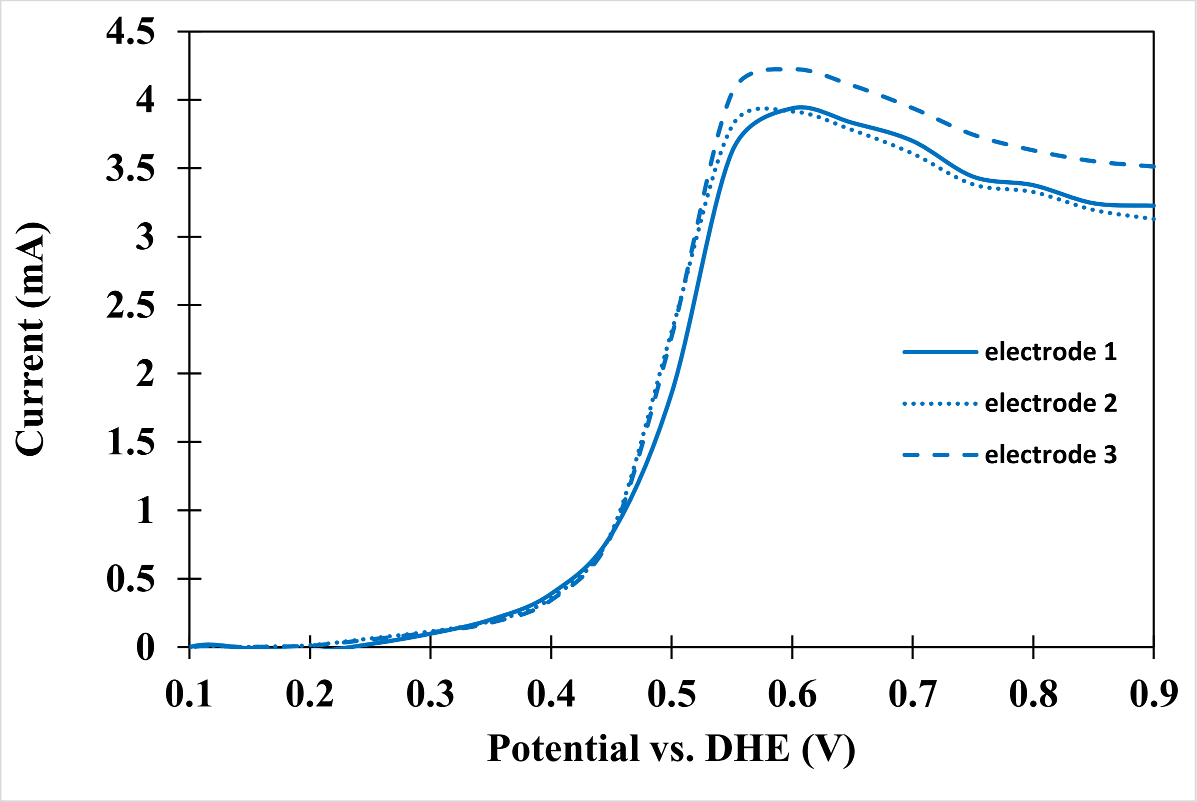

Figure D.1: Polarization curves for the oxidation of 0.100 M ethanol (0.5 mL min^{-1}) at 80 ℃ in a nine-anode PEM cell at three 40% PtNi/C anodes.

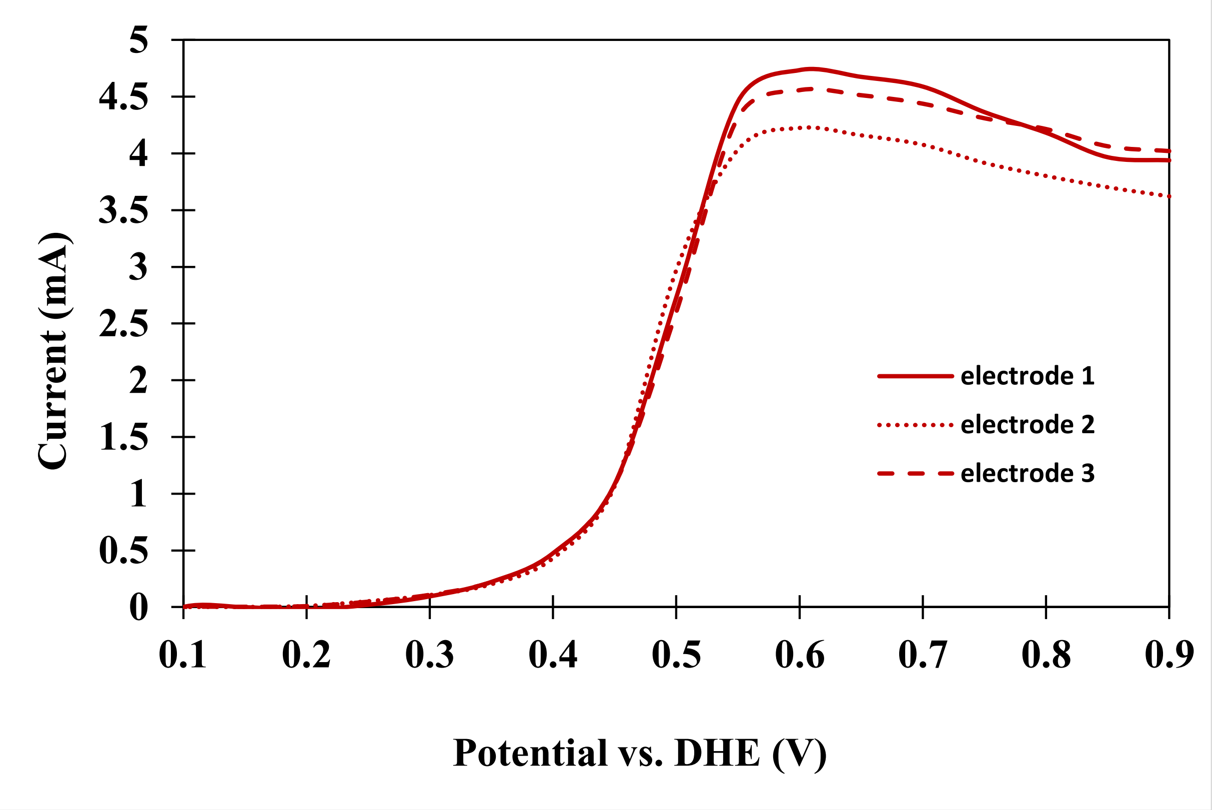

Figure D.2: Polarization curves for the oxidation of 0.100 M ethanol (0.5 mL min^{-1}) at 80 °C in a nine-anode PEM cell at three 20% PtCu/C anodes.

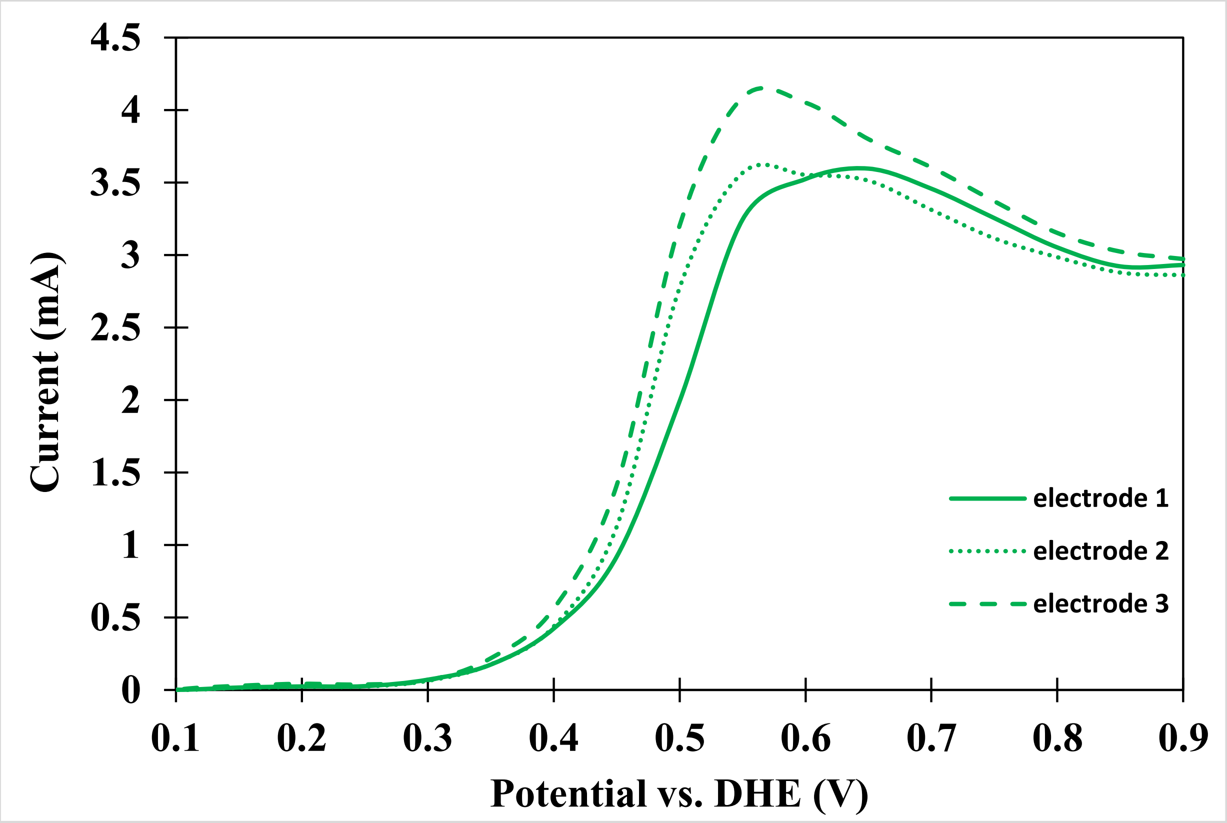

Figure D.3: Polarization curves for the oxidation of 0.100 M ethanol (0.5 mL min^{-1}) at 80 °C in a nine-anode PEM cell at three 40% PtFe/C anodes.

Appendix E

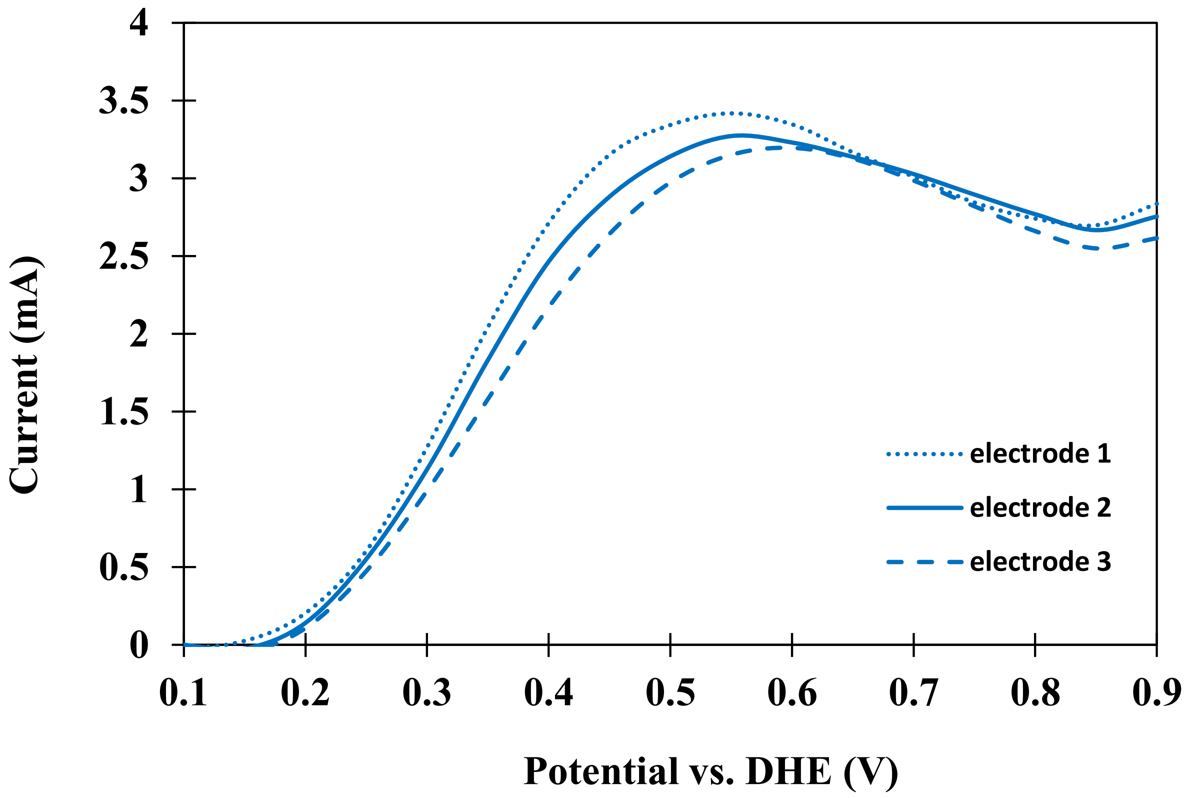

Figure E.1: Polarization curves for the oxidation of 0.100 M ethanol (0.5 mL min^{-1}) at 80 ℃ in a nine-anode PEM cell at three PtRu/C anodes.

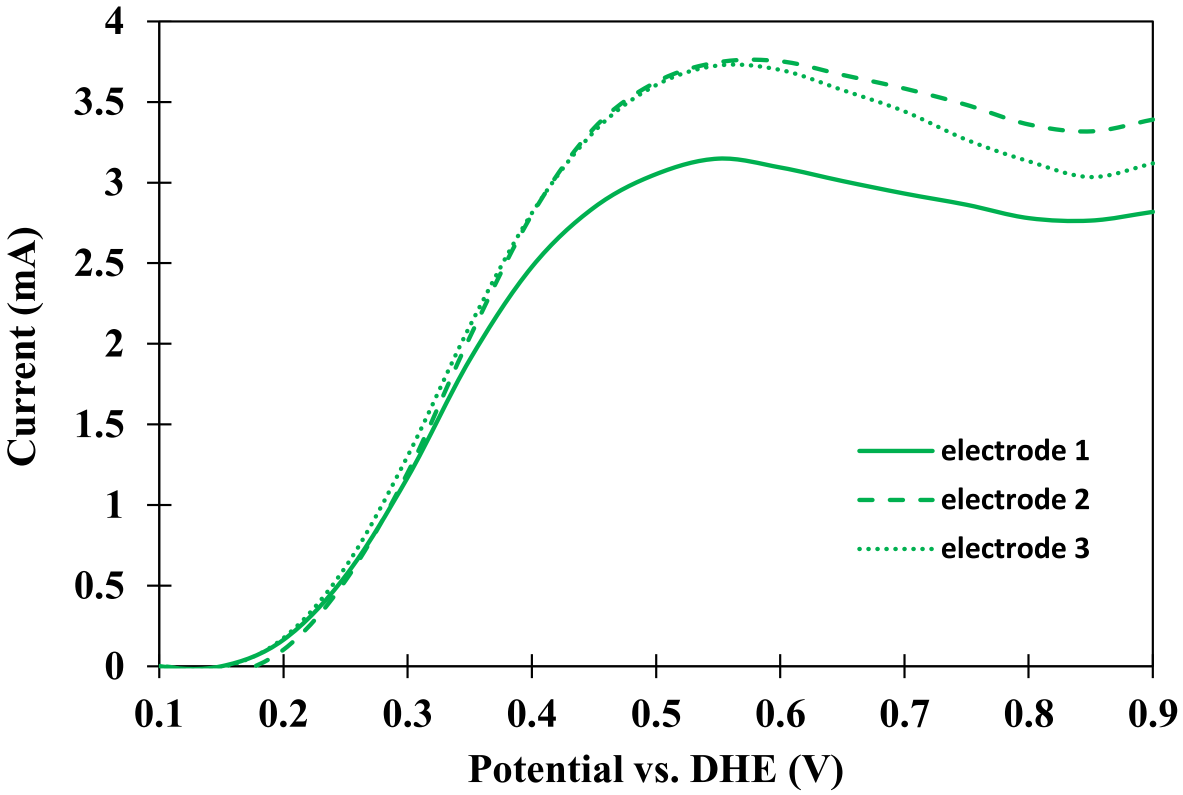

Figure E.2: Polarization curves for the oxidation of 0.100 M ethanol (0.5 mL min^{-1}) at 80 ℃ in a nine-anode PEM cell at three PtRuCu/C anodes.